Biaxial Buckling of Laminated Composite Plates

Young Soo Kim

A Thesis

in

The Department

of

Mechanical Engineering

Presented Partial Fulfillment of the Requirements

for the Degree of Doctor of Philosophy at

Concordia University

Montreal, Quebec, Canada

April 1995

ISBN 0-612-01284-0

Canada

ABSTRACT

Biaxial Buckling of Laminated Composite Plates

Young Soo Kim, Ph.D.
Concordia University, 1995

Buckling behaviour of laminated composite plates subjected to biaxial inplane loading was theoretically studied, numerically analyzed, and experimentally determined. This research was motivated from a need to understand the buckling behaviour of laminated composites in structures such as aircraft fuselages and body-skin of automobiles or ships with various inplane loads and supporting mechanisms.

A plate specimen was developed for this study. The proposed specimen has a slight modification from the ideal rectangular plate and its admissibility was fully investigated with nonlinear finite element analysis (N-FEA) and experiments. Deflection characteristics using different boundary conditions of the postbuckled plates were also experimentally investigated to obtain admissible analytical deflection functions and boundary conditions for the theoretical and numerical analyses. Experimental values of the strains and deflections at the centre and rim of the plates were compared with the results from N-FEA to find governing deflection function for the theoretical formulations. N-FEA was carried out for the two types of boundary conditions, i.e. uniform pressure and uniform end-shortening, to simulate the actual boundary behaviour of plate in experiments. Comparing experimental results with the two N-FEA results for the two different boundary conditions, it was found that results using N-FEA with the uniform pressure loading condition agreed better with experimental results.

For the analysis of the critical buckling load of biaxially loaded plates, solutions of classical laminated plate theory (CLPT) were compared with results from linear or nonlinear finite element analyses (L-FEA, N-FEA) and experiments. In addition, effects of biaxial load ratios, k, on the critical buckling load and postbuckling response were experimentally determined and compared with analytical results.

For biaxial buckling, effects of flexural stiffness ratio, ζ, and inplane stiffness ratio, ξ, induced from the stacking sequence variation were investigated through nonlinear finite element analyses and experiments.

In addition to the extended application of Southwell Plot Buckling Criterion (SPBC), a new buckling criterion, Minimum Slope Buckling Criterion (MSBC), was proposed for the experimental determination of catastrophic buckling failure load of composite plates.

ACKNOWLEDGEMENTS

I would like to thank all those faculty members who have contributed to my education. In particular, I wish to express my sincere appreciation to my supervisor, Professor S. V. Hoa, for his continued encouragement and support. I also thank Professor C. Marsh, Professor H. K. Ha, Professor A. E. Blach and Professor X. R. Xiao for their encouragement.

Many thanks to the graduate students of the Department of Mechanical Engineering for their friendship. I am also grateful to all members of the CONCORDIA CENTRE FOR COMPOSITES for many fruitful discussions and suggestions. I much appreciate the help of Mr. P. Ouellette, Mr. D. Lefebvre and Ms. L. Li, in the preparation of my experiments.

I thank my wife, Jiwon, for her patience and encouragement which she gave so devotedly and also my children, Junghyang, Jungbeen and Jungeun, for the refreshing distraction which they provided. I also thank my parents and parents-in-law for their support and encouragement.

Contents

List of Figures ix

List of Tables xxii

List of Symbols xxiii

List of Acronyms xxv

1 Introduction 1

1.1 Background 1

1.2 Review of Previous Works 3

1.2.1 Theoretical Works 3

1.2.2 Numerical Works 6

1.2.3 Experimental Works 7

1.3 Objectives of the research 10

2 Plate Buckling Theory 13

2.1 Classical Laminated Plate Theory 13

2.2 Buckling Criteria of Simply Supported Plate 24

3 Development of Biaxial Plate Specimen 27

3.1 Design of Biaxial Plate Specimen 27

3.1.1 Ideal and Modified Plate Specimen 27

3.1.2 Fabrication of Modified Plate Specimen 28
3.2 Validity of Modified Plate Specimen 36
3.2.1 Numerical Validation 36
3.2.2 Experimental Validation 49

4 Boundary Conditions Considerations **55**
4.1 Boundary behaviour of Postbuckled Plate 55
4.2 Simply Supported Boundary Conditions 56
4.3 Closed Form Solution by Energy Method 58
4.3.1 Ritz Method for Postbuckling behaviour 58
4.3.2 A Closed Form Solution for Uniform End-Shortening 60
4.4 Uniform Pressure and Uniform End-Shortening 63
4.5 Selection of Boundary Conditions 63

5 Numerical Analysis for Biaxial Buckling **68**
5.1 Finite Element Analysis 68
5.2 Effect of Stiffness Ratio (Cross-ply Laminate) 73
5.2.1 16-layer Plate Specimen 74
5.2.2 20-layer Plate Specimen 110
5.3 Effect of Layup Angle 128
5.3.1 16-layer Plate Specimen 128
5.3.2 20-layer Plate Specimen 140

6 Biaxial Buckling Experiments **143**
6.1 Biaxial Testing Machine 143
6.2 Visualization by Shadow Moiré 144
6.3 Buckling Experiments 148
6.3.1 Uniaxial Loading Experiments 148
6.3.2 Biaxial Loading Experiments 161

6.3.3 Shadow Moiré Experiments 168
6.4 Experimental Buckling Criteria 177
6.4.1 Southwell Plot Buckling Criterion (SPBC) 177
6.4.2 Minimum Slope Buckling Criterion (MSBC) 182

7 Discussion **184**
7.1 Reliability of Modified Plate Specimen 184
7.2 Effect of Laminate Thickness 186
7.3 Effect of Layup Angle 189
7.4 Effect of Stiffness Ratio 192
7.4.1 Orthotropic Specimen 192
7.4.2 Anisotropic Specimen 200
7.4.3 Mode Jumping Analysis 205

8 Contributions and Conclusions **208**

Bibliography **210**

List of Figures

1.1 Typical buckling behaviour of simply supported rectangular plates showing a stable equilibrium path, a) under biaxial loading, b) under uniaxial loading. 4

1.2 View of biaxial buckling test of Graphite/Epoxy composite laminated plate. 10

2.1 Description of inplane stress resultants. 15

2.2 Description of moments and shear stress resultants. 15

2.3 Rotation angle between on-axes(x-y) and off-axes(x'-y'). 19

3.1 Schematic drawings of the biaxial loading device. a) Ideal setup, b) Modified setup. 29

3.2 Cure cycle of the plate specimens. 30

3.3 The S-line for strain comparison between ideal plate specimen and modified plate specimen by N-FEA. 38

3.4 Input data for N-FEA of ideal plate (1:meshed elements, 2:nodal points, 3:prescribed loads, 4:boundary conditions). 39

3.5 Input data for N-FEA of modified plate (1:meshed elements, 2:nodal points, 3:prescribed loads, 4:boundary conditions). 40

3.6 Fffects of specimen modifications on the critical buckling loads of biaxially loaded OP-16-11 plate from L-FEA and N-FEA. 41

3.7 Specimen modification effects on the biaxial buckling behaviour of OP-16-11 plate from N-FEA. 42
3.8 Continuous buckling deformation of ideal plate specimen OP-16-11 with biaxial loading ($P_x : P_y = 1 : 1$) from N-FEA. 43
3.9 Continuous buckling deformations of modified plate specimen OP-16-11 with biaxial loading ($P_x : P_y = 1 : 1$) from N-FEA. 44
3.10 X-strain (strain along x-direction, ϵ_x) distribution along x direction of ideal plate specimen OP-16-11 with biaxial loading, $P_x = P_y = 3$kN ($P_x : P_y = 1 : 1$), from N-FEA. 45
3.11 Y-strain (strain along y-direction, ϵ_y) distribution of ideal plate specimen OP-16-11 with biaxial loading, $P_x = P_y = 3$kN ($P_x : P_y = 1 : 1$), from N-FEA. 46
3.12 X-strain(ϵ_x) distribution of modified plate specimen OP-16-11 with biaxial loading, $P_x = P_y = 3$kN ($P_x : P_y = 1 : 1$), from N-FEA. 47
3.13 Y-strain(ϵ_y) distribution of modified plate specimen OP-16-11 with biaxial loading, $P_x = P_y = 3$kN ($P_x : P_y = 1 : 1$), from N-FEA. 48
3.14 Location of strain gauges on the experimental plate specimens, a) front side, b) back side. 51
3.15 Experimental setup of loading grips with a modified specimen. 51
3.16 Y-strains, ϵ_y, along the S-line of OP-16-11(see Figure 3.3) ideal plate specimen with various biaxial loadings from N-FEA. 52
3.17 Y-strains, ϵ_y, along the S-line of OP-16-11(see Figure 3.3) modified plate specimen with various biaxial loadings from N-FEA. 52
3.18 Strains at plate centre for OP-16-11 modified plate under biaxial loading with N-FEA. 53
3.19 Comparing the experimental and numerical strains for OP-16-11 modified plate at plate centre, under biaxial loading. 53

3.20 Y-strains along the S-line for OP-16-11 modified plate under biaxial loading with N-FEA. 54
3.21 Comparing the experimental y-strains along the S-line for OP-16-11 modified plate under biaxial loading with N-FEA. 54

4.1 Postbuckled shapes and stresses of simply supported plate under biaxial loading. a) Actual behaviour, b) Assumed as uniform pressure loading, c) Assumed as uniform end-shortening. 57
4.2 Plate specimen and its supporting mechanism. a) Ideal and modified specimen with strain gauge, b) Various simple supporting conditions. . 62
4.3 Axial load and boundary stress distributions for Plate#1 with uniform end-shortening condition. a) Axial load vs. n, b) Boundary stresses vs. n. 65
4.4 Boundary displacement at postbuckling state for Plate#2 with uniform edge stress in compression. a) N-FEA for ideal plate, b) N-FEA for modified plate. 65
4.5 Biaxial postbuckling behaviour (axial load vs. deflection) for composite plate, Plate#2, when $P_x : P_y = 1 : 1$. a) N-FEA for ideal plate, b) N-FEA for modified plate (Note: i=ideal, m=modified, ud=uniform end-shortening, up=uniform pressure). 66
4.6 Experimental and N-FEA postbuckling behaviour(P_x vs. w_{max}) for Plate#2. a) Experiment with $P_x : P_y = 1 : 1$, b) Experiment with $P_x : P_y = 1 : 0.9$ 67

5.1 A sketch on the SHELL99 in ANSYS program : 3-D 8-node shell element 72
5.2 X-axis uniaxial loading behaviour of the 16-layer orthotropic plates for various flexural stiffness ratio, $\zeta = 1.4 \sim 14.3$, by N-FEA. 76
5.3 Successive views of postbuckling behaviour of the 16-layer orthotropic plate, OP-16-11, with uniaxial loading along x-axis ($P_x : P_y = 1 : 0$). . 77

5.4 Successive views of postbuckling behaviour of the 16-layer orthotropic plate, OP-16-44, with uniaxial loading along x-axis ($P_x : P_y = 1 : 0$). . 78
5.5 Successive views of postbuckling behaviour of the 16-layer orthotropic plate, OP-16-71, with uniaxial loading along x-axis ($P_x : P_y = 1 : 0$). . 79
5.6 X-strain(ϵ_x) distribution of the 16-layer orthotropic plate, OP-16-11 with uniaxial loading along x-axis, $P_x = 5$kN ($P_x : P_y = 1 : 0$). 80
5.7 Y-strain(ϵ_y) distribution of the 16-layer orthotropic plate, OP-16-11 with uniaxial loading along x-axis, $P_x = 5$kN ($P_x : P_y = 1 : 0$). 81
5.8 X-strain(ϵ_x) distribution of the 16-layer orthotropic plate, OP-16-44 with uniaxial loading along x-axis, $P_x = 5$kN ($P_x : P_y = 1 : 0$). 82
5.9 Y-strain(ϵ_y) distribution of the 16-layer orthotropic plate, OP-16-44 with uniaxial loading along of x-axis, $P_x = 5$kN ($P_x : P_y = 1 : 0$). 83
5.10 X-strain(ϵ_x) distribution of the 16-layer orthotropic plate, OP-16-71 with uniaxial loading along x-axis, $P_x = 5$kN ($P_x : P_y = 1 : 0$). 84
5.11 Y-strain(ϵ_y) distribution of the 16-layer orthotropic plate, OP-16-71 with uniaxial loading along x-axis, $P_x = 5$kN ($P_x : P_y = 1 : 0$). 85
5.12 Y-axis uniaxial loading behaviour of the 16-layer orthotropic plates for various flexural stiffness ratio, $\zeta = 1.4 \sim 14.3$, by N-FEA. 88
5.13 Successive views of postbuckling behaviour of the 16-layer orthotropic plate, OP-16-11, with uniaxial loading along y-axis ($P_x : P_y = 0 : 1$). . 89
5.14 Successive views of postbuckling behaviour of the 16-layer orthotropic plate, OP-16-44, with uniaxial loading along y-axis ($P_x : P_y = 0 : 1$). . 90
5.15 Successive view of postbuckling behaviour of the 16-layer orthotropic plate, OP-16-71, with uniaxial loading along y-axis ($P_x : P_y = 0 : 1$). . 91
5.16 X-strain(ϵ_x) distribution of the 16-layer orthotropic plate, OP-16-11 with uniaxial loading along y-axis, $P_x = 5$kN ($P_x : P_y = 0 : 1$). 92
5.17 Y-strain(ϵ_y) distribution of the 16-layer orthotropic plate, OP-16-11 with uniaxial loading along y-axis, $P_x = 5$kN ($P_x : P_y = 0 : 1$). 93

5.18 X-strain(ϵ_x) distribution of the 16-layer orthotropic plate, OP-16-44 with uniaxial loading along y-axis, $P_x = 5$kN ($P_x : P_y = 0 : 1$). 94
5.19 Y-strain(ϵ_y) distribution of the 16-layer orthotropic plate, OP-16-44 with uniaxial loading along y-axis, $P_x = 5$kN ($P_x : P_y = 0 : 1$). 95
5.20 X-strain(ϵ_x) distribution of the 16-layer orthotropic plate, OP-16-71 with uniaxial loading along y-axis, $P_x = 5$kN ($P_x : P_y = 0 : 1$). 96
5.21 Y-strain(ϵ_y) distribution of the 16-layer orthotropic plate, OP-16-71 with uniaxial loading along y-axis, $P_x = 5$kN ($P_x : P_y = 0 : 1$). 97
5.22 Biaxial buckling behaviour for various flexural stiffness ratio, $\zeta = 1.4 \sim 14.3$, on the 16-layer orthotropic plates by N-FEA. 100
5.23 Successive views of postbuckling behaviour of the 16-layer ortnotropic plate, OP-16-11, with biaxial loadings ($P_x : P_y = 1 : 1$). 101
5.24 Successive views of postbuckling behaviour of the 16-layer orthotropic plate, OP-16-44, with biaxial loadings ($P_x : P_y = 1 : 1$). 102
5.25 Successive views of postbuckling behaviour of the 16-layer orthotropic plate, OP-16-71, with biaxial loadings ($P_x : P_y = 1 : 1$). 103
5.26 X-strain(ϵ_x) distribution of the 16-layer orthotropic plate, OP-16-11 with biaxial loadings, $P_x = P_y = 3$kN ($P_x : P_y = 1 : 1$). 104
5.27 Y-strain(ϵ_y) distribution of the 16-layer orthotropic plate, OP-16-11 with biaxial loadings, $P_x = P_y = 3$kN ($P_x : P_y = 1 : 1$). 105
5.28 X-strain(ϵ_x) distribution of the 16-layer orthotropic plate, OP-16-44 with biaxial loadings, $P_x = P_y = 3$kN ($P_x : P_y = 1 : 1$). 106
5.29 Y-strain(ϵ_y) distribution of the 16-layer orthotropic plate, OP-16-44 with biaxial loadings, $P_x = P_y = 3$kN ($P_x : P_y = 1 : 1$). 107
5.30 X-strain(ϵ_x) distribution of the 16-layer orthotropic plate, OP-16-71 with biaxial loadings, $P_x = P_y = 3$kN ($P_x : P_y = 1 : 1$). 108
5.31 Y-strain(ϵ_y) distribution of the 16-layer orthotropic plate, OP-16-71 with biaxial loadings, $P_x = P_y = 3$kN ($P_x : P_y = 1 : 1$). 109

5.32 X-axis uniaxial loading behaviour of the 20-layer orthotropic plates for various flexural stiffness ratio, $\zeta = 1.3 \sim 14.3$, by N-FEA. 111
5.33 Successive views of postbuckling behaviour of the 20-layer orthotropic plate, OP-20-11, with uniaxial loading along x-axis ($P_x : P_y = 1 : 0$). . 112
5.34 Successive views of postbuckling behaviour of the 20-layer orthotropic plate, OP-20-55, with uniaxial loading along x-axis ($P_x : P_y = 1 : 0$). . 113
5.35 Successive views of postbuckling behaviour of the 20-layer orthotropic plate, OP-20-82, with uniaxial loading along x-axis ($P_x : P_y = 1 : 0$). . 114
5.36 Successive views of postbuckling behaviour of the 20-layer orthotropic plate, OP-20-100, with uniaxial loading along x-axis ($P_x : P_y = 1 : 0$). . 115
5.37 Y-axis uniaxial loading behaviour of the 20-layer orthotropic plates for various flexural stiffness ratio, $\zeta = 1.3 \sim 14.3$, by N-FEA. 117
5.38 Successive views of postbuckling behaviour of the 20-layer orthotropic plate, OP-20-11, with uniaxial loading along y-axis ($P_x : P_y = 0 : 1$). . 118
5.39 Successive views of postbuckling behaviour of the 20-layer orthotropic plate, OP-20-55, with uniaxial loading along y-axis ($P_x : P_y = 0 : 1$). . 119
5.40 Successive views of postbuckling behaviour of the 20-layer orthotropic plate, OP-20-82, with uniaxial loading along y-axis ($P_x : P_y = 0 : 1$). . 120
5.41 Successive views of postbuckling behaviour of the 20-layer orthotropic plate, OP-20-100, with uniaxial loading along y-axis ($P_x : P_y = 0 : 1$). . 121
5.42 Biaxial buckling behaviour of the 20-layer orthotropic plates for various flexural stiffness ratio, $\zeta = 1.3 \sim 14.3$, by N-FEA. 123
5.43 Successive views of postbuckling behaviour of the 20-layer orthotropic plate, OP-20-11, with biaxial loadings ($P_x : P_y = 1 : 1$). 124
5.44 Successive views of postbuckling behaviour of the 20-layer orthotropic plate, OP-20-55, with biaxial loadings ($P_x : P_y = 1 : 1$). 125
5.45 Successive views of postbuckling behaviour of the 20-layer orthotropic plate, OP-20-82, with biaxial loadings ($P_x : P_y = 1 : 1$). 126

5.46 Successive views of postbuckling behaviour of the 20-layer orthotropic plate, OP-20-100, with biaxial loadings ($P_x : P_y = 1 : 1$). 127
5.47 Effects of layup angle on the x-loaded buckling ($P_x : P_y = 1 : 0$) of the 16-layup orthotropic laminate with changing layup angle from (0/-90) to (60/-30) by N-FEA. 130
5.48 X-strain(ϵ_x) distribution of the 16-layer generally orthotropic plate, OP-16-45 with ((45/-45)x4), by x-uniaxial loading of $P_x = 10$kN ($P_x : P_y = 1 : 0$). 131
5.49 Y-strain(ϵ_y) distribution of the 16-layer generally orthotropic plate, OP-16-45 with ((45/-45)x4), by x-uniaxial loading of $P_x = 10$kN ($P_x : P_y = 1 : 0$). 132
5.50 X-strain(ϵ_x) distribution of the 16-layer generally orthotropic plate, OP-16-63 with ((60/-30)x4), by x-uniaxial loading of $P_x = 10$kN ($P_x : P_y = 1 : 0$). 133
5.51 Y-strain(ϵ_y) distribution of the 16-layer generally orthotropic plate, OP-16-63 with ((60/-30)x4), by x-uniaxial loading of $P_x = 10$kN ($P_x : P_y = 1 : 0$). 134
5.52 Effects of layup angle on the biaxial loading ($P_x : P_y = 1 : 1$) of the 16-layup orthotropic laminate with changing layup angle from (0/-90) to (60/-30) by N-FEA. 135
5.53 X-strain(ϵ_x) distribution of the 16-layer generally orthotropic plate, OP-16-45 with ((45/-45)x4), by biaxial loading of $P_x = P_y = 5$kN ($P_x : P_y = 1 : 1$). 136
5.54 Y-strain(ϵ_y) distribution of the 16-layer generally orthotropic plate, OP-16-45 with ((45/-45)x4), by biaxial loading of $P_x = P_y = 5$kN ($P_x : P_y = 1 : 1$). 137

5.55 X-strain(ϵ_x) distribution of the 16-layer generally orthotropic plate, OP-16-63 with ((60/-30)x4), by biaxial loading of $P_x = P_y = 5$kN ($P_x : P_y = 1 : 1$). 138
5.56 Y-strain(ϵ_y) distribution of the 16-layer generally orthotropic plate, OP-16-63 with ((60/-30)x4), by biaxial loading of $P_x = P_y = 5$kN ($P_x : P_y = 1 : 1$). 139
5.57 Effects of layup angle on the x-loaded buckling ($P_x : P_y = 1 : 0$) of the 20-layup orthotropic laminate with changing layup angle from (0/-90) to (60/-30) by N-FEA. 141
5.58 Effects of layup angle to the biaxial loading ($P_x : P_y = 1 : 1$) of the 20-layup orthotropic laminate, with changing layup angle from (0/-90) to (60/-30) by N-FEA. 142

6.1 The experimental setup for biaxial buckling test. 145
6.2 A sketch on the mechanism of Shadow Moiré visualization method. . . 147
6.3 The arrangement of Shadow Moiré apparatus used in experiments. . . 147
6.4 Comparison of load-deflection response between experimental and N-FEA results of OP-16-11 plate with uniaxial loading along x-axis ($P_x : P_y = 1 : 0$). 151
6.5 Comparison of load-deflection response between experimental and N-FEA results of OP-16-11 plate with uniaxial loading along y-axis ($P_x : P_y = 0 : 1$). 152
6.6 Comparison of load-deflection response between experimental and N-FEA results of OP-16-44 plate with uniaxial loading along x-axis ($P_x : P_y = 1 : 0$). 153
6.7 Comparison of load-deflection response between experimental and N-FEA results of OP-16-44 plate with uniaxial loading along y-axis ($P_x : P_y = 0 : 1$). 154

6.8 Comparison of load-deflection response between experimental and N-FEA results of OP-16-71 plate with uniaxial loading along x-axis (P_x : $P_y = 1 : 0$). 155
6.9 Comparison of load-deflection response between experimental and N-FEA results of OP-16-71 plate with uniaxial loading along y-axis (P_x : $P_y = 0 : 1$). 156
6.10 Comparison of load deflection response between experimental and N-FEA results of AP-16-45 plate with uniaxial loading along x-axis (P_x : $P_y = 1 : 0$). 157
6.11 Comparison of load-deflection response between experimental and N-FEA results of AP-16-45 plate with uniaxial loading along y-axis (P_x : $P_y = 0 : 1$). 158
6.12 Comparison of load-deflection response between experimental and N-FEA results of AP-16-63 plate with uniaxial loading along x-axis (P_x : $P_y = 1 : 0$). 159
6.13 Comparison of load-deflection response between experimental and N-FEA results of AP-16-63 plate with uniaxial loading along y-axis (P_x : $P_y = 0 : 1$). 160
6.14 Comparison of load-deflection response between experimental and N-FEA results of OP-16-11 plate with biaxial loadings ($P_x : P_y = 1 : 1$). 163
6.15 Comparison of load-deflection response between experimental and N-FEA results of OP-16-44 plate with biaxial loadings ($P_x : P_y = 1 : 1$). . 164
6.16 Comparison of load-deflection response between experimental and N-FEA results of OP-16-71 plate with biaxial loadings ($P_x : P_y = 1 : 1$). . 165
6.17 Comparison of load-deflection response between experimental and N-FEA results of AP-16-45 plate with biaxial loadings ($P_x : P_y = 1 : 1$). . 166
6.18 Comparison of load-deflection response between experimental and N-FEA results of AP-16-63 plate with biaxial loadings ($P_x : P_y = 1 : 1$). . 167

6.19 Shadow Moiré picture for the 16-layer plates of OP-16-11, a) x-axis uniaxial loading, $P_x : P_y = 1 : 0$, b) y-axis uniaxial loading, $P_x : P_y = 0 : 1$. 170
6.20 Shadow Moiré picture for the 16-layer plates of OP-16-71, a) x-axis uniaxial loading, $P_x : P_y = 1 : 0$, b) y-axis uniaxial loading, $P_x : P_y = 0 : 1$. 171
6.21 Shadow Moiré picture for the 16-layer plates of OP-16-11, a) early state of biaxial buckling, $P_x = P_y$=2 kN, b) full-developed biaxial buckling, $P_x = P_y = 3$kN. 172
6.22 Shadow Moiré picture for the 16-layer plates of OP-16-71, a) early state of biaxial buckling, $P_x = P_y$=2 kN, b) full-developed biaxial buckling, $P_x = P_y = 3$kN. 173
6.23 Shadow Moiré picture for the 12-layer plate, OP-12-11, a) biaxial buckling,$P_x = P_y$, b) x-axis uniaxial buckling, $P_x : P_y = 1 : 0$, c) y-axis uniaxial buckling, $P_x : P_y = 0 : 1$. 174
6.24 Shadow Moiré picture for the 16-layer plate, AP-16-36, a) biaxial buckling,$P_x : P_y = 1 : 1$, b) x-axis uniaxial buckling, $P_x : P_y = 1 : 0$, c) y-axis uniaxial buckling, $P_x : P_y = 0 : 1$. 175
6.25 Shadow Moiré picture for the 16-layer plate, AP-16-45, a) biaxial buckling,$P_x : P_y = 1 : 1$, b) x-axis uniaxial buckling, $P_x : P_y = 1 : 0$, c) y-axis uniaxial buckling, $P_x : P_y = 0 : 1$. 176
6.26 Determination of the buckling initiation load from Southwell Plots for the biaxial and uniaxial loading of OP-16-11 plates from the experiments. 180
6.27 Determination of the buckling initiation load from Southwell Plots for the biaxial and uniaxial loading of OP-16-44 plates from the experiments. 181

6.28 Determination of the buckling initiation load by Minimum Slope of Buckling Criterion (MSBC) for the biaxial and uniaxial buckling experiments. 183

7.1 Thickness effects on the biaxial buckling response of 12-, 16- and 20-layer symmetric laminate with equal (0/-90)s layup sequence from N-FEA. 187

7.2 Thickness effects on the biaxial buckling response of 12-, 16- and 20-layer symmetric laminate with equal (0/-90)s layup sequence from analytical and experimental results. 188

7.3 Effects of layup angle on the x-uniaxial loading ($P_x : P_y = 1 : 0$) for symmetric cross-ply laminate by CLPT, N-FEA and experiments where P^*_{cx} is the value of P_{cx} when $\theta = 0$ (P_{cx} is critical load). 190

7.4 Effects of layup angle on the biaxial loading ($P_x : P_y = 1 : 1$) for symmetric cross-ply laminate by CLPT, N-FEA and experiments, where P^*_{cb} is the value of P_{cb} when $\theta = 0$ (P_{cb} is critical load). 191

7.5 Experimental determination of the buckling initiation load from SPBC (Southwell Plot Buckling Criterion) and ultimate load from MSBC (Minimum Slope of Buckling Criterion) for OP-16-11 plate with various loadings (1st data). 193

7.6 Experimental determination of the buckling initiation load from SPBC (Southwell Plot Buckling Criterion) and ultimate load from MSBC (Minimum Slope of Buckling Criterion) for OP-16-11 plate with various loadings (2nd data). 194

7.7 Experimental determination of the buckling initiation load from SPBC (Southwell Plot Buckling Criterion) and ultimate load from MSBC (Minimum Slope of Buckling Criterion) for OP-16-44 plate with various loadings. 195

7.8 Experimental determination of the buckling initiation load from SPBC (Southwell Plot Buckling Criterion) and ultimate load from MSBC (Minimum Slope of Buckling Criterion) for OP-16-71 plate with various loadings. 196

7.9 Experimental determination of the buckling initiation load from SPBC (Southwell Plot Buckling Criterion) and ultimate load from MSBC (Minimum Slope of Buckling Criterion) for OP-20-11 plate with various loadings. 197

7.10 Experimental determination of the buckling initiation load from SPBC (Southwell Plot Buckling Criterion) and ultimate load from MSBC (Minimum Slope of Buckling Criterion) for OP-20-55 plate with various loadings. 198

7.11 Experimental determination of the buckling initiation load from SPBC (Southwell Plot Buckling Criterion) and ultimate load from MSBC (Minimum Slope of Buckling Criterion) for OP-20-82 plate with various loadings. 199

7.12 Experimental determination of the buckling initiation load from SPBC (Southwell Plot Buckling Criterion) and ultimate load from MSBC (Minimum Slope of Buckling Criterion) for OP-16-45 plate with (45/-45)x4, under various loadings. 201

7.13 Experimental determination of the buckling initiation load from SPBC (Southwell Plot Buckling Criterion) and ultimate load from MSBC (Minimum Slope of Buckling Criterion) for OP-16-63 plate with (60/-30)x4, under various loadings. 202

7.14 Experimental determination of the buckling initiation load from SPBC (Southwell Plot Buckling Criterion) and ultimate load from MSBC (Minimum Slope of Buckling Criterion) for OP-20-45 plate with (45/-45)x5, under various loadings. 203

7.15 Experimental determination of the buckling initiation load from SPBC (Southwell Plot Buckling Criterion) and ultimate load from MSBC (Minimum Slope of Buckling Criterion) for OP-20-63 plate with (60/-30)x5, under various loadings. 204
7.16 Mode jumping analysis for the orthotropic laminates having higher stiffness ratios, a)for OP-16-71 plate, b)for OP-16-80 plate. 207

List of Tables

3.1 Physical characteristics of NCT301 Graphite/Epoxy prepreg tape. . . 30

3.2 Material properties of the NCT-301 Graphite/Epoxy. 31

3.3 Dimensions and lay-up sequence of the modified plate specimens for L-FEA, L-FEA and experiments. 32

3.4 In-plane and flexural stiffnesses of the modified plate specimens for L-FEA, N-FEA and experiments. 33

3.5 Stiffness ratios and stiffness constants of the modified plate specimens for L-FEA, N-FEA and experiments. 34

3.6 Global stiffness ratio and critical buckling load of the modified plate specimen from theory and N-FEA. 35

4.1 Dimensions and engineering data of the composite plates for analyses and experiments. 62

List of Symbols

[A]	In-plane stiffness matrix of composite laminate
a	Length of a plate
[B]	In-plane/flexural coupling matrix of an unsymmetric laminate
b	width of a plate
[C]	Stiffness matrix in the generalized Hooke's law
[D]	Flexural stiffness matrix of composite laminate
D_I	Sum of normal components of flexural stiffness, i.e., $D_I = D_{11} + D_{22}$
D_{II}	Sum of shear components of flexural stiffness, i.e., $D_{II} = 2(D_{12} + 2D_{66})$
D_T	Global stiffness, i.e., $D_T = D_I + D_{II}$
E_i	Young's modulus in the i-th direction; $i = x, y, z$
G_{ij}	Shear modulus from the i-th surface to j-th direction; $ij = xy, yz, xz$
h	Total thickness of laminate
h_o	Thickness of unit ply
h_w	Thickness of unit ply in wet composite roll
k	Load ratio, $k = P_y/P_x$ or $k = N_y/N_x$, of the biaxial buckling state
N_{cb}	Critical biaxial stress resultant
N_{ci}	Critical buckling stress resultant in the i-th direction; $i = x, y$
L_{ij}	Differential operator representing stiffness
N_{ij}, Q_{ij}	Inplane and shear stress resultant components
[J]	Coordinate transformation matrix

P_{cb}	Critical biaxial buckling load.
P_{ci}	Critical buckling load in the i-th direction; $i = x, y$
P_i	Compressive inplane load in the i-th direction; $i = x, y, z$
q_{ij}	Reduced stiffness terms for plane stress
R	Aspect ratio of the plate
[S]	Compliance matrix in the generalized Hooke's law
s	Pitch of grating in Shadow Moiré method
U_b	Strain energy due to bending deformation
U_s	Strain energy due to inplane deformation
u, v, w	Displacement functions in the $x, y,$ directions
V	Potential energy due to external load
Λ	Differential operator related to inplane load
Π	Total potential energy
θ	Rotation angle between the in-plane load direction and the fiber orientation
ϕ	Illumination angle in Shadow Moiré method
σ_i	Normal stress along i-th direction; $i = x, y, z$
σ_{ij}	Shear stress on ixj plane; $i = j = x, y, z$
ϵ_i	Normal strain along i-th direction; $i = x, y, z$
ϵ_{ij}	Shear strain on ixj plane; $i = j = x, y, z$
ξ	Inplane stiffness ratio, i.e., $\xi = A_{11}/A_{22}$
ζ	Flexural stiffness ratio, i.e., $\zeta = D_{11}/D_{22}$

List of Acronyms

ANSYS	:A commercial FEM packaged program for ANalysis SYStems by Swanson Analysis Systems Inc., USA
CLPT	:Classical Laminated Plate Theory
C-SOL	:Closed Form Solution
EXP	:Experimental Results
MSBC	:Minimum Slope Buckling Criterion from the experimental load-deflection curves
N-FEA	:Non-linear Finite Element Analyses
N-FEA-i-ud	:Non-linear Finite Element Analyses for ideal plate with uniform end-shortening conditions
N-FEA-i-up	:Non-linear Finite Element Analyses for ideal plate with uniform pressure loading conditions
N-FEA-m-ud	:Non-linear Finite Element Analyses for modified plate with uniform end-shortening conditions
N-FEA-m-up	:Non-linear Finite Element Analyses for modified plate with uniform pressure loading conditions
NLPT	:Nonlinear Laminated Plate Theory
SPBC	:Southwell Plot Buckling Criterion from experimental load-deflection curves
-S_f-	:Free boundary surface: $N_n = N_{ns} = M_n = \frac{\partial M_{ns}}{\partial s} + Q_n = 0$

-S_r-	:Restrained boundary surface with normal loading:
	$N_n \neq 0$ and $u_n = N_{ns} = M_n = 0$
	where, u_n is incremental displacement
-S_u-	:Unrestrained boundary surface without loading:
	$N_n = N_{ns} = w = M_n = 0$
	(where, n and s denote normal and tangential directions
	respectively on the surface of plate edge.)
S_r-S_f-S_r-S_f	:Simply supported boundary condition: two edges supported other
	two edges free, i.e., a boundary condition of beam-plate
S_r-S_u-S_r-S_u	:Simply supported boundary condition: two edges restrained by
	loading grip and other two opposite edge unrestrained, i.e.,
	a boundary condition of simply supported rectangular plate
	having uniaxial loadings with two unrestrained edges
S_r-S_r-S_r-S_r	:Simply supported boundary condition: all four edges restrained
	with loading grips ,i.e., a boundary condition of simply supported
	rectangular plate having various biaxial loadings
	or uniaxial loadings with fully restrained edges

Chapter 1

Introduction

1.1 Background

Laminated composite plates are widely used in many structural applications, not only in aerospace structures but also in automobile or marine constructions, in situations where weight saving and higher structural performance are required. Laminated composite plates are made of layers, each layer consisting of parallel fibers embedded in a matrix. These layers are laid up and cured in an autoclave to consolidate the fibers and the matrix of the whole laminate. The preferred mechanical properties could be obtained by controlling the stacking sequence and the fiber orientation in each layer. Therefore laminated composite plates are generally anisotropic bodies comprised with multiple layers, where each layer can be considered as an orthotropic material.

Even though the anisotropy has been considered as a merit of laminated composite plates owing to the selective strength ratio along the two material axes, most design engineers still hesitate to utilize it due to the complexibility of the analytical solutions. For stability problems, a significant amount of work has been done on plates subjected to uniaxial loading and some works has been done on theoretical formulation for plates subjected to biaxial loadings. Most composite structures are subjected to loadings

in 2-directions Therefore, experimental verification of the strength ratio effects on buckling is required for the design of composite plate structures subjected to biaxial inplane loading.

Plates may undergo buckling failure in the presence of inplane loading. Any plate subjected to inplane compressive loading remains in a primary stable equilibrium state until the inplane loads reach the critical buckling values. With a small enough load increment beyond the critical loading point, the plate can not remain in the primary equilibrium state but shifts to a secondary stable equilibrium state having a large transverse deflections. Thus the buckling phenomenon is usually described as a bifurcation mode which indicates the splitting of the equilibrium path into two or more theoretically admissible secondary paths of equilibrium. When a plate undergoes buckling failure, one of the secondary paths is a mathematically unstable equilibrium path which occurs with no more lateral deflections and the other is a stable equilibrium path with large deflections as shown in Figure 1-1. No matter what type of secondary equilibrium path is followed by the primary stable equilibrium state, the secondary path shows severely weakened inplane strength with lateral deflections due to the coupled bending deformations. Finally the plate may reach a higher mode of buckling or catastrophic failure depending on the boundary conditions. For this reason, buckling analysis has been essentially required in the design of plate structures to validate their dynamic stability and engineering reliability.

1.2 Review of Previous Works

1.2.1 Theoretical Works

Based on the principle of energy conservation, various linear or nonlinear approximation methods have been developed for the theoretical analysis of buckling of laminated plates. Linear buckling theory has been applied to determine the critical buckling load by assuming that the deformation is small and the inplane strain-displacement relation is linear. The stability analysis of laminated composite plates has been well documented by Lekhnitskii [1], Leissa [2], Ashton [3], and Whitney [4]. Linear approximate solutions were obtained using energy formulation in conjunction with classical beam deflection functions by Ashton and Waddoups [5][6]. Also, extensive closed form solutions were presented with the application of double Fourier series by Whitney [7][8] and Leissa [9]. These energy based linear approximate solutions predict only the upperbound of the critical buckling load and mode shapes but fail to depict the secondary equilibrium path after bifurcation point, namely postbuckling behaviour.

On the other hand, nonlinear buckling theory has been developed to analyze the postbuckling behaviour taking into account the effects of large deflection by introducing nonlinear strain-deformation relations. In the nonlinear plate buckling, the basic displacement function considering the large deflections were first suggested by Von Kármán [10] and also the concept of effective width was introduced by von Kármán, Schler, and Donnell [11]. Early works on the postbuckling analyses of homogeneous plates were performed by Cox [12], Timoshenko [13], and Marguerre [14], on the basis of energy methods. A direct energy minimization technique has been applied to the postbuckling analysis of laminated plates using numerical method by Minguet, Dugundji and Lagace [15].

Numerous nonlinear approximate solutions were obtained by simulating the buck-

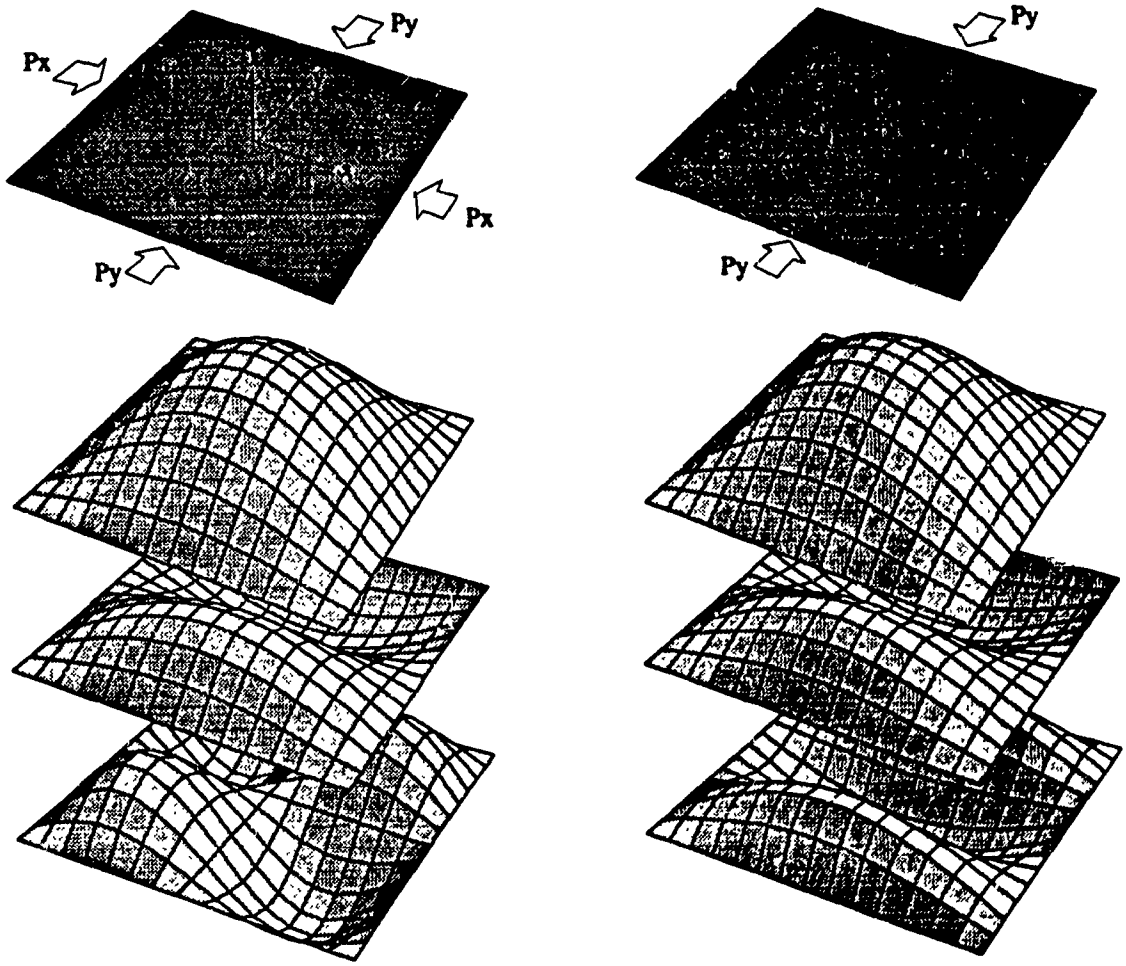

Figure 1.1: Typical buckling behaviour of simply supported rectangular plates showing a stable equilibrium path, a) under biaxial loading, b) under uniaxial loading.

ling deflection as series functions, namely Fourier series, power series or trigonometric functions. Fourier series solutions were well presented by Levy [16], Coan [17], Yamaki [18], Yusuff [19], Harris [20], Prabnakara and Chia [21], Prabhakara [22]. Also, power series were applied by Stein [23], Chandra and Raju [24], and trigonometric functions were applied by Walker [25], Rhodes and Harvey [26], and Stein [27]. On the other hand, Turvey and Wittrick [28] used the dynamic relaxation method to study the post-buckling behaviour of laminated plates. Extensive theories and examples dealing with the large deflection behaviour of laminated plates were discussed by Chia [29]. As a more complicated topic, buckling analysis for the biaxially loaded plate has been reported only in a few theoretical or parametric studies by Harris [30], Turvey [31], Tung and Surdenas [32]. However, they were mainly concerned with about the numerical approximate solutions, to predict the limiting bound in ordor to avoid biaxial collapse with application of power series.

Recently, higher order theories are used to take into account the effect of transverse shear and rotatory inertia on the nonlinear behaviour of postbuckling of laminated plates by Lo et al. [33][34], Reddy [35][36], Cho et al. [37], Chang-Huang [38], Moazzami-Sandhu [39]. These effects were originally reported by Reissner and Mindlin by assuming a linear variation of stresses and strains through the plate thickness. However those analyses quickly lead to very complicated algebra and require expensive computational processes since more variables are added to describe the displacement fields. To have an efficient calculation, a few researchers tried to rely on numerical methods, like higher order finite element methods, such as Kant et al. [40] and Yuan and Miller [41]. Based on the prior results of Berger [42], Zaghloul and Kennedy [43], Sathyamoorthy [44], and Chia [29], it was found that the effects of shear deflection and rotatory inertia are very small and negligible in cases where the span-to-thickness ratio is greater than 25 in laminated composite plate. Considering the values of span-to-thickness ratios, from maximum 140 to minimum 70, of the plate specimens used

in this research, the higher order theories are not necessary in the present biaxial buckling analyses.

1.2.2 Numerical Works

The aforementioned theoretical approach is effective in the calculation of critical buckling load or in the study of postbuckling behaviour from closed form solutions which were formulated by the assumed governing deflection function. But it is not effective in the determination of postbuckling deformation or stress and strain distributions of the buckled plate, especially in case that the plate has a complicated shape or complicated boundary conditions, due to the error of the assumed governing deflection function. There are very limited choices in selecting the admissible governing deflection functions to simulate the actual deformations of buckled plate and also to satisfy the boundary conditions. Another obstacle in the theoretical approach is the requirement of complicated calculation process to get the displacements, stresses and strains, due to the large deflection nonlinearities.

To overcome these limitations of theoretical methods, numerical methods like the finite difference, boundary element and finite element methods have been frequently used. The finite difference method is particularly useful for plates having mixed boundary conditions or varying flexural stiffness. It is based on an approximate calculation in which the derivatives of the deflection functions satisfy the boundary conditions [45][46]. However it is difficult to find a suitable model of deflection functions that correspond to an actual deformation in cases where the plate has free boundaries or holes. The boundary element method, based on integral equations rather than differential ones, was recently introduced in plate stability problems. Even though it has major advantages with regard to the high accuracy and computational efficiency, the boundary element method has difficulties to solve large deflection problems because a higher-order model is required in each discrete domain. Recently, with incremental

approximation technique, only a few fundamental solutions were introduced for plate buckling problem with large deflection theory by Elzein [47].

In view of its excellent applicability to multi-layered structures, the finite element method is a powerful tool for the buckling analysis of laminated composite plates. The generality of its element shape function that covers large deformations and the accuracy of its predictions compared to previous methods are particularly attractive for plate buckling analysis. By the applications of multi-layered shell elements or three dimensional elements we can obtain not only a global buckling strength-deformation response but also local inter-laminar stresses or strains between any two specific layers. For the efficient calculation of inter-laminar stresses and deformations, a few researchers developed the higher order or hybrid finite element method such as Kant et al. [40], Yuan and Miller [41], Laschet and Jeusette [48], Chen and Yang [49].

In this research, using the commercial finite element analysis software ANSYS [50], linear finite element analysis was applied to determine the critical biaxial buckling load for various boundary and loading conditions. In addition, a nonlinear finite element analysis was extensively applied to obtain the post-buckling behaviour, deflections, stresses and strains, considering large deflection nonlinearity of the laminated plates.

1.2.3 Experimental Works

Experimental works on the buckling and postbuckling of laminated composite plates are scarce. After the nonlinear large deflection equations were suggested by Von Kármán [10], some important experimental results on the uniaxial buckling - a plate loaded with uniaxial compressive loading - of the rectangular plates were reported by Stein [23], Mandell [51], Ashton and Love [52], Spier [53], Minguet, Dugundji and Lagace [15], Englestad et al. [54], Chai et al. [55]. In 1959, Stein [23] experimentally investigated the postbuckling behaviour of simply supported rectangular aluminum-

alloy flat plates subjected to uniaxial compression. Comparisons were made for total end-shortening, local strains and deflections by comparing Stain's experimental data and the linearized solutions obtained by expanding the displacements into a power series.

For laminated composite plates, Mandell [51] carried out an extensive buckling experiments for various materials, including boron and glass fiber reinforced composite plates in 1968. In that research, individual knife-edge supporter was introduced to acquire 4 sided simply supported boundary conditions and the experimental buckling loads were determined by the application of Southwell Plot from a load-deflection curve. The main purpose of that research was experimental determination of critical buckling load of laminated plates subjected to uniaxial loadings. In the analysis of buckling modes, the experimental results revealed that most plates buckled into the first mode. A few plates, buckled into the second or third mode. These phenomena appeared for highly anisotropic plates like $[(0_7/-90_1)]_s$, $[(0_8/-90_2)]_s$, $[(0)_8]_s$ and $[(0)_{10}]_s$ plates.

In 1989, Minguet et al. [15] carried out an experimental investigation on the post-buckling behaviour of laminated plates to verify their theoretical solutions from direct energy minimization technique. Also, Chai et al. [55] carried out an extensive complementary experimental investigation to confirm the theoretical solutions in 1991, where load-deflection curves and postbuckling strain distributions were experimentally obtained for uniaxially loaded rectangular laminated composite plates.

Up to now, experiments on the plate loaded with biaxial compressive loading considering various axial load combinations can not be found in the literature. Only a parametric diagnosis from the basic buckling differential equation was performed by Libove [56] in 1983 and Tung [32]. In the research of the author, to investigate the biaxial buckling behaviour of laminated composite plate for various combination

of axial loads, extensive experimental works have been carried out for symmetrically laminated orthotropic and anisotropic composite plates. For the experimental investigation, a biaxial testing machine having four independent actuators and position controllers, as shown in Figure 1-2, was used. A modified rectangular specimen was designed and fabricated to accommodate the simultaneous biaxial loading by the biaxial testing machine. Experimental values of critical buckling load, the behaviour of load-deflection and strain distributions were compared with numerical and theoretical results. Also, Shadow Moiré technique was employed to visualize the postbuckling deflections at different load-ratios, stiffness-ratios and lay-up angles of the composite plate specimen.

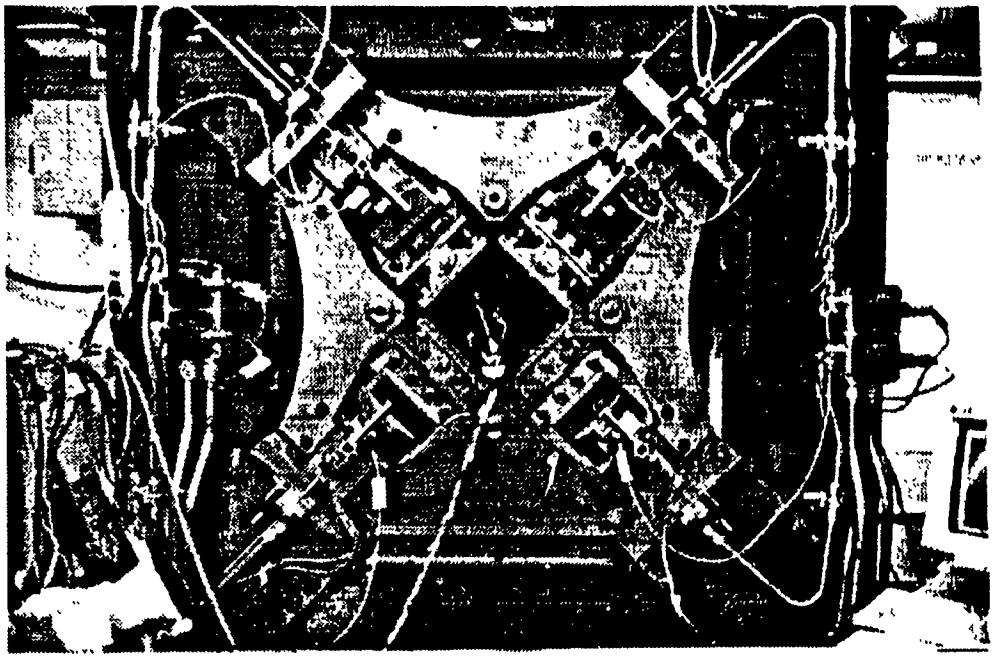

Figure 1.2: View of biaxial buckling test of Graphite/Epoxy composite laminated plate.

1.3 Objectives of the research

Laminated composite plate structures, like the skin structure of aircraft fuselage or the body-skin of automobiles and ships, are generally exposed to biaxial inplane loadings. Biaxial buckling mode shapes generally appeared in the inplane loaded rectangular plates when the plates have any type of fully-supported boundary condition, like S_r-S_r-S_r-S_r or S_r-S_u-S_r-S_u. Even if the plate is uniaxially loaded, the plate may experience a biaxial stress state and may reveal a biaxial deflection due to the interaction of axial loads and reaction forces from the boundaries. This then can be considered as a biaxially loaded case.

On the other hand, it was observed that the critical buckling load and load-deflection behaviour changed with respect to the load ratio along the two axes. In particular, the critical buckling load shows a minimum value when the plate is sub-

jected to uniform biaxial loadings, i.e., two axes having the same value of axial load. Considering more generalized loading and boundary conditions, biaxial buckling analyses and experiments may produce more relevant design parameters than conventional uniaxial analyses and experiments. However, to the author's knowledge, no experimental work has been done on the biaxial buckling of laminated composite plate under various combinations of the biaxial loadings even though a significant amount of experimental work has been done on the buckling of composite plates subjected to uniaxial compressive loading. The spin-off benefits of this research can be the generation of design data for the applications of laminated composite plates considering a generalized inplane load and supporting mechanism.

To achieve the above mentioned research objective successfully, the author divided this research into four targets as follows. In view of no precedent experimental verification, the first step of this research was focused on the developement of a suitable experimental specimen to simulate the actual buckling behaviour of plate structures. A plate specimen was proposed and its admissibility was fully investigated with nonlinear finite element analysis(N-FEA) from ANSYS program [50]. Through the study on the actual buckling of plate structures, the experimental model was selected as the four-sides simply supported square laminated plate, which was subjected to uniform compression by four independent rigid loading grips.

The second step of this research was concentrated on the modelling of boundary behaviour of postbuckled plate subjected to biaxial loads with various axial load ratios, k. Plate boundaries were changed from a straight line to a partly curved line due to the large transverse deflection of the plate in the postbuckling state. Also the stress distribution on the plate boundaries was changed from uniform continuous stresses in the prebuckling state to nonuniform discontinuous stresses in the postbuckling state. To obtain more accurate boundary conditions, the author executed N-FEA

for the two different boundary conditions, i.e., uniform pressure and uniform end-shortening, simulating the actual boundary behaviour of experiments. Comparing the experimental results with the two numerical analyses having two different loading conditions, it was found that results from the analysis with uniform pressure loading condition agreed better with experimental results.

The third step of this research was aimed at determining the effect of flexural stiffness ratio, ζ, and inplane stiffness ratio, ξ, which was induced from the stacking sequence change. From the energy theorem, in simply supported plate buckling, CLPT says that the critical buckling energy and the critical buckling loads are not affected by the stacking sequence of the plate if the lay-up angle was maintained. However experimental results revealed different critical buckling load response and post buckling behaviour from the Classical Laminated Plate Theory (CLPT). Also, the buckling mode jumping phenomenon was observed to happen during the buckling test for specific plates having a very large flexural stiffness ratio, ζ. This experimental mode jumping phenomenon was verified with N-FEA from ANSYS.

The final step of this research emphasized on the study of buckling failure criteria derived from the author's experimental results. This is a new practical buckling criterion for the design of laminated plate structures. Southwell Plot Buckling Criterion (SPBC) was applied to determine the initial buckling load. Although this technique was suggested to apply only for determining the critical load of a column, it was extended to a fully simply supported plate subjected to a biaxial inplane compression loadings. On the other hand, Minimum Slope Buckling Criterion (MSBC) was proposed by the author to determine the catastrophic failure loads at the postbuckling state.

Chapter 2

Plate Buckling Theory

2.1 Classical Laminated Plate Theory

The required theory to analyze the buckling of laminated composite plates is more complicated than that of isotropic homogeneous plates. This is particularly true in case of unsymmetrically stacked angle-ply laminates because of the existence of coupling terms due to the bending and stretching effect. In practical applications of thin plates, the magnitude of the tractions on the surface of middle plane is relatively small compared to the bending and inplane stresses, particularly on the state of plane stress conditions.

In the derivation of the laminated plate buckling equations, the basic assumption is the Kirchhoff hypothesis implying that the effects of the transverse shear deformation are neglected. Relying on this hypothesis, the equations are valid in case that the thickness of a plate is small in comparison with its lateral dimension. On the standard x, y, z coordinates system, as shown in Figures 2-1 and 2-2, the displacements on the x, y, z directions are denoted by u, v, w respectively. To construct the governing equations for the plate buckling, following assumptions are required.

- The plate is constructed by an arbitrary number of layers of orthotropic ply-group bonded together. However, the two principal axes of each individual layer need not coincide with the x, y axes of the laminated plate, i.e., general angle-ply laminate is considered.

- The plate is thin, i.e., the thickness h is much smaller than the other physical dimensions.

- In–plane strains ϵ_x, ϵ_y and ϵ_{xy} are small compared to unity.

- In order to include in plane force effects, nonlinear terms in the equations of motion involving products of stresses and plate slopes are retained.

- Transverse shear strains ϵ_{xz} and ϵ_{yz} are negligible and tangential displacements u and v are linear functions of the z coordinate according to the Kirchhoff assumptions.

- The transverse normal strain ϵ_z is negligible.

- Each ply obeys Hooke's law.

- The plate has uniform thickness.

- Rotatory inertia terms are negligible.

- Transverse shear stresses, σ_{xz} and σ_{yz}, vanish on the surfaces $z = \pm h/2$

Constitutive Equations

Most theoretical equations are formulated by introducing an admissible deflection function which satisfies the given boundary conditions. From the above mentioned

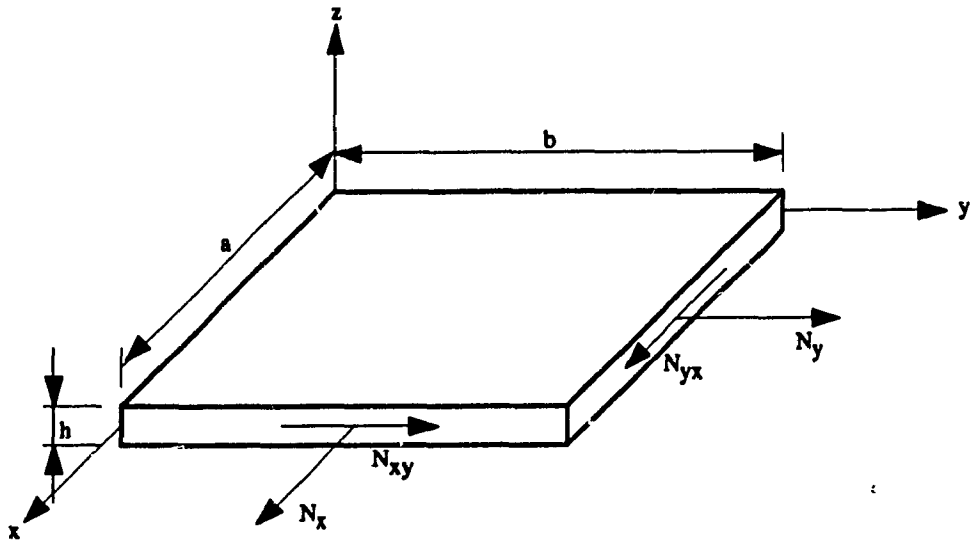

Figure 2.1: Description of inplane stress resultants.

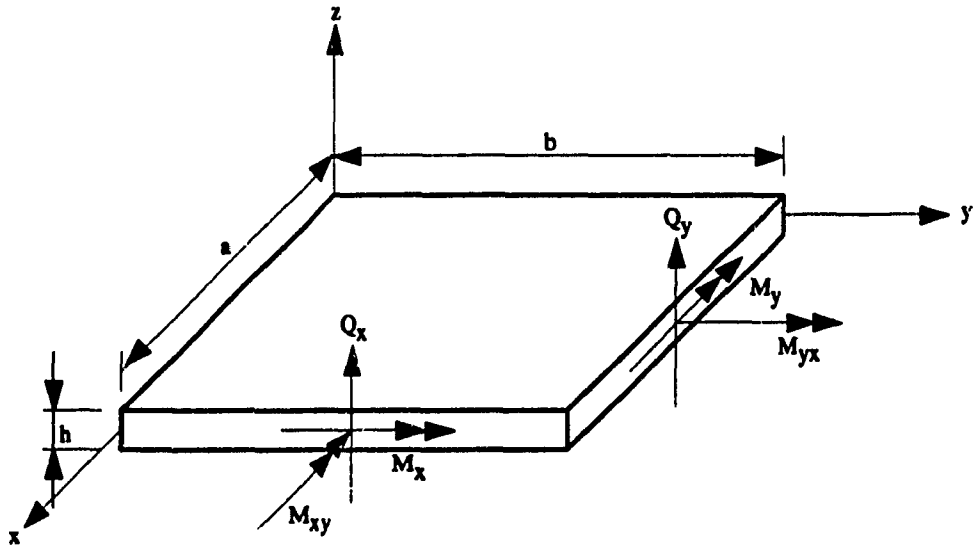

Figure 2.2: Description of moments and shear stress resultants.

assumptions the lateral deflection, w, and tangential displacements, u and v, are of the form

$$\begin{aligned} u &= u^o(x,y,t) + z f_1(x,y,t) \\ v &= v^o(x,y,t) + z f_2(x,y,t) \end{aligned} \tag{2.1}$$

$$w = w(x,y,t) \tag{2.2}$$

where u^o and v^o are tangential displacements of the middle plane. On the other hand, strain-displacement relations of the small deformation theory can be written as

$$\begin{gathered} \epsilon_x = \frac{\partial u}{\partial x}, \qquad \epsilon_y = \frac{\partial v}{\partial y}, \qquad \epsilon_{xy} = \frac{\partial u}{\partial y} + \frac{\partial v}{\partial x} \\ \epsilon_z = \frac{\partial w}{\partial z} = 0, \quad \epsilon_{yz} = \frac{\partial w}{\partial y} + \frac{\partial v}{\partial z} = 0, \quad \epsilon_{xz} = \frac{\partial w}{\partial x} + \frac{\partial u}{\partial z} = 0 \end{gathered} \tag{2.3}$$

Introducing equations (2.1) and (2.2) into the strain-displacement relations of equation (2.3), the unknown functions of equation (2.1) can be written as

$$f_1(x,y,t) = -\frac{\partial w}{\partial x}, \quad f_2(x,y,t) = -\frac{\partial w}{\partial y} \tag{2.4}$$

Thus the strain-displacement relations of anisotropic plates are of the form

$$\begin{aligned} \epsilon_x &= \epsilon_x^o + z\kappa_x \\ \epsilon_y &= \epsilon_y^o + z\kappa_y \\ \epsilon_{xy} &= \epsilon_{xy}^o + z\kappa_{xy} \end{aligned} \tag{2.5}$$

where

$$\epsilon_x^o = \frac{\partial u^o}{\partial x}, \quad \epsilon_y^o = \frac{\partial v^o}{\partial y}, \quad \epsilon_{xy}^o = \frac{\partial u^o}{\partial y} + \frac{\partial v^o}{\partial x} \tag{2.6}$$

$$\kappa_x = -\frac{\partial^2 w}{\partial x^2}, \quad \kappa_y = -\frac{\partial^2 w}{\partial y^2}, \quad \kappa_{xy} = -2\frac{\partial^2 w}{\partial x \partial y} \tag{2.7}$$

Equation (2.5) describes the strain-displacement relations of plates of small deformation and it coincides with the classical homogeneous plate theory.

For the postbuckling analysis of laminated plate, the strain-displacement relation should be formulated by including higher order terms as mentiond by Chia [29]. By including higher order terms, the large deflection nonlinear strain-displacement relations of anisotropic laminated plates are

$$\epsilon_x = \epsilon_x^n + z\kappa_x = \frac{\partial u^o}{\partial x} + \frac{1}{2}(\frac{\partial w}{\partial x})^2 - z\frac{\partial^2 w}{\partial x^2} \tag{2.8}$$

$$\epsilon_y = \epsilon_y^n + z\kappa_y = \frac{\partial v^o}{\partial y} + \frac{1}{2}(\frac{\partial w}{\partial y})^2 - z\frac{\partial^2 w}{\partial y^2} \tag{2.9}$$

$$\epsilon_{xy} = \epsilon_{xy}^n + z\kappa_{xy} = \frac{\partial u^o}{\partial y} + \frac{\partial v^o}{\partial x} + \frac{\partial w}{\partial y}\frac{\partial w}{\partial y} - 2z\frac{\partial^2 w}{\partial x \partial y} \tag{2.10}$$

The generalized Hooke's law, describing the two dimensional stress and strain relation, can be written in the following form:

$$\begin{aligned} \{\sigma\} &= [\mathrm{C}]\{\epsilon\} \\ \{\epsilon\} &= [\mathrm{S}]\{\sigma\} \end{aligned} \tag{2.11}$$

where

$$\begin{aligned} [\mathrm{S}] &= [\mathrm{C}]^{-1} \\ \{\sigma\} &= [\sigma_x, \sigma_y, \sigma_z, \sigma_{yz}, \sigma_{xz}, \sigma_{xy}]^T \\ \{\epsilon\} &= [\epsilon_x, \epsilon_y, \epsilon_z, \epsilon_{yz}, \epsilon_{xz}, \epsilon_{xy}]^T \end{aligned}$$

Assuming that the z–axis is perpendicular to a plane of symmetry, the stress strain relation reduces in the case of monoclinic symmetry as

$$[\mathrm{C}] = \begin{bmatrix} c_{11} & c_{12} & c_{13} & 0 & 0 & c_{16} \\ c_{21} & c_{22} & c_{23} & 0 & 0 & c_{26} \\ c_{31} & c_{32} & c_{33} & 0 & 0 & c_{36} \\ 0 & 0 & 0 & c_{44} & c_{45} & 0 \\ 0 & 0 & 0 & c_{54} & c_{55} & 0 \\ c_{61} & c_{62} & c_{63} & 0 & 0 & c_{66} \end{bmatrix} \tag{2.12}$$

where the number of independent elastic stiffness components are reduced to 13 because of symmetry. Also, to determine the principal stress and strain of the anisotropic plate, it is necessary to consider the off-axes stress and strain components which have a rotated angle θ with respect to the on-axis coordinate on the plane of the plate as shown in Figure 2-3. Introducing $m = \cos\theta$ and $n = \sin\theta$, the transformed stress σ_i' and strain ϵ_i' are given by

$$\begin{aligned} \{\sigma_i'\} &= [\mathrm{J}]\{\sigma_i\} \\ \{\epsilon_i'\} &= [\mathrm{J^T}]^{-1}\{\epsilon_i\} \end{aligned} \tag{2.13}$$

$$[\mathrm{J}] = \begin{bmatrix} m^2 & n^2 & 0 & 0 & 0 & 2mn \\ n^2 & m^2 & 0 & 0 & 0 & -2mn \\ 0 & 0 & 1 & 0 & 0 & 0 \\ 0 & 0 & 0 & m & -n & 0 \\ 0 & 0 & 0 & n & m & 0 \\ -mn & mn & 0 & 0 & 0 & m^2 - n^2 \end{bmatrix} \tag{2.14}$$

Considering an approximate state of plane stress, the transverse normal strain ϵ_z can be transformed using terms of stiffness from the Hooke's law.

$$\epsilon_z = -\frac{c_{13}}{c_{33}}\epsilon_x - \frac{c_{23}}{c_{33}}\epsilon_y - \frac{c_{36}}{c_{33}}\epsilon_{xy} \tag{2.15}$$

By introducing the reduced stiffness terms q_{ij}, the plane stress strain relation for the k^{th} layer becomes

$$\begin{Bmatrix} \sigma_x \\ \sigma_y \\ \sigma_{xy} \end{Bmatrix} = \begin{bmatrix} q_{11} & q_{12} & q_{16} \\ q_{12} & q_{22} & q_{26} \\ q_{16} & q_{26} & q_{66} \end{bmatrix} \begin{Bmatrix} \epsilon_x \\ \epsilon_y \\ \epsilon_{xy} \end{Bmatrix} \tag{2.16}$$

$$q_{ij} = c_{ij} - \frac{c_{i3}c_{j3}}{c_{33}} \tag{2.17}$$

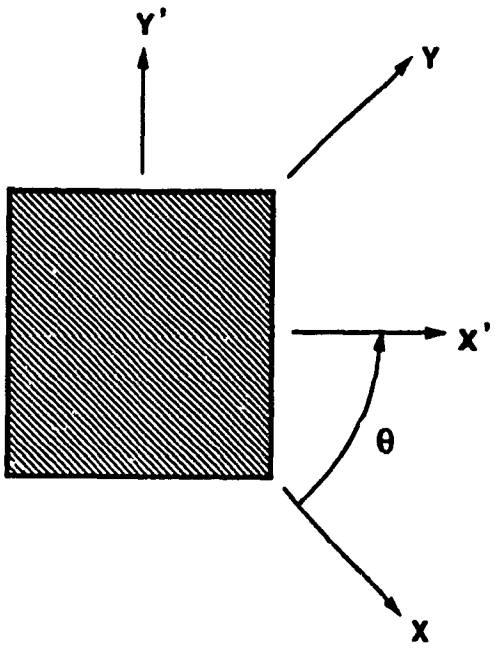

Figure 2.3: Rotation angle between on-axes(x-y) and off-axes(x'-y').

The inplane stress and moment resultant are obtained by integrating of the stress and moment through the thickness;

$$\begin{aligned}(N_x, N_y, N_{xy}) &= \int_{-h/2}^{h/2} (\sigma_x, \sigma_y, \sigma_{xy}) dz \\ (Q_x, Q_y) &= \int_{-h/2}^{h/2} (\sigma_{xz}, \sigma_{yz}) dz \\ (M_x, M_y, M_{xy}) &= \int_{-h/2}^{h/2} (\sigma_x, \sigma_y, \sigma_{xy}) z dz\end{aligned} \tag{2.18}$$

These resultants are illustrated in Fig.2-1 and 2-2. Using equations (2.5), (2.12) and (2.14), the inplane stress and moment resultant equations yield the following

constitutive relations

$$\left\{\begin{array}{c} N_x \\ N_y \\ N_{xy} \\ \cdots \\ M_x \\ M_y \\ M_{xy} \end{array}\right\} = \left[\begin{array}{cccccccc} A_{11} & A_{12} & A_{16} & \vdots & B_{11} & B_{12} & B_{16} \\ A_{12} & A_{22} & A_{26} & \vdots & B_{12} & B_{22} & B_{26} \\ A_{16} & A_{26} & A_{66} & \vdots & B_{16} & B_{26} & B_{66} \\ \cdots & \cdots & \cdots & \cdots & \cdots & \cdots & \cdots \\ B_{11} & B_{12} & B_{16} & \vdots & D_{11} & D_{12} & D_{16} \\ B_{12} & B_{22} & B_{26} & \vdots & D_{12} & D_{22} & D_{26} \\ B_{16} & B_{26} & B_{66} & \vdots & D_{16} & D_{26} & D_{66} \end{array}\right] \left\{\begin{array}{c} \epsilon_x^o \\ \epsilon_y^o \\ \epsilon_{xy}^o \\ \cdots \\ \kappa_x \\ \kappa_y \\ \kappa_{xy} \end{array}\right\} \tag{2.19}$$

where A_{ij}, B_{ij} and D_{ij} are integrated stiffness coefficients of the following form

$$(A_{ij}, B_{ij}, D_{ij}) = \int_{-h/2}^{h/2} q_{ij}(1, z, z^2)dz \tag{2.20}$$

Equation (2.19) can be written in the abbreviated form as

$$\left\{\begin{array}{c} \{N\} \\ \cdots \\ \{M\} \end{array}\right\} = \left[\begin{array}{ccc} [\mathbf{A}] & \vdots & [\mathbf{B}] \\ \cdots & \cdots & \cdots \\ [\mathbf{B}] & \vdots & [\mathbf{D}] \end{array}\right] \left\{\begin{array}{c} \{\epsilon^o\} \\ \cdots \\ \{\kappa\} \end{array}\right\} \tag{2.21}$$

Governing Differential Equations

The governing equation for plate buckling problems can be formulated using the differential equation of static equilibrium, energy methods, and dynamic approaches. The equilibrium equation is obtained by considering the simultaneous bending and inplane stretching of the plate. Consider a plate subjected to lateral loads which are prescribed as inplane stress resultants, N_x, N_y and N_{xy}. Summing forces in x, y and z direction on an infinitesimal plate element produces the following equilibrium equations as written by Whitney [4]

$$\frac{\partial N_x}{\partial x} + \frac{\partial N_{xy}}{\partial y} - Q_x \frac{\partial w}{\partial x} + p_x = 0$$

$$\begin{aligned} \frac{\partial N_{xy}}{\partial x} + \frac{\partial N_y}{\partial y} - Q_y\frac{\partial w}{\partial y} + p_y = 0 \\ \frac{\partial Q_x}{\partial x} + \frac{\partial Q_y}{\partial y} + N_x\frac{\partial^2 w}{\partial x^2} + 2N_{xy}\frac{\partial^2 w}{\partial x \partial y} + N_y\frac{\partial^2 w}{\partial y^2} + q = 0 \end{aligned} \tag{2.22}$$

where p_x and p_y denote the body forces or tangential forces acting on the surfaces of the plate along x and y direction, and also q denotes the lateral pressure in z direction as discussed by Timoshenko [45]. On the other hand, variation of moment about x and y axes yields

$$\begin{aligned} Q_x &= \frac{\partial M_x}{\partial x} + \frac{\partial M_{xy}}{\partial y} \\ Q_y &= \frac{\partial M_{xy}}{\partial x} + \frac{\partial M_y}{\partial y} \end{aligned} \tag{2.23}$$

However the transverse shear resultants Q_x and Q_y are small compared to other resultants, also the tangential slopes $\frac{\partial w}{\partial x}$ and $\frac{\partial w}{\partial y}$ are typically small at the elastic buckling limit. Therefore the above equilibrium equation can be simplified as

$$\begin{aligned} \frac{\partial N_x}{\partial x} + \frac{\partial N_{xy}}{\partial y} + p_x = 0 \\ \frac{\partial N_{xy}}{\partial x} + \frac{\partial N_y}{\partial y} + p_y = 0 \\ \frac{\partial^2 M_x}{\partial x^2} + 2\frac{\partial^2 M_{xy}}{\partial x \partial y} + \frac{\partial^2 M_y}{\partial y^2} + N_x\frac{\partial^2 w}{\partial x^2} + 2N_{xy}\frac{\partial^2 w}{\partial x \partial y} + N_y\frac{\partial^2 w}{\partial y^2} + q = 0 \end{aligned} \tag{2.24}$$

Let us consider the inplane load as two parts – the first part which exists before the initiation of buckling, and the second part which is concerned with the buckling deformations – to analyze the buckling phenomenon in detail by supposing prebuckling displacements and postbuckling deflections. Introducing a load factor, λ, equation (2.21) also can be divided in two parts. Let these two parts be denoted by using the superscripts i(prebuckling) and b(postbuckling) as follows

$$N_j = N_j^i + N_j^b$$

$$
\begin{aligned}
&= (\mathbf{A}\epsilon^o + \mathbf{B}\kappa) + \lambda(\mathbf{A}\epsilon^o + \mathbf{B}\kappa) \\
M_j &= M_j^i + M_j^b \\
&= (\mathbf{B}\epsilon^o + \mathbf{D}\kappa) + \lambda(\mathbf{B}\epsilon^o + \mathbf{D}\kappa)
\end{aligned} \tag{2.25}
$$

It is assumed that the plate remains flat before the onset of buckling and there is no additional variation of tangential or lateral load on the plate surfaces during the buckling process, i.e.,

$$
\begin{aligned}
w &= w^b \\
p_i &= p_i^i \\
q &= q^i
\end{aligned} \tag{2.26}
$$

For the first part of the equations, describing the state of the plate before buckling takes place, the magnitude of the inplane load is less than the critical buckling load and the inplane deformation is due to pure compression of the flat plate. Considering $w^i = 0$, equations (2.24),(2.25) and (2.26) yield the governing differential equations,

$$
\begin{aligned}
\frac{\partial N_x^i}{\partial x} + \frac{\partial N_{xy}^i}{\partial y} + p_x^i &= 0 \\
\frac{\partial N_{xy}^i}{\partial x} + \frac{\partial N_y^i}{\partial y} + p_y^i &= 0 \\
\frac{\partial^2 M_x^i}{\partial x^2} + 2\frac{\partial^2 M_{xy}^i}{\partial x \partial y} + \frac{\partial^2 M_y^i}{\partial y^2} + q^i &= 0
\end{aligned} \tag{2.27}
$$

For the second part of the equations, describing the state of the plate when the inplane load exceeds the buckling load and gives rise to the postbuckling mode, the magnitude of the inplane load is a little more than the critical buckling load and it creates lateral deflections. Substituting equations (2.25) and (2.26) into equation (2.24) and subtracting equation (2.27), the buckling governing equations in terms of stress resultants are

$$
\begin{aligned}
&\frac{\partial N_x^b}{\partial x} + \frac{\partial N_{xy}^b}{\partial y} = 0 \\
&\frac{\partial N_{xy}^b}{\partial x} + \frac{\partial N_y^b}{\partial y} = 0 \\
&\frac{\partial^2 M_x^b}{\partial x^2} + 2\frac{\partial^2 M_{xy}^b}{\partial x \partial y} + \frac{\partial M_y^b}{\partial y} + N_x^i \frac{\partial^2 w}{\partial x^2} + 2N_{xy}^i \frac{\partial^2 w}{\partial x \partial y} + N_y^i \frac{\partial^2 w}{\partial y^2} \\
&\qquad + (N_x^b \frac{\partial^2 w}{\partial x^2} + 2N_{xy}^b \frac{\partial^2 w}{\partial x \partial y} + N_y^b \frac{\partial^2 w}{\partial y^2}) = 0
\end{aligned}
\tag{2.28}
$$

The last three terms, N_{ij}^b, of the third equation of equations (2.28) have considerably smaller magnitudes compared to the others because λ is small compared to 1 in equation (2.25). Therefore these terms are normally dropped.

The above mentioned two governing formulations, equations (2.27) and (2.28), have further meaning and it is better to be understood by rewriting them as matrix equations by introducing differential operators.

Therefore, in the prebuckled state, the governing equations satisfy the following conditions, $w = 0$ and $\kappa_x^i = \kappa_y^i = \kappa_{xy}^i = 0$, because the plate is still flat and it has no displacement along the z-axis. Consequently, from equations (2.5), (2.19) and (2.27), the governing equilibrium equations can be written as

$$
\begin{bmatrix} L_{11} & L_{12} & L_{13} \\ L_{21} & L_{22} & L_{23} \\ L_{31} & L_{32} & (L_{33} - \Lambda) \end{bmatrix} \begin{Bmatrix} u \\ v \\ w \end{Bmatrix} = \begin{Bmatrix} -p_x^i \\ -p_y^i \\ -q^i \end{Bmatrix} \tag{2.29}
$$

Secondly on the state of postbuckling, there is no additional bodyforce variation and also $w \neq 0$ and $\kappa_x^i = \kappa_y^i = \kappa_{xy}^i \neq 0$. Substituting equations (2.5) and (2.19) into equation (2.28) the matrix form of governing equation can be written as

$$\begin{bmatrix} L_{11} & L_{12} & L_{13} \\ L_{21} & L_{22} & L_{23} \\ L_{31} & L_{32} & (L_{33}-\Lambda) \end{bmatrix} \begin{Bmatrix} u \\ v \\ w \end{Bmatrix} = \begin{Bmatrix} 0 \\ 0 \\ 0 \end{Bmatrix} \tag{2.30}$$

where all L_{ij} are differential operators representing the stiffness and Λ is also a differential operator denoting the inplane load as

$$\begin{aligned}
L_{11} &= A_{11}\frac{\partial^2}{\partial x^2} + 2A_{16}\frac{\partial^2}{\partial x \partial y} + A_{66}\frac{\partial^2}{\partial y^2} \\
L_{22} &= A_{22}\frac{\partial^2}{\partial y^2} + 2A_{26}\frac{\partial^2}{\partial x \partial y} + A_{66}\frac{\partial^2}{\partial x^2} \\
L_{33} &= D_{11}\frac{\partial^4}{\partial x^4} + 4D_{16}\frac{\partial^4}{\partial x^3 \partial y} + 2(D_{12}+2D_{66})\frac{\partial^4}{\partial x^2 \partial y^2} + \\
&\quad 4D_{26}\frac{\partial^4}{\partial x \partial y^3} + D_{22}\frac{\partial^4}{\partial y^4} \\
L_{12} &= L_{21} = A_{16}\frac{\partial^2}{\partial x^2} + (A_{12}+A_{66})\frac{\partial^2}{\partial x \partial y} + A_{26}\frac{\partial^2}{\partial y^2} \\
L_{13} &= L_{31} = -B_{11}\frac{\partial^3}{\partial x^3} - 3B_{16}\frac{\partial^3}{\partial x^2 \partial y} - (B_{12}+2B_{66})\frac{\partial^3}{\partial x \partial y^2} - B_{26}\frac{\partial^3}{\partial y^3} \\
L_{23} &= L_{32} = -B_{16}\frac{\partial^3}{\partial x^3} - (B_{12}+2B_{66})\frac{\partial^3}{\partial x^2 \partial y} - 3B_{26}\frac{\partial^3}{\partial x \partial y^2} - B_{22}\frac{\partial^3}{\partial y^3} \\
\Lambda &= N_x\frac{\partial^2}{\partial x^2} + 2N_{xy}\frac{\partial^2}{\partial x \partial y} + N_y\frac{\partial^2}{\partial y^2}
\end{aligned} \tag{2.31}$$

2.2 Buckling Criteria of Simply Supported Plate

For symmetrically laminated plates, the inplane/flexural coupling terms $B_{ij} = 0$ and $L_{13} = L_{23} = 0$ in equations (2.31). Since the inplane part is uncoupled from the transverse part of the nontrivial matrix equation of the equation (2.30), the transverse displacements are governed by

$$D_{11}\frac{\partial^4}{\partial x^4} + 4D_{16}\frac{\partial^4}{\partial x^3 \partial y} + 2(D_{12}+2D_{66})\frac{\partial^4}{\partial x^2 \partial y^2} + 4D_{26}\frac{\partial^4}{\partial x \partial y^3} + D_{22}\frac{\partial^4}{\partial y^4}$$

$$= N_x \frac{\partial^2}{\partial x^2} + 2N_{xy} \frac{\partial^2}{\partial x \partial y} + N_y \frac{\partial^2}{\partial y^2} \quad (2.32)$$

Considering $D_{16} = D_{26} = 0$ and $N_{xy} = 0$ for the orthotropic laminate plates, i.e., specially orthotropic plate, under biaxial loadings, above governing differential equation can be written as

$$D_{11} \frac{\partial^4 w}{\partial x^4} + 2(D_{12} + 2D_{66}) \frac{\partial^4 w}{\partial x^2 \partial y^2} + D_{22} \frac{\partial^4 w}{\partial y^4} = N_x \frac{\partial^2 w}{\partial x^2} + N_y \frac{\partial^2 w}{\partial y^2} \quad (2.33)$$

Let us assume the plate deflection function, w, as one of double Fourier series which satisfies the simply supported boundary conditions discussed in Chapter 4.

$$w = \sum_{m=1}^{\infty} \sum_{n=1}^{\infty} a_{mn} \sin \frac{m\pi x}{a} \sin \frac{n\pi y}{b} \quad (2.34)$$

where a_{mn} is the maximum deflection amplitude with $m, n = 1, 2, 3, \ldots$. Consequently for the biaxially loaded orthotropic laminate, the critical buckling load along x-axis, P_{xcr}, can be obtained by introducing the aspect ratio, R, and the biaxial load ratio, k, as follows

$$\begin{aligned} N_{xcr} &= \frac{\pi^2 [D_{11} m^4 + 2(D_{12} + 2D_{66}) m^2 n^2 R^2 + D_{22} n^4 R^4]}{R^2 b^2 (m^2 + k n^2 R^2)} \\ P_{xcr} &= \int_0^b N_{xcr} dy \\ R &= \frac{a}{b} \\ k &= \frac{N_y}{N_x} \end{aligned} \quad (2.35)$$

If we consider the first buckling mode of simply supported orthotropic square plate with $a = b$ and $m = n = 1$, equation (2.33) can be reconstructed as following.

$$\{D_{11} + D_{22} + 2(D_{12} + 2D_{66})\} \frac{\partial^4 w}{\partial x^4} = \{N_x + N_y\} \frac{\partial^2 w}{\partial x^2} \quad (2.36)$$

As a special case of orthotropic laminates, if we consider cross-ply laminates having various stacking sequences, it is true that the sum of two major and minor flexural

stiffness terms, $D_I = D_{11} + D_{22}$, is constant and also the sum of other tangential stiffness terms, $D_{II} = 2(D_{12} + 2D_{66})$ is constant as tabulated in Table 3.5. Thus equation (2.36) is simplified as follows

$$\{D_I + D_{II}\}\frac{\partial^4 w}{\partial x^4} = \{N_x + N_y\}\frac{\partial^2 w}{\partial x^2} \tag{2.37}$$

where

$$\begin{aligned} D_I &= D_{11} + D_{22} = \text{Constant} \\ D_{II} &= 2(D_{12} + 2D_{66}) = \text{Constant} \end{aligned} \tag{2.38}$$

Consequently, if the axial load ratio k was prescribed, the critical biaxial buckling load of specially orthotropic square plate can be summarized as the function of the global flexural stiffness value, D_T, as following.

$$\begin{aligned} N_{xcr} &= \frac{\pi^2 D_T}{b^2(1+k)} = \text{Constant} \\ P_{xcr} &= bN_{xcr} = \text{Constant} \end{aligned} \tag{2.39}$$

where,

$$D_T = D_I + D_{II} = \text{Constant} \tag{2.40}$$

Therefore, as long as we focused on the first buckling mode of biaxially loaded square plates having the same thickness, the critical buckling load is constant no matter what kind of layup sequence (cross-ply laminates) was made. For example, the global flexural stiffness values, $D_T = D_I + D_{II}$, are all the same for variously stacked 12-layer, 16-layer or 20-layer cross-ply laminates with different axial flexural stiffness ratios, ζ, as shown in Table 3.6.

Chapter 3

Development of Biaxial Plate Specimen

3.1 Design of Biaxial Plate Specimen

3.1.1 Ideal and Modified Plate Specimen

Theoretical research for plate buckling is usually applied for the case of rectangular or square plates because of the simplicity of coordinate systems and admissible shape functions of deformed plates. In experimental work where uniaxial loading is applied the rectangular plates are preferred due to the ease in load application and specimen fabrication.

However, practical arrangement of biaxial tests for rectangular plates have many obstacles to solve. This is because four loading grips create interferences at each corner of the specimen during the continuous biaxial compression process. Figure 3-1 a). shows a schematic diagram of the biaxial loading arrangement where interferences between loading grips can occur. Ideally, the four loading grips would fit exactly on the four edges of the plates. However interference occurs because loading fixture at

edge BC can not go further to the right without interfering with fixtures at edges AB and CD which are coming down and up.

One way of overcoming this obstacle would be to make the specimen size larger than that of the loading fixtures as shown in Figure 3-1 b). In this new arrangement, there is no load at the corners. The new arrangement is therefore not exactly the same as the ideal case of rectangular plate under uniform biaxial compression. Also, a premature failure occurs at points A_1, A_2, B_1, B_2 etc. due to the the cutting action of the loading fixture on the specimen.

Another way to avoid the interference and premature failure at each corner is to cut the corners of the specimen along the solid line A_1A_2, B_1B_2, C_1C_2 and D_1D_2 as Figure 3-1 b). This modified specimen does not have exactly the same shape as the ideal rectangular plate. However, if the corner cut sizes were kept small relative to the plate dimension, this modified plate specimen may be used as a substitute for the ideal plate specimen in the experimental determination of critical buckling loads and postbuckling responses.

To study the admissibility of this modification, linear and nonlinear finite element analyses were carried out to investigate the deviations of the critical buckling loads, load-deflection responses and strain distributions between modified plates and ideal ones.

3.1.2 Fabrication of Modified Plate Specimen

Plate specimens were manufactured with NCT301 Graphite/Epoxy prepreg tapes produced by Newport Composites Inc.. Physical characteristics of NCT301 Graphite/Epoxy prepreg as obtained from the manufacturer are shown in Table 3.1. Before curing, the prepreg tapes were cut and laid up on a flat aluminum base plate. Then, these

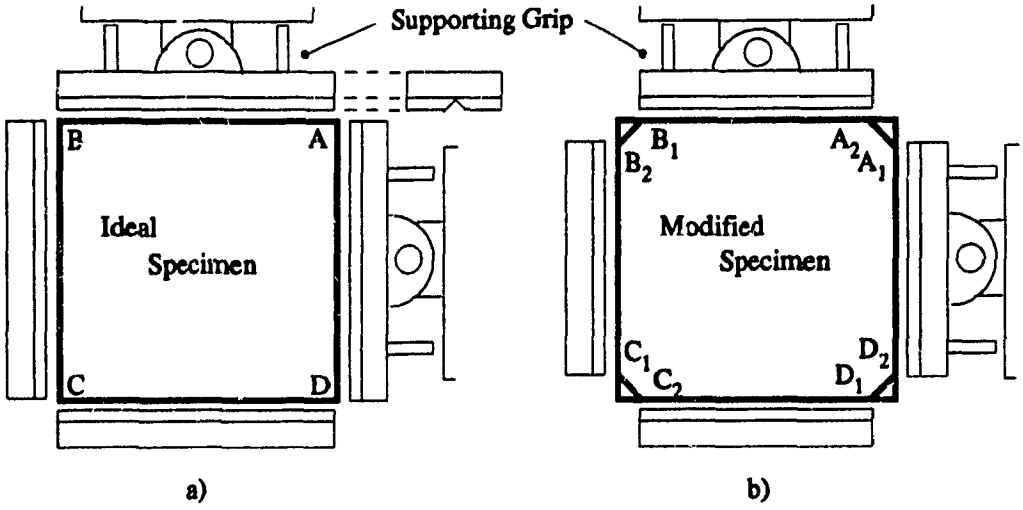

Figure 3.1: Schematic drawings of the biaxial loading device. a) Ideal setup, b) Modified setup.

wet prepreg laminates were packed with release film, breather, resin absorber and vacuum bag. All the plate specimens were cured in an autoclave using a cure cycle shown in Figure 3-2. After the curing process, the laminates were exposed to the ultrasonic scanning system to detect any internal defect. An MTS was used to get the mechanical properties of the cured NCT301 Graphite/Epoxy composite unidirectional laminate which are shown in Table 3.2. In this research, the author fabricated three groups of plate specimens, quasi isotropic, orthotropic and anisotropic laminate, where each group has three different series of layup thickness, i.e., 12, 16 and 20 plies. Dimensions and layup sequence are summarized in Table 3.3. Moreover each series of laminates were fabricated with various stacking sequences in order to determine the effects of stiffness ratio, ξ and ζ, as shown in Tables 3.4 and 3.6.

Table 3.1: Physical characteristics of NCT301 Graphite/Epoxy prepreg tape.

Property	Value
Fiber weight	230 g/sq.m
Resin content (by weight)	40 %
Volatile content	Less than 1.0 %
Gel time	10 - 16 min. at 220°F (104 °C)
Warranty period	90 days at 40°F or below

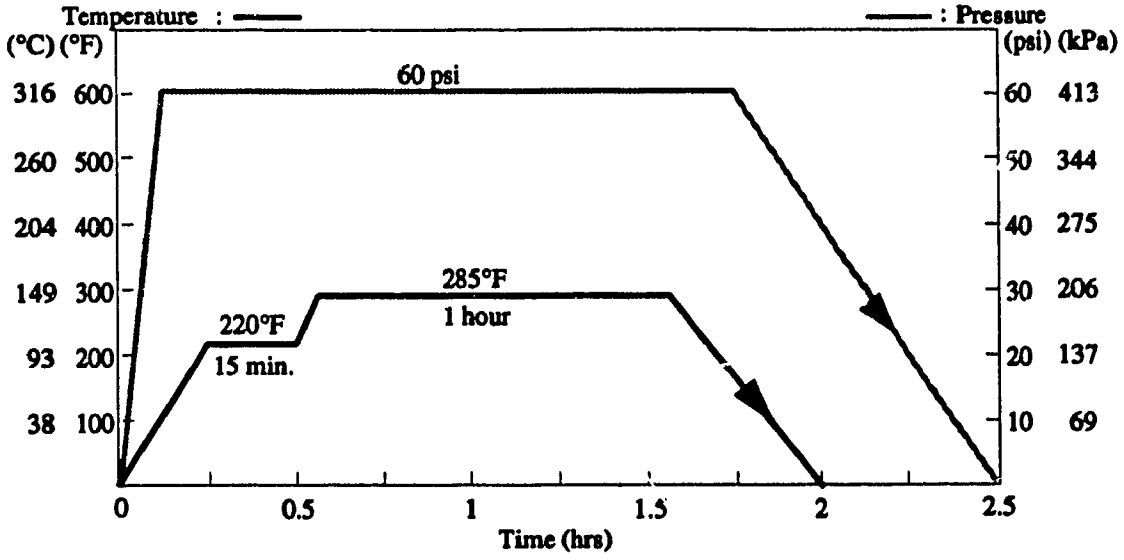

Figure 3.2: Cure cycle of the plate specimens.

Table 3.2: Material properties of the NCT-301 Graphite/Epoxy.

Symbol and Property	Value	Units
E_x, Young's modulus in the fiber direction	113.9	GPa
E_y, Young's modulus in the transverse direction	7.9	GPa
E_z, Out-of-plane Young's modulus	7.9	GPa
ν_{xy}, Poisson's ratio	0.28	
ν_{yz}, Poisson's ratio	0.4	
ν_{yx}, Poisson's ratio	0.02	
G_{xy}, In-plane shear modulus	3.1	GPa
G_{xz}, Out-of-plane shear modulus	3.1	GPa
G_{yz}, Out-of-plane shear modulus	2.8	GPa
X^T, Longitudinal tensile strength	1621.0	MPa
Y^T, Transverse tensile strength	48.3	MPa
S, Longitudinal shear strength	33.3	MPa
ε_x^*, Maximum longitudinal strain	14231×10^{-6}	
ε_y^*, Maximum transverse strain	6048×10^{-6}	
ε_s^*, Maximum longitudinal shear strain	10615×10^{-6}	
h_o, Thickness of unit ply	0.138	mm
ρ, Density	1480.0	kg/m^3

Table 3.3: Dimensions and lay-up sequence of the modified plate specimens for L-FEA, L-FEA and experiments.

Group	Lay-up		Dimension		
	Series	Stacking and orientation	a x b x h (mm)	a_c (mm)	a_c/a (%)
Ortho-tropic Plate (OP)	OP-12	$[(0/90)_3]_s$ ~ $[0_5/90]s$	240x240x1.67	18	7.5
	OP-16	$[(0/90)_4]_s$ ~ $[0_7/90]s$	240x240x2.22	18	7.5
	OP-20	$[(0/90)_5]_s$ ~ $[0_5/90]s$	240x240x2.78	18	7.5
Aniso-tropic Plate (AP)	AP-12	$[(30/-60)_3]_s$ ~ $[(60/-30)_3]_s$	240x240x1.67	18	7.5
	AP-16	$[(30/-60)_4]_s$ ~ $[(60/-30)_4]_s$	240x240x2.22	18	7.5
	AP-20	$[(30/-60)_5]_s$ ~ $[(60/-30)_5]_s$	240x240x2.78	18	7.5
Quasi-Isotropic Plate	I P-16	$[(0/90/45/-45)_2]_s$	240x240x2.22	18	7.5

Table 3.4: In-plane and flexural stiffnesses of the modified plate specimens for L-FEA, N-FEA and experiments.

Plate I. D.	Lay-up Code	In-plane Stiffness (MN/m)						Flexural Stiffness (N·m)					
		A_{11}	A_{22}	A_{12}	A_{66}	A_{16}	A_{26}	D_{11}	D_{22}	D_{12}	D_{66}	D_{16}	D_{26}
OP-12-11	$[(0/90)_3]_s$	102	102	3.8	5.2	0	0	29	18	0.8	1.2	0	0
OP-12-21	$[(0_2/90)_2]_s$	132	72	3.8	5.2	0	0	37	10	0.8	1.2	0	0
OP-12-33	$[0_3/90_3]_s$	102	102	3.8	5.2	0	0	39	8	0.8	1.2	0	0
OP-12-51	$[0_5/90]_s$	161	43	3.8	5.2	0	0	44	3	0.8	1.2	0	0
OP-12-60	$[0_6]_s$	191	13	3.8	5.2	0	0	44	3	0.8	1.2	0	0
OP-16-11	$[(0/90)_4]_s$	136	136	5.1	7.0	0	0	65	47	2.1	2.9	0	0
OP-16-22	$[(0_2/90_2)_2]_s$	136	136	5.1	7.0	0	0	74	38	2.1	2.9	0	0
OP-16-44	$[0_4/90_4]_s$	136	136	5.1	7.0	0	0	93	19	2.1	2.9	0	0
OP-16-71	$[0_7/90]_s$	225	47	5.1	7.0	0	0	104	8	2.1	2.9	0	0
OP-16-80	$[0_8]_s$	254	18	5.1	7.0	0	0	104	7	2.1	2.9	0	0
OP-20-11	$[(0/90)_5]_s$	170	170	6.4	8.7	0	0	123	95	4.1	5.6	0	0
OP-20-32	$[(0_3/90_2)_2]_s$	200	141	6.4	8.7	0	0	161	57	4.1	5.6	0	0
OP-20-55	$[0_5/90_5]_s$	170	170	6.4	8.7	0	0	180	38	4.1	5.6	0	0
OP-20-82	$[0_8/90_2]_s$	259	81	6.4	8.7	0	0	202	16	4.1	5.6	0	0
OP-20-100	$[0_{10}]_s$	318	22	6.4	8.7	0	0	204	14	4.1	5.6	0	0
AP-16-36	$[(30/-60)_4]_s$	92	92	49	51	25	-25	42	33	20	21	14	-6.4
AP-16-45	$[(45/-45)_4]_s$	78	78	64	65	0	0	32	32	26	27	4.5	4.5
AP-16-63	$[(60/-30)_4]_s$	92	92	49	51	-25	25	33	42	20	21	-6.4	14
AP-20-36	$[(30/-60)_5]_s$	115	115	61	64	32	-32	81	67	39	41	26	-14
AP-20-45	$[(45/-45)_5]_s$	97	97	80	82	0	0	62	62	51	53	7.1	7.1
AP-20-63	$[(60/-30)_5]_s$	115	115	61	64	-32	32	67	81	39	41	-14	26
IP-16-45	$[(0/90/45/-45)_2]_s$	107	107	34	36	0	0	54	43	9.6	10.4	1.7	1.7

Table 3.5: Stiffness ratios and stiffness constants of the modified plate specimens for L-FEA, N-FEA and experiments.

Plate I. D.	Lay-up Code	$\xi = (\frac{A_{11}}{A_{22}})$	$\zeta = (\frac{D_{11}}{D_{22}})$	$D_I = (D_{11}+D_{22})$	$D_{II} = 2(D_{12}+2D_{66})$	N-FEA (Yes/No)	Experimented (Yes/No)
OP-12-11	$[(0/90)_3]_s$	1.0	1.6	47.2	6.6	Yes	Yes
OP-12-21	$[(0_2/90)_2]_s$	1.8	3.6	47.2	6.6	Yes	Yes
OP-12-33	$[0_3/90_3]_s$	1.0	4.7	47.2	6.6	Yes	Yes
OP-12-51	$[0_5/90]_s$	3.7	13.7	47.2	6.6	No	No
OP-12-60	$[0_6]_s$	14.3	14.3	47.2	6.6	No	No
OP-16-11	$[(0/90)_4]_s$	1.0	1.4	111.8	15.6	Yes	Yes
OP-16-22	$[(0_2/90_2)_2]_s$	1.0	2.0	111.8	15.6	No	No
OP-16-44	$[0_4/90_4]_s$	1.0	4.7	111.8	15.6	Yes	Yes
OP-16-71	$[0_7/90]_s$	4.7	13.9	111.8	15.6	Yes	Yes
OP-16-80	$[0_8]_s$	14.3	14.3	111.8	15.6	Yes	No
OP-20-11	$[(0/90)_5]_s$	1.0	1.3	218.3	30.5	Yes	Yes
OP-20-32	$[(0_3/90_2)_2]_s$	1.4	2.8	218.3	30.5	No	No
OP-20-55	$[0_5/90_5]_s$	1.0	4.7	218.3	30.5	Yes	Yes
OP-20-82	$[0_8/90_2]_s$	3.2	12.8	218.3	30.5	Yes	Yes
OP-20-100	$[0_{10}]_s$	14.3	14.3	218.3	30.5	Yes	No
AP-16-36	$[(30/-60)_4]_s$	1.0	1.3	75.7	123.8	Yes	Yes
AP-16-45	$[(45/-45)_4]_s$	1.0	1.0	63.7	159.8	Yes	Yes
AP-16-63	$[(60/-30)_4]_s$	1.0	0.8	75.7	123.8	Yes	Yes
AP-20-36	$[(30/-60)_5]_s$	1.0	1.2	147.9	241.7	Yes	Yes
AP-20-45	$[(45/-45)_5]_s$	1.0	1.0	124.4	312.2	Yes	Yes
AP-20-63	$[(60/-30)_5]_s$	1.0	0.8	147.9	241.7	Yes	Yes
I P-16-45	$[(0/90/45/-45)_2]_s$	1.0	1.3	96.7	60.7	Yes	Yes

Table 3.6: Global stiffness ratio and critical buckling load of the modified plate specimen from theory and N-FEA.

Plate I. D.	Lay-up Code	Global Stiffness D_T(N.m)	Critical Buckling Load			Experimented (Yes/No)
			Theoretical Ideal P_{cr}(kN)	Theoretical Modified P_{cr}(kN)	N-FEA P_{cr}(kN)	
OP-12-11	$[(0/90)_3]_s$	53.8	2.21	1.99	—	Yes
OP-12-21	$[(0_2/90)_2]_s$	53.8	2.21	1.99	—	Yes
OP-12-33	$[0_3/90_3]_s$	53.8	2.21	1.99	—	Yes
OP-12-51	$[0_5/90]_s$	53.8	2.21	1.99	—	No
OP-12-60	$[0_6]_s$	53.8	2.21	1.99	—	No
OP-16-11	$[(0/90)_4]_s$	127.4	5.24	4.71	4.65	Yes
OP-16-22	$[(0_2/90_2)_2]_s$	127.4	5.24	4.71	—	No
OP-16-44	$[0_4/90_4]_s$	127.4	5.24	4.71	4.65	Yes
OP-16-71	$[0_7/90]_s$	127.4	5.24	4.71	4.50	Yes
OP-16-80	$[0_8]_s$	127.4	5.24	4.71	4.40	No
OP-20-11	$[(0/90)_5]_s$	248.8	10.23	9.20	9.05	Yes
OP-20-32	$[(0_3/90_2)_2]_s$	248.8	10.23	9.20	—	No
OP-20-55	$[0_5/90_5]_s$	248.8	10.23	9.20	9.05	Yes
OP-20-82	$[0_8/90_2]_s$	248.8	10.23	9.20	8.80	Yes
OP-20-100	$[0_{10}]_s$	248.8	10.23	9.20	8.65	No
AP-16-36	$[(30/-60)_4]_s$	199.5	under 8.20	under 7.38	7.10	Yes
AP-16-45	$[(45/-45)_4]_s$	220.5	under 9.06	under 8.16	8.40	Yes
AP-16-63	$[(60/-30)_4]_s$	199.5	under 8.20	under 7.38	6.90	Yes
AP-20-36	$[(30/-60)_5]_s$	389.6	under 6.20	under 14.41	14.20	Yes
AP-20-45	$[(45/-45)_5]_s$	436.6	under 17.95	under 16.15	16.40	Yes
AP-20-63	$[(60/-30)_5]_s$	389.6	under 16.20	under 14.41	14.00	Yes
IP-16-45	$[(0/90/45/-45)_2]_s$	157.4	under 6.47	under 5.82	—	Yes

3.2 Validity of Modified Plate Specimen

3.2.1 Numerical Validation

To investigate the admissibility of the modified plate specimen as a substitute of ideal plate, linear and nonlinear finite element analyses were made using ANSYS program [50]. First of all, effects of corner modification on the critical buckling load were calculated numerically by monitoring the reduction of the critical buckling load from ideal plate to modified one while increasing the modification ratio, a_c/a, as shown in Figures 3-3.

For linear and nonlinear finite element analyses with ANSYS program, 8-node multi-layered shell element, SHELL99, was used. This element can allow up to 100 different layers in a laminate. Each model was meshed with more than 148 elements with different densities from centre to the corner of the plate as presented in Figure 3-4 and Figure 3-5. At each modification ratio, such as 2.5%, 5%, 7.5%, 10% of a_c/a, critical buckling load was computed by linear finite element method with the full-subspace eigenvalue extraction approach while controlling the maximum error norm value to be less than 10^{-6}. The results of this L-FEA for the two kinds of modified plates, corner-unloaded and corner-cut, are presented in Figure 3-6.

On the other hand, nonlinear finite element analysis was performed to obtain more accurate postbuckling behaviour and strain distribution on the surface of the plate specimen. A small initial deflection, less than $0.08mm$, was prescribed by the action of infinitesimal lateral pressure to invoke large deflection N-FEA successfully. Also, $15 \sim 25$ steps of load increments were imposed with different intervals to secure more accurate bifurcation point and postbuckling behaviour. Moreover, the convergence was checked by controlling the maximum deflection error norm, Δu, to be less than $10^{-6}mm$ with more than 25 times of iteration in each load step. These N-FEA results

for the influence of corner modification were plotted in Figure 3-7. From the load-deflection curves in Figure 3-7, it can be found that all the curves are the same trend and each curve shows a parallel transition according to the modification ratio. In addition to this, nearly linear relation was obtained in the plot of the critical load v.s. modification ratio as shown in Figure 3-6. Consequently, it is obvious that the modified specimen does not produce significant error when it is used as a substitute for an ideal plate specimen as long as $a_c/a < 7.5\%$

Another aspect on the investigation of the validity of the modified specimen was focused on the comparison of load-deflection behaviour and strain distribution of the two specimens, ideal and modified, through the applications of the N-FEA. For the biaxial buckling of OP-16-11 plate, the continuous buckling deformations for ideal and modified plates are shown in Figure 3-8 and Figure 3-9, where the global shapes of buckling deformation of the two plates are identical except the value of the maximum transverse deflection, w_{max}.

Also, detailed views of the surface strain distribution are illustrated in Figures 3-10, 3-11, 3-12 and 3-13. These four pictures describe the surface strain distributions of the ideal and modified plates when the two plate are subjected to the same amount of biaxial load, $P_x = P_y = 3$kN, as shown in Figure 3-8 e) and Figure 3-9 e). Comparing the bidirectional strain distributions(ϵ_x,ϵ_y) of the ideal and modified specimens, truly similar strain distributions appeared at the centre of the plate. On the other hand the strain concentrations are not severely high at the corners of the modified plate.

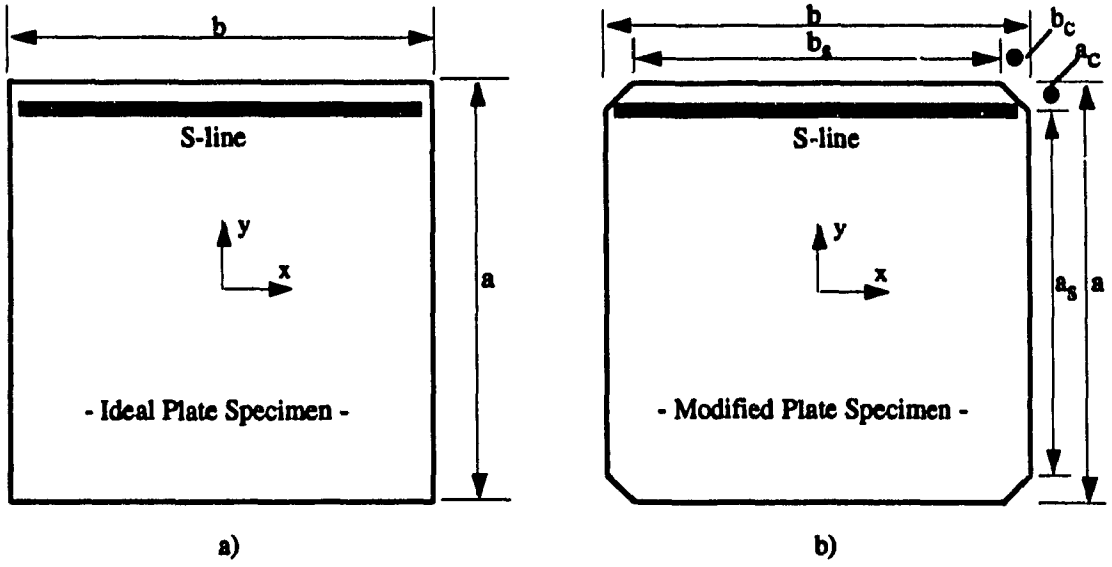

Figure 3.3: The S-line for strain comparison between ideal plate specimen and modified plate specimen by N-FEA.

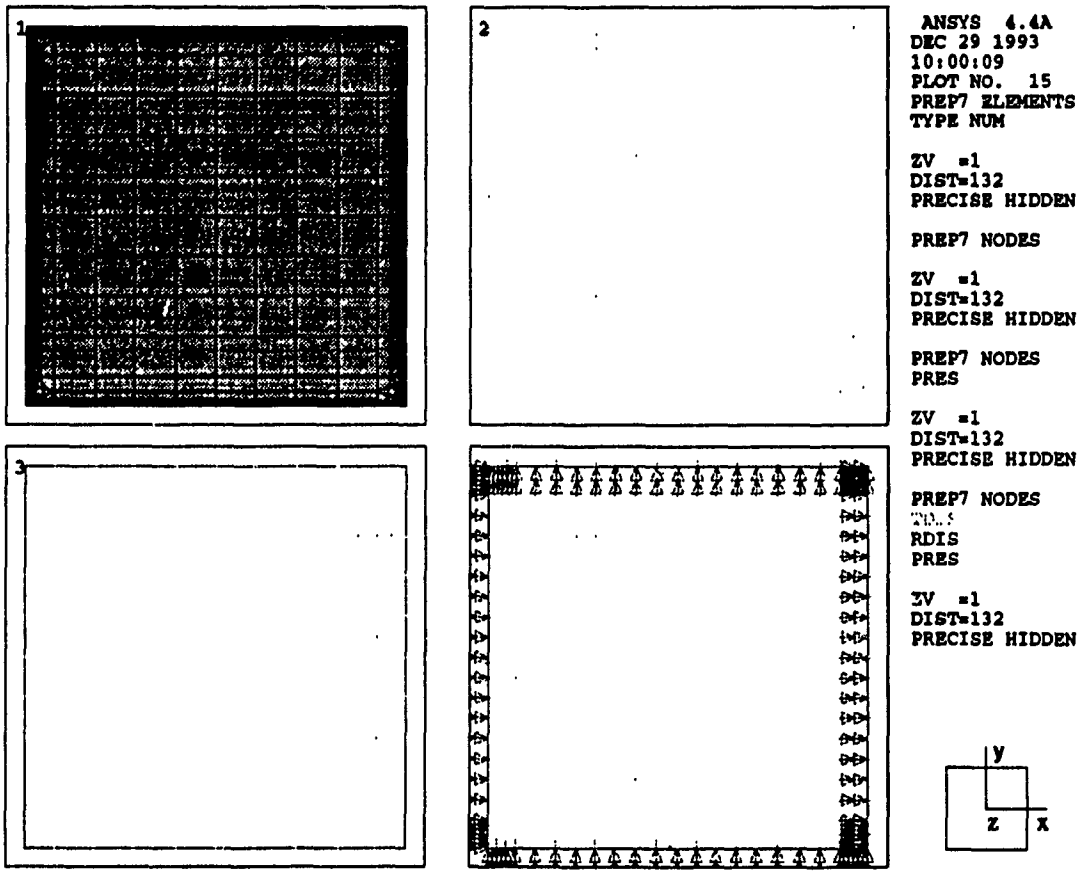

Figure 3.4: Input data for N-FEA of ideal plate (1:meshed elements, 2:nodal points, 3:prescribed loads, 4:boundary conditions).

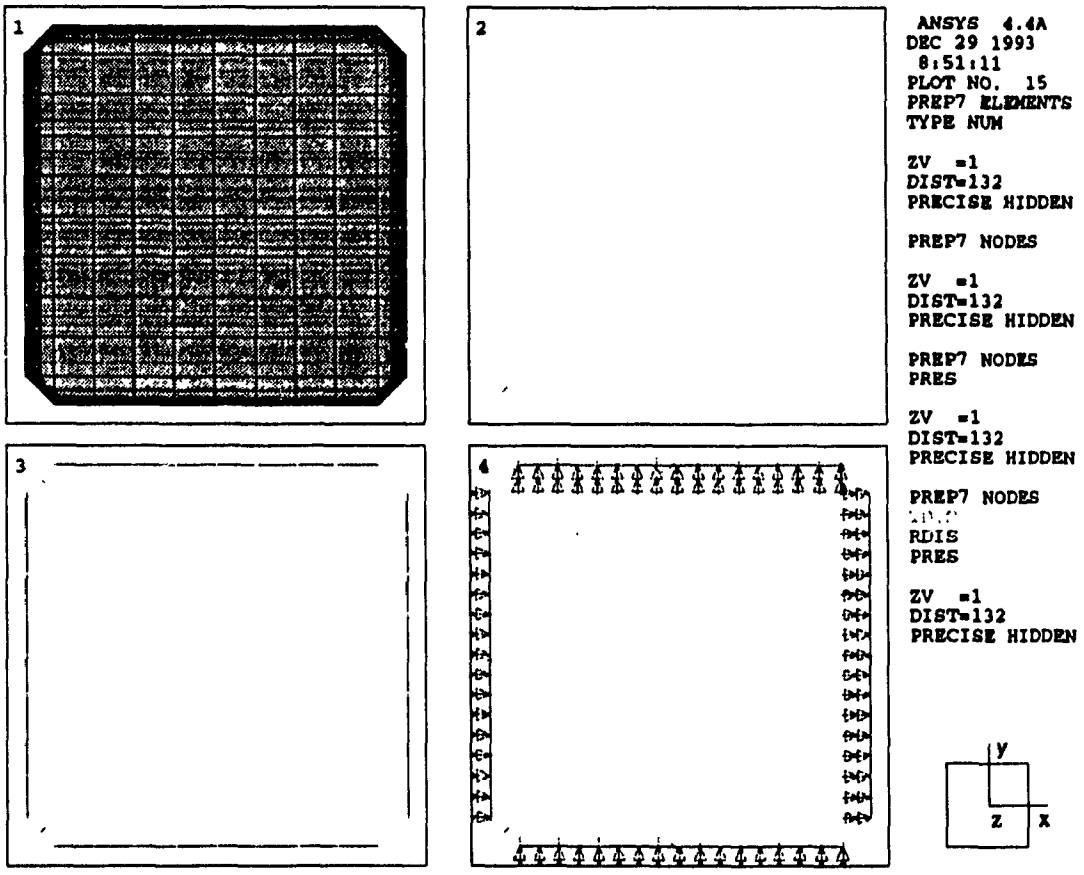

Figure 3.5: Input data for N-FEA of modified plate (1:meshed elements, 2:nodal points, 3:prescribed loads, 4:boundary conditions).

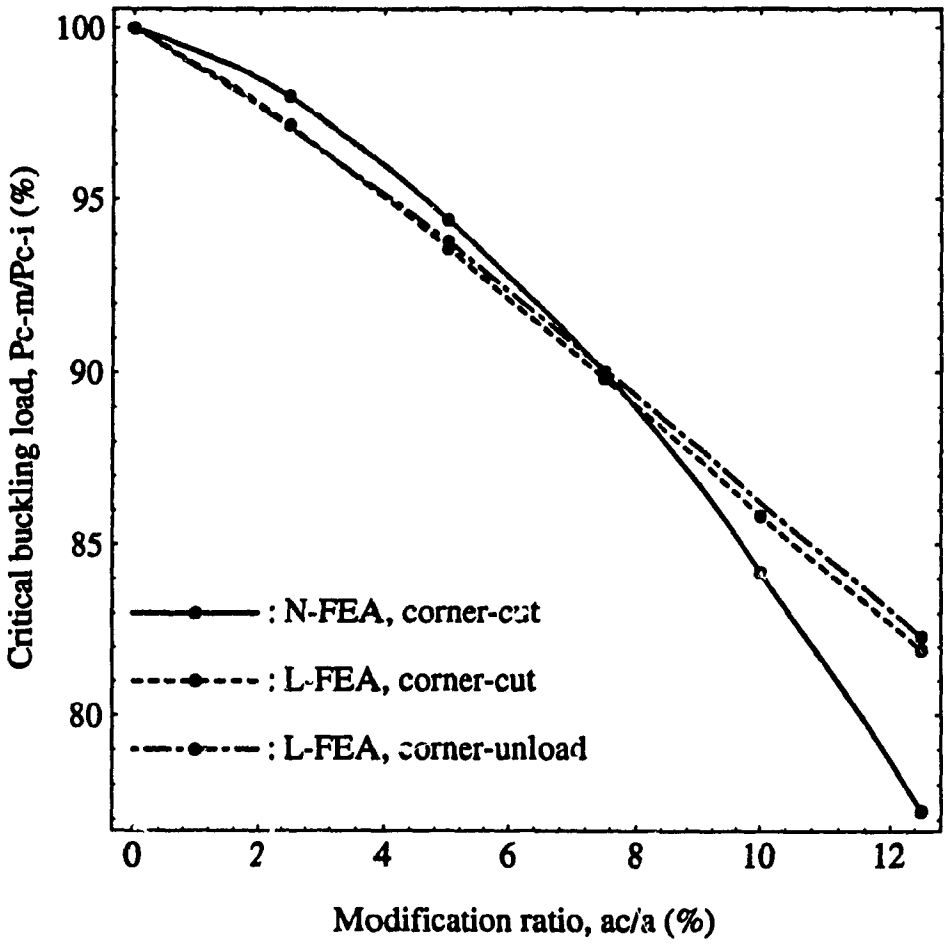

Figure 3.6: Effects of specimen modifications on the critical buckling loads of biaxially loaded OP-16-11 plate from L-FEA and N-FEA.

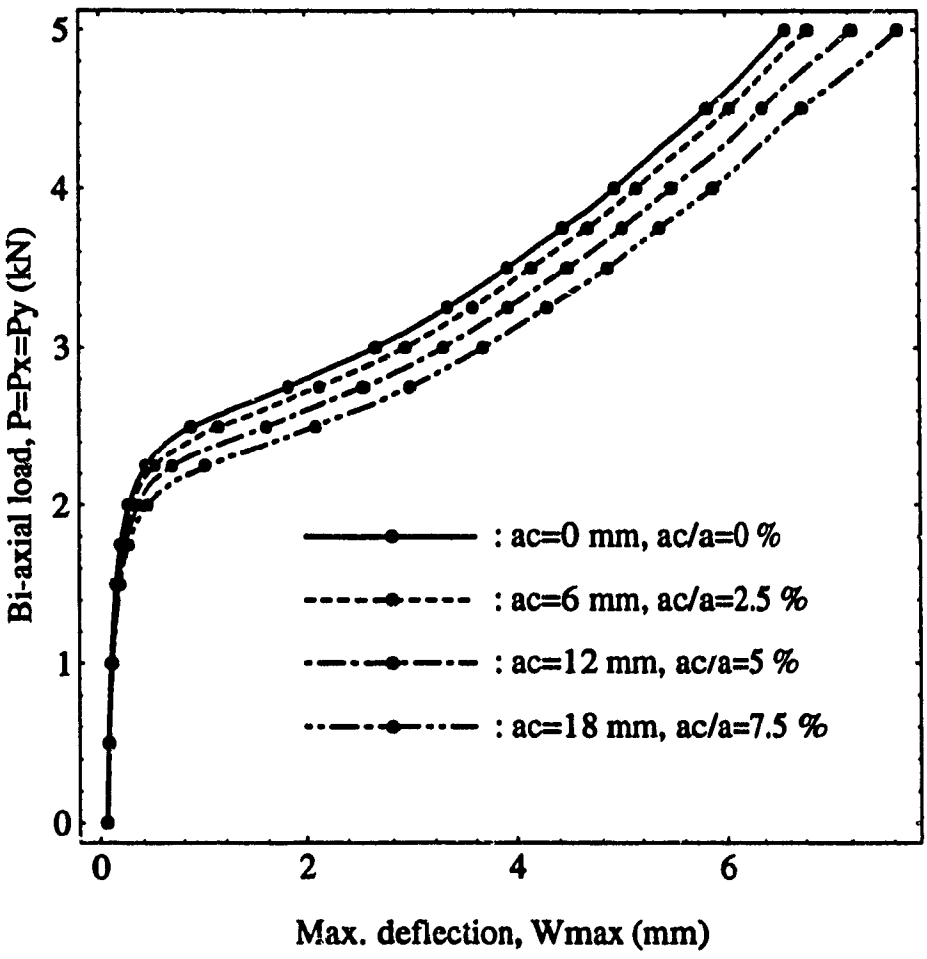

Figure 3.7: Specimen modification effects on the biaxial buckling behaviour of OP-16-11 plate from N-FEA.

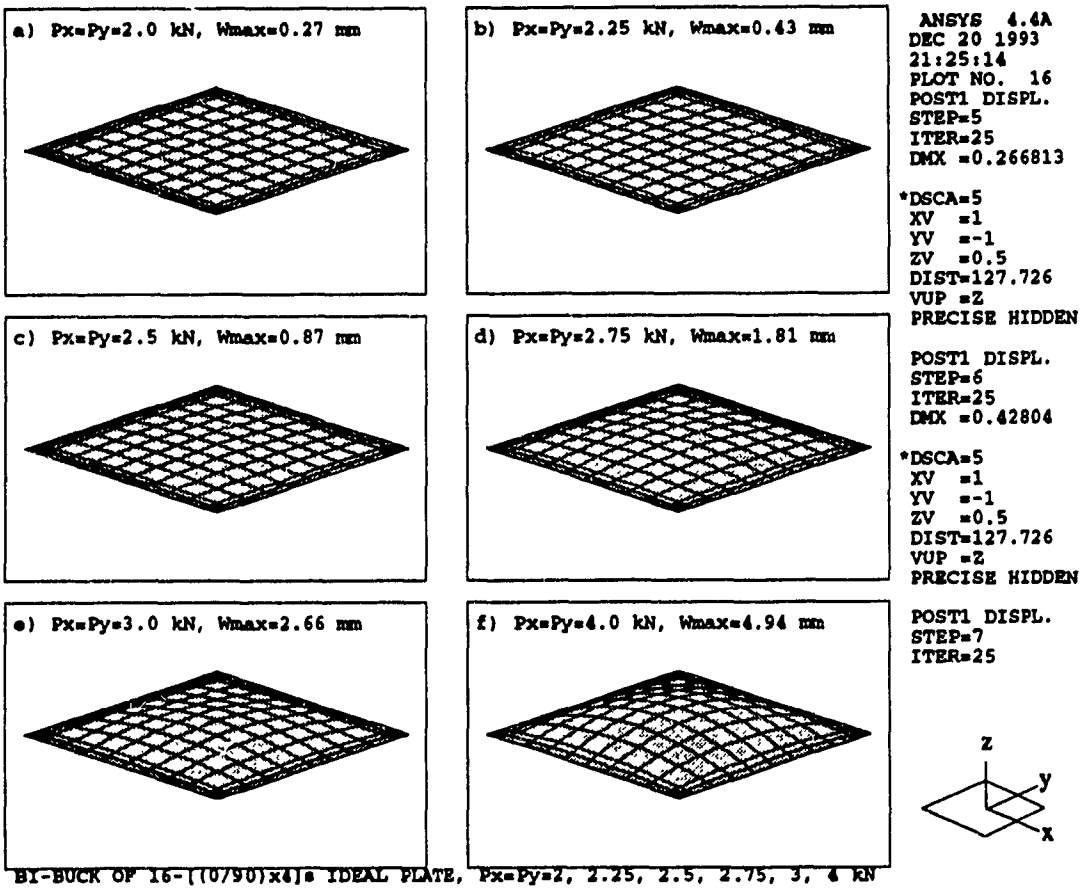

Figure 3.8: Continuous buckling deformation of ideal plate specimen OP-16-11 with biaxial loading ($P_x : P_y = 1 : 1$) from N-FEA.

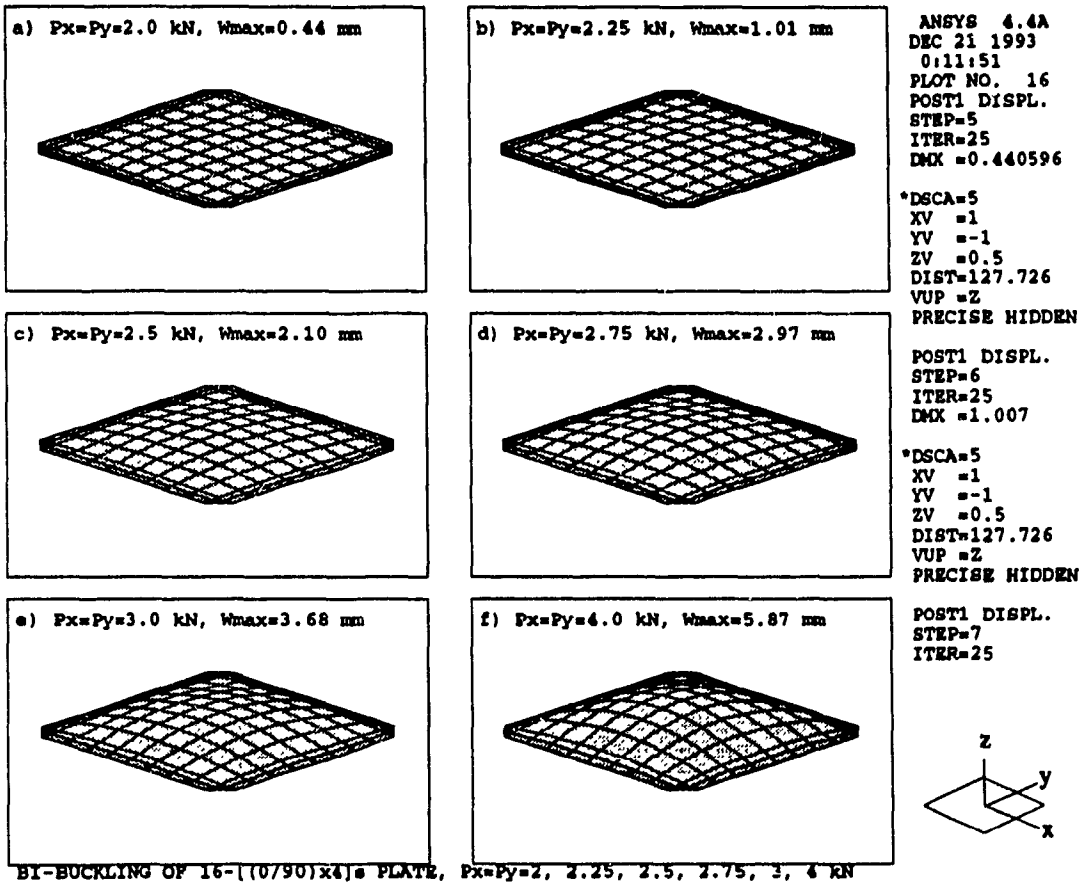

Figure 3.9: Continuous buckling deformations of modified plate specimen OP-16-11 with biaxial loading ($P_x : P_y = 1 : 1$) from N-FEA.

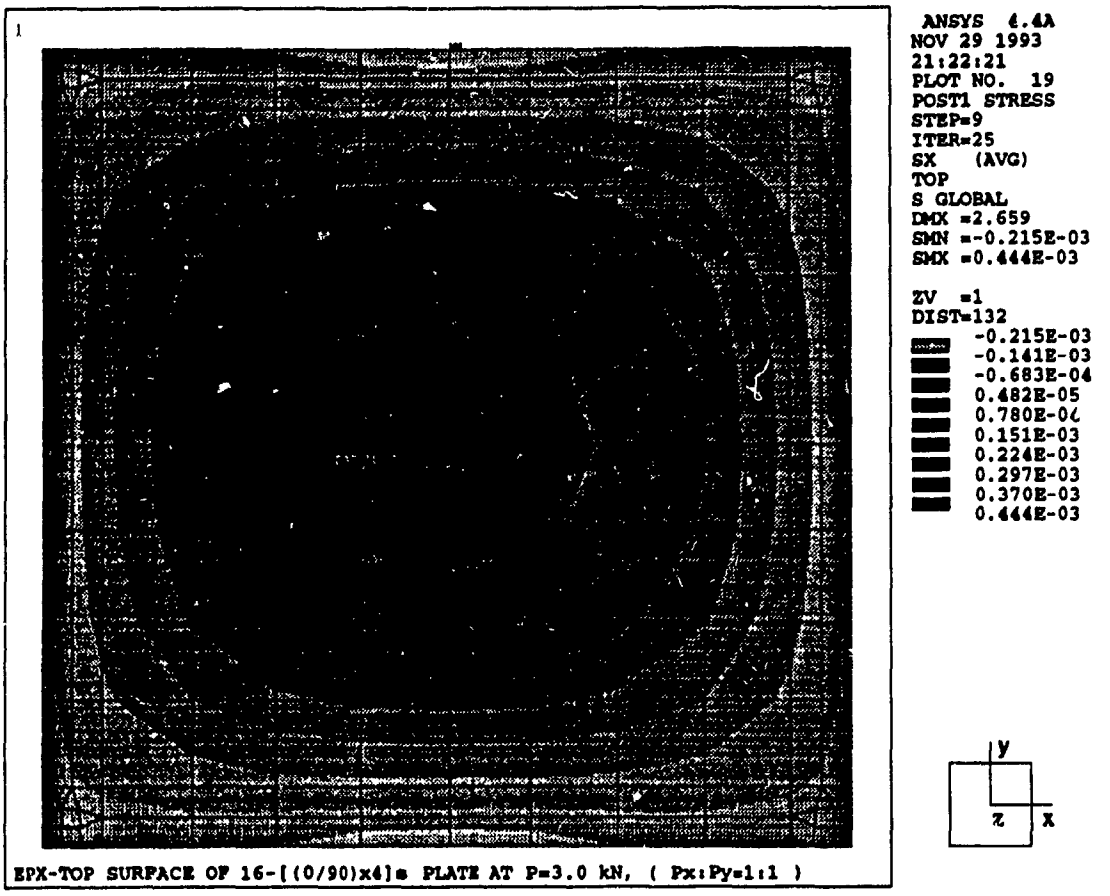

Figure 3.10: X-strain (strain along x-direction, ϵ_x) distribution along x direction of ideal plate specimen OP-16-11 with biaxial loading, $P_x = P_y = 3$kN ($P_x : P_y = 1 : 1$), from N-FEA.

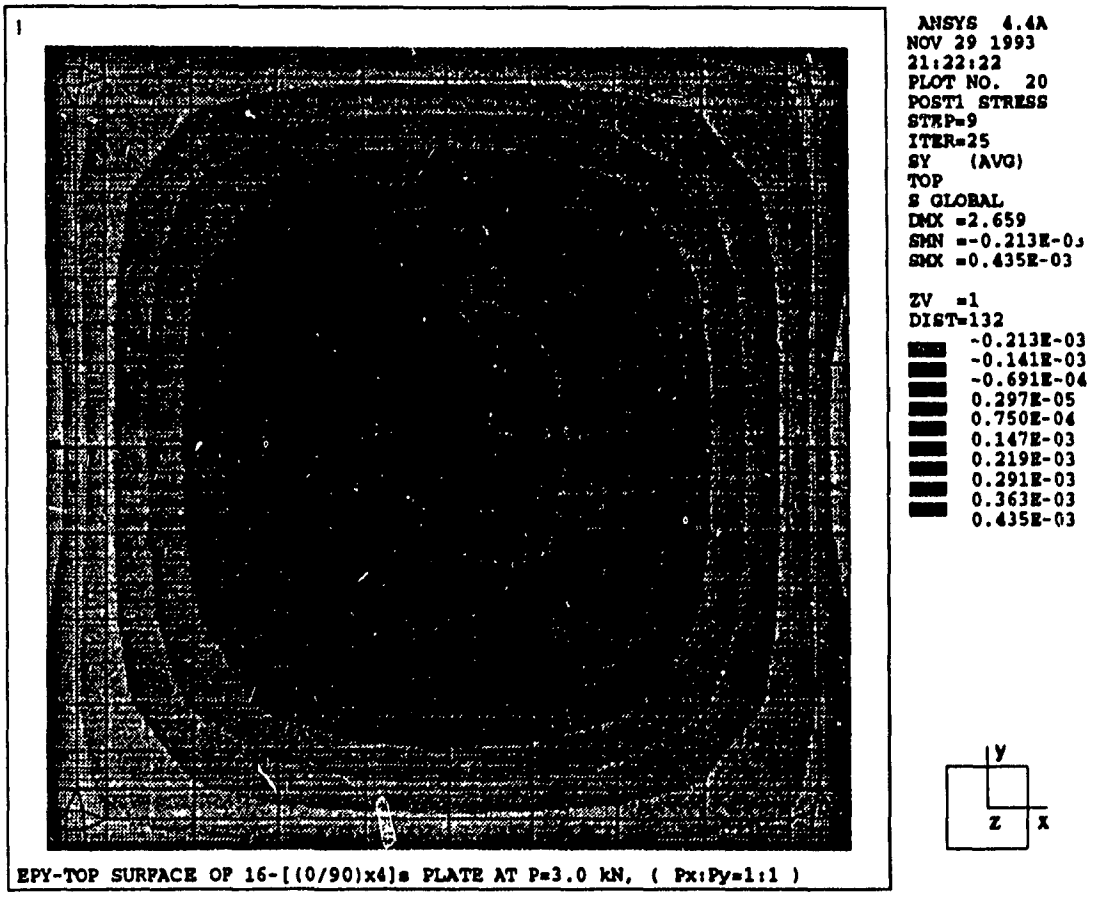

Figure 3.11: Y-strain (strain along y-direction, ϵ_y) distribution of ideal plate specimen OP-16-11 with biaxial loading, $P_x = P_y = 3\text{kN}$ ($P_x : P_y = 1 : 1$), from N-FEA.

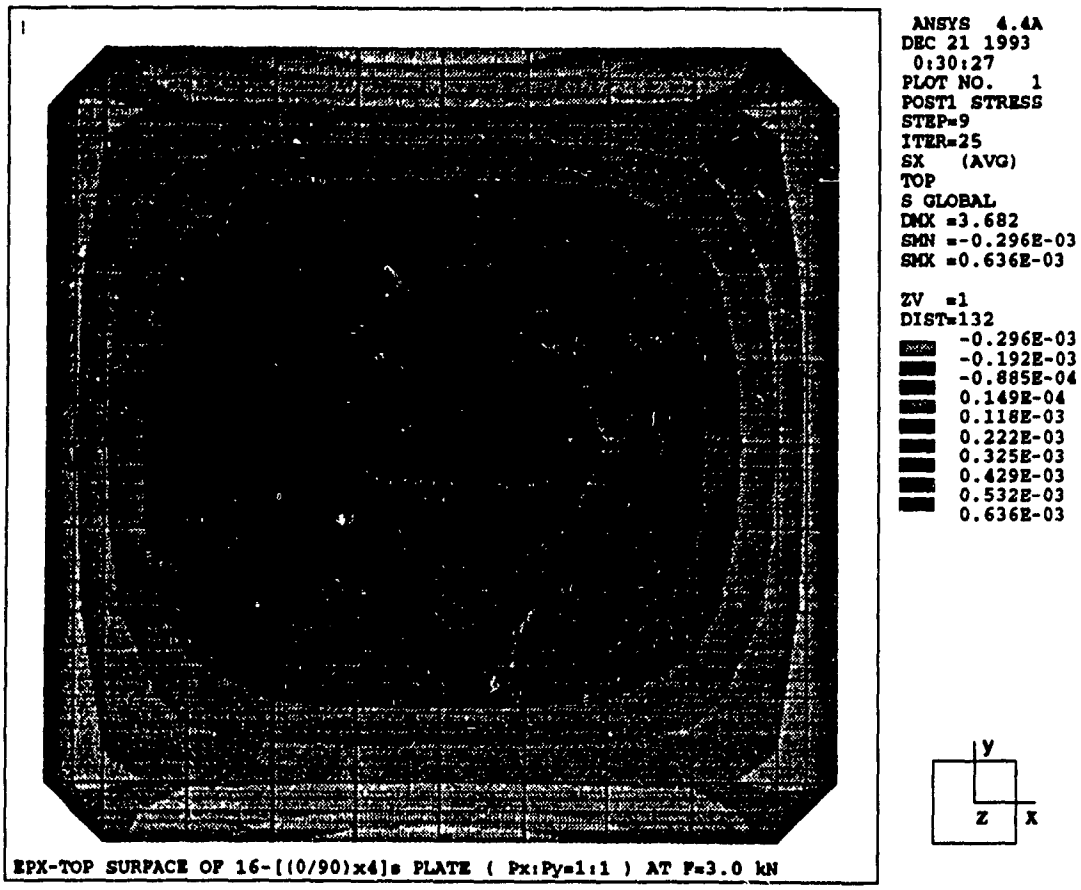

Figure 3.12: X-strain(ϵ_x) distribution of modified plate specimen OP-16-11 with biaxial loading, $P_x = P_y = 3$kN ($P_x : P_y = 1 : 1$), from N-FEA.

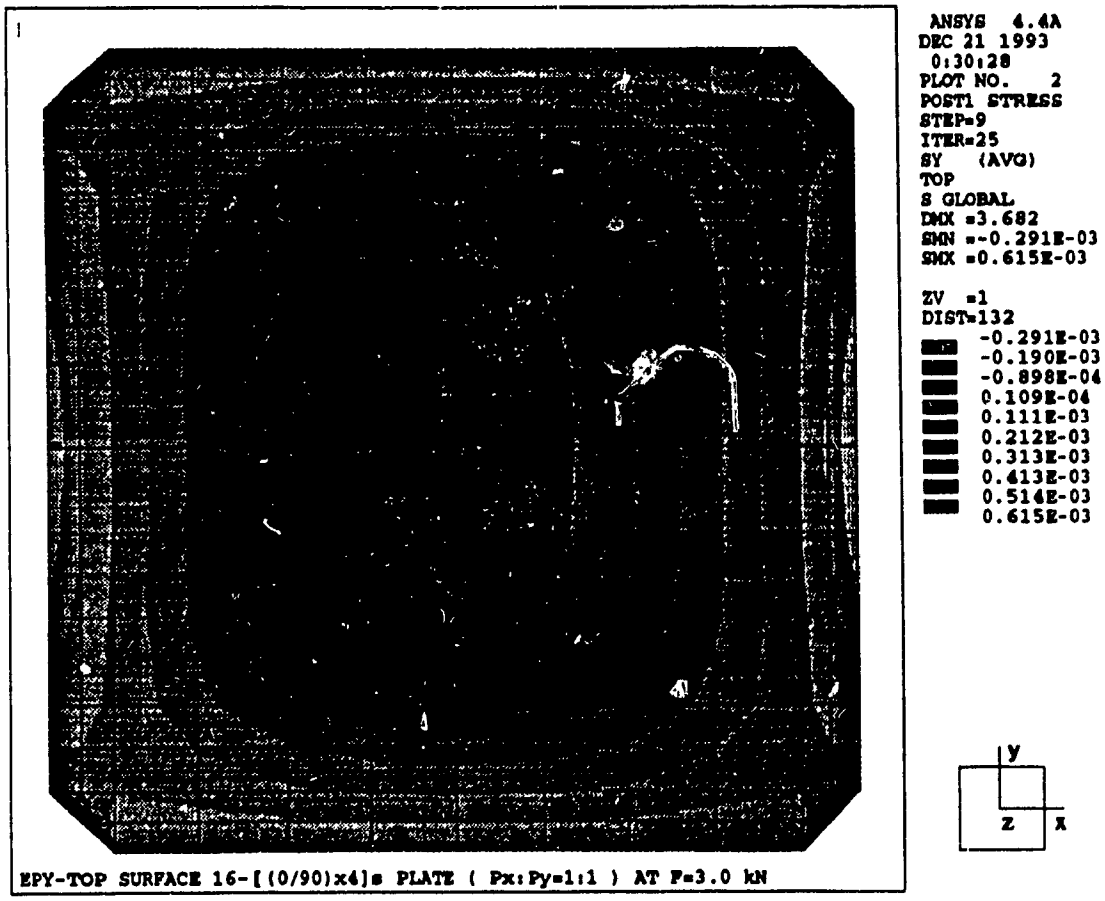

Figure 3.13: Y-strain(ϵ_y) distribution of modified plate specimen OP-16-11 with biaxial loading, $P_x = P_y = 3$kN ($P_x : P_y = 1 : 1$), from N-FEA.

3.2.2 Experimental Validation

To confirm numerical results on specimen modification effects with experiments, the strain distributions at the centre and rim area along the S-line of the plate was investigated (S-line is shown in Figure 3-3). Strain gauges were located in the centre area of the plate, four gauges on each side with #1 ~ #4 and #21 ~ #24 as shown in Figure 3-14. These gauges were intended to examine the admissibility of the testing area where effects of modifications could be neglected. Five strain gauges, #5 ~ #9, were also located on the rim area along the S-line to examine the continuity and uniformity of contact between the specimen and loading grips. The specimens were tested in a biaxial machine as shown in Figure 3-15.

Concerning plate buckling experiments under biaxial compressive deformation, the strain inspection is meaningful because the plate boundaries change from straight lines with full-contact with loading grips at the early stage to parabolic curves with incomplete contact at postbuckled state. In fact, this boundary behaviour is the result of the global deflection shape of the postbuckled plate. In Figures 3-16 and 3-17, numerical results for the Y-strain values(strain values along y-direction, ϵ_y) at the rim area along the S-line are presented for the ideal plate and modified plate of OP-16-11, where the two strain distributions correspond well in early stage of postbuckling. Furthermore, in a high level of buckling load (i.e., 5 kN), the wave-like curve of y-stain(ϵ_y) along S-line shows the possibility of incomplete contact at boundaries. These boundary behaviours will be discussed more fully in Chapter 4.

To secure the strain behaviour of the centre of the plate, four strain values of front and back surface of OP-16-11 specimen were plotted in Figure 3-18 by N-FEA. From this figure, an equalized strain distribution was found in the centre of plate and it was already verified from the x- and y-strain distributions of centre area in Figure 3-12 and Figure 3-13. On the other hand, in Figure 3-19, the experimental strain values

were compared with that of N-FEA, where all experimental strain plots revealed the same contour as numerical strain values. In the same manner, Y-strain values(ϵ_y) at the rim area along the S-line were presented in Figure 3-20 and compared with experiments in Figure 3-21, where the two strain values revealed as a conformed curves. In this experimental validation process to check the admissibility of the modified plate specimen, as we know, one unfortunate thing is that the ideal plate specimen is obviously impossible to be tested without modification. For this reason, only after the full-comparisons of numerical results between ideal and modified plate specimen, the experimental data were compared with numerical results only for the case of modified plate specimen.

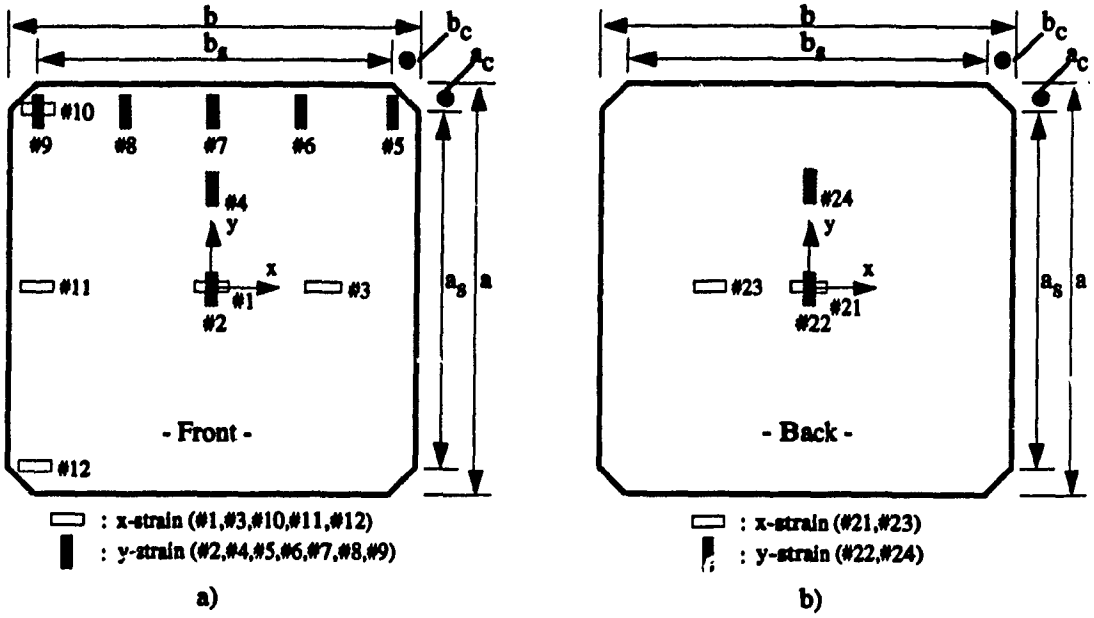

Figure 3.14: Location of strain gauges on the experimental plate specimens, a) front side, b) back side.

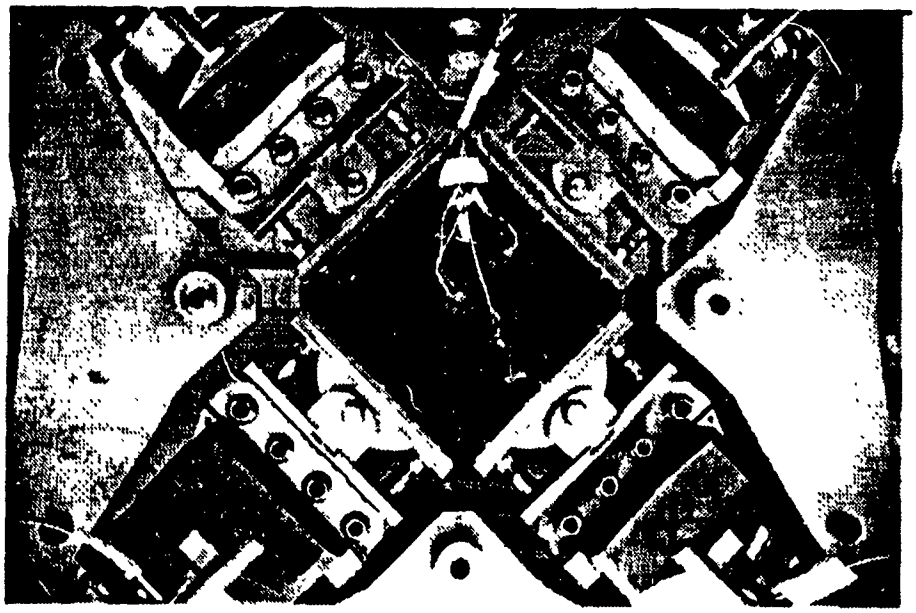

Figure 3.15: Experimental setup of loading grips with a modified specimen.

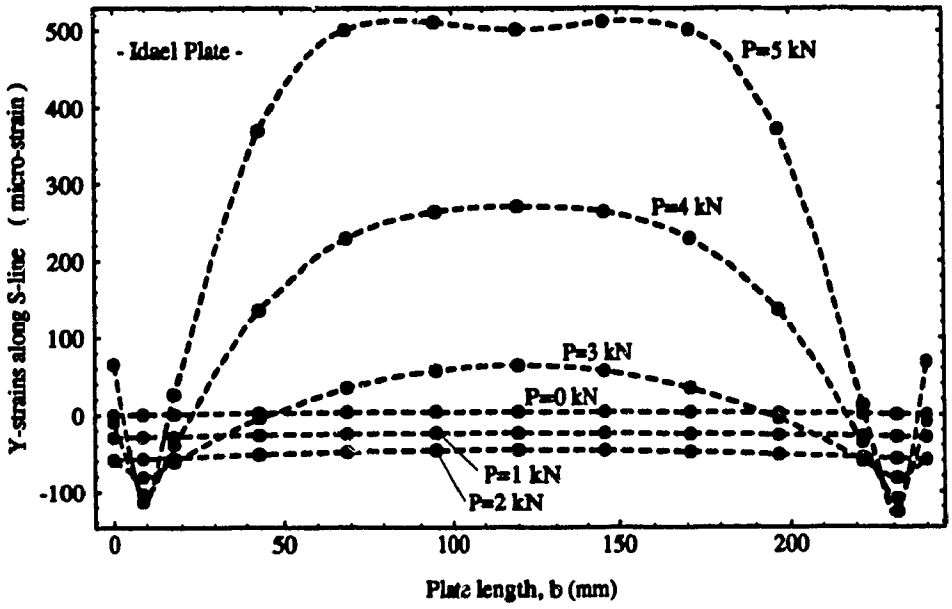

Figure 3.16: Y-strains, ϵ_y, along the S-line of OP-16-11(see Figure 3.3) ideal plate specimen with various biaxial loadings from N-FEA.

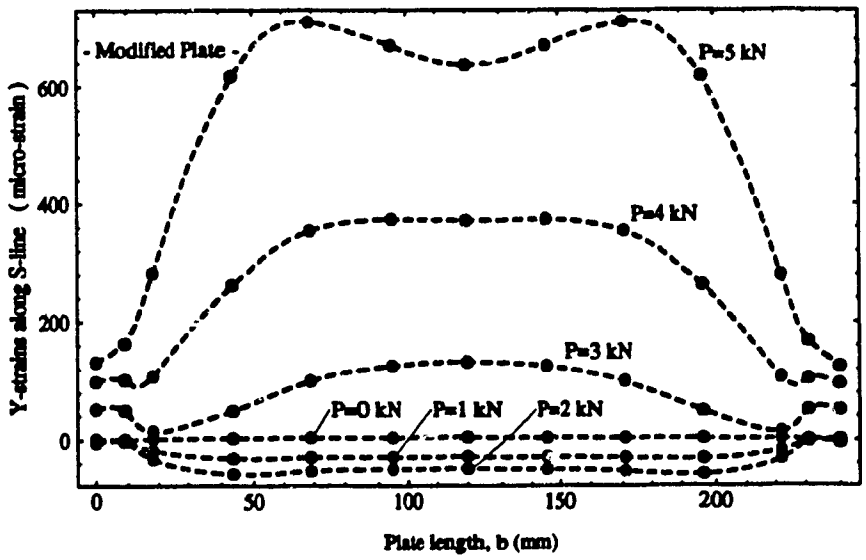

Figure 3.17: Y-strains, ϵ_y, along the S-line of OP-16-11(see Figure 3.3) modified plate specimen with various biaxial loadings from N-FEA.

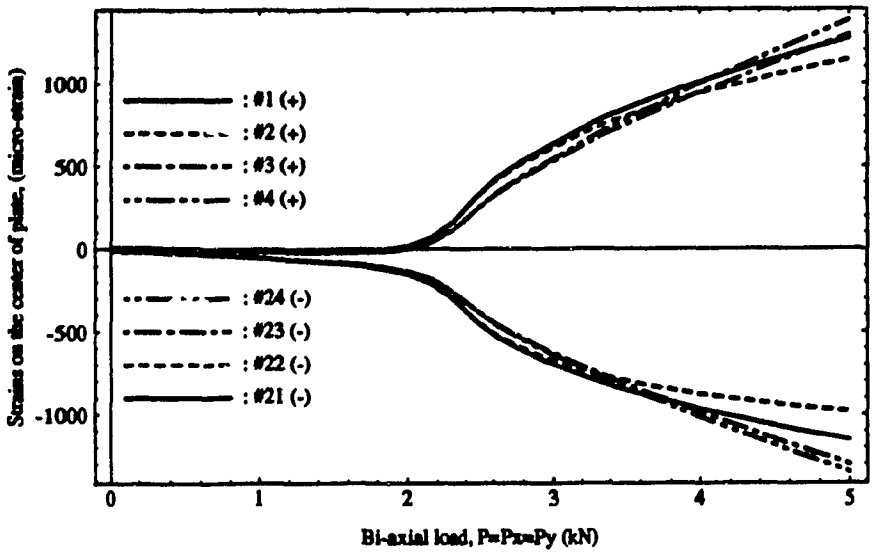

Figure 3.18: Strains at plate centre for OP-16-11 modified plate under biaxial loading with N-FEA.

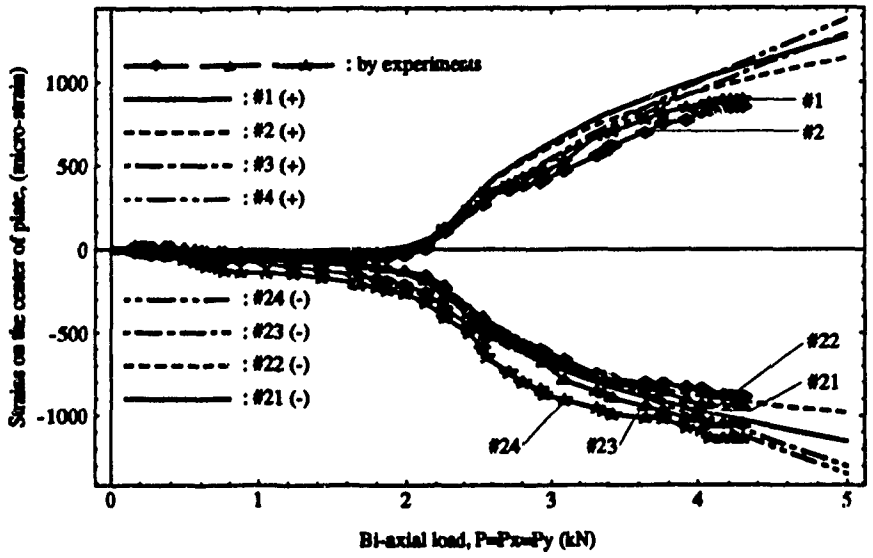

Figure 3.19: Comparing the experimental and numerical strains for OP-16-11 modified plate at plate centre, under biaxial loading.

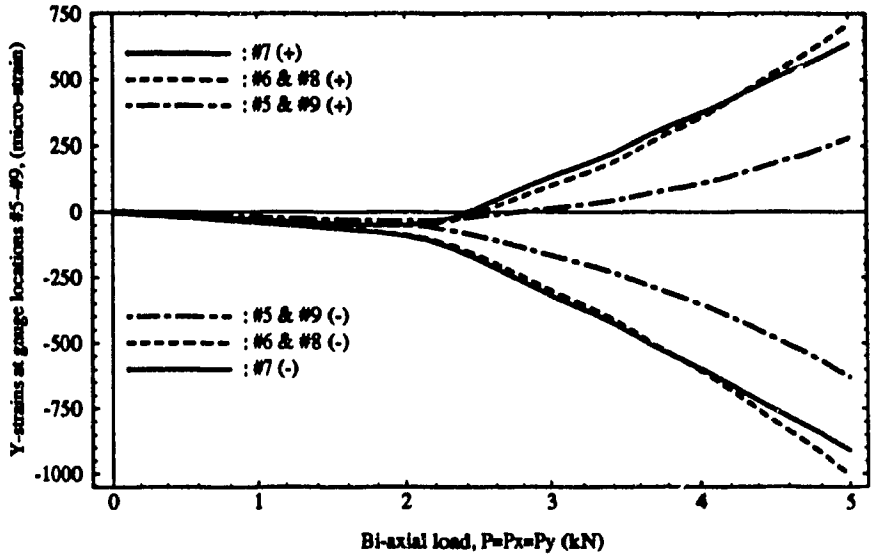

Figure 3.20: Y-strains along the S-line for OP-16-11 modified plate under biaxial loading with N-FEA.

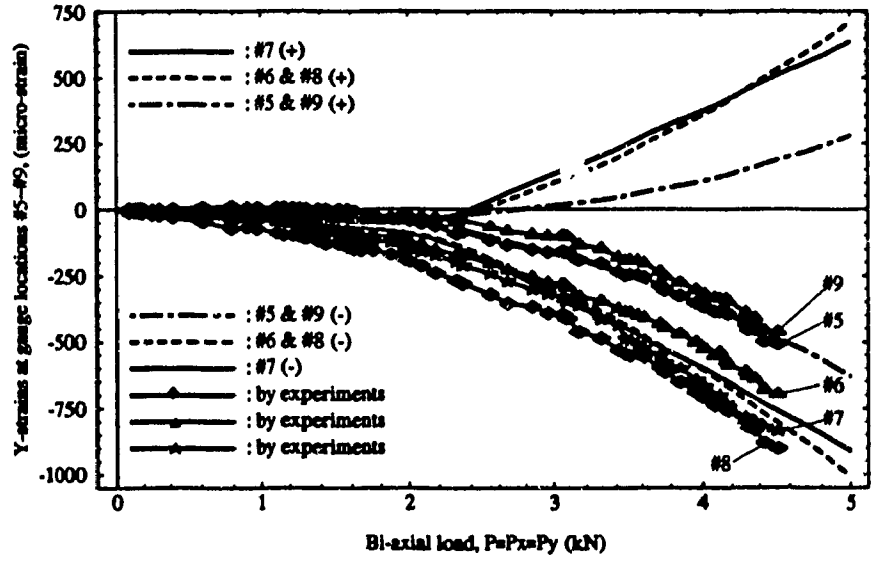

Figure 3.21: Comparing the experimental y-strains along the S-line for OP-16-11 modified plate under biaxial loading with N-FEA.

Chapter 4

Boundary Conditions Considerations

4.1 Boundary behaviour of Postbuckled Plate

From information obtained in the literature on the biaxial buckling for the composite laminates, it was found that there was a severe limitation in the analytical methods to interpret the actual behaviour of the plate at postbuckling state. The main restrictions of the analytical methods are due to the limited choice of displacement functions and loading conditions. In numerous theoretical researches on the plate buckling and post-buckling problems, all analyses have been conducted under simplified boundary loading conditions, i.e., uniform pressure loading and uniform end-shortening. Uniform end-shortening boundary condition can be made by the compression with the rigid bar bonded with plate. Uniform pressure loading condition is hard to be made but it traditionally has been constructed by mean of rigid bars. However, it can be realized that the actual conditions of plate boundaries are neither of them.

At the postbuckling state, the plate boundaries changed from straight lines to partly curved lines due to the large transverse deflection. Also the boundary stresses

change from uniform-continuous to nonuniform-discontinuous distributions as shown in Figure 4-1. Consequently the boundary condition of postbuckled plate is time variant. In this research, the approximate and numerical analyses for the postbuckled plates assuming two different loading conditions, uniform pressure and uniform end-shortening were carried out.

4.2 Simply Supported Boundary Conditions

The analytical expressions for the boundary conditions of all edges simply supported at postbuckling state can be described as the the combination of loading conditions and supporting conditions. As shown in Figure 4-2 b) i)*, for the homogeneous isotropic plate compressed by frictionless loading bars with knife edge, the two supporting conditions are

$$w = (\frac{\partial^2 w}{\partial x^2} + \nu\frac{\partial^2 w}{\partial y^2}) = 0 \quad \text{at } x = \pm b \tag{4.1}$$

$$w = (\frac{\partial^2 w}{\partial y^2} + \nu\frac{\partial^2 w}{\partial x^2}) = 0 \quad \text{at } y = \pm a \tag{4.2}$$

Also, the additional sets of loading conditions are

$$u^o = \int_{-b}^{b}[\frac{1}{E}(\frac{\partial^2 F}{\partial y^2} - \nu\frac{\partial^2 F}{\partial x^2}) - \frac{1}{2}(\frac{\partial w}{\partial x})^2]dx = \delta_x, \quad P_x = h\int_{-a}^{a}\frac{\partial^2 F}{\partial y^2}dy, \quad \text{at } x = \pm b \tag{4.3}$$

$$v^o = \int_{-a}^{a}[\frac{1}{E}(\frac{\partial^2 F}{\partial x^2} - \nu\frac{\partial^2 F}{\partial y^2}) - \frac{1}{2}(\frac{\partial w}{\partial y})^2]dy = \delta_y, \quad P_y = h\int_{-b}^{b}\frac{\partial^2 F}{\partial x^2}dx, \quad \text{at } y = \pm a \tag{4.4}$$

where F is any type of admissible stress function.

However aforementioned boundary conditions are true only at the prebuckling state in a strict sense.

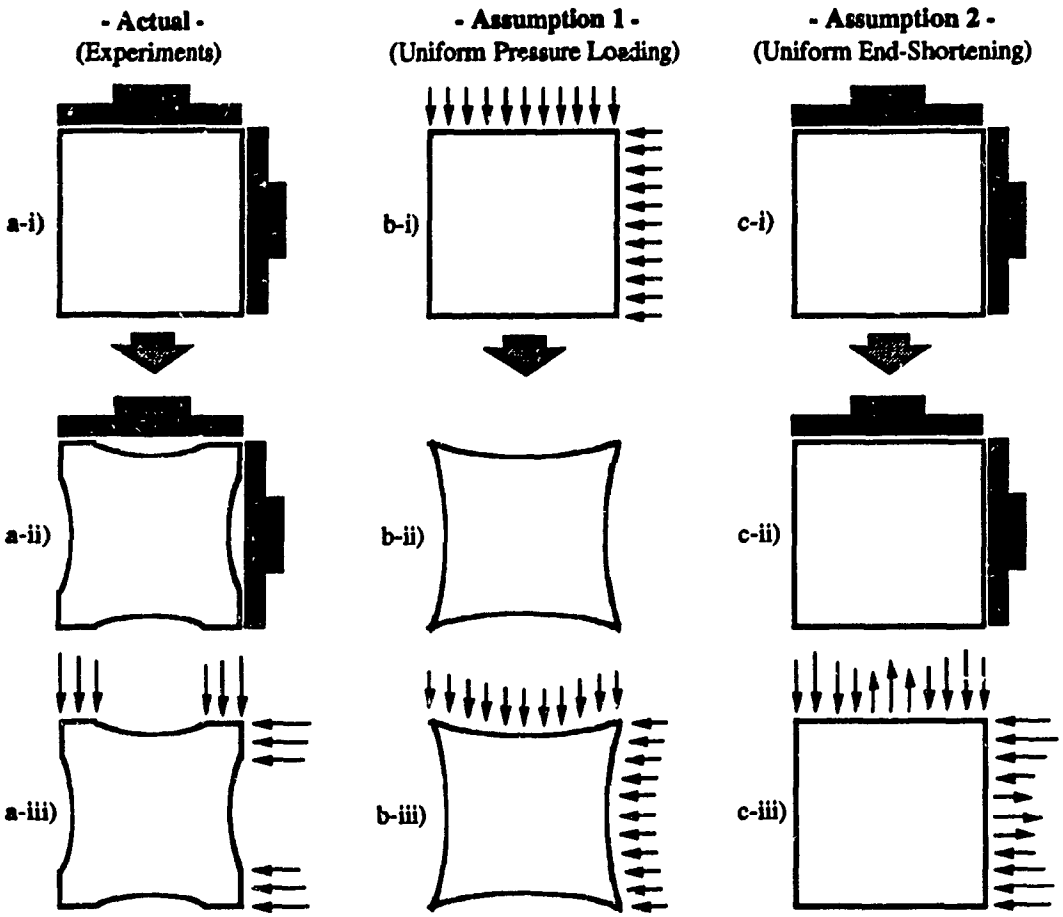

Figure 4.1: Postbuckled shapes and stresses of simply supported plate under biaxial loading. a) Actual behaviour, b) Assumed as uniform pressure loading, c) Assumed as uniform end-shortening.

4.3 Closed Form Solution by Energy Method

4.3.1 Ritz Method for Postbuckling behaviour

Various approximate solutions for plate buckling problems have been presented on the basis of minimum potential energy theorem, i.e., Ritz method, Galerkin method, perturbation technique, finite difference method, finite element method, etc. The Ritz method is one of the convenient methods for obtaining approximate solutions to boundary value problems [29]. This method is governed by the stationary value of potential energy as follows.

$$\Pi(u^o, v^o, w) = U_b + U_s + V = \text{stationary value} \tag{4.5}$$

$$u^o = \sum_{m=1}^{\infty}\sum_{n=1}^{\infty} A_{mn}u_{mn}(x,y),\ v^o = \sum_{m=1}^{\infty}\sum_{n=1}^{\infty} B_{mn}v_{mn}(x,y),\ w = \sum_{m=1}^{\infty}\sum_{n=1}^{\infty} C_{mn}w_{mn}(x,y) \tag{4.6}$$

Where u^o and v^o denote the inplane displacements of the middle plane of the plate, and w describes the deflection surface of the buckled plate, satisfying the boundary conditions. Also, from the equation (4.5), total potential energy Π is the sum of the strain energy due to bending, U_b, the strain energy due to inplane shortening, U_s, and potential energy due to external load, V.

Including the large deflection nonlinearity, the strain-displacement relations of anisotropic plates are already given in equations (2.8)~(2.10). The strain energy stored in the laminate can be presented as the sum of the strain energy due to bending, U_b, and the strain energy due to inplane shortening, U_s, at middle plane as follows[4][29].

$$\begin{aligned} U &= U_s + U_b = \frac{1}{2}\int_{\frac{-h}{2}}^{\frac{h}{2}}\int_{-a}^{a}\int_{-b}^{b}\{\sigma_x(\epsilon_x^n + z\kappa_x) + \sigma_y(\epsilon_y^n + z\kappa_y) + \sigma_{xy}(\epsilon_{xy}^n + z\kappa_{xy})\}dxdydz \\ &= \frac{1}{2}\int_{-a}^{a}\int_{-b}^{b}\{A_{11}(\epsilon_x^n)^2 + 2A_{12}\epsilon_x^n\epsilon_y^n + A_{22}(\epsilon_y^n)^2 + 2(A_{16}\epsilon_x^n + A_{26}\epsilon_y^n)\epsilon_{xy}^n + A_{66}(\epsilon_{xy}^n)^2\}dxdy \\ &\quad + \frac{1}{2}\int_{-a}^{a}\int_{-b}^{b}\{D_{11}(\frac{\partial^2 w}{\partial x^2})^2 + 2D_{12}\frac{\partial^2 w}{\partial x^2}\frac{\partial^2 w}{\partial y^2} + D_{22}(\frac{\partial^2 w}{\partial y^2})^2 + 4D_{66}(\frac{\partial^2 w}{\partial x \partial y})^2 \end{aligned}$$

$$+4(D_{16}\frac{\partial^2 w}{\partial x^2}+D_{26}\frac{\partial^2 w}{\partial y^2})\frac{\partial^2 w}{\partial x \partial y}\}dxdy \tag{4.7}$$

where, the stress-strain relation and the integrated stiffness coefficients, A_{ij} and D_{ij}, can be written as same form as equations (2.16) and (2.20):

$$\{\sigma\} = [q]\{\epsilon\} \tag{4.8}$$

$$(A_{ij}, D_{ij}) = \int_{-\frac{h}{2}}^{\frac{h}{2}} q_{ij}(1, z^2)dz \tag{4.9}$$

The above equation was derived for the symmetric laminate. Thus the bending-stretching coupling terms were identically zero, i.e., $B_{ij} = 0$. The potential energy due to external load, V, is

$$V = \int_{-a}^{a}\int_{-b}^{b} pw\, dxdy + \int_{s} \mathbf{N}^T \cdot \mathbf{u}\, ds \tag{4.10}$$

where, p, $\mathbf{N}^T$ and $\mathbf{u}$ indicate transverse pressure, applied inplane force per unit length and the normal component of displacement at the boundary respectively. Finally the stationary value of the total potential energy can be expressed as a minimization problem.

$$\frac{\partial \Pi}{\partial A_{mn}} = 0, \quad \frac{\partial \Pi}{\partial B_{mn}} = 0, \quad \frac{\partial \Pi}{\partial C_{mn}} = 0 \tag{4.11}$$

Like other approximation methods, if the assumed deflection functions are suitably chosen to describe the displacement of the actual plate, the Ritz method provides an accurate solutions by using a simple series functions. A severe restriction remains to find admissible displacement functions to satisfy the boundary condition at postbuckling state.

Traditionally the uniform pressure loading condition has been acquired by means of the uniform end-shortening with rigid bars in real experimental determination of buckling load and postbuckling response as conducted by Mandell [51]. Therefore a closed form solution(C-SOL) for biaxial buckling of isotropic plate under the uniform

end-shortening boundary condition was considered, as shown in Figure 4-1. Based on the previous discussion for the displacement function, we can take the displacement functions as follow.

$$\begin{aligned} u^o &= C_x \sin\frac{\pi x}{a}\cos\frac{\pi y}{2b} - e_x x \\ v^o &= C_y \sin\frac{\pi y}{a}\cos\frac{\pi x}{2b} - e_y y \\ w &= w_{max}\cos\frac{\pi x}{2b}\cos\frac{\pi y}{2a} \end{aligned} \tag{4.12}$$

where, e_x, e_y are constants indicating the uniform strain along x and y-direction respectively.

4.3.2 A Closed Form Solution for Uniform End-Shortening

For an isotropic plate or a symmetric laminate constructed with isotropic plies, all terms of the inplane and flexural stiffness are simplified as $A = A_{ij}$ and $D = D_{ij}$. Now, all the energy terms discussed in equations (4.7) and (4.10) are as follows;

$$U_s = A\int_{-a}^{a}\int_{-b}^{b}\{(\epsilon_x^n)^2 + (\epsilon_y^n)^2 + 2\nu\epsilon_x^n\epsilon_y^n + \frac{1}{2}(1-\nu)(\epsilon_{xy}^n)^2\}dxdy \tag{4.13}$$

$$U_b = \frac{D\pi^4 ab}{32}(w_{max})(\frac{1}{a^2}+\frac{1}{b^2})^2 \tag{4.14}$$

$$V = \int_s \mathbf{N}^T \cdot \mathbf{u} ds = P_x\, u^o_{(x=b)} + P_y\, v^o_{(y=a)} = P_x\delta_x + P_y\delta_y \tag{4.15}$$

where, P_x, P_y indicate external inplane load on each axis and, δ_x, δ_y are the end-shortening x and y axis at plate boundary. In the case of co-uniform biaxial end-shortening buckling of square plate, i.e., $k = 1$ or $N_x = N_y$, we have $a = b$, $C_x = C_y = C$, $e_x = e_y = e$, $P_x = P_y = P$ and $\delta_x = \delta_y$. As a case study, for the isotropic plate(Plate#1) as shown in Table 1, critical biaxial buckling load can be solved from its stationary equation, equation (4.11), as following form:

$$\frac{\partial\Pi}{\partial C} = 0; \;\rightsquigarrow\; C = 0.14\frac{w_{max}^2}{a} \tag{4.16}$$

$$\frac{\partial\Pi}{\partial w_{max}} = 0; \;\rightsquigarrow\; w_{max}^2 = 2.25a^2e - 0.712h^2 \tag{4.17}$$

If we put P_c and e_c as the critical value of P and e, the critical biaxial buckling load and strain values are

$$P_c = 43834\frac{h^3}{a} = 4 \text{ kN}, \quad e_c = 0.316\frac{h^2}{a^2} = 108 \times 10^{-6} \tag{4.18}$$

In above equations, the critical load P_c was obtained from the equation of stresses as shown in equation (4.19) and more detail description can be found from Timoshenko [13]. Moreover the stress distribution on the boundary of the plate at postbuckling state can be expressed as a simple C-SOL as follows.

$$\sigma_x|_{(x=b)} = \sigma_y|_{(y=a)} = 38000\frac{h^2}{a^2}(n-1)(1.2\cos\frac{\pi y}{2b} - 0.44) - 21900\frac{h^2}{a^2}n \tag{4.19}$$

where $n = e/e_c = \delta/\delta_c$. More converged solutions can be obtained by adding more terms, i.e., $e_x x$ or $e_x x^2$, in equation (4-12), but the equations would become highly complicated [19]. To investigate the validity of this C-SOL, the maximum deflection and the boundary behaviour of postbuckled plate were compared with the results of N-FEA in Figure 4-3.

Table 4.1: Dimensions and engineering data of the composite plates for analyses and experiments.

Table 1. Dimensions and engineering data of analytical and experimental plate specimen

Plate#1 : Isotropic Plate		Plate#2 : Orthotropic Plate Specimen			
Dimensions & Stiffnesses		Material Spec.		Dimensions & Stiffnesses	
Code	Isotropic	Material		Code	[(0/90)4]
a, mm	120	Brand	NCT301	a, mm	240
b, mm	120	Fiber	Graphite	b, mm	240
h, mm	2.22	Matrix	Epoxy	h, mm	2.21
a_c,mm ;(a_c/2a,%)	18 ; (7.5)			a_c,mm ;(a_c/a,%)	18 ; (7.5)
b_c,mm ;(b_c/2b,%)	18 ; (7.5)	Ply Constants		b_c,mm; (b_c/b,%)	18 ; (7.5)
ν,	0.3	Ex, GPa	113.9	A11, A22, kN / mm	136.1, 136.1
E, GPa	48.5	Ey, GPa	7.971	A12, A66, kN / mm	5.08, 6.96
A, kN / mm	118.3	ν_x	0.286	D11, D22, kN mm	65.0, 46.8
D, kN mm	48.6	Es, GPa	3.113	D12, D66, kN mm	2.1, 2.8

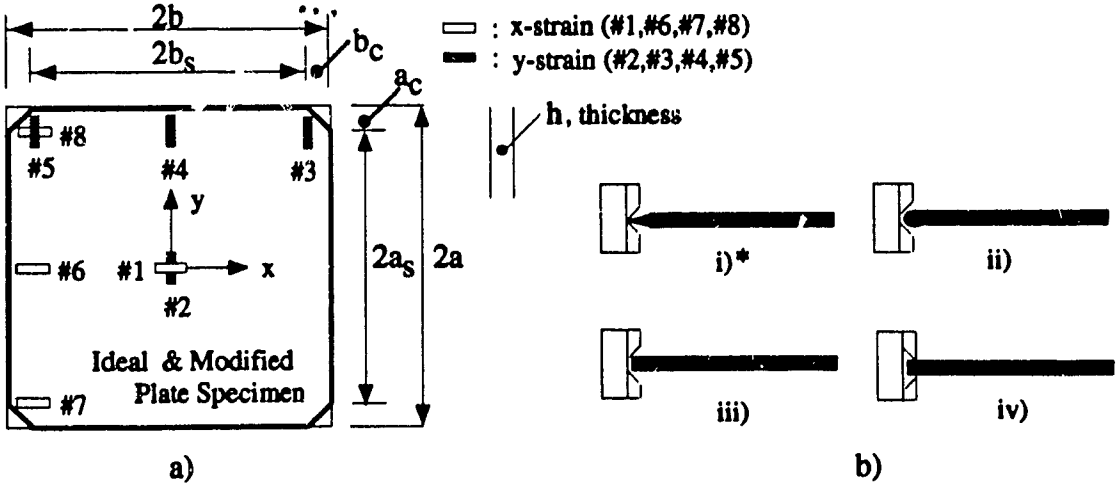

Figure 4.2: Plate specimen and its supporting mechanism. a) Ideal and modified specimen with strain gauge, b) Various simple supporting conditions.

4.4 Uniform Pressure and Uniform End-Shortening

Figure 4-1 a) shows the behaviour of postbuckled plate under biaxial loading. It describes the deformed boundaries and nonuniform-discontinuous stress distributions. Figures 4-1 b) and c) represent the two assumed loading conditions used in most analytical approximation methods. The two assumed conditions are strictly the same at prebuckling state and we can obtain the same critical buckling load. However beyond the critical load, we should choose one of them. Normally uniform end-shortening is preferred in various approximation methods. It is true that the assumption of uniform pressure loading (Assumption 1) leads to larger deflection than uniform end-shortening case (Assumption 2). In geometrical aspects of buckled plate, Assumption 2 looks closer to the actual state than Assumption 1 in early stage of postbuckling. But in a highly postbuckled state, Assumption 1 leads to more comparable solution than Assumption 2. as shown in Figure 4-6 Authors investigate analytically the difference of the two assumed cases through the C-SOL and N-FEA. On the other hand, the analytical results are compared with the experimental results for the orthotropic composite plates.

4.5 Selection of Boundary Conditions

To validate the C-SOL obtained under uniform end-shortening condition, the axial load and boundary stresses are compared with N-FEA results as shown in Figure 4-3. From equation (4.16), we have the critical buckling load of C-SOL as $P_c = 3.996$ kN rather than that of N-FEA as $P_c = 3.268$ kN. In the load response from Figure 4-3 a), the errors diverge quickly according to the effective end-shortening, $n = e/e_c = \delta/\delta_c$. Also, the boundary stresses represent a similar distributions but C-SOL values are larger than values of N-FEA.

In Figure 4-4, the displacement of plate boundary was depicted for ideal and modified plate under uniform pressure loading for Plate #2, where the modified plate shows much larger boundary displacements than the ideal one. However, considering n value is only 1 or 2 for the practical buckling modes, the boundary displacements of the two models are acceptably the same and it means the modified specimen is valid for the substitute of the ideal plate specimen.

Figure 4-5 reveals the effects of the assumed loading conditions for ideal and modified plates. Beyond the critical buckling load, the two loading conditions show a wide difference in terms of the increase of postbuckling deflections. Finally the experimental load-deflection responses are plotted along with the N-FEA results for the two extreme loading conditions, as shown in Figure 4-6. Here we can find that even though the plates were subjected to the uniform end-shortening by rigid bars, their postbuckling behaviours are chosen to the theoretical uniform pressure loading condition for an isotropic ideal material. More discussions on the boundary behaviour could be found from the literature [62][63].

Consequently, in plate biaxial postbuckling analysis, it can be concluded that the analyses using the uniform pressure loading condition renders a solution that agrees better with our experimental results than the analysis with uniform end-shortening condition.

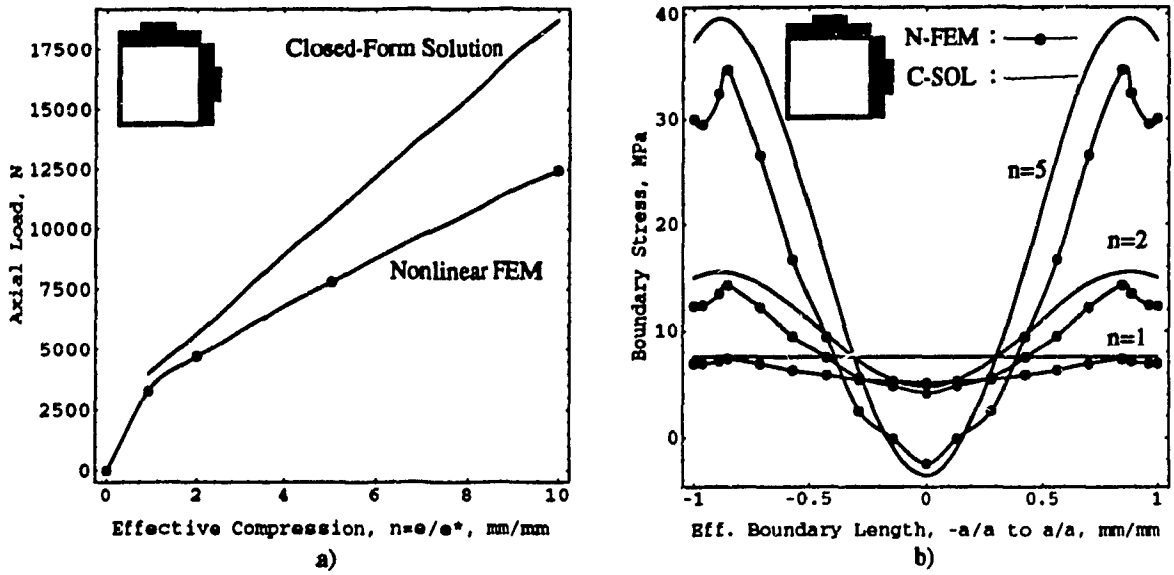

Figure 4.3: Axial load and boundary stress distributions for Plate#1 with uniform end-shortening condition. a) Axial load vs. n, b) Boundary stresses vs. n.

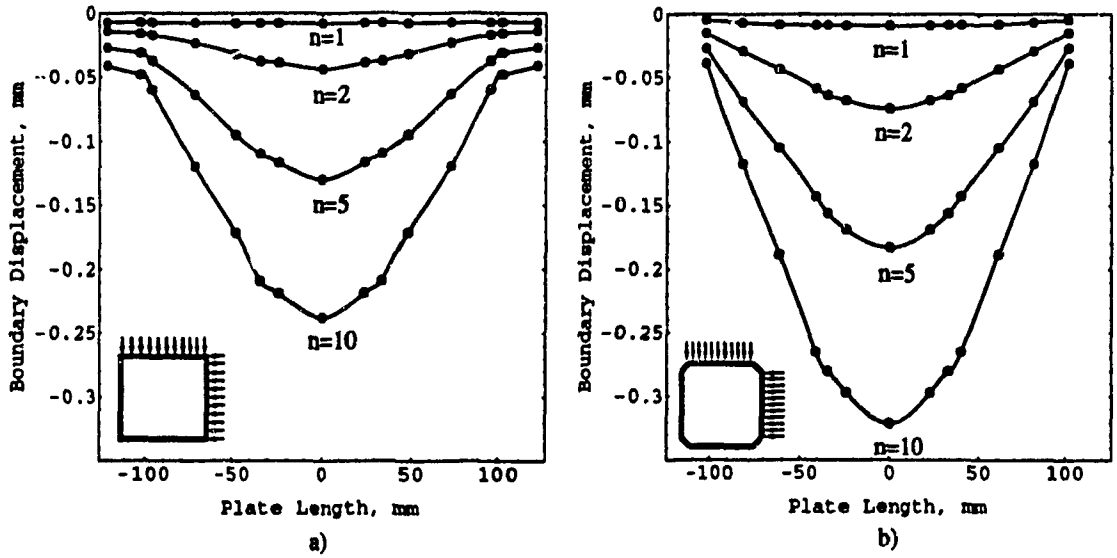

Figure 4.4: Boundary displacement at postbuckling state for Plate#2 with uniform edge stress in compression. a) N-FEA for ideal plate, b) N-FEA for modified plate.

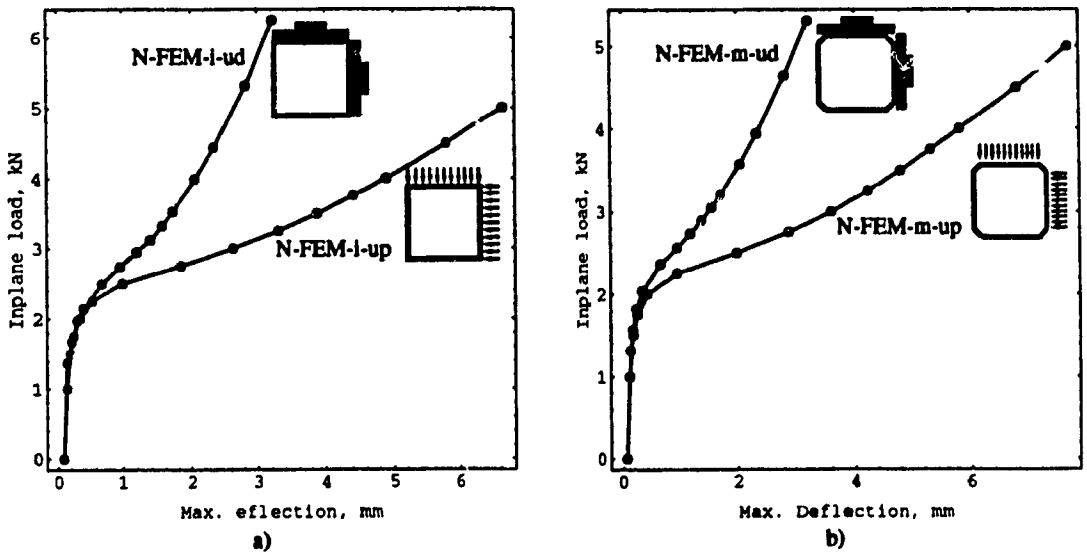

Figure 4.5: Biaxial postbuckling behaviour (axial load vs. deflection) for composite plate, Plate#2, when $P_x : P_y = 1 : 1$. a) N-FEA for ideal plate, b) N-FEA for modified plate (Note: i=ideal, m=modified, ud=uniform end-shortening, up=uniform pressure).

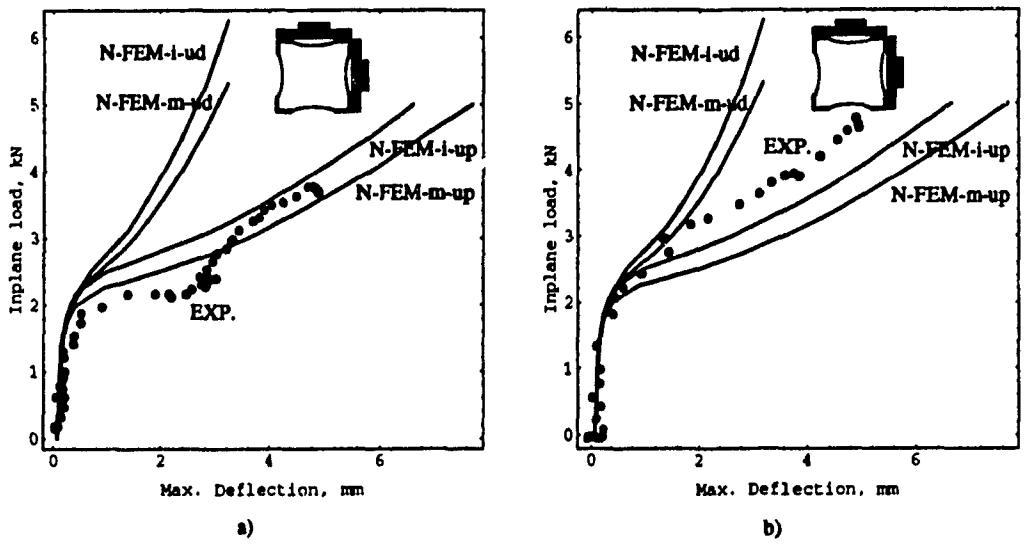

Figure 4.6: Experimental and N-FEA postbuckling behaviour(P_x vs. w_{max}) for Plate#2. a) Experiment with $P_x : P_y = 1 : 1$, b) Experiment with $P_x : P_y = 1 : 0.9$

Chapter 5

Numerical Analysis for Biaxial Buckling

5.1 Finite Element Analysis

Normally two types of numerical approach have been used on the analysis of buckling problem, i.e., L-FEA with eigenvalue formulation and N-FEA with large deflection small strain formulation. ANSYS program has these two approaches for stability and postbuckling analysis of structures. Linear buckling analysis in ANSYS program uses eigenvalue formulation to determine the bifurcation load, so called eigenvalues or scale factors as in the following equation,

$$[K]\{\phi_i\} = \lambda_i[S]\{\phi_i\} \tag{5.1}$$

where

$$\begin{aligned} [K] &= \text{structure stiffness matrix} \\ \{\phi_i\} &= \text{eigenvectors} \\ \lambda_i &= \text{eigenvalues} \\ [S] &= \text{stress stiffness matrix} \end{aligned} \tag{5.2}$$

As the extraction procedure of eigenvalues and eigenvectors, full subspace iteration method is applied, which was described in detail by Bathe [57]. The convergence was checked by requiring that all of the requested eigenvalues satisfy the convergence ratio, i.e.,

$$e_i = \left| \frac{(\lambda_i)_n - (\lambda_i)_{n-1}}{(\lambda_i)_n} \right| < \text{tolerance} \tag{5.3}$$

where

$$\begin{aligned} e_i &= \text{error of } i\text{-th eigenvalue as computed in iteration } n \\ (\lambda_i)_n &= \text{value of } i\text{-th eigenvalue as computed in iteration } n \\ (\lambda_i)_{n-1} &= \text{value of } i\text{-th eigenvalue as computed in iteration } n-1 \end{aligned} \tag{5.4}$$

In the L-FEA of ANSYS software, if the applied load is unity, the eigenvalue is the buckling load and the eigenvector is the buckling shape. Also, the first eigenvalue and eigenvector are of interest in most engineering problems. L-FEA of ANSYS program can only predict the upper bound of the actual buckling load but its advantage is faster and easier determination of critical load.

However, if the rotations are large while the mechanical strains are still small, a large deflection nonlinear finite element method can be used from ANSYS program. This large deflection analysis assumes the displacements are large enough to significantly affect the flexural stiffness of the structure. Since the stiffness and displacement affect each other, iterative minmization technique like Newton-Raphson method is required to obtain the correct displacements. Through the finite element formulation, system equilibrium equations are presented as a set of simultaneous equations, i.e.,

$$[K]\{u\} = \{F^a\} \tag{5.5}$$

where

$$[K] = \text{structure stiffness matrix}$$

$$\begin{aligned} \{u\} &= \text{vector of unknown DOF values} \\ \lambda_i &= \text{eigenvalues} \\ \{F^a\} &= \text{vector of applied load} \end{aligned} \tag{5.6}$$

If the coefficient matrix $[K]$ is itself a function of the unknown DOF(degrees of freedom) values or their derivative, above system equation is a nonlinear equation. For this nonlinear system, ANSYS software uses Newton-Raphson method as an iterative process written as in the followings, for the i-th iteration,

$$[K_i^T]\{\Delta u_i\} = \{F^a\} - \{F_i^{nr}\} \tag{5.7}$$

$$\{u_{i+1}\} = \{u_i\} - \{\Delta u\} \tag{5.8}$$

where

$$\begin{aligned} [K_i^T] &= \text{tangent stiffness matrix} \\ \{u_i\} &= \text{displacement vector} \\ \{F_i^{nr}\} &= \text{restoring force vector calculated from the element stresses} \end{aligned} \tag{5.9}$$

In the above equations, both $[K_i^T]$ and $\{F_i^{nr}\}$ are evaluated based on the values given by $\{u_i\}$ and the right-hand side of equation (5.7) is the residual or out-of-balance load vector when the system is out-of equilibrium. To check the convergence, the displacement increment method is selected as the equation of the vector norm as

$$\| \{\Delta u_i\} \| < \text{tolerance} \tag{5.10}$$

In addition, a small perturbation is required to start the buckling behaviour and it is a very small imperfection prescribed by the original geometry or a very small force. SHELL99 element - 100 layer structural shell element - was selected for this N-FEA work on the biaxial plate buckling from ANSYS program as shown in Figure 5-1. SHELL99 is 3-D 8-node shell element with rotation and shear deflection. It can

have two shapes, triangular and quadrilateral element with following shape functions,

$$\begin{Bmatrix} u \\ v \\ w \end{Bmatrix} = \sum_{i=1}^{8} \psi_i \begin{Bmatrix} u_i \\ v_i \\ w_i \end{Bmatrix} + \sum_{i=1}^{8} \psi_i \frac{rt_i}{2} \begin{bmatrix} a_{1,i} & b_{1,i} \\ a_{2,i} & b_{2,i} \\ a_{3,i} & b_{3,i} \end{bmatrix} \begin{Bmatrix} \theta_{x,i} \\ \\ \theta_{y,i} \end{Bmatrix} \tag{5.11}$$

where

$$\begin{aligned}
\psi_i &= \text{shape functions, given with } u, v, ..., \text{ as in following equations} \\
u &= \frac{1}{4}\{u_I(1-s)(1-t)(-1-s-t) + u_J(1+s)(1-t)(-1+s-t) \\
&\quad + u_K(1-s)(1+t)(-1-s+t) + u_L(1+s)(1+t)(-1+s+t)\} \\
&\quad + \frac{1}{2}\{u_M(1-s^2)(1-t) + u_N(1-s)(1-t^2) \\
&\quad + u_O(1+s)(1-t^2) + u_P(1-s^2)(1+t)\} \\
v &= \frac{1}{4}\{v_I(1-s)(1-t).....(\text{analogous to } u) \\
u_i, v_i, w_i &= \text{displacement of node } i \\
r_i &= \text{thickness coordinate} \\
t_i &= \text{thickness at node } i \\
\{a\} &= \text{unit vector in } s\text{-direction} \\
\{b\} &= \text{unit vector in plane of element and normal to \{a\}} \\
\theta_{x,i} &= \text{rotation of node i about vector \{a\}} \\
\theta_{y,i} &= \text{rotation of node i about vector \{b\}}
\end{aligned} \tag{5.12}$$

The integration points are 2-through the thickness and 2x2 for the inplane domain for quadrilateral element and also 2 for through-the-thickness and 3-for the inplane domain for triangular element. SHELL99 allows up to 100 different layers. The possible load types are bilinear pressure and temperature load across the plane of the element. This element has linear pressure and temperature along each edge and through the thickness. Main assumptions and restrictions of SHELL99 element are summarized as follows,

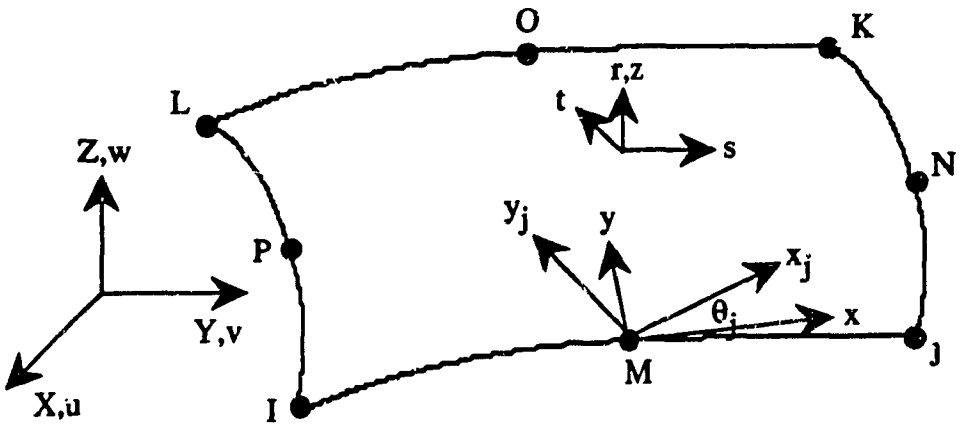

Figure 5.1: A sketch on the SHELL99 in ANSYS program : 3-D 8-node shell element

- Normals to the centre plane are assumed to remain straight after deformation.
- There is no significant stiffness associated with rotation of the element about the r axis. However, a normal value of stiffness is present to prevent free rotation at the node.
- The bonding of layers is perfect without slip.
- Interlaminar shear stresses are calculated on the assumption of no shear on the top and bottom surfaces of the element

5.2 Effect of Stiffness Ratio (Cross-ply Laminate)

Normally laminated composite plates process a different inplane stiffness, A_{ij}, and flexural stiffness, D_{ij}, according to the stacking sequences. In the case of angle-ply or cross-ply lamination, the existence of a major-axis and a minor-axis of stiffnesses is a strong point of composite materials compared to other conventional materials from the design point of view. Also, the ratios of these major stiffnesses and minor stiffnesses, i.e., inplane stiffness ratio ($\xi = \frac{A_{11}}{A_{22}}$) and flexural stiffness ratio ($\zeta = \frac{D_{11}}{D_{22}}$), are determined from the sequence of stacking.

For 12-, 16- and 20-layer orthotropic and anisotropic laminates, various stiffness ratios are obtained as presented in Tables 3.5. From these data, even if the thickness and the number of layers are the same, the inplane stiffness ratio ξ varies from 1 to 14.3 and the flexural stiffness ratio ζ varies from 1.3 to 14.3 in orthotropic laminates. In consideration of these huge differences in stiffness ratios by virtue of stacking sequence, there is a question - what are the effects of stiffness ratios on plate buckling ?

On the other hand, we know that the critical buckling loads are not affected by the flexural stiffness ratio, ζ, but by the amount of global stiffness, D_T, as mentioned in equation (2.39) of the buckling theory discussed in Chapter 2, especially for the simply supported orthotropic laminates. If this theory is correct, i.e., the stiffness ratio does not affect to the buckling stability, we do not need to select the stronger axis any more in the designing of plate structures.

To clarify this doubtful point on the effects of stiffness ratio in buckling, N-FEA was carried out for various laminated orthotropic plates as mentioned in Table 3.5. Numerical input data for this N-FEA, element meshes and boundary conditions, were prescribed in the same manner as in numerical analysis in Chapter 3, as presented in

Figure 3-5.

A small initial deflections, less than 0.064mm (2.8% of plate thickness, 2.22 mm) for 16-layer and 0.044 mm (1.6 % of plate thickness, 2.78 mm) for 20-layer modified plate specimen, was applied to invoke large deflection nonlinear finite element analysis. To obtain comprehensive buckling data, the uniaxial or biaxial load was continuously imposed with 20 steps of load increment from prebuckling to postbuckling state. The convergence was checked by controlling the displacement increment norm, $\| \Delta u \|$ to be less than $10^{-6}mm$ with 25 times iterations in each step.

5.2.1 16-layer Plate Specimen

Uniaxial Loading along X-axis

Figure 5-2 shows an integrated view of all the uniaxial buckling behaviour of the various 16-layer orthotropic plates subject to x-axis uniaxial loading with S_r-S_r-S_r-S_r boundary conditions. The plate used were OP-16-11 to OP-16-80 specimen series, denoted in Table 3-5. From the lower detailed view of the shaded area in Figure 5-2, we can find that the values of critical buckling load do not vary very much with change in the flexural stiffness ratio, i.e., $P_{cr} = 4.65 \sim 4.40$ kN for $\zeta = 1.4 \sim 14.30$.

However, in postbuckling behaviour, the specimen having higher stiffness ratio exhibits faster development of postbuckling deflection. It could be understood that, for the x-axis uniaxial load, even if a plate is stiff in x-direction due to a high stiffness ratio it is more unstable in postbuckled state. For example, postbuckling behaviour of OP-16-80 specimen ($\zeta = 14.3$) reveals very fast development in lateral deflection amount in postbuckling state. From this result, for the effect of stiffness ratio, it can be stated that the major flexural stiffness(D_{11}) itself does not govern the buckling stability but minor stiffness(D_{22}) also has an effect on the buckling behaviour of

laminated plate structure. Figures 5-3, 5-4 and 5-5 display successive views of buckling behaviour for each specimen of OP-16-11, OP-16-44 and OP-16-71 respectively in order to check the continuous buckling deformation. Here three picture demonstrate global shapes of buckled plates and values of maximum deflection (w_{max}) each under same amount of loadings, i.e., 3 kN, 4 kN, 4.5 kN, 5 kN, 6 kN and 8 kN. If we compare w_{max} values among three plates, we can make the same conclusion mentioned above.

Also, the following three pairs of figures, Figures 5-6 and 5-7, Figures 5-8 and 5-9, Figures 5-10 and 5-11, exhibit detailed views of x- and y-axis strain distributions in the early state of postbuckling with 5.0 kN of the x-axis load. In view of these strain fields, we can figure out the deformation of the postbuckled plate, i.e., deformation of OP-16-11 specimen is more stable than OP-16-71 specimen because OP-16-11 shows a concentric circular strains distribution along x- and y-axes but OP-16-71 specimen reveals circular strain distribution along x-axis but totally elliptic strain distribution along y-axis.

Consequently, based on the above numerical results, it can be concluded that a plate having smaller flexural stiffness ratio shows higher postbuckling strength than a plate with higher stiffness ratio in the uniaxial loading (along major stiffness axis, i.e., x-axis in this case) of a simply supported rectangular laminate.

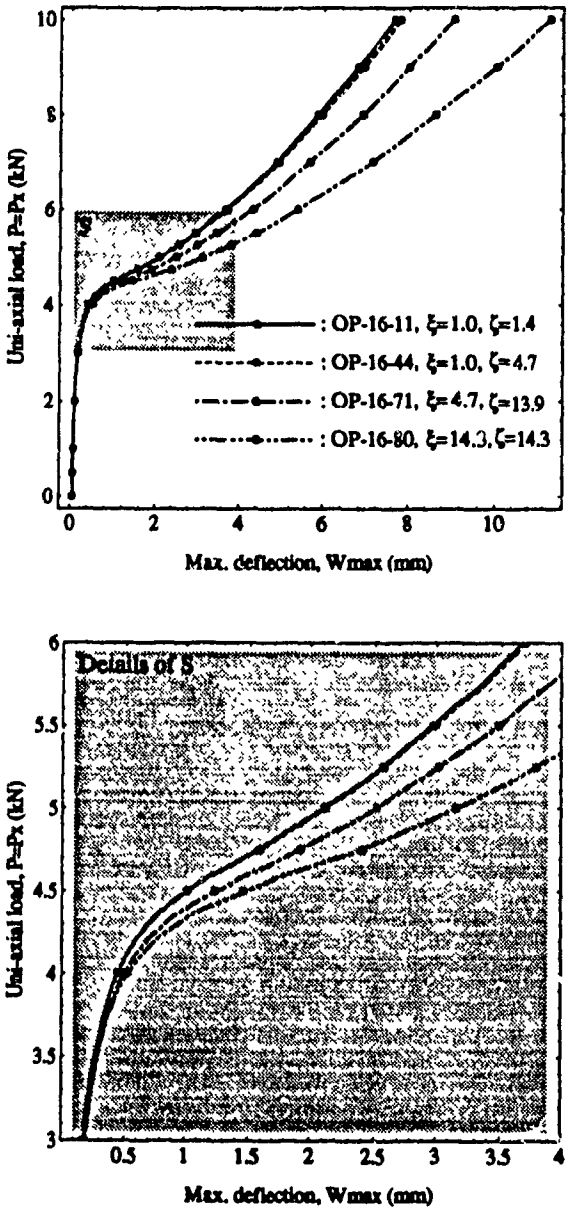

Figure 5.2: X-axis uniaxial loading behaviour of the 16-layer orthotropic plates for various flexural stiffness ratio, $\zeta = 1.4 \sim 14.3$, by N-FEA.

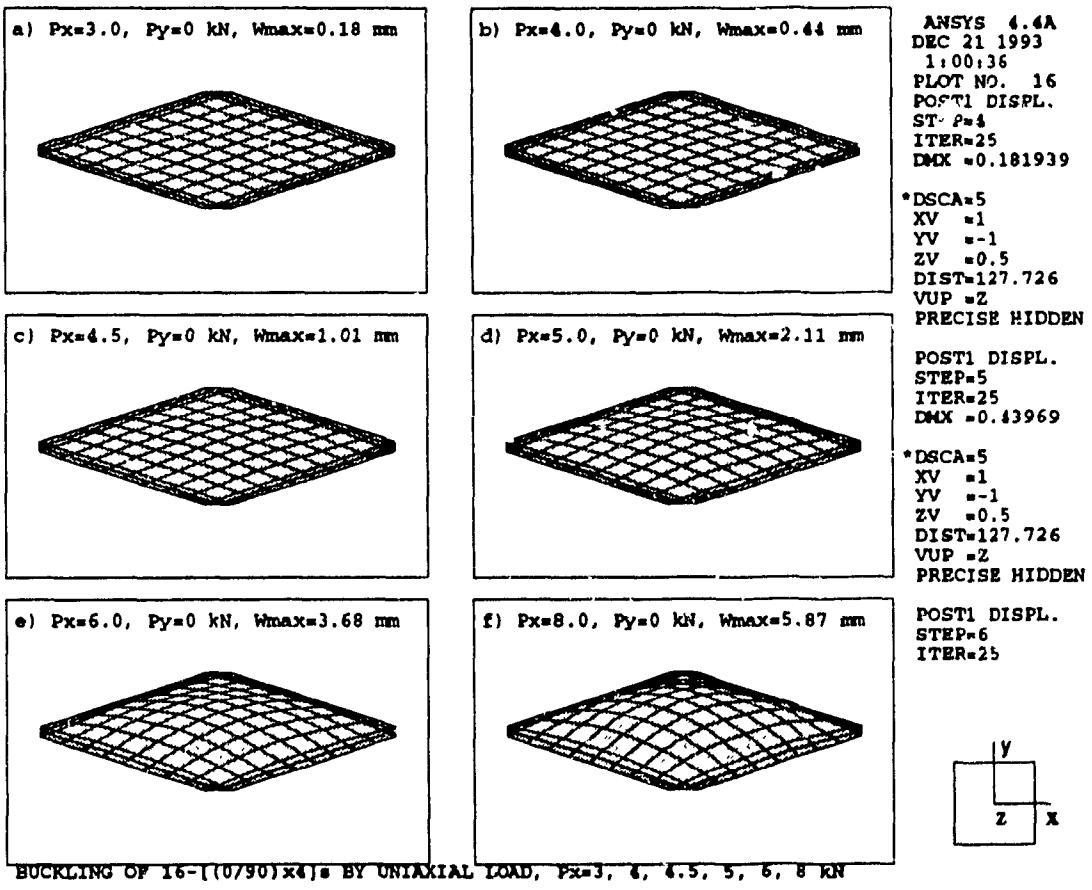

Figure 5.3: Successive views of postbuckling behaviour of the 16-layer orthotropic plate, OP-16-11, with uniaxial loading along x-axis ($P_x : P_y = 1 : 0$).

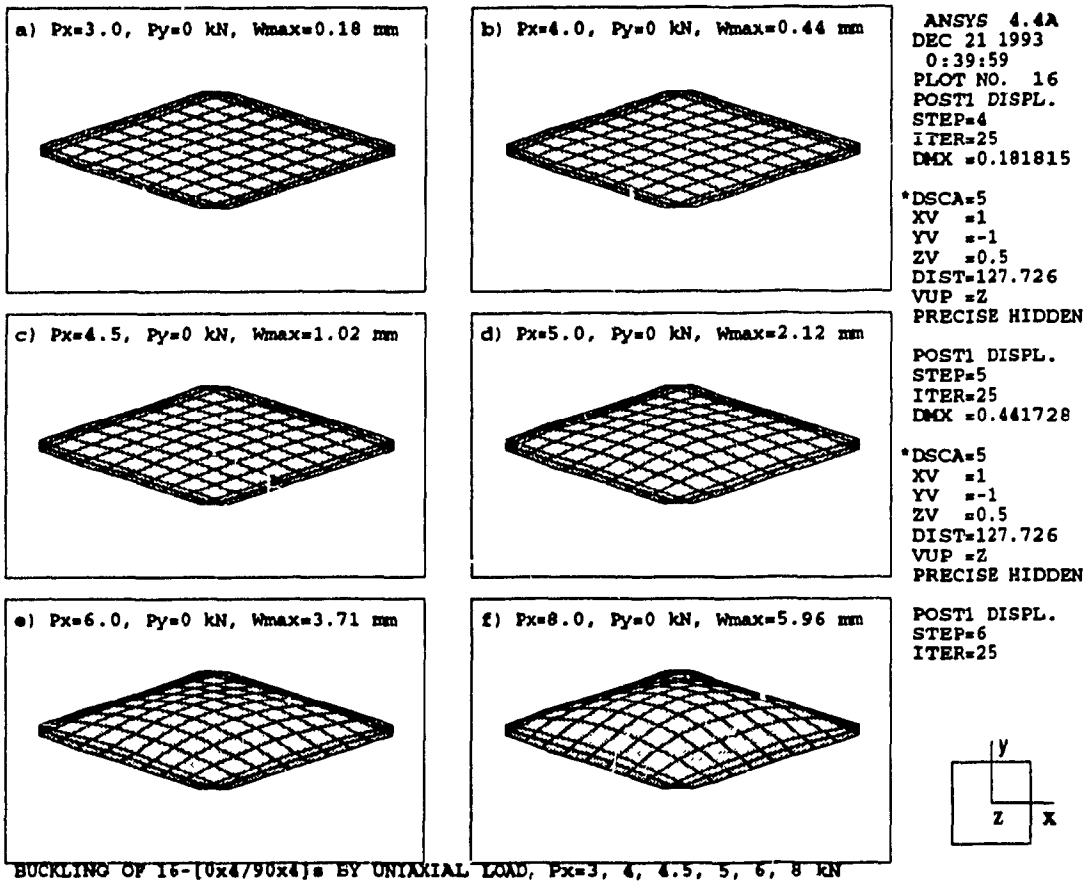

Figure 5.4: Successive views of postbuckling behaviour of the 16-layer orthotropic plate, OP-16-44, with uniaxial loading along x-axis ($P_x : P_y = 1 : 0$).

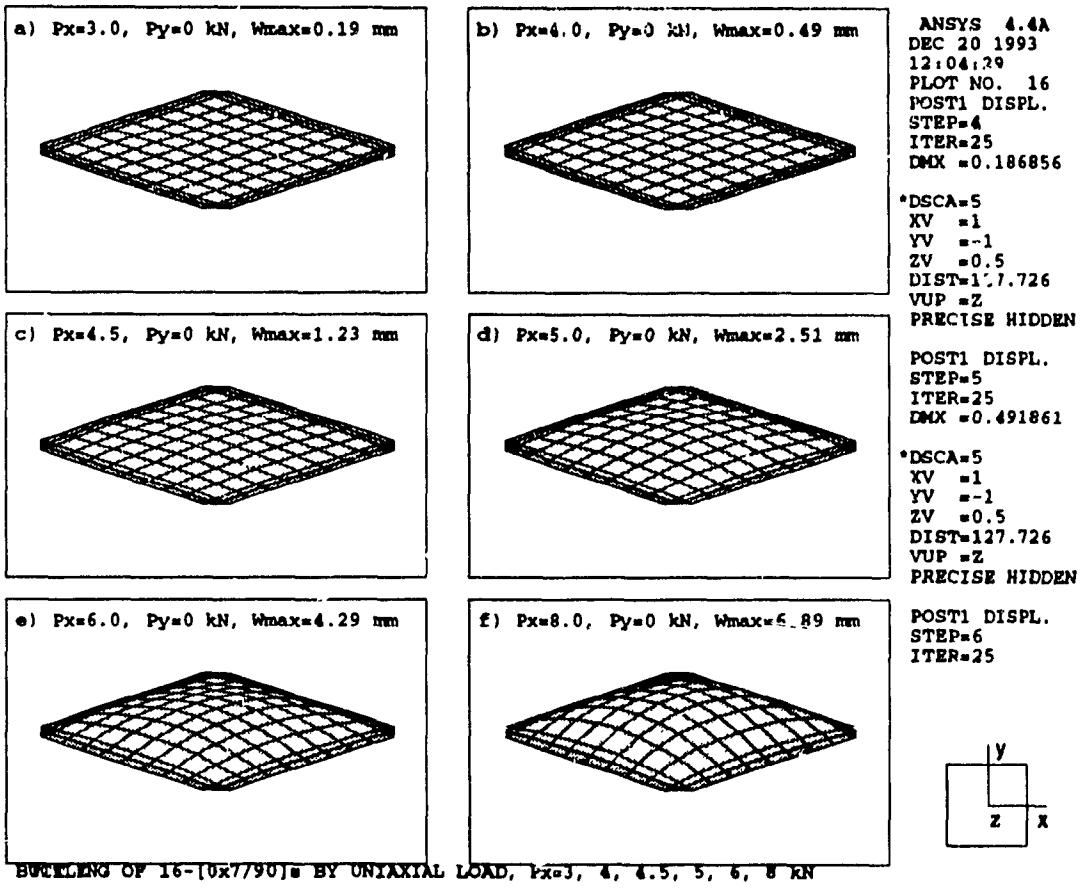

Figure 5.5: Successive views of postbuckling behaviour of the 16-layer orthotropic plate, OP-16-71, with uniaxial loading along x-axis ($P_x : P_y = 1 : 0$).

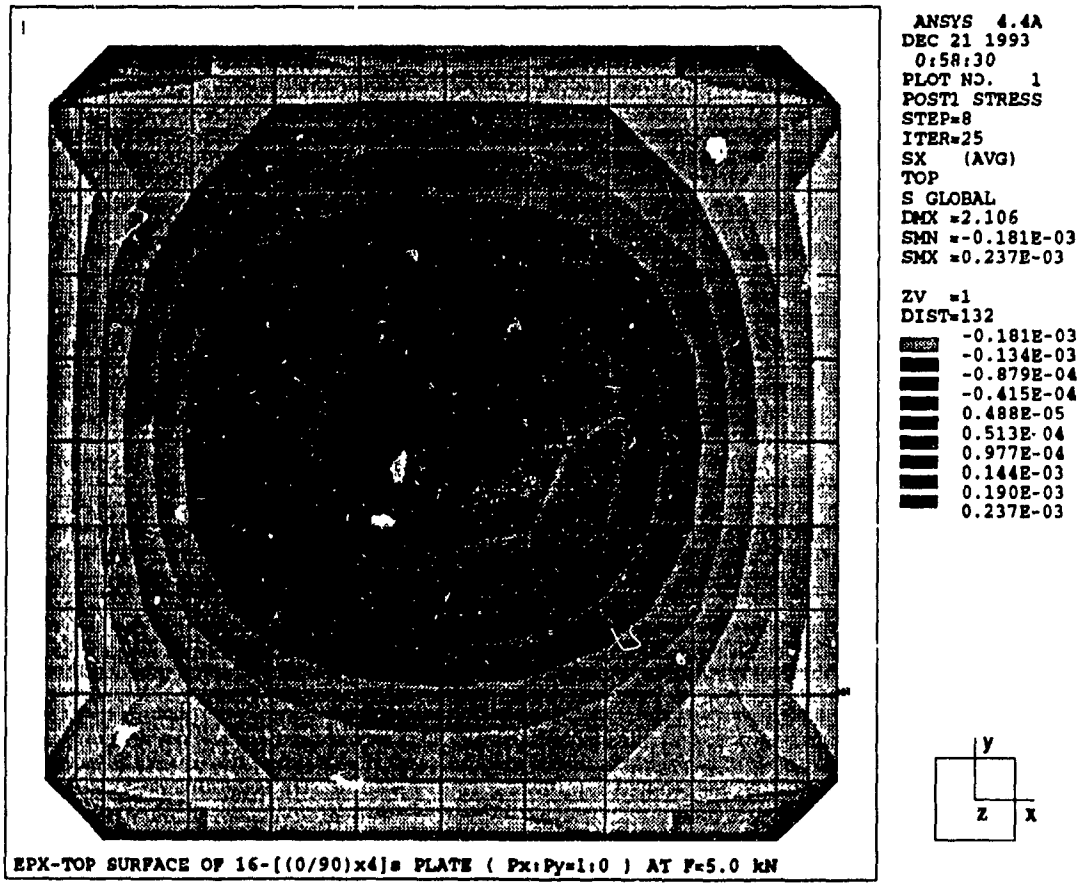

Figure 5.6: X-strain(ϵ_x) distribution of the 16-layer orthotropic plate, OP-16-11 with uniaxial loading along x-axis, $P_x = 5$kN ($P_x : P_y = 1 : 0$).

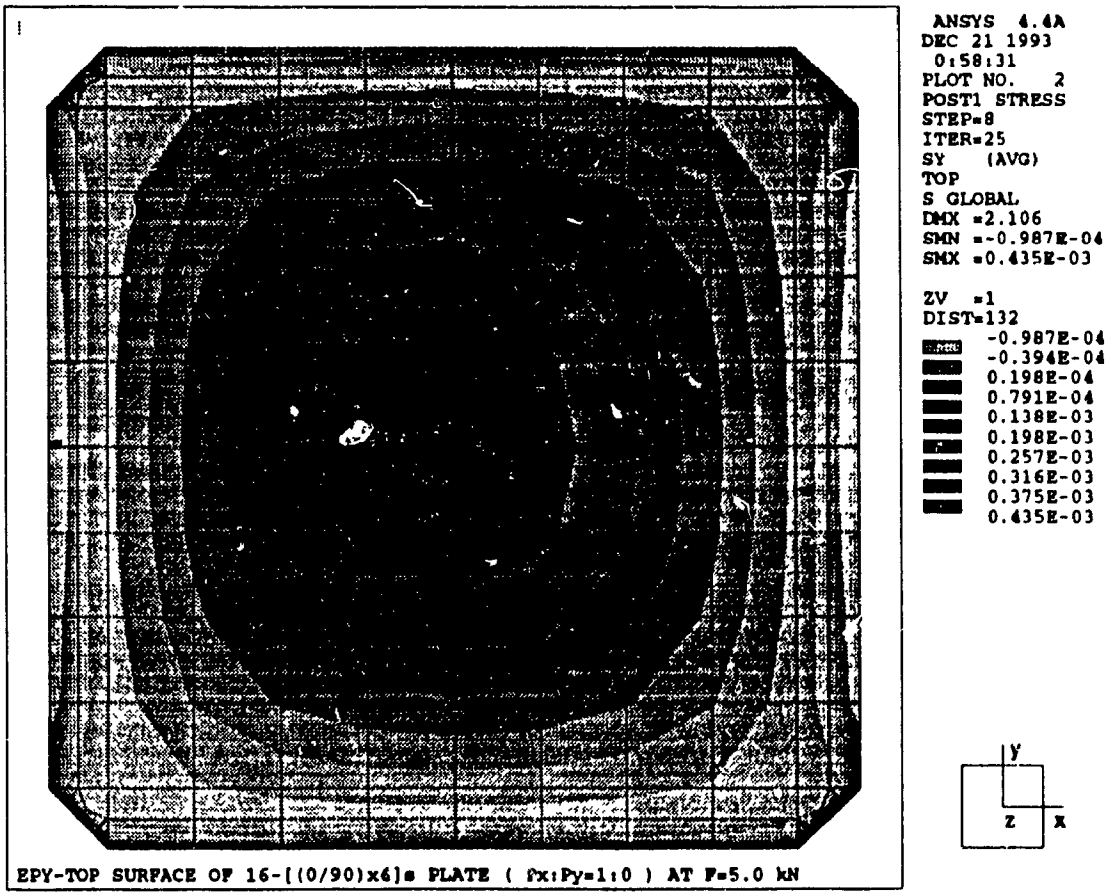

Figure 5.7: Y-strain(ϵ_y) distribution of the 16-layer orthotropic plate, OP-16-11 with uniaxial loading along x-axis, $P_x = 5$kN ($P_x : P_y = 1 : 0$).

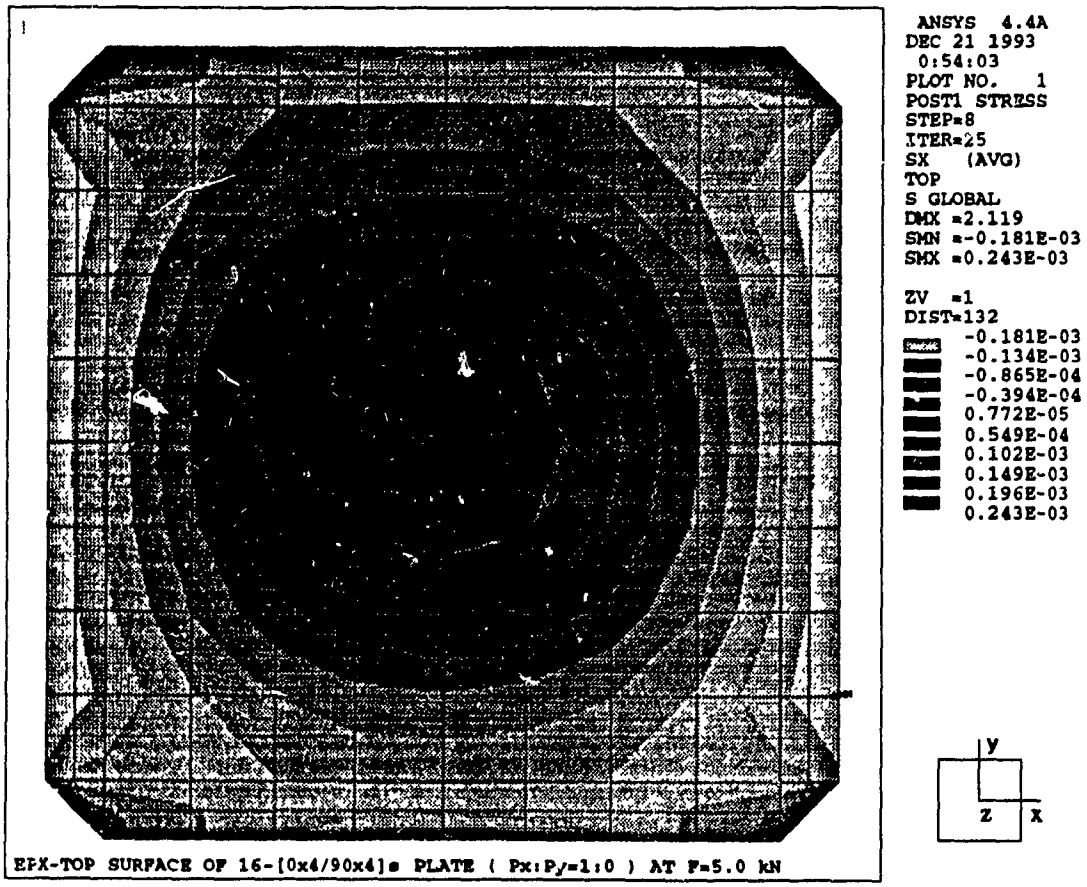

Figure 5.8: X-strain(ϵ_x) distribution of the 16-layer orthotropic plate, OP-16-44 with uniaxial loading along x-axis, $P_x = 5\text{kN}$ ($P_x : P_y = 1 : 0$).

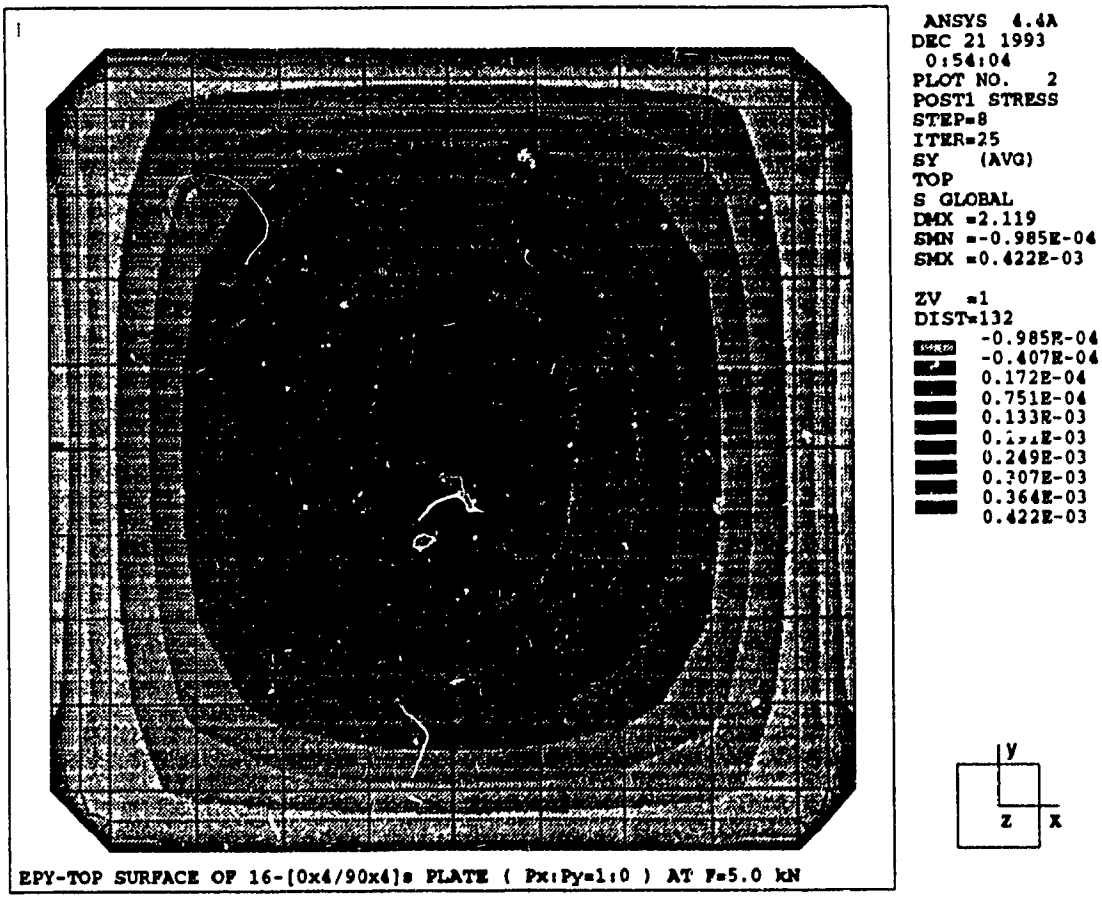

Figure 5.9: Y-strain(ϵ_y) distribution of the 16-layer orthotropic plate, OP-16-44 with uniaxial loading along of x-axis, $P_x = 5$kN ($P_x : P_y = 1 : 0$).

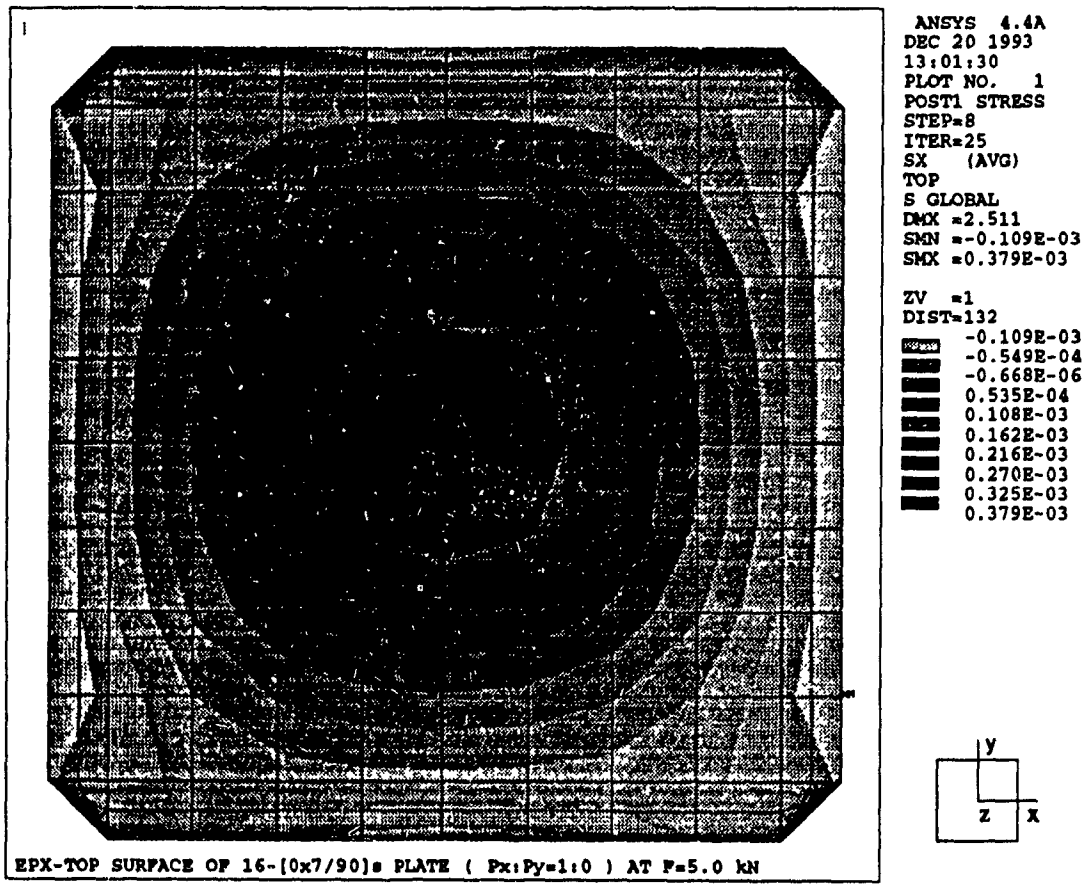

Figure 5.10: X-strain(ϵ_x) distribution of the 16-layer orthotropic plate, OP-16-71 with uniaxial loading along x-axis, $P_x = 5\text{kN}$ ($P_x : P_y = 1 : 0$).

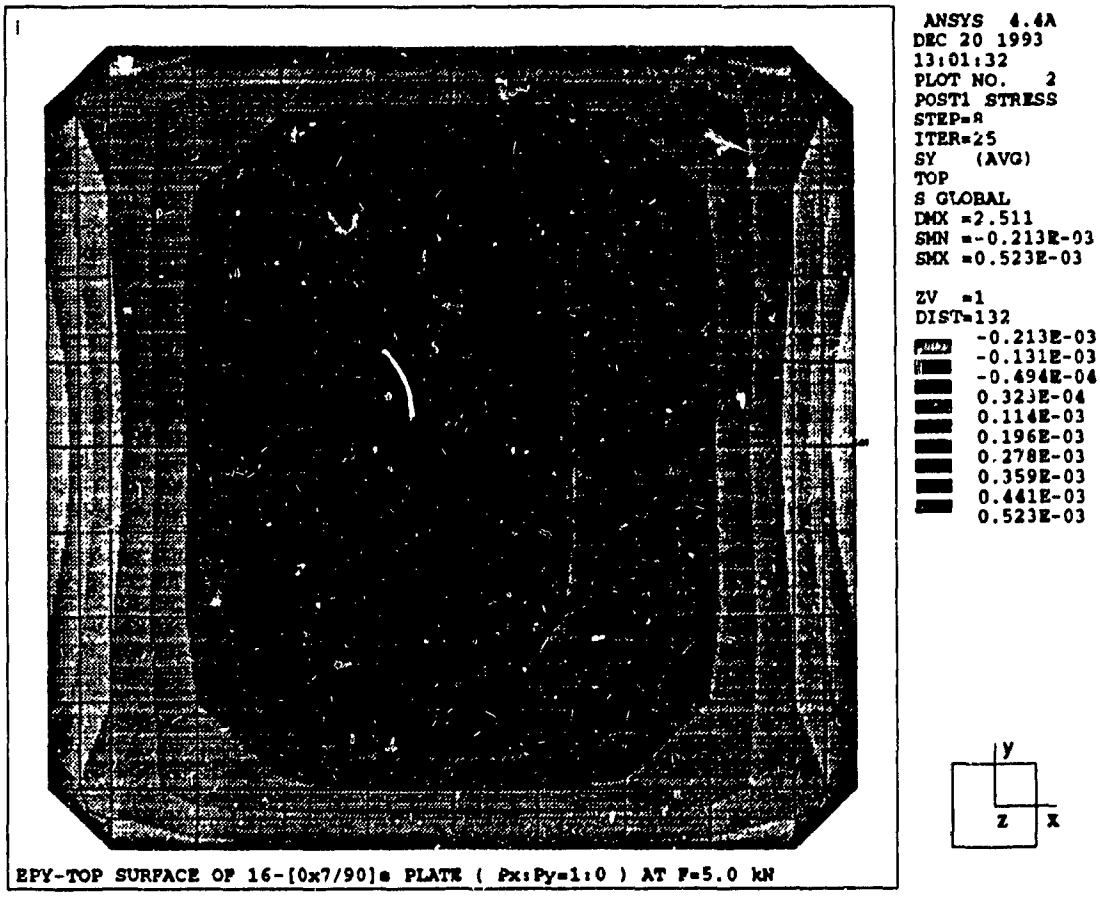

Figure 5.11: Y-strain(ϵ_y) distribution of the 16-layer orthotropic plate, OP-16-71 with uniaxial loading along x-axis, $P_x = 5$kN ($P_x : P_y = 1 : 0$).

Uniaxial Loading along Y-axis

Integrated views of all the uniaxial buckling behaviour of the various 16-layer orthotropic laminates subject to y-axis uniaxial loading under S_r-S_r-S_r-S_r boundary conditions are presented in Figure 5-12. Four curves, in Figure 5-12, belong to four different plates each having a different stiffness ratio ζ due to varied stacking sequences from OP-16-11 to OP-16-80 layup series denoted in Table 3-5. From the lower detailed view of the shaded area in Figure 5-12, we can find that the values of critical buckling loads depend very much on the flexural stiffness ratio, i.e., $P_{cy} = 4.5 \sim 3.8$ kN for $\zeta = 1.4 \sim 14.3$.

Based on these postbuckling responses with y-axis uniaxial loading, plates having unbalanced stacking sequences like OP-16-71 and OP-16-80 specimen exhibit lower critical buckling load than plates having balanced stacking sequence like OP-16-11 and OP-16-44 specimen. Also, concerning the contours of the four different load-deflection curves, plates having higher stiffness ratios (OP-16-71 and OP-16-80) display close-to-unstable postbuckling behaviour, similar to the buckling of beam-plate of S_r-S_f-S_r-S_f, while plates having lower stiffness ratios (OP-16-11 and OP-16-44) undergo 1st mode of normal buckling. Here the close-to-unstable behaviour means very large deflection within small load increments.

Figures 5-13, 5-14 and 5-15 display successive views of buckling behaviour for each specimen of OP-16-11, OP-16-44 and OP-16-71 respectively. A mode jumping phenomenon was found in OP-16-71 specimen where the mode jumped to the 3rd buckling mode directly. This phenomenon is never expected in theoretical study based on energy method. However, in author's point of view, N-FEA produced the 3rd mode deflection when the flexural stiffness ratio exceeds some ultimate value, i.e., $\zeta \geq 12.0$. It was numerically validated through author's numerous N-FEA works many times.

On the other hand, this phenomenon can be understood that; in the buckling of simply supported plate which has a higher stiffness ratio, i.e., highly anisotropic plate, if the plate undergoes the 1st mode buckling, it requires a harmonic deflection along major-stiffness axis and minor-stiffness axis equally as mentioned in equation (2.34). However, the required critical buckling load along major-stiffness axis (x-axis in this problem) is 3-times higher than the critical buckling load of minor-stiffness axis (y-axis in this problem). it can be understood from careful considerations of the meaning of stiffness ratio, $\zeta = D_{11}/D_{22} \geq 12.0$.

Also, three pairs of strain figures, Figures 5-16 and 5-17, Figures 5-18 and 5-19, Figures 5-20 and 5-21, exhibit detailed views of x- and y-axis strain distributions in the early state of postbuckling with 5.0 kN of the y-load. The figures, especially Figures 5-20 and 5-21, show a complete strain views of mode-jumping behaviour by generation of the 3rd mode of deflection. The author confirmed these jumping phenomena in case of the buckling with ideal plate specimen too. It means these mode-jumping phenomena are not the problem of the modification of the specimen shape, i.e., modification ratio of a_c/a, but rather it is a result of the effect of flexural stiffness ratio ζ.

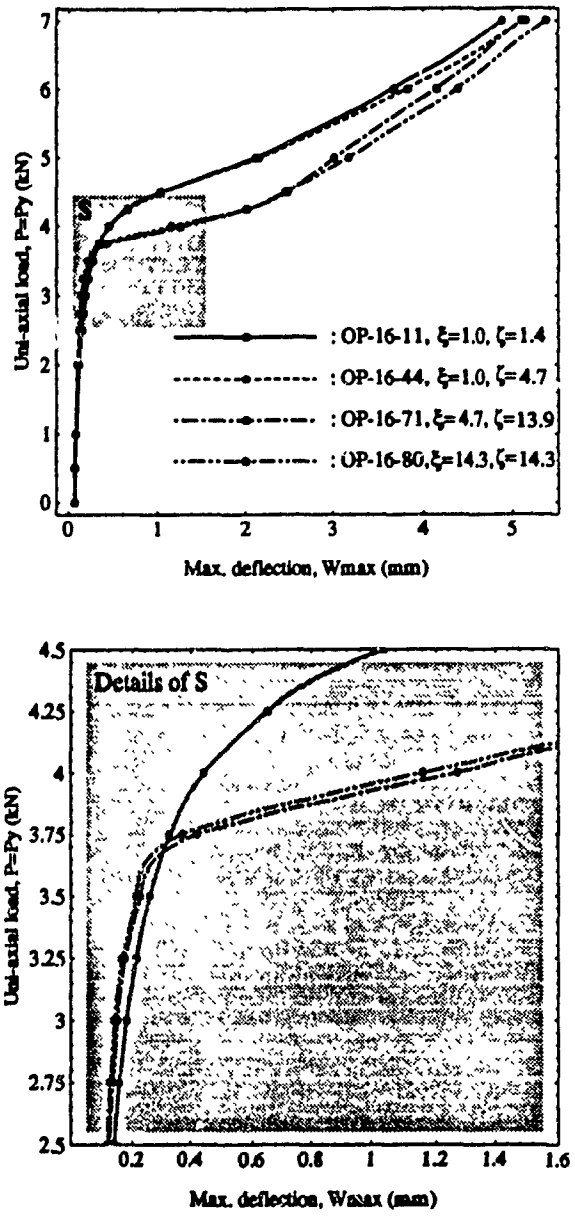

Figure 5.12: Y-axis uniaxial loading behaviour of the 16-layer orthotropic plates for various flexural stiffness ratio, $\zeta = 1.4 \sim 14.3$, by N-FEA.

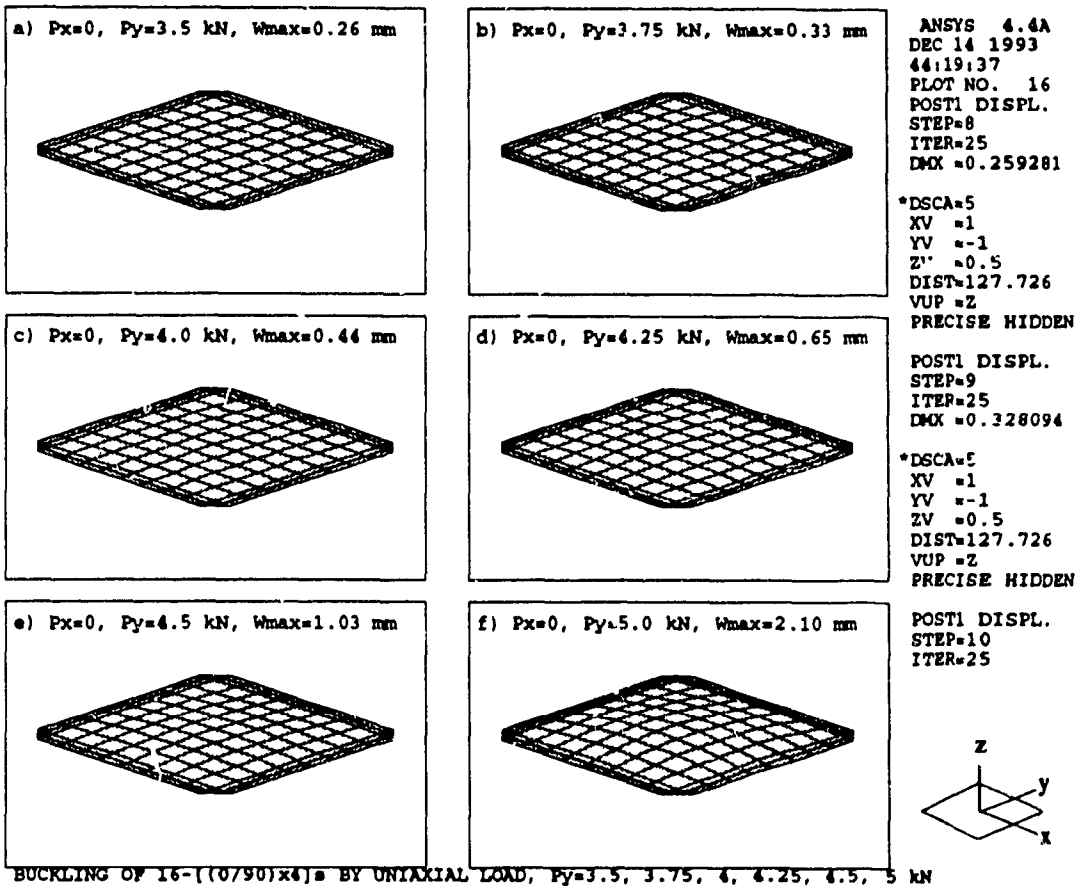

Figure 5.13: Successive views of postbuckling behaviour of the 16-layer orthotropic plate, OP-16-11, with uniaxial loading along y-axis ($P_x : P_y = 0 : 1$).

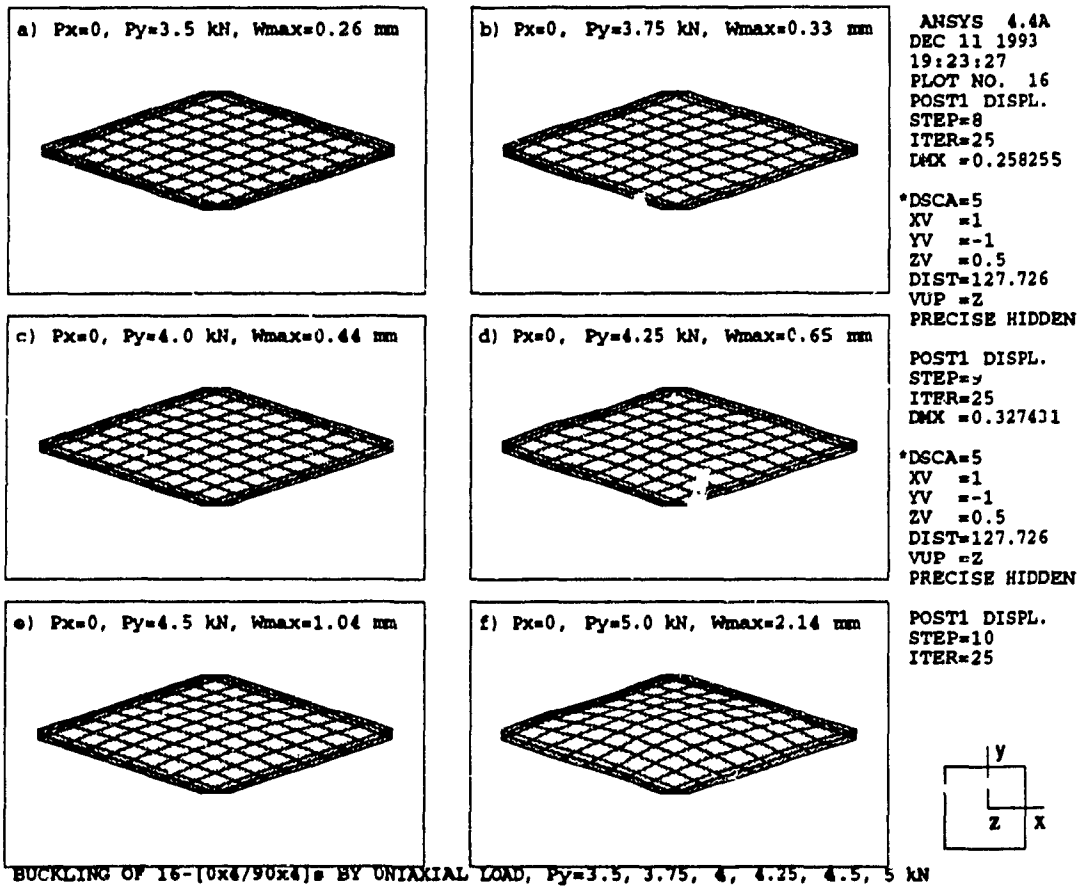

Figure 5.14: Successive views of postbuckling behaviour of the 16-layer orthotropic plate, OP-16-44, with uniaxial loading along y-axis ($P_x : P_y = 0 : 1$).

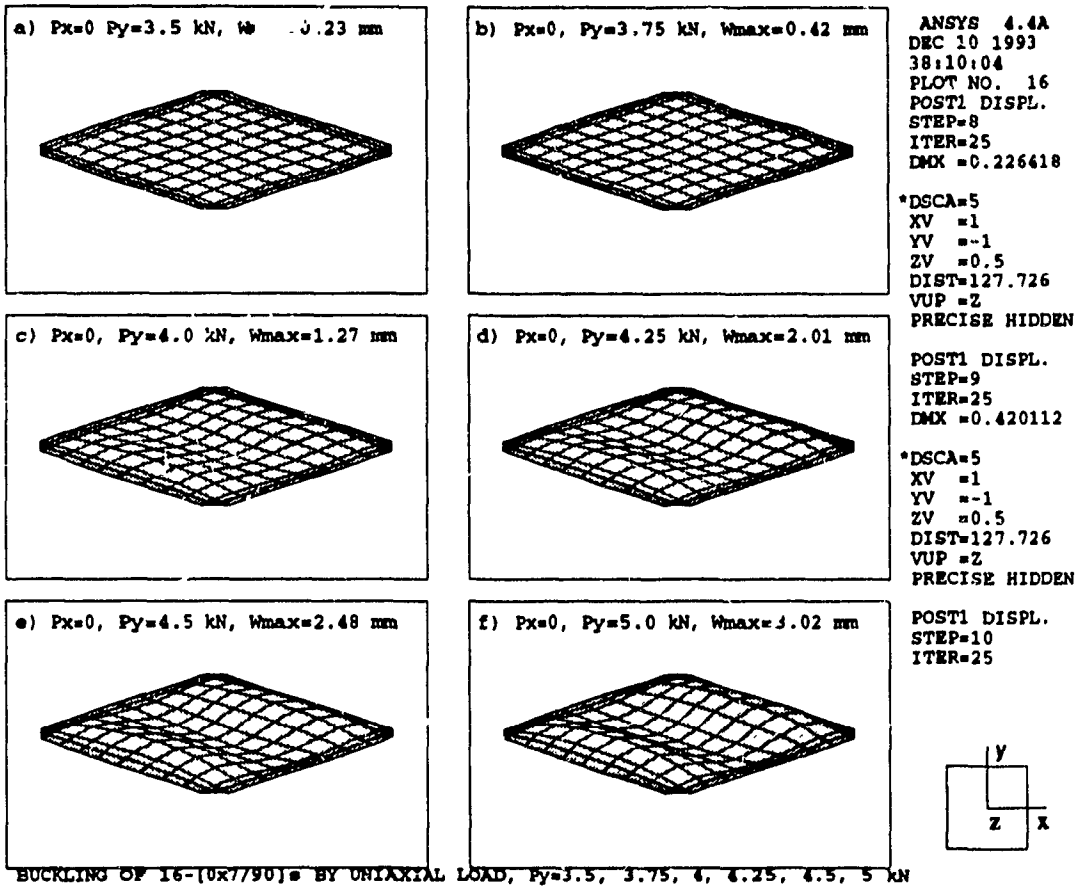

Figure 5.15: Successive view of postbuckling behaviour of the 16-layer orthotropic plate, OP-16-71, with uniaxial loading along y-axis ($P_x : P_y = 0 : 1$).

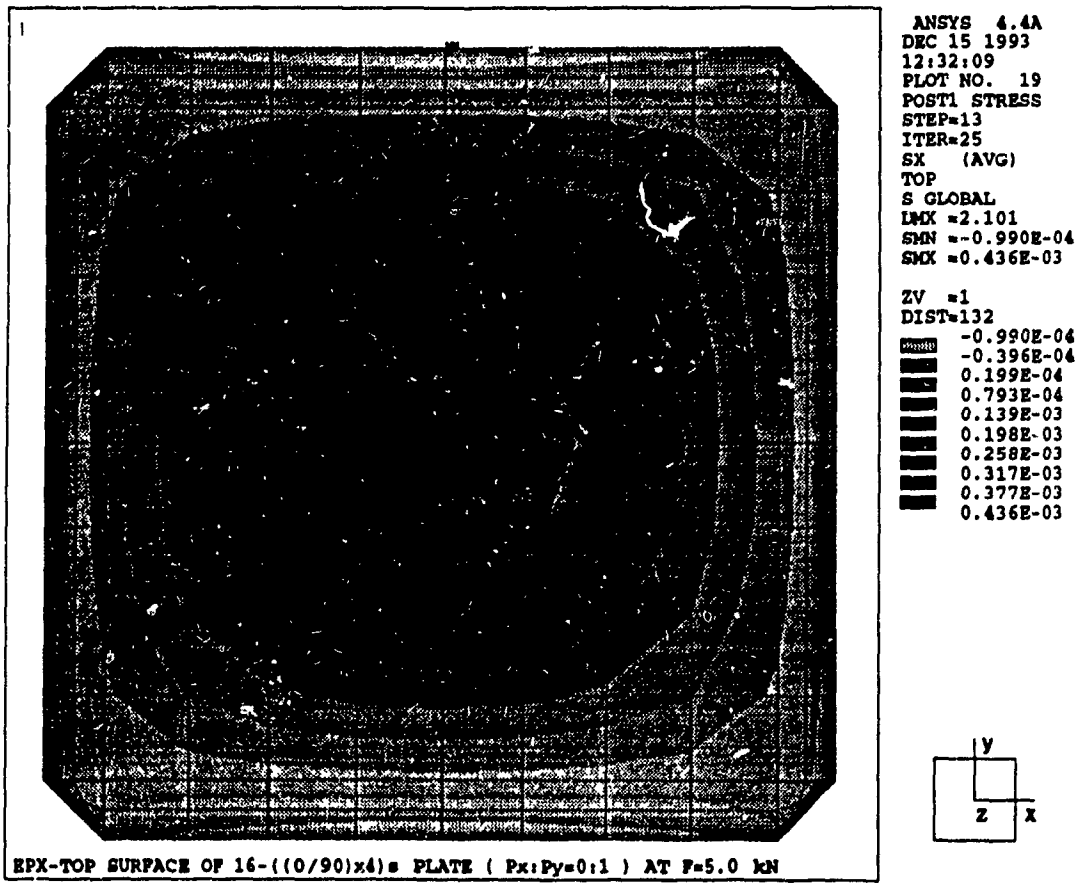

Figure 5.16: X-strain(ϵ_x) distribution of the 16-layer orthotropic plate, OP-16-11 with uniaxial loading along y-axis, $P_x = 5\text{kN}$ ($P_x : P_y = 0 : 1$).

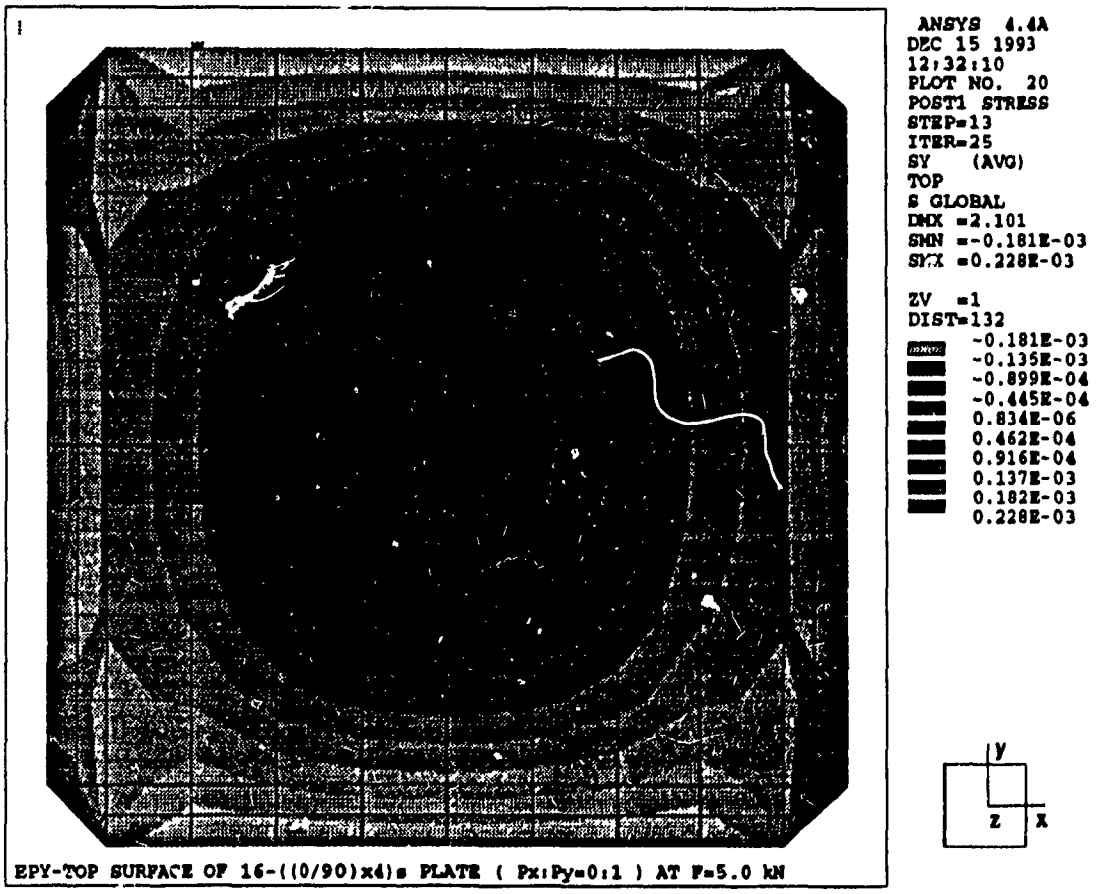

Figure 5.17: Y-strain(ϵ_y) distribution of the 16-layer orthotropic plate, OP-16-11 with uniaxial loading along y-axis, $P_x = 5\text{kN}$ ($P_x : P_y = 0 : 1$).

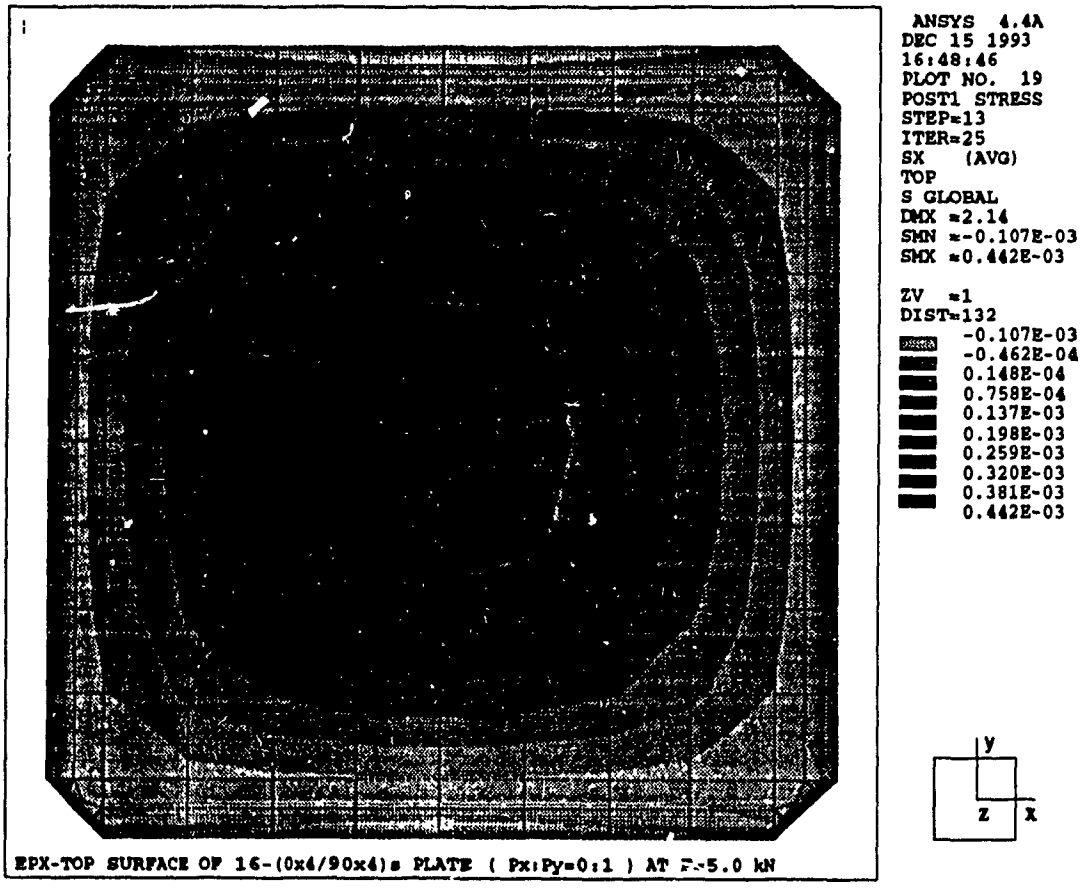

Figure 5.18: X-strain(ϵ_x) distribution of the 16-layer orthotropic plate, OP-16-44 with uniaxial loading along y-axis, $P_x = 5\text{kN}$ ($P_x : P_y = 0 : 1$).

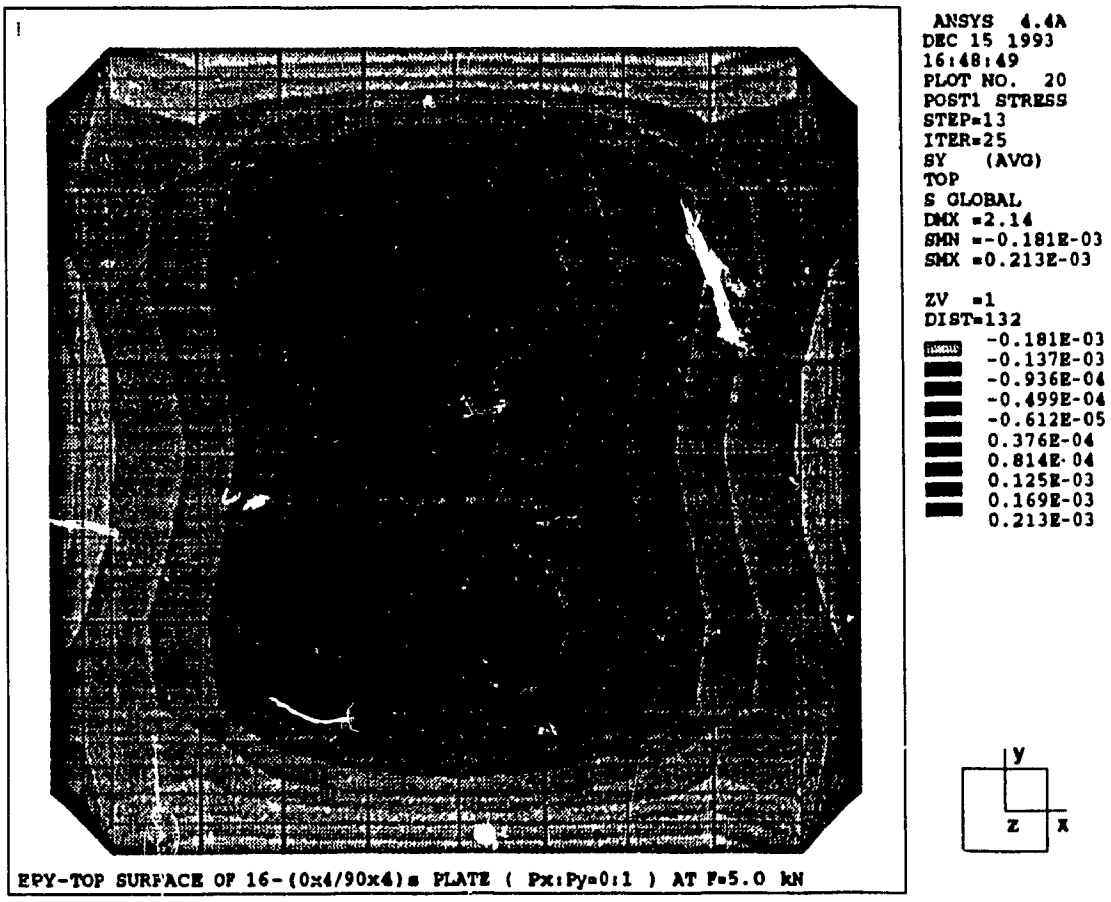

Figure 5.19: Y-strain(ϵ_y) distribution of the 16-layer orthotropic plate, OP-16-44 with uniaxial loading along y-axis, $P_x = 5\text{kN}$ ($P_x : P_y = 0 : 1$).

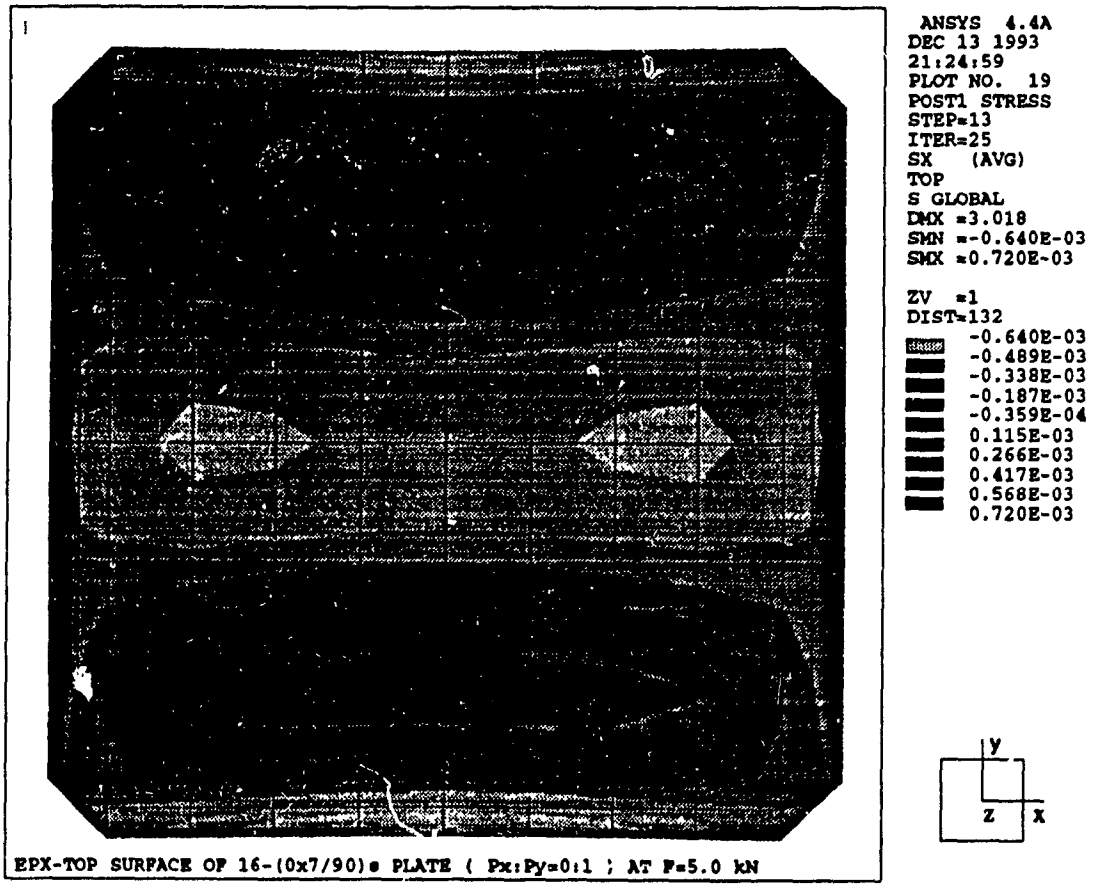

Figure 5.20: X-strain(ϵ_x) distribution of the 16-layer orthotropic plate, OP-16-71 with uniaxial loading along y-axis, $P_x = 5\text{kN}$ ($P_x : P_y = 0 : 1$).

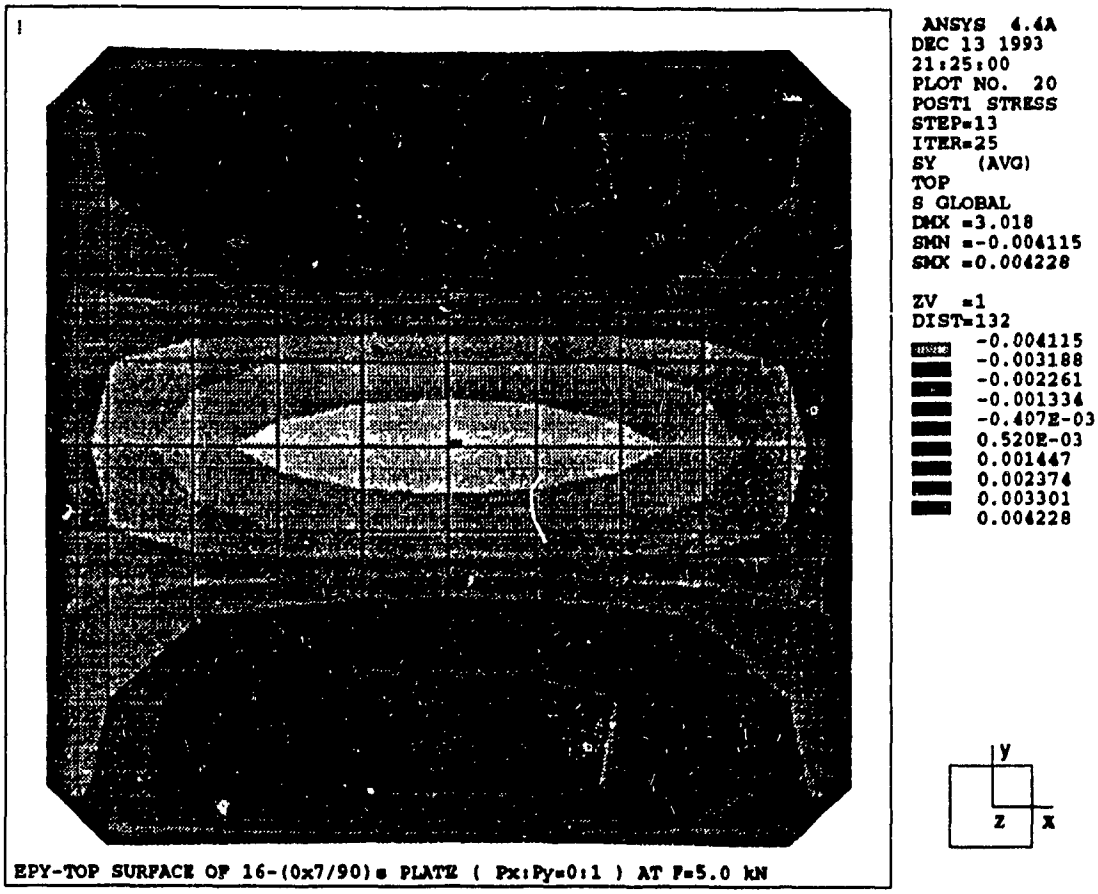

Figure 5.21: Y-strain(ϵ_y) distribution of the 16-layer orthotropic plate, OP-16-71 with uniaxial loading along y-axis, $P_x = 5\text{kN}$ ($P_x : P_y = 0 : 1$).

Biaxial Loading

Figure 5-22 shows also an integrated view of all the biaxial buckling behaviour of the various 16-layer orthotropic laminates subject to a simultaneously increasing biaxial loading with S_r-S_r-S_r-S_r boundary conditions, from OP-16-11 to OP-16-80 specimen series, denoted in Table 3-5. Vews of global load-deflection behaviour, in Figure 5-22, denote that plate having balanced layup like OP-16-11 produce more stable postbuckling behaviour than unbalanced plate like OP-16-71 or OP-16-80.

Also, from the lower detailed view of Figure 5-22, we can find that the values of critical buckling load do not vary very much according to the flexural stiffness ratio, i.e., $P_{cb} = 2.3 \sim 2.4$ kN for $\zeta = 1.4 \sim 14.30$ and the tendencies of the graphs are almost the same as the case of x-axis uniaxial buckling in Figure 5-2. Comparing three detail views - "Detail of S" - of Figures 5-2, 5-12 and 5-22, we can find the stiffness ratio effect on the bifurcation mechanism near the buckling point. That is, in case of uniaxial loading, the major flexural stiffness(D_{11}) governs totally the critical buckling load value when the loading axis is major axis (x-axis in this problem). However, the minor flexural stiffness(D_{22}) does not govern the critical buckling load value when the loading axis is minor axis (y-axis in this problem). It means the major stiffness(D_{11}) governs the critical buckling load in any case of uniaxial buckling, i.e., x-uniaxial or y-uniaxial loading. Finally, in case of biaxial buckling, the major flexural stiffness(D_{11}) mainly governs the critical buckling load value and the effect of minor flexural stiffness(D_{22}) is very minimal.

In Figures 5-23, 5-24 and 5-25, successive views of postbuckling deflections for each OP-16-11, OP-16-44 and OP-16-71 specimen were presented. All specimens reveal normal and stable 1st mode buckling deflections as similarly as the case of x-axis uniaxial buckling.

Also, the subsequent three pairs of views of strain distribution, Figures 5-26 and 5-27, Figures 5-28 and 5-29, Figures 5-30 and 5-31, exhibit detailed view of x- and y-axis strain distributions in the early state of postbuckling with 3.0 kN under biaxial loading. Comparing x-strains from Figures 5-26, 5-28 and 5-30, all plate produce a concentric circular distributions of strain. However, if we compare y-strains from Figures 5-27, 5-29 and 5-31, the highly unbalanced plate(OP-16-71) reveals very unstable strain field by showing two separated elliptic strain distributions.

Consequently, it is clear that these figures back up well the previous buckling behaviour of Figure 5-22.

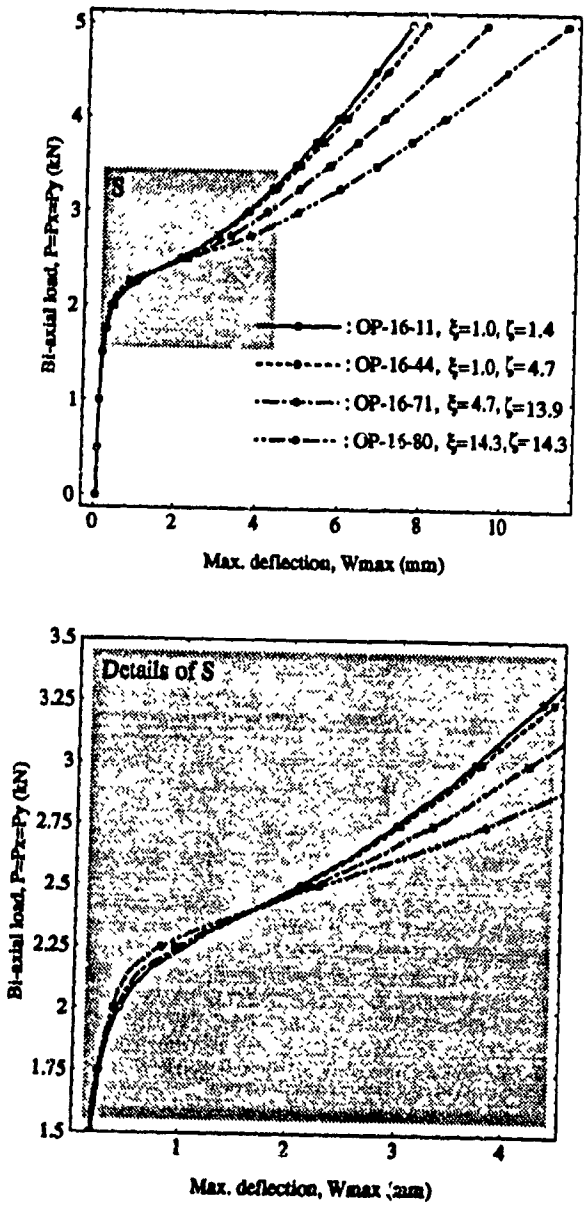

Figure 5.22: Biaxial buckling behaviour for various flexural stiffness ratio, $\zeta = 1.4 \sim 14.3$, on the 16-layer orthotropic plates by N-FEA.

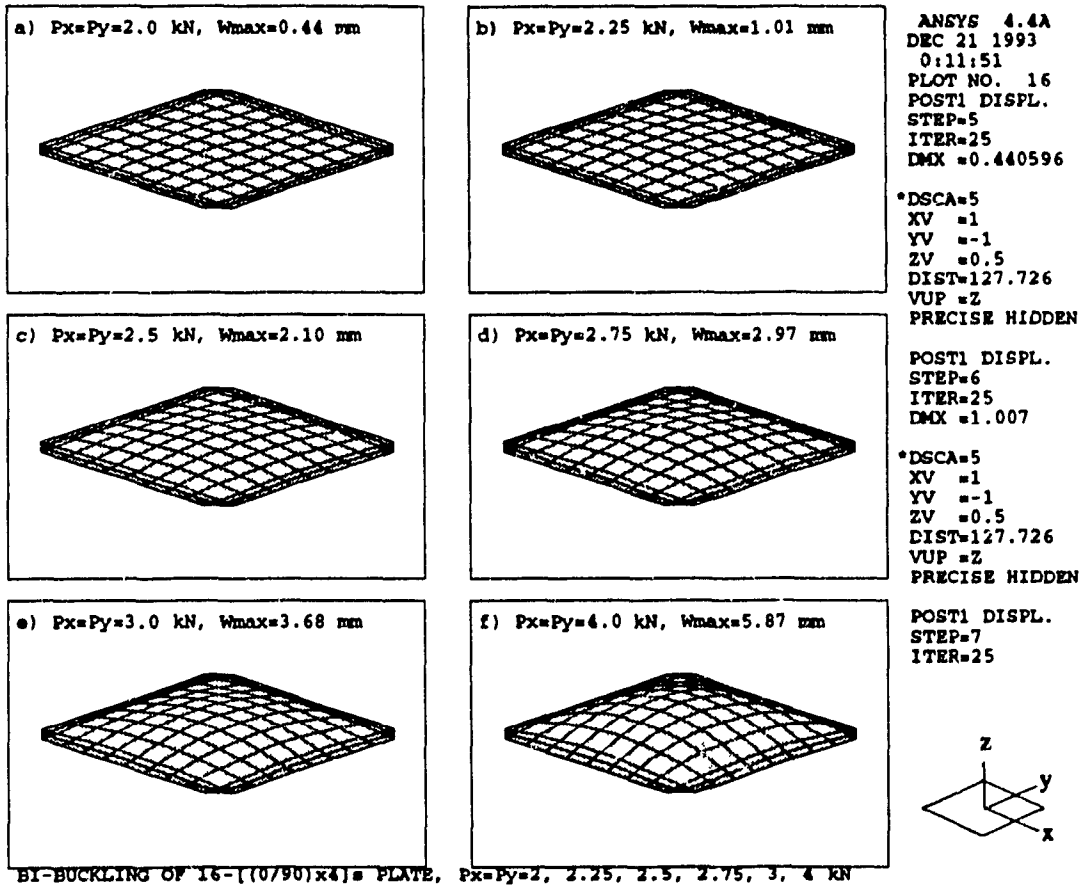

Figure 5.23: Successive views of postbuckling behaviour of the 16-layer orthotropic plate, OP-16-11, with biaxial loadings ($P_x : P_y = 1 : 1$).

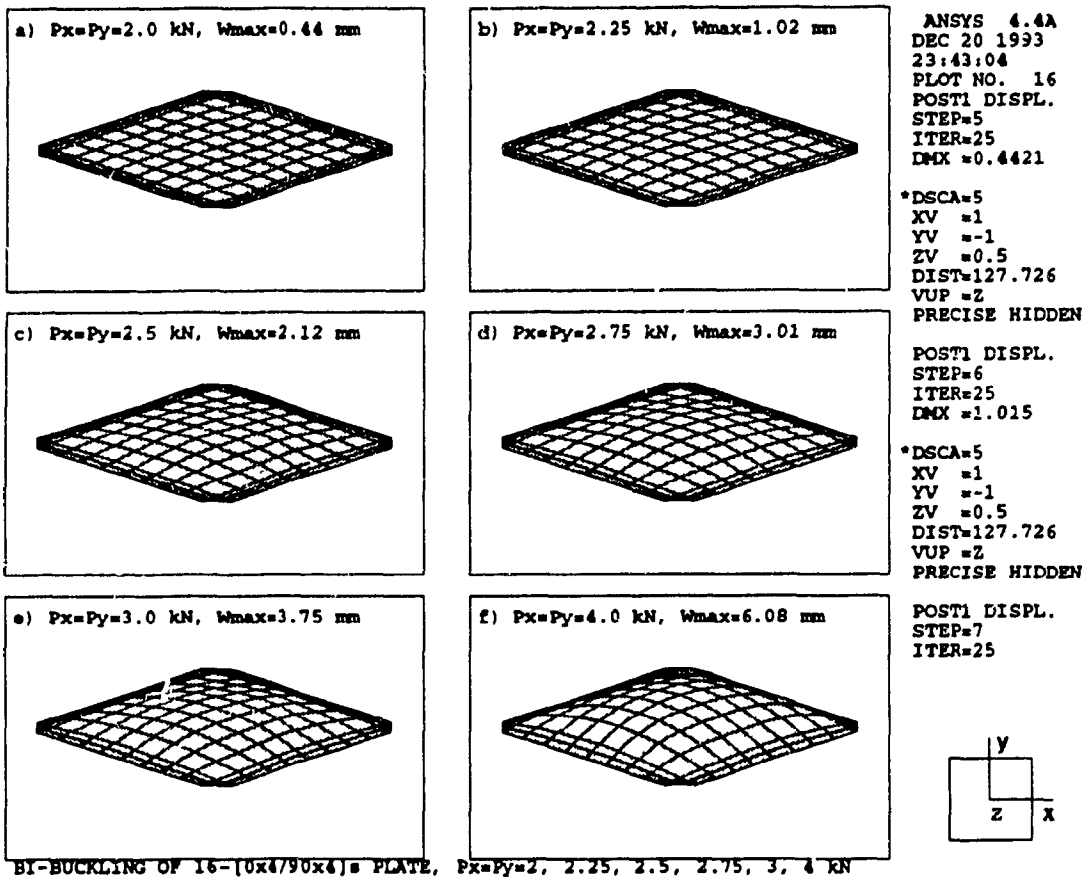

Figure 5.24: Successive views of postbuckling behaviour of the 16-layer orthotropic plate, OP-16-44, with biaxial loadings ($P_x : P_y = 1 : 1$).

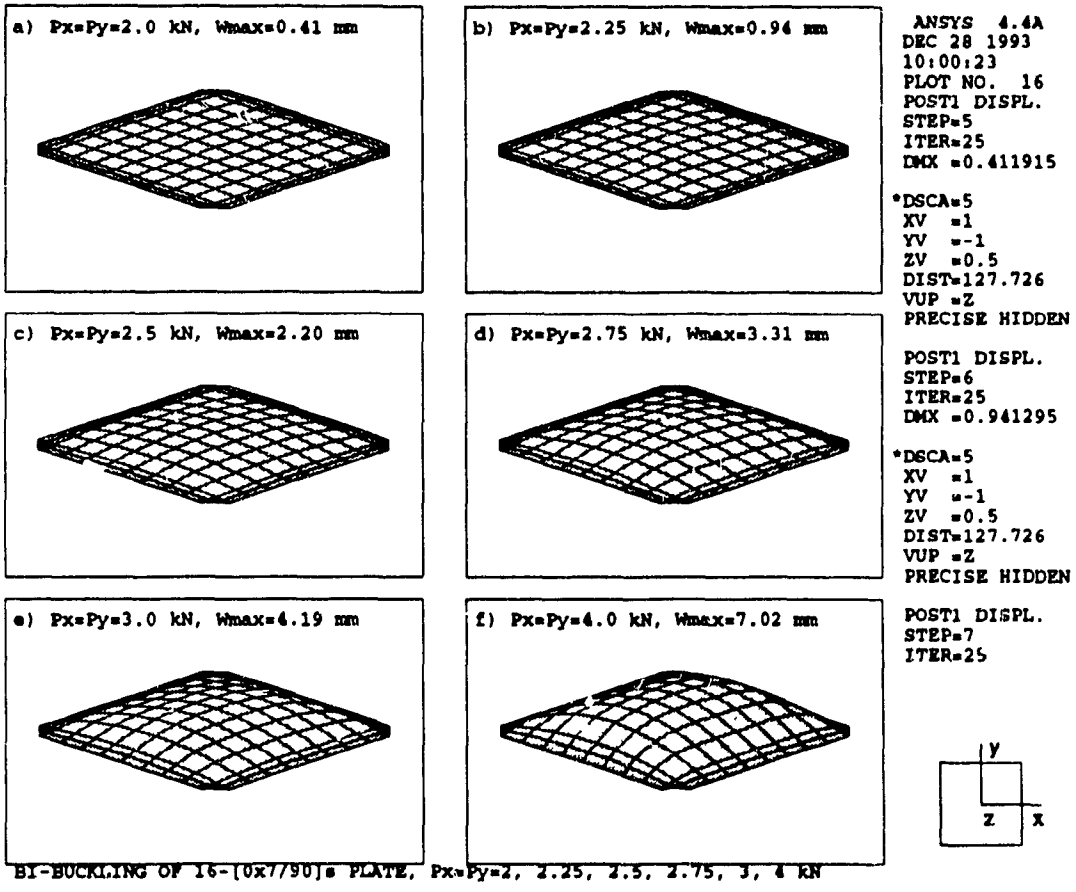

Figure 5.25: Successive views of postbuckling behaviour of the 16-layer orthotropic plate, OP-16-71, with biaxial loadings ($P_x : P_y = 1 : 1$).

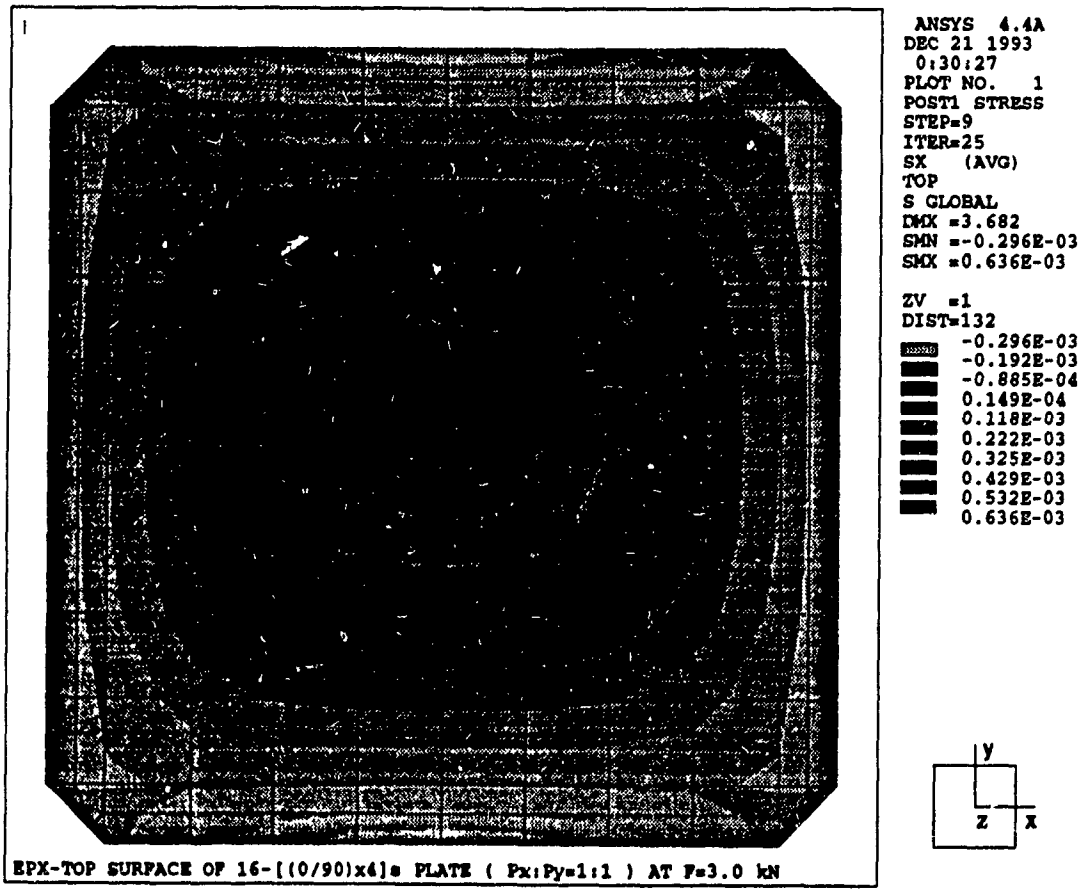

Figure 5.26: X-strain(ϵ_x) distribution of the 16-layer orthotropic plate, OP-16-11 with biaxial loadings, $P_x = P_y = 3$kN ($P_x : P_y = 1 : 1$).

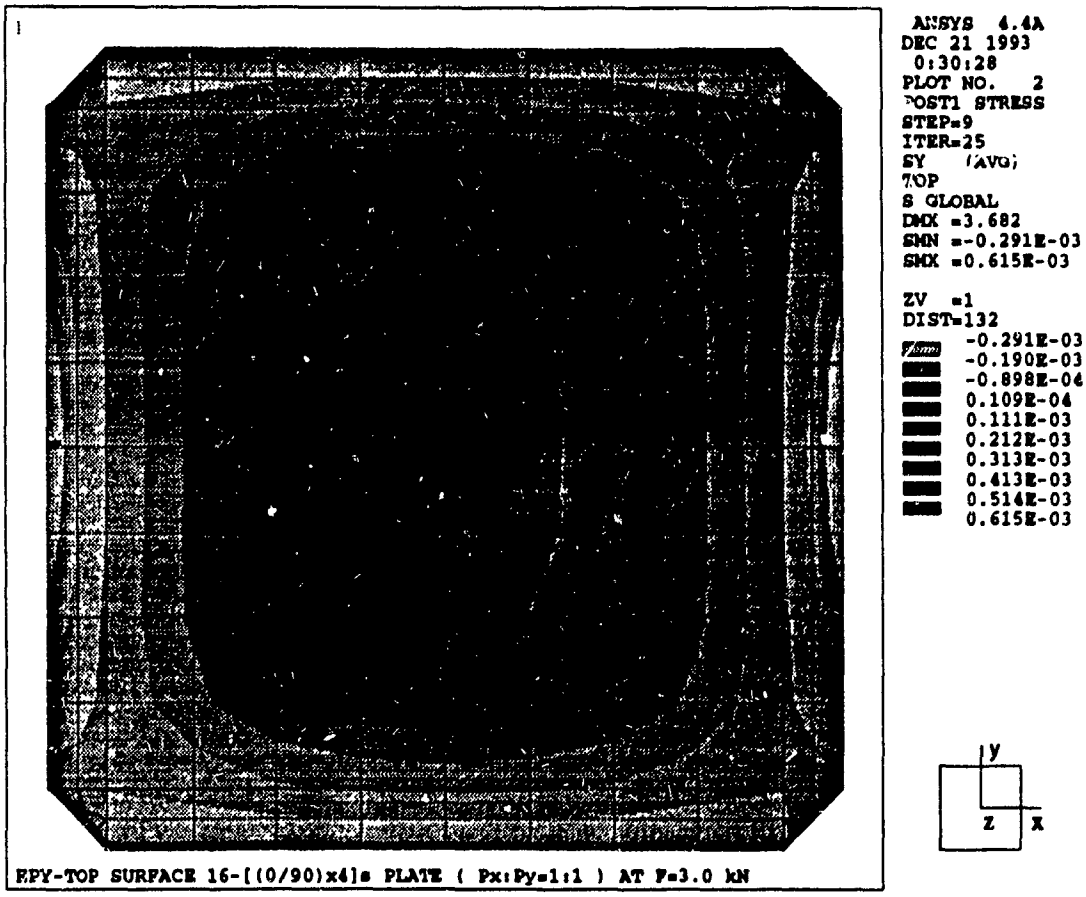

Figure 5.27: Y-strain(ϵ_y) distribution of the 16-layer orthotropic plate, OP-16-11 with biaxial loadings, $P_x = P_y = 3$kN ($P_x : P_y = 1 : 1$).

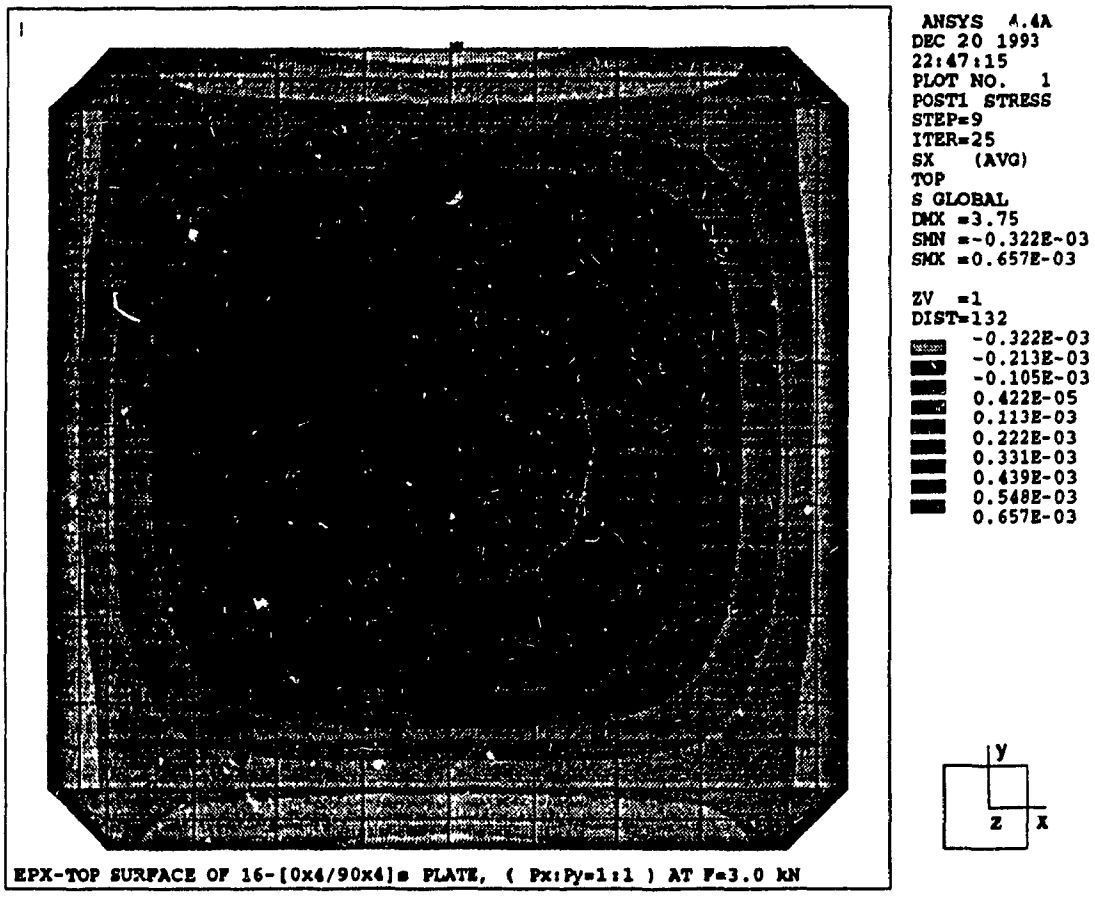

Figure 5.28: X-strain(ϵ_x) distribution of the 16-layer orthotropic plate, OP-16-44 with biaxial loadings, $P_x = P_y = 3\text{kN}$ ($P_x : P_y = 1 : 1$).

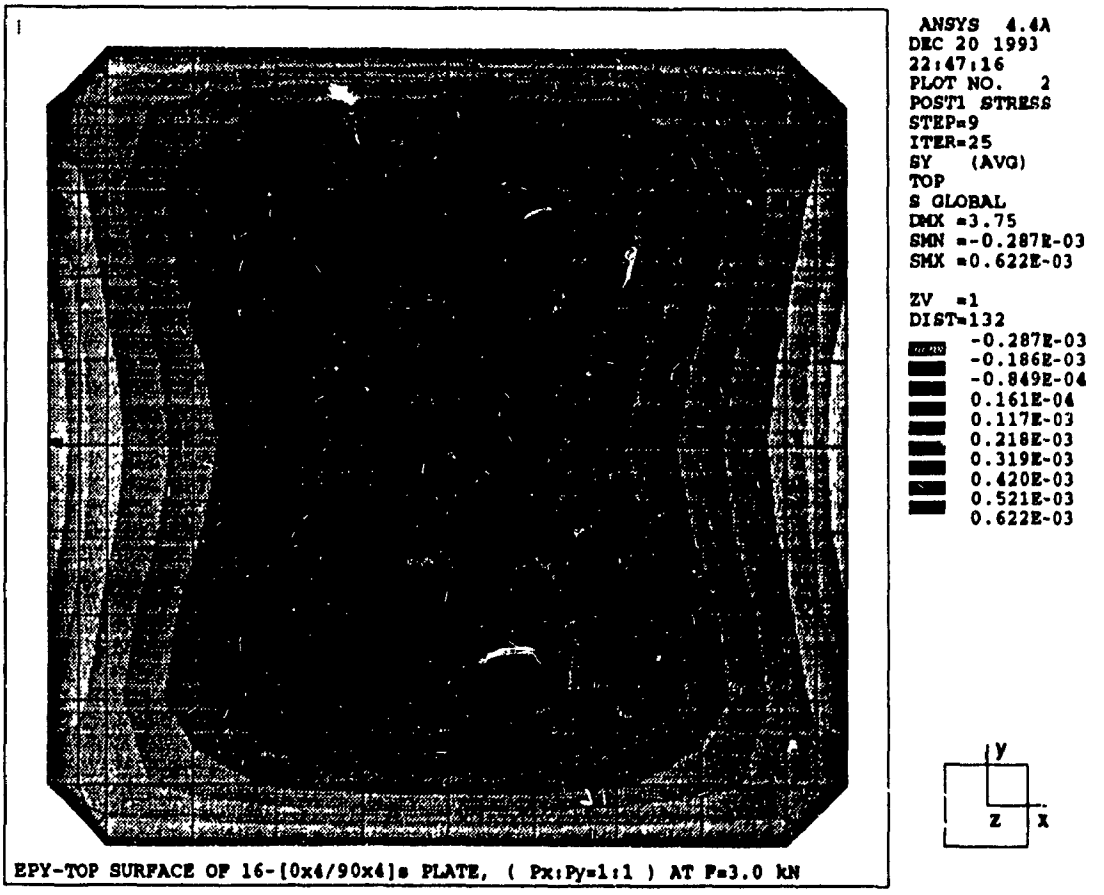

Figure 5.29: Y-strain(ϵ_y) distribution of the 16-layer orthotropic plate, OP-16-44 with biaxial loadings, $P_x = P_y = 3\text{kN}$ ($P_x : P_y = 1 : 1$).

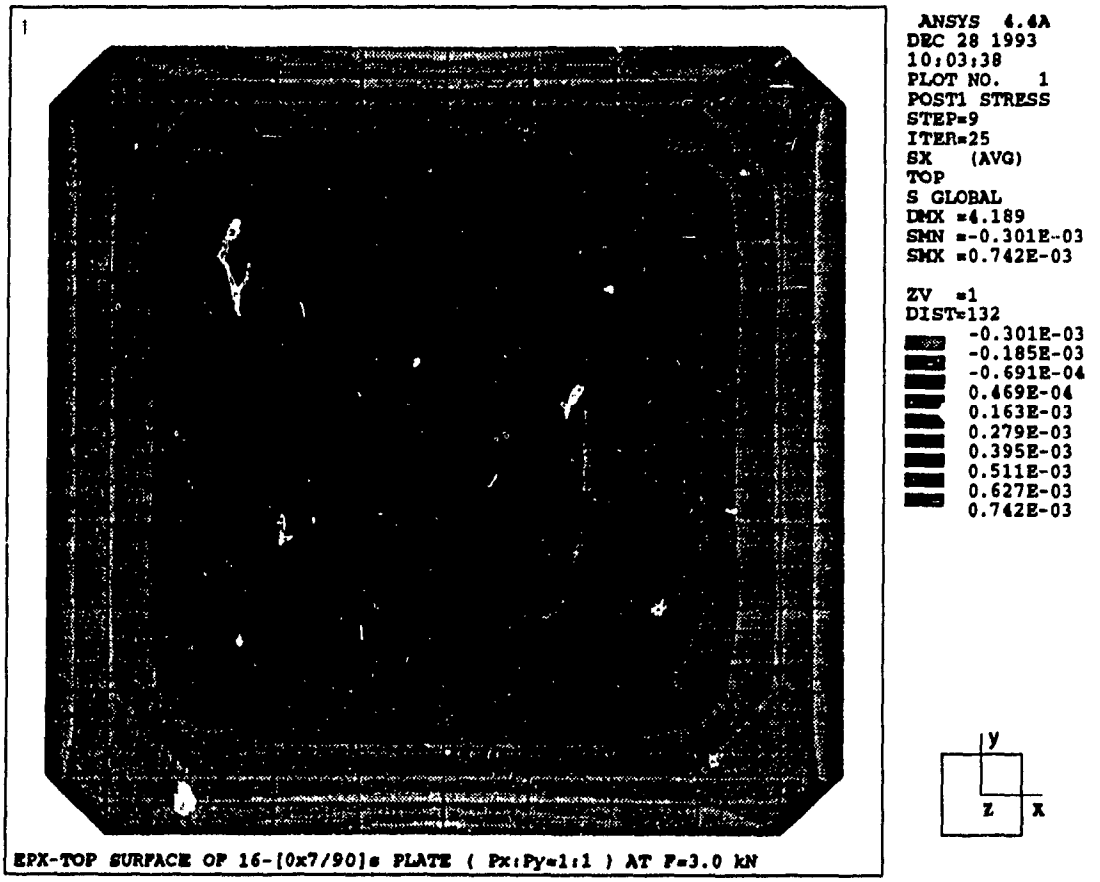

Figure 5.30: X-strain(ϵ_x) distribution of the 16-layer orthotropic plate, OP-16-71 with biaxial loadings, $P_x = P_y = 3\text{kN}$ ($P_x : P_y = 1 : 1$).

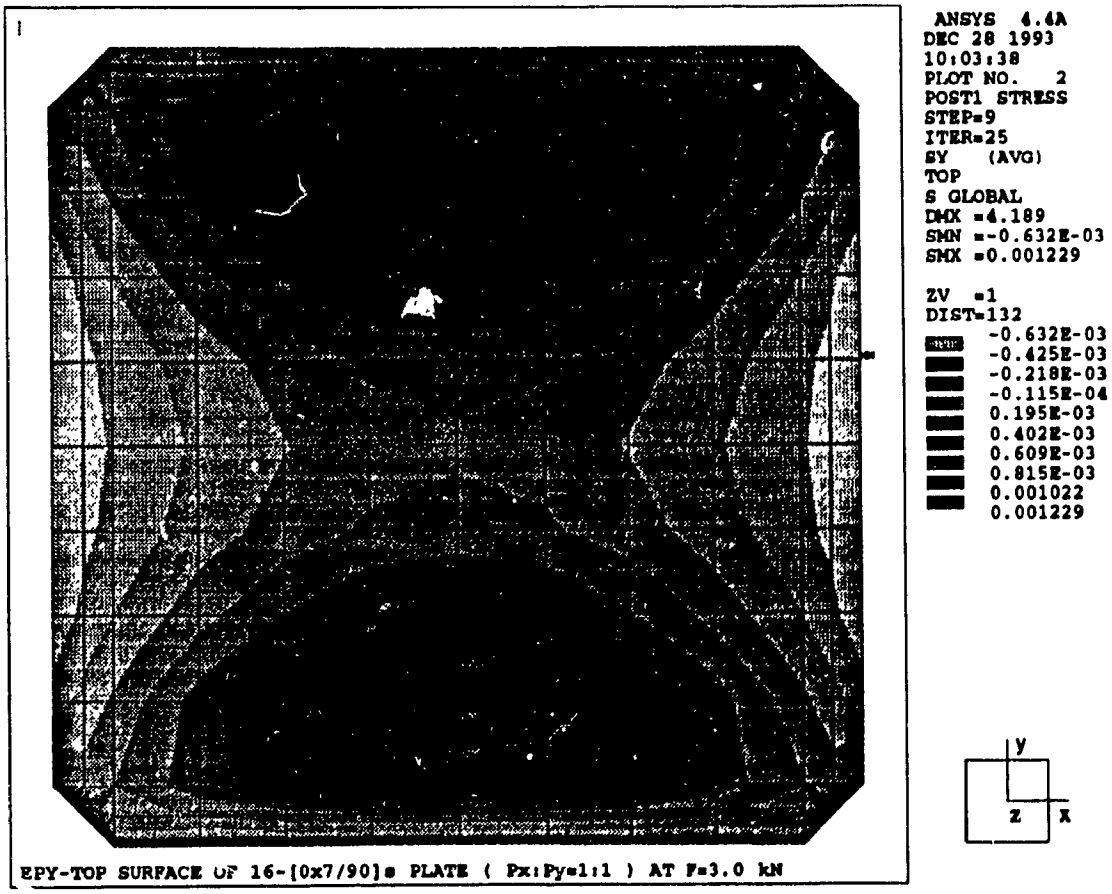

Figure 5.31: Y-strain(ϵ_y) distribution of the 16-layer orthotropic plate, OP-16-71 with biaxial loadings, $P_x = P_y = 3\text{kN}$ ($P_x : P_y = 1 : 1$).

5.2.2 20-layer Plate Specimen

Uniaxial Loading along X-axis

Figure 5-32 shows an integrated view of all buckling behaviour of the various 20-layer orthotropic plates subject to x-axis uniaxial loading with S_r-S_r-S_r-S_r boundary conditions. Analysis models were chosen as OP-20-11 to OP-16-200 specimen series, denoted in Table 3-5. From the upper global and lower detailed view of the shaded area in Figure 5-32, we can find that the values of the critical buckling load do not vary very much according to the flexural stiffness ratio, as $P_{cr} = 9.05 \sim 8.65$ kN for $\zeta = 1.3 \sim 14.3$.

However, in postbuckling behaviour, the specimen having a higher stiffness ratio exhibits more sharpened development of postbuckling deflection. It could be said that, for the x-axis uniaxially loaded orthotropic plate, even if a plate is stiffened in x-direction, due to the high stiffness ratio it is more unstable in postbuckled state and it easily reaches a catastrophic failure. Figures 5-33, 5-34, 5-35 and 5-36 display successive views of buckling behaviour for each specimen of OP-20-11, OP-20-55, OP-20-82 and OP-20-100 respectively. All f the views reconfirm the buckling behaviours in Figure 5-32 and it can be noted that plate with higher stiffness ratio has higher lateral deflection, w_{max}, in postbuckling state.

Also, all detailed views of x- and y-axis strain distributions in the early state of postbuckling with 5.0 kN of the x-load were obtained and all of them were well-matched with Figure 5-32 (not shown here).

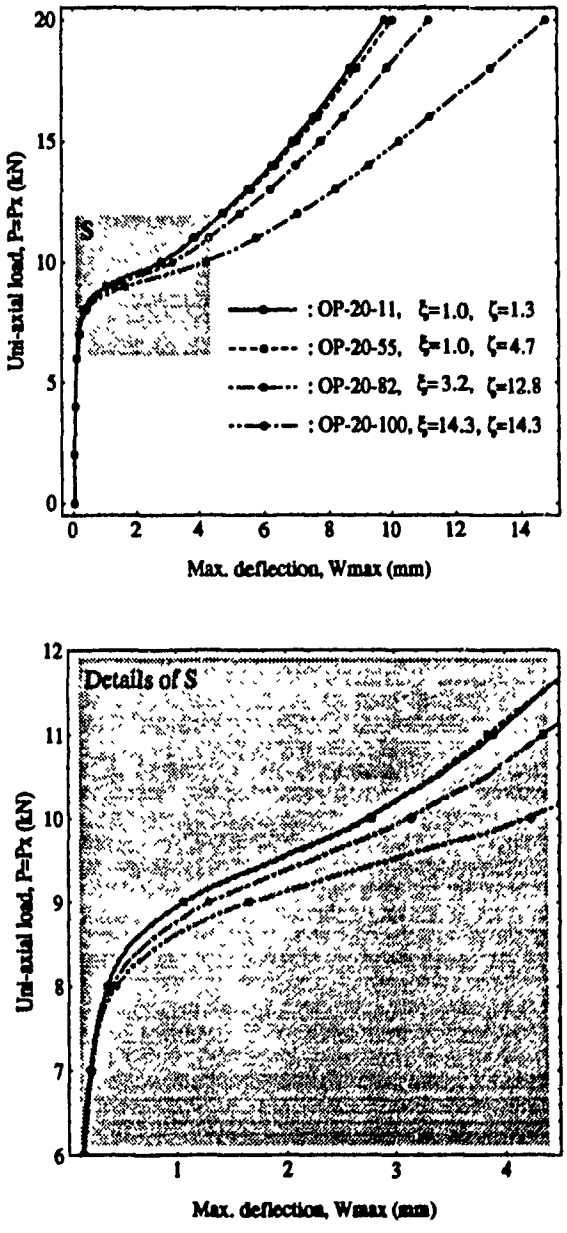

Figure 5.32: X-axis uniaxial loading behaviour of the 20-layer orthotropic plates for various flexural stiffness ratio, $\zeta = 1.3 \sim 14.3$, by N-FEA.

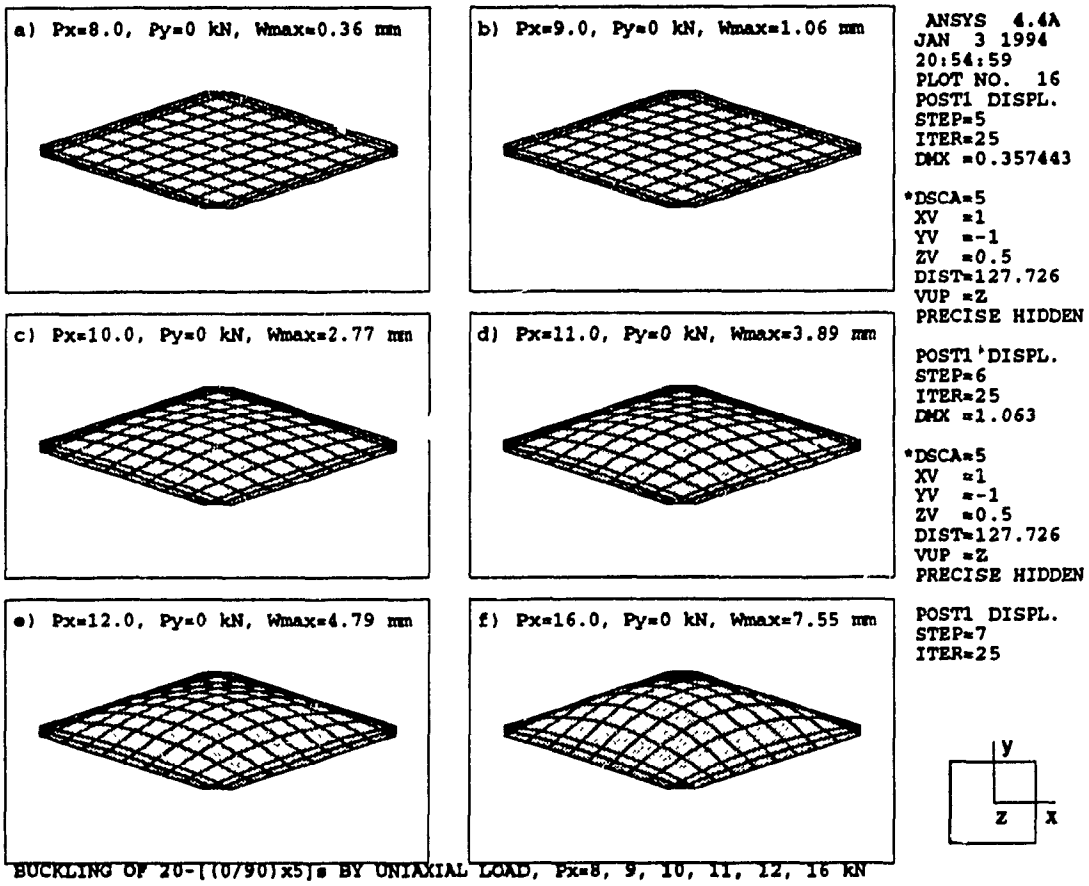

Figure 5.33: Successive views of postbuckling behaviour of the 20-layer orthotropic plate, OP-20-11, with uniaxial loading along x-axis ($P_x : P_y = 1 : 0$).

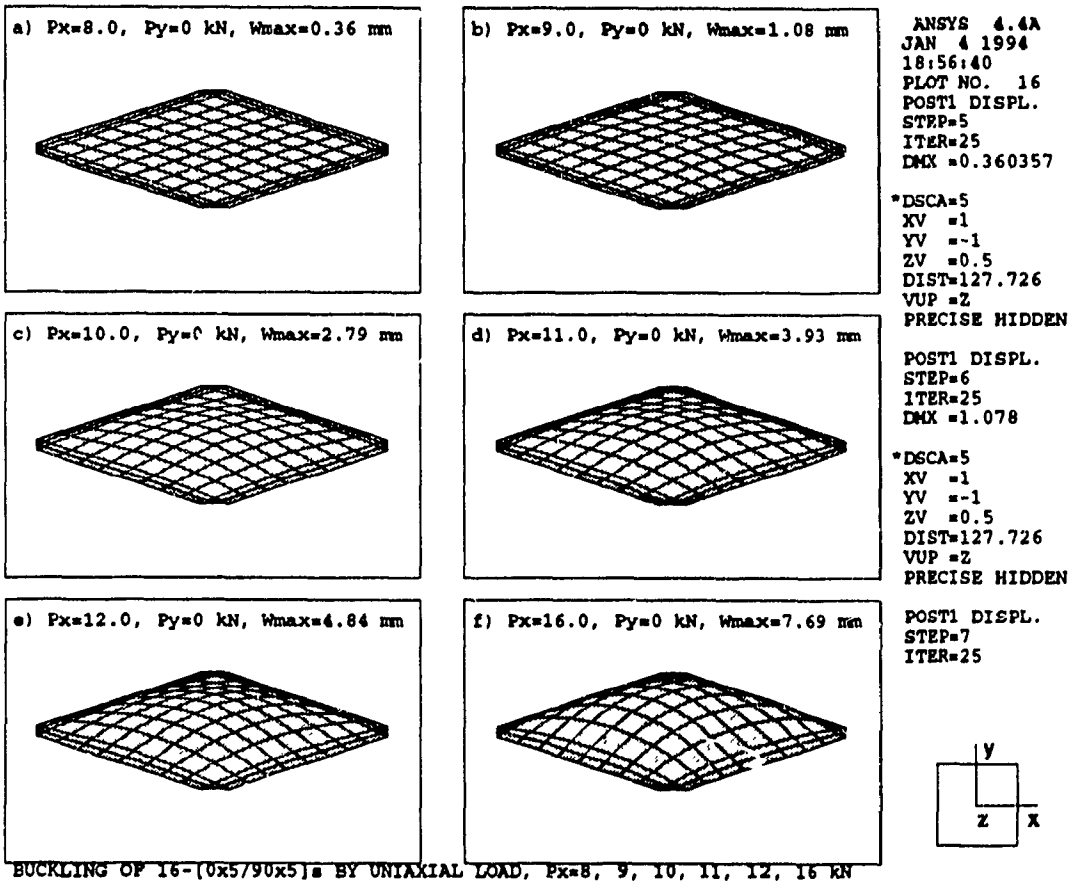

Figure 5.34: Successive views of postbuckling behaviour of the 20-layer orthotropic plate, OP-20-55, with uniaxial loading along x-axis ($P_x : P_y = 1 : 0$).

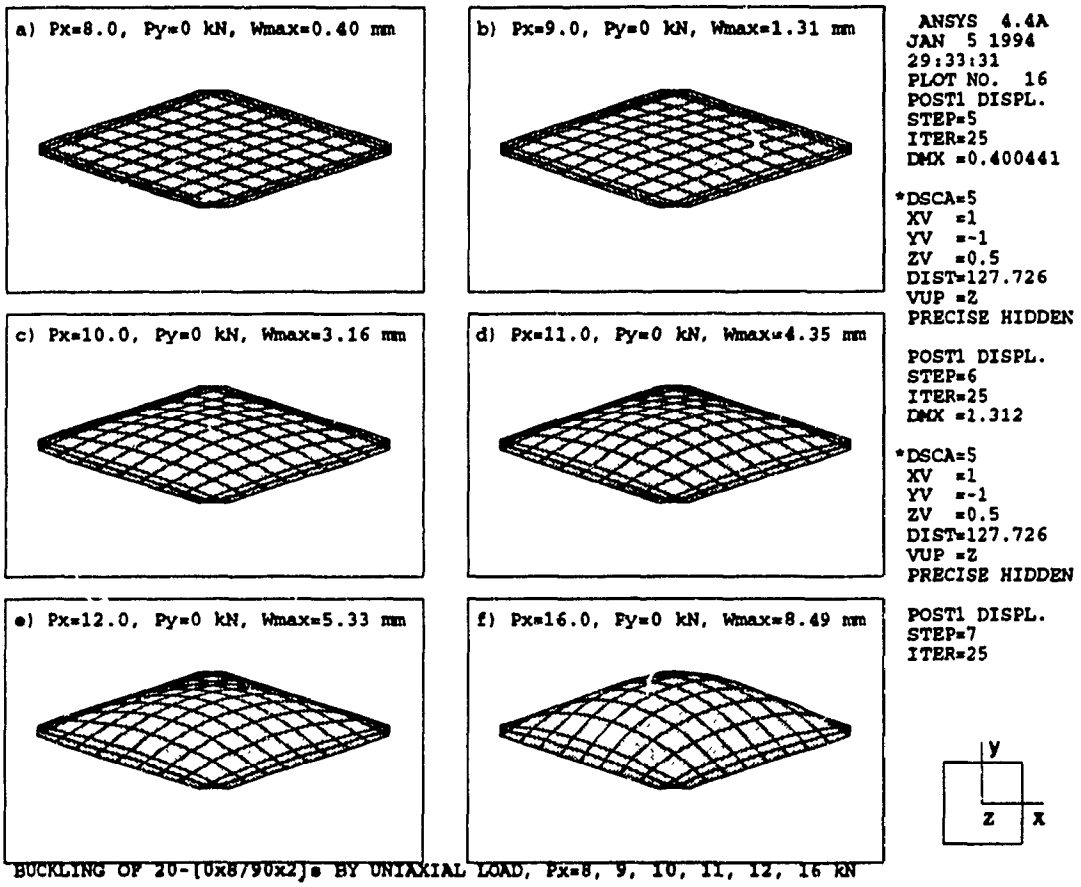

Figure 5.35: Successive views of postbuckling behaviour of the 20-layer orthotropic plate, OP-20-82, with uniaxial loading along x-axis ($P_x : P_y = 1 : 0$).

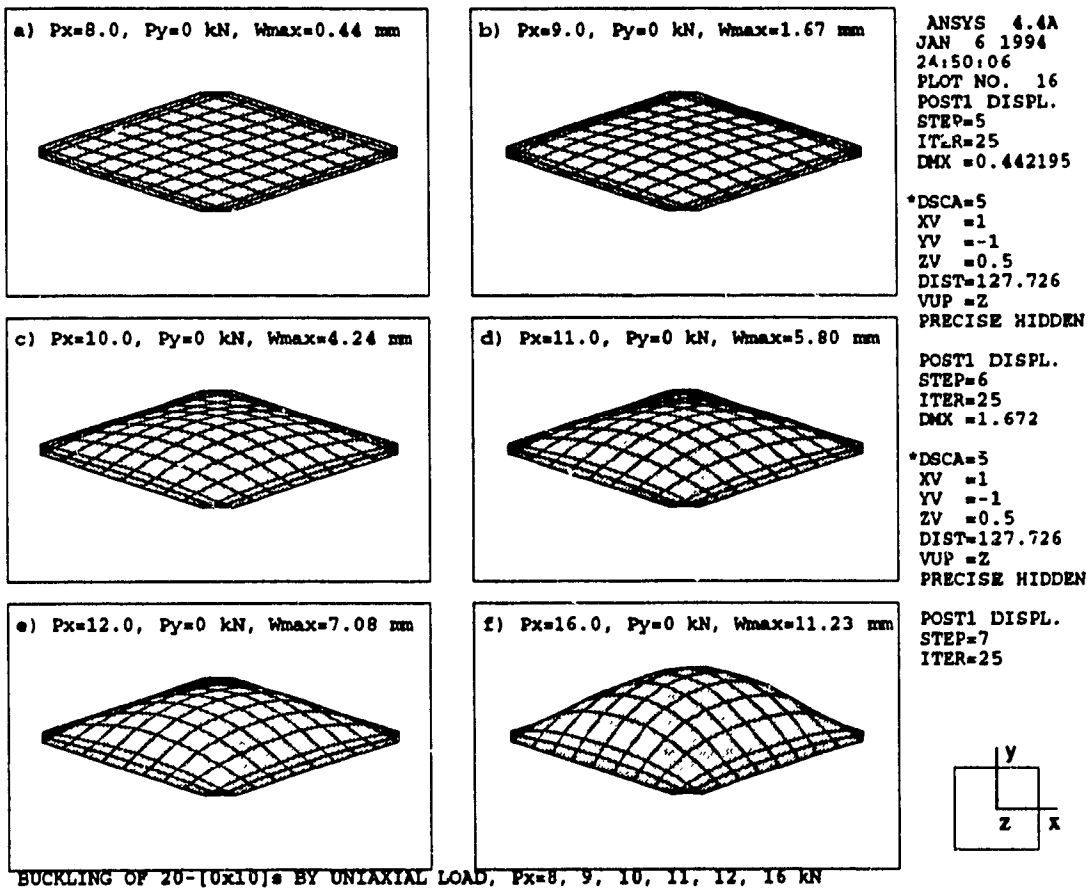

Figure 5.36: Successive views of postbuckling behaviour of the 20-layer orthotropic plate, OP-20-100, with uniaxial loading along x-axis ($P_x : P_y = 1 : 0$).

Uniaxial Loading along Y-axis

Figure 5-37 shows also an integrated view of all the uniaxial loading behaviour of the various 20-layer orthotropic laminates subject to y-axis uniaxial loading with S_r-S_r-S_r-S_r boundary conditions. For this analysis, specimen models were chosen as OP-20-11$\sim$ OP-20-100 specimen series as tabulated on Table 3-5. From the lower detailed view of the shaded area in Figure 5-37, we see that the values of the critical buckling load vary according to the flexural stiffness ratio, i.e., $P_{cy} = 9.1 \sim 8.0$ kN for $\zeta = 1.3 \sim 14.30$. However, from the postbuckling responses, the plates having a higher stiffness ratio, like specimens OP-20-82 and OP-20-100, exhibit weaker postbuckling behaviour than the plate with a regular stacking sequence like specimens OP-20-11 and OP-20-55.

Through the inspection of Figures 5-38, 5-39, 5-40 and 5-41, successive views of postbuckling deflections for each OP-20-11, OP-20-55, OP-20-82 and OP-20-100 specimen, very different responses are found according to the stiffness ratio ζ. From the two groups of different curves, it can be interpreted that the plate with irregular stacking sequence, like specimens OP-20-82 and OP-20-100, behave differently from the regular plate such as OP-20-11 or OP-20-55 specimen. The major differences are early buckling and mode jumping phenomena that go from 1st mode to the 3rd buckling mode directly. These phenomena were also confirmed in the analysis of 16-layer laminates. On the other hand, the strain distributions were investigated in the same manner as for the case of 16-layer and they were also well matched to Figure 5-37 (not shown here).

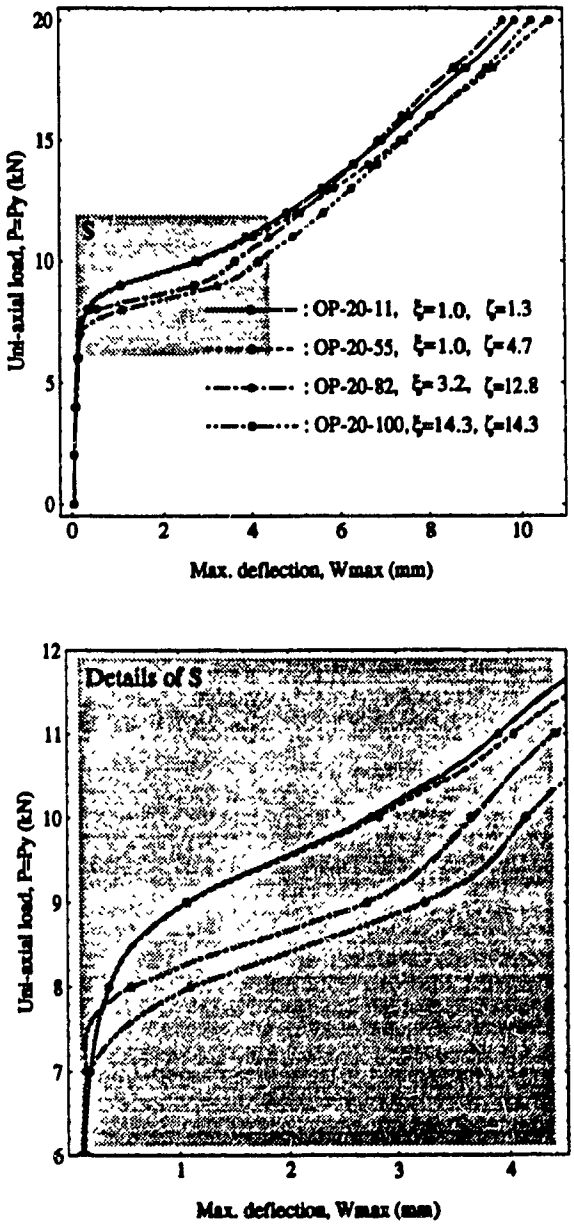

Figure 5.37: Y-axis uniaxial loading behaviour of the 20-layer orthotropic plates for various flexural stiffness ratio, $\zeta = 1.3 \sim 14.3$, by N-FEA.

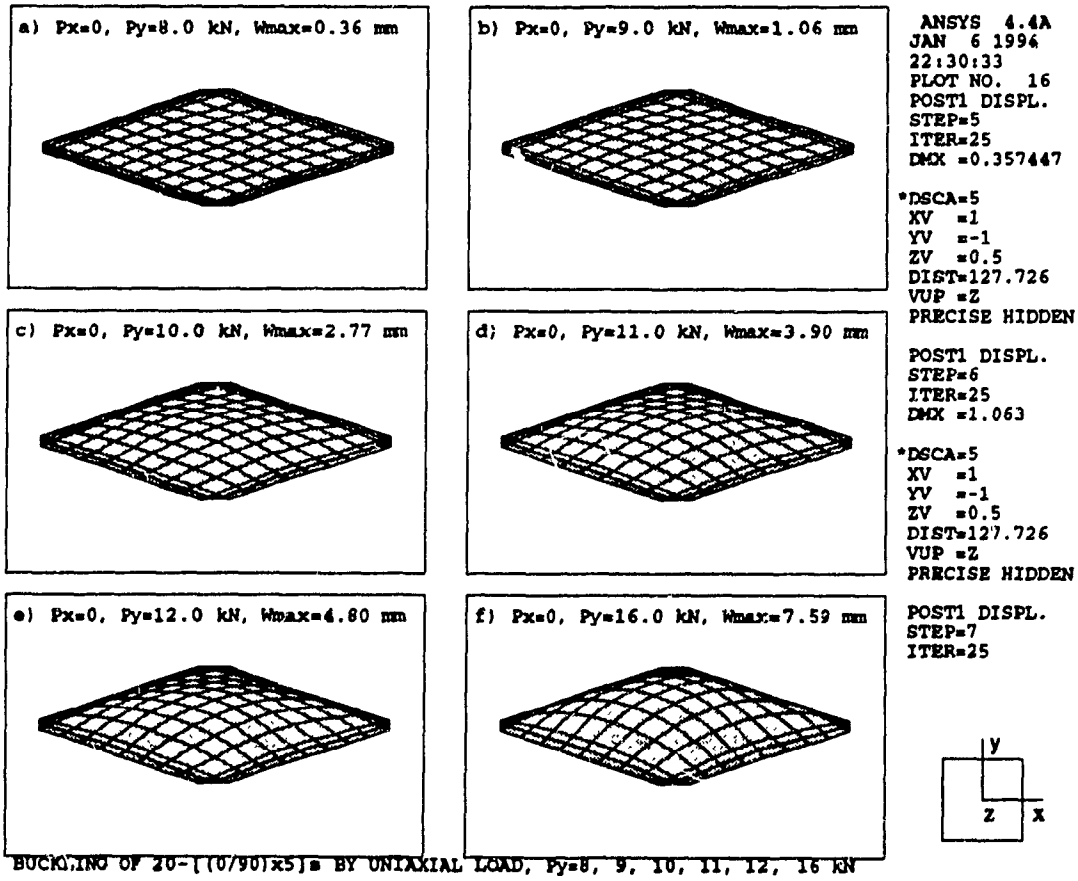

Figure 5.38 Successive views of postbuckling behaviour of the 20-layer orthotropic plate, OP-20-11, with uniaxial loading along y-axis ($P_x : P_y = 0 : 1$).

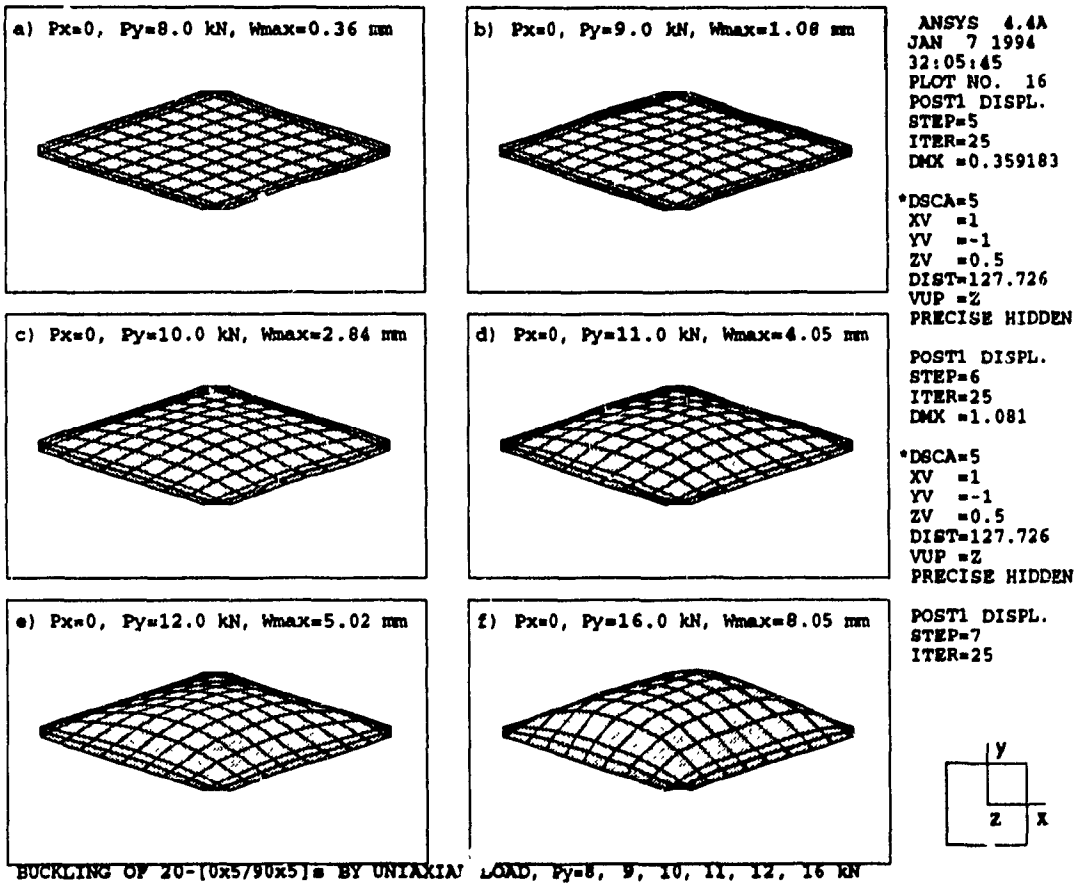

Figure 5.39: Successive views of postbuckling behaviour of the 20-layer orthotropic plate, OP-20-55, with uniaxial loading along y-axis ($P_x : P_y = 0 : 1$).

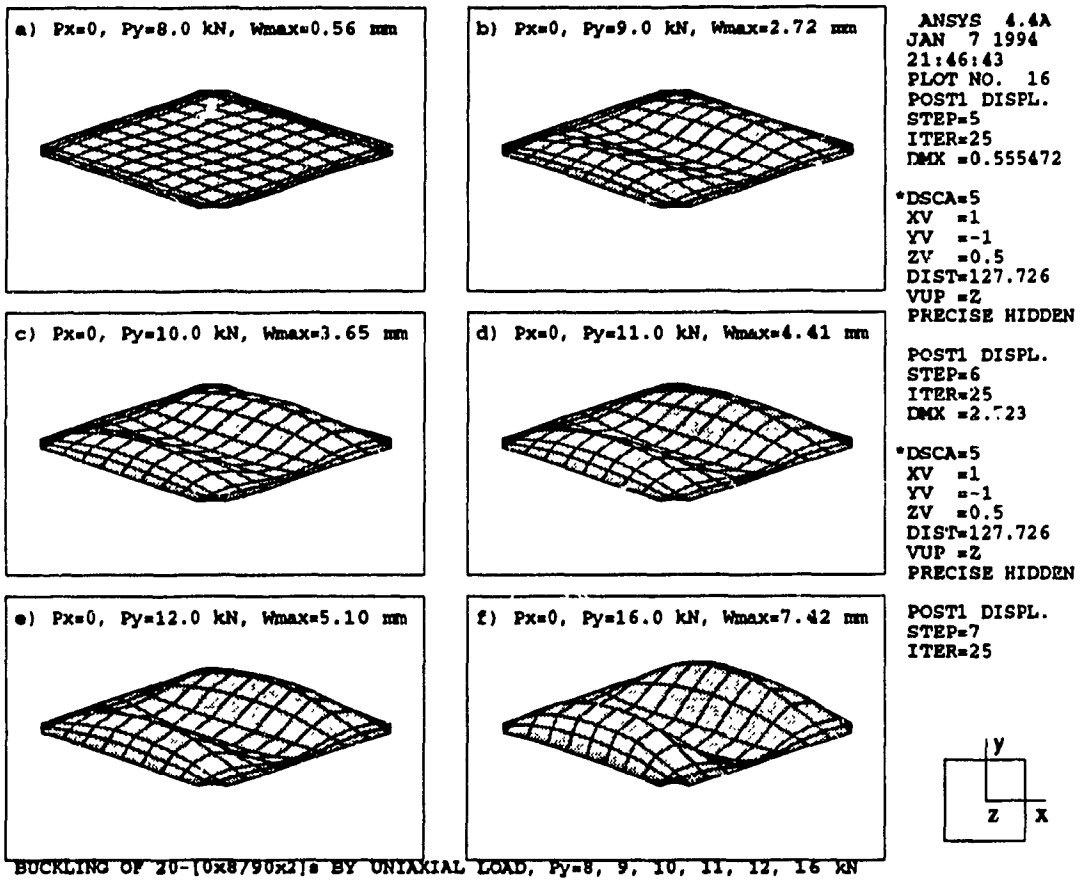

Figure 5.40: Successive views of postbuckling behaviour of the 20-layer orthotropic plate, OP-20-82, with uniaxial loading along y-axis ($P_x : P_y = 0 : 1$).

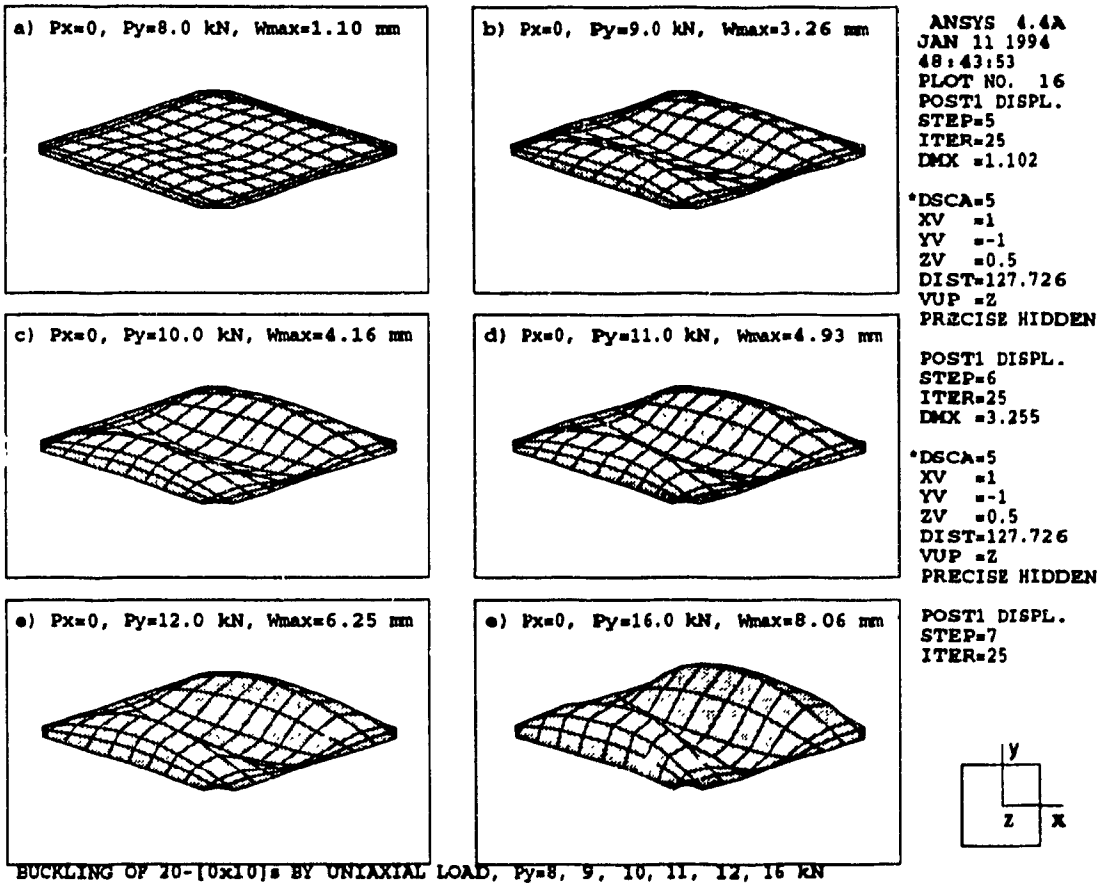

Figure 5.41: Successive views of postbuckling behaviour of the 20-layer orthotropic plate, OP-20-100, with uniaxial loading along y-axis ($P_x : P_y = 0 : 1$).

Biaxial Loading

Figure 5-42 shows an integrated view of all the biaxial loading behaviour of the various 20-layer orthotropic laminates subject to a simultaneously increasing biaxial loading with the boundary conditions of S_r-S_r-S_r-S_r.

OP-20-11 to OP-20-100 specimen series, presented in Table 3-5, were used in this numerical analysis, . From the upper global view and lower detailed view of Figure 5-42, we can find that the values of the critical buckling load do not vary much with to the flexural stiffness ratio, i.e., $P_{cb} = 4.5 \sim 4.4$ kN for $\zeta = 1.3 \sim 14.30$. Also, with the investigations of postbuckling responses, plates having a higher stiffness ratio reveal more weakened postbuckling behaviour than plates with a regular stacking sequence. The tendency of the graphs is almost the same as the case of x-axis uniaxial buckling of 16-layer laminate as shown in Figure 5-2.

By the inspection of the Figures 5-43, 5-44, 5-45 and 5-46, which show successive views of postbuckling deflections for each OP-20-11, OP-20-55, OP-20-82 and OP-20-100 specimen, all specimens reveal a normal and stable 1st mode buckling deflection as the case of x-axis uniaxial loading. Here also we can find that the global stiffness(D_T), the sum of major stiffness(D_{11}) and minor stiffness(D_{22}), governs the critical buckling load as discussed in 16-layer plate.

Also, the surface strain distributions for the biaxial buckling of these five 20-layer plates were obtained and compared to each other. All the strain distributions were well matched with the successive buckling behaviours of Figures 5-43, 5-44, 5-45 and 5-46 (not shown here).

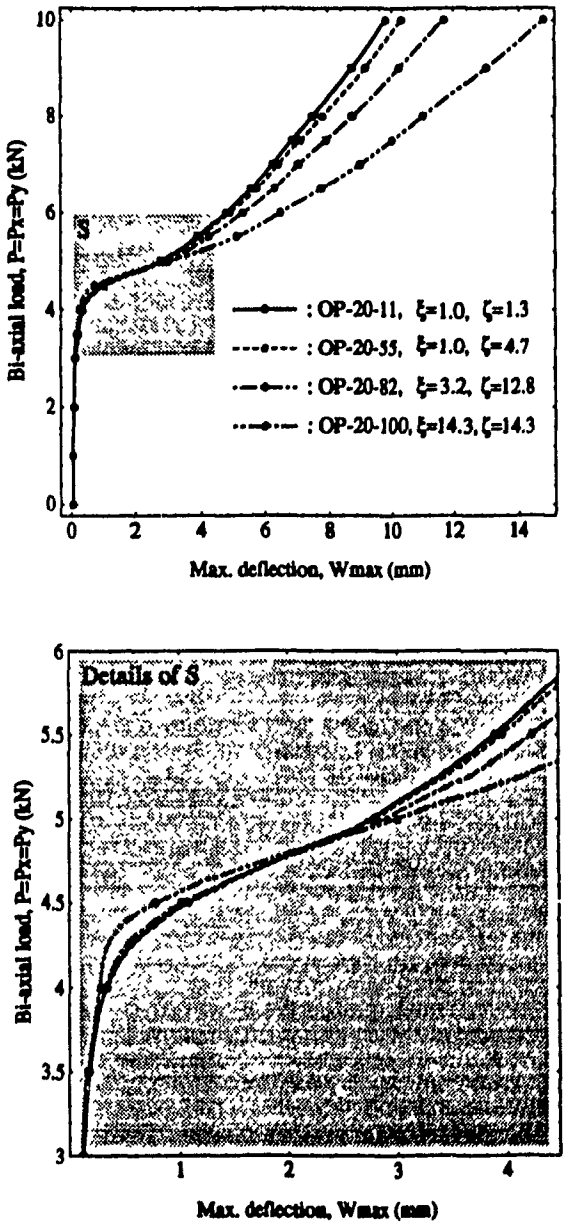

Figure 5.42: Biaxial buckling behaviour of the 20-layer orthotropic plates for various flexural stiffness ratio, $\zeta = 1.3 \sim 14.3$, by N-FEA.

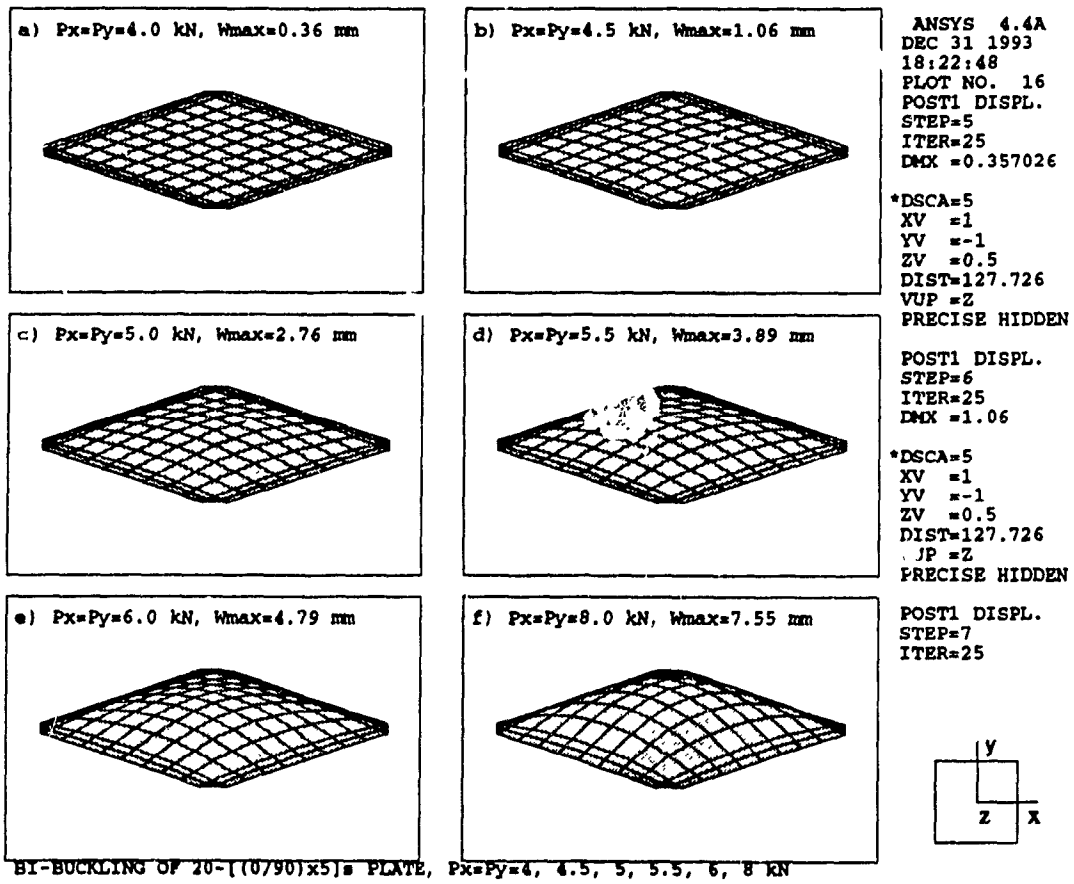

Figure 5.43: Successive views of postbuckling behaviour of the 20-layer orthotropic plate, OP-20-11, with biaxial loadings ($P_x : P_y = 1 : 1$).

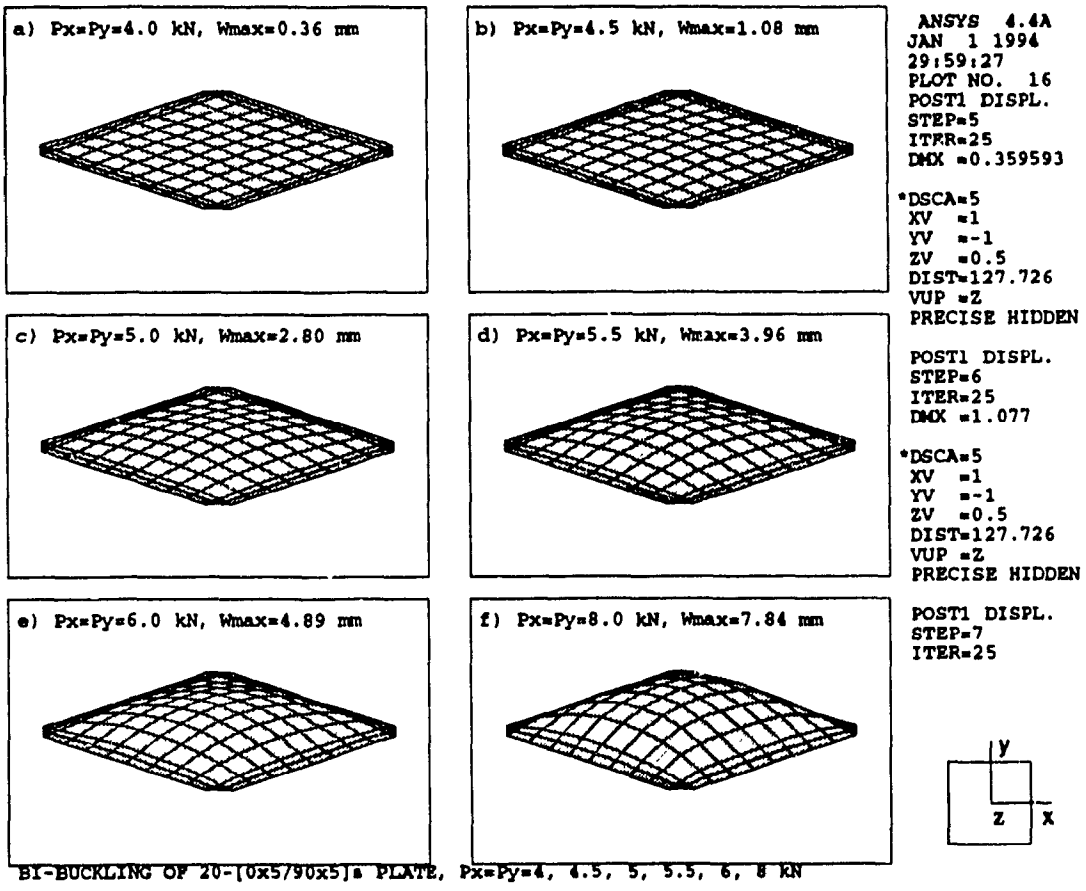

Figure 5.44: Successive views of postbuckling behaviour of the 20-layer orthotropic plate, OP-20-55, with biaxial loadings ($P_x : P_y = 1 : 1$).

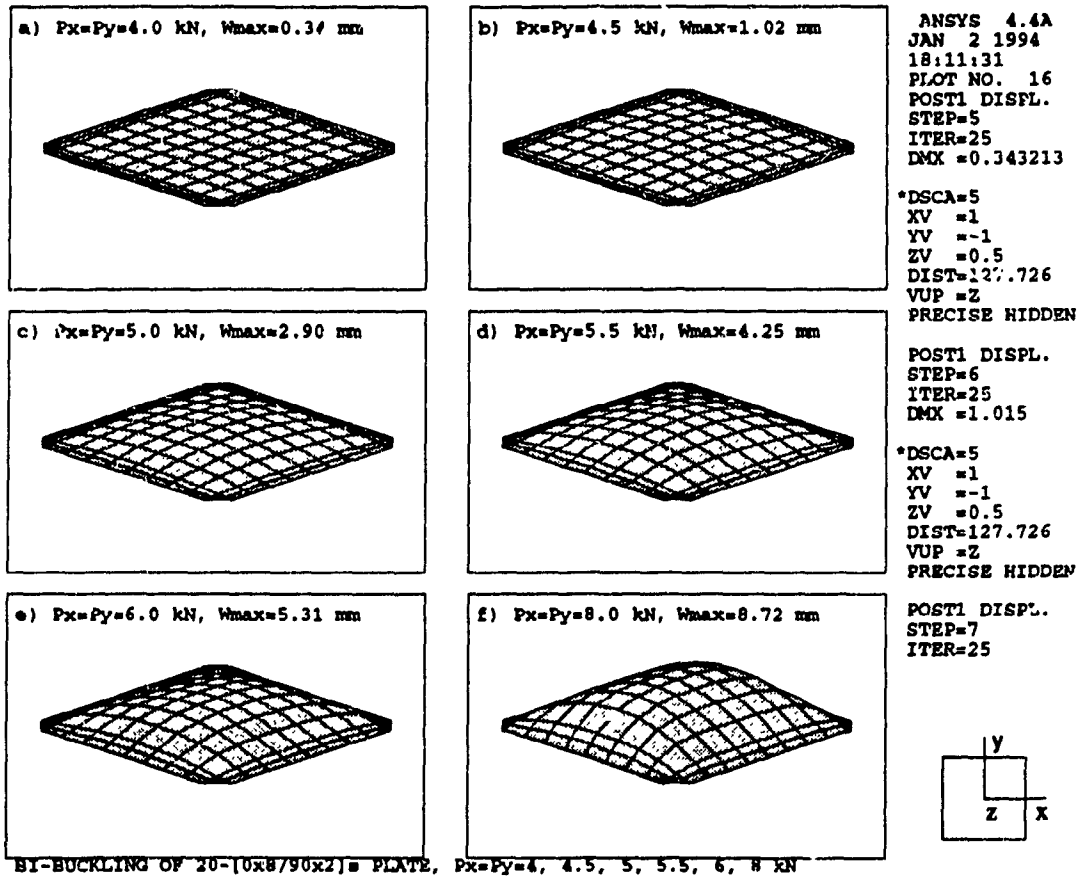

Figure 5.45: Successive views of postbuckling behaviour of the 20-layer orthotropic plate, OP-20-82, with biaxial loadings ($P_x : P_y = 1 : 1$).

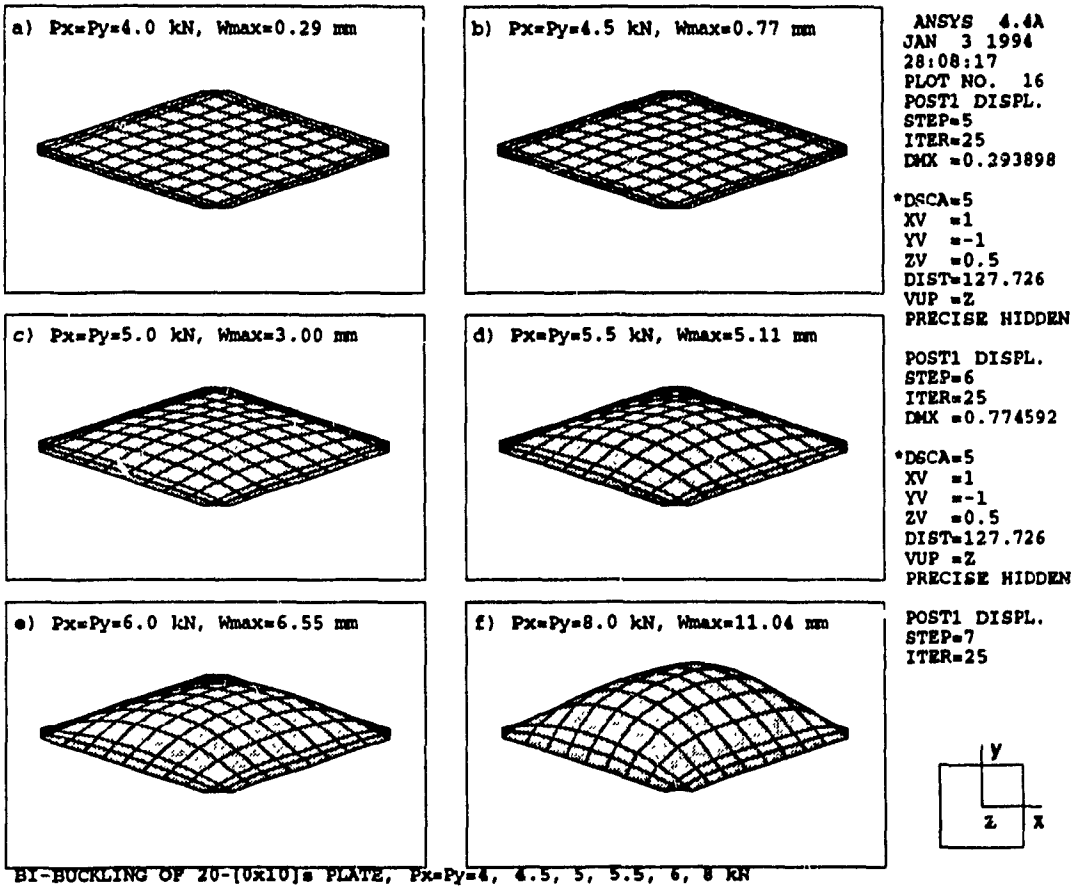

Figure 5.46: Successive views of postbuckling behaviour of the 20-layer orthotropic plate, OP-20-100, with biaxial loadings ($P_x : P_y = 1 : 1$).

5.3 Effect of Layup Angle

The effects of layup angle for the composite plate buckling have been studied by many other researchers such as Leissa [2], Ashton [3], and Whitney [4]. Here, the terminology of layup angle means the angle between the direction of fibers and the direction of loading in orthotropically laminated plates with general off-axis, i.e., generally orthotropic plates as shown in Figure 7-3 and Figure 7-4. Most of the results were limited to the buckling of uniaxially loaded laminates based on the theoretical study with insufficient experimental verifications. Moreover, the layup angle effects on the biaxial buckling of plates have not been validated with experiments. For this reason, N-FEA was executed for 16- and 20-layer composite laminates with the layup angle of $(0/-90)$, $(30/-60)$, $(45/-45)$ and $(60/-30)$.

5.3.1 16-layer Plate Specimen

As the N-FEA results for 16-layer plates, Figure 5-47 shows the load-deflection curves for uniaxial buckling of the four different plates. AP-16-45 specimen with $(45/-45)$ of layup angle demonstrates its critical buckling load to be almost twice the critical load of the AP-16-11 specimen with $(0/-90)$ layup angle. This phenomenon can be understood from the value of coupling terms between bending and twisting, D_{16} and D_{26}. However these terms can be neglected when the number of plies is increased infinitely as mentioned by Leissa [2], Tsai and Hahn [58] [59]. For the validation of the load-deflection behaviour of angle-ply laminates, detailed distributions of x- and y-strain on the surface of plates are plotted such as Figures 5-48 and 5-49 for the specimen of AP-16-45, and also Figures 5-50 and 5-51 for the specimen of AP-16-63.

Also, Figure 5-52 reveals the biaxial buckling behaviour of the four off-axis orthotropic laminates. From the detailed view, the critical buckling load increases according to the change of layup angle from $(0/-90)$ to $(45/-45)$ in the same pattern

as the case of uniaxial loading. In the same manner as the uniaxial loading, strain distributions on the surface of plates are presented in Figures 5-53 and 5-54 for the specimen of AP-16-45, and in Figures 5-55 and 5-56 for the specimen of AP-16-63.

From the figure of strain field for uniaxial loading as shown in Figure 5-48~5-51, the strain distribution of angle-ply laminate is more unstable than that of orthotropic laminate like OP-16-11 or OP-20-11. Especially, for (60/-30) or (30/-60) plate's strain field, shown in Figure 5-50 and 5-51, strains in corner area are more highly concentrated than normal orthotropic plate. Generally, the angle-ply laminates reveal more non-homogeneous strain distribution.

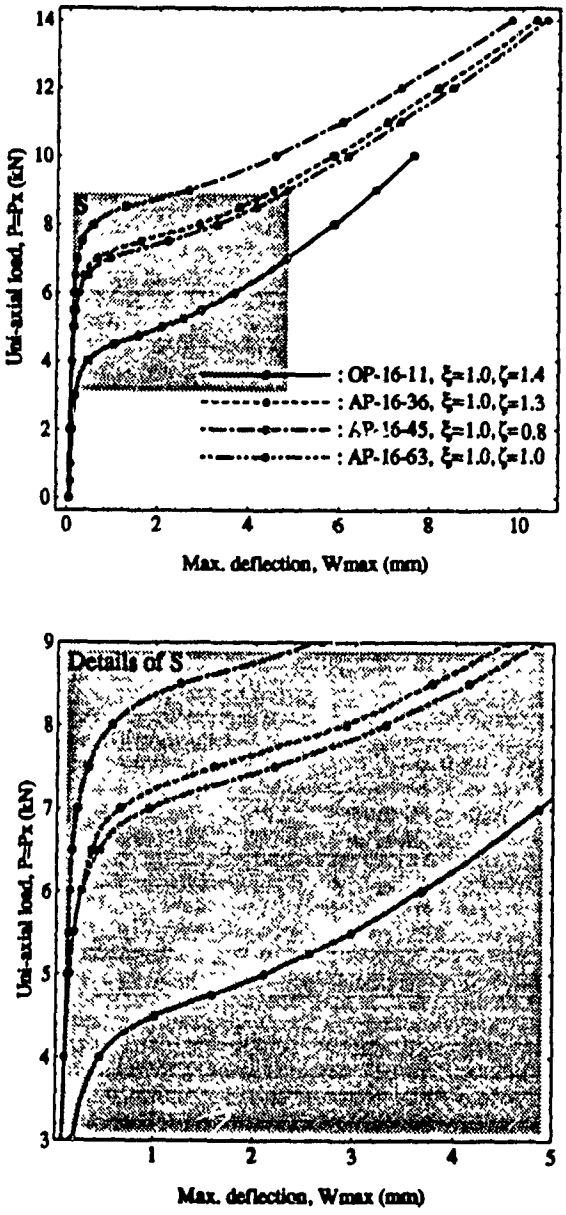

Figure 5.47: Effects of layup angle on the x-loaded buckling ($P_x : P_y = 1 : 0$) of the 16-layup orthotropic laminate with changing layup angle from (0/-90) to (60/-30) by N-FEA.

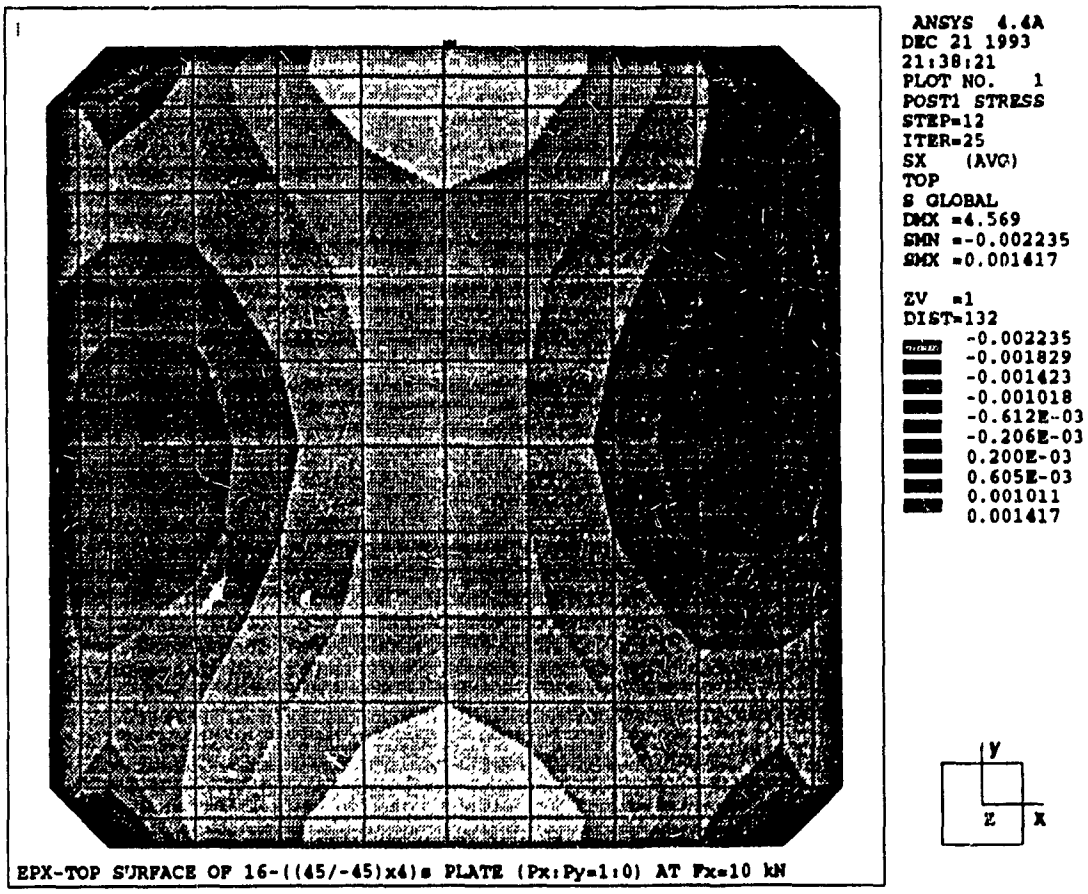

Figure 5.48: X-strain(ϵ_x) distribution of the 16-layer generally orthotropic plate, OP-16-45 with ((45/-45)x4), by x-uniaxial loading of $P_x = 10$kN ($P_x : P_y = 1 : 0$).

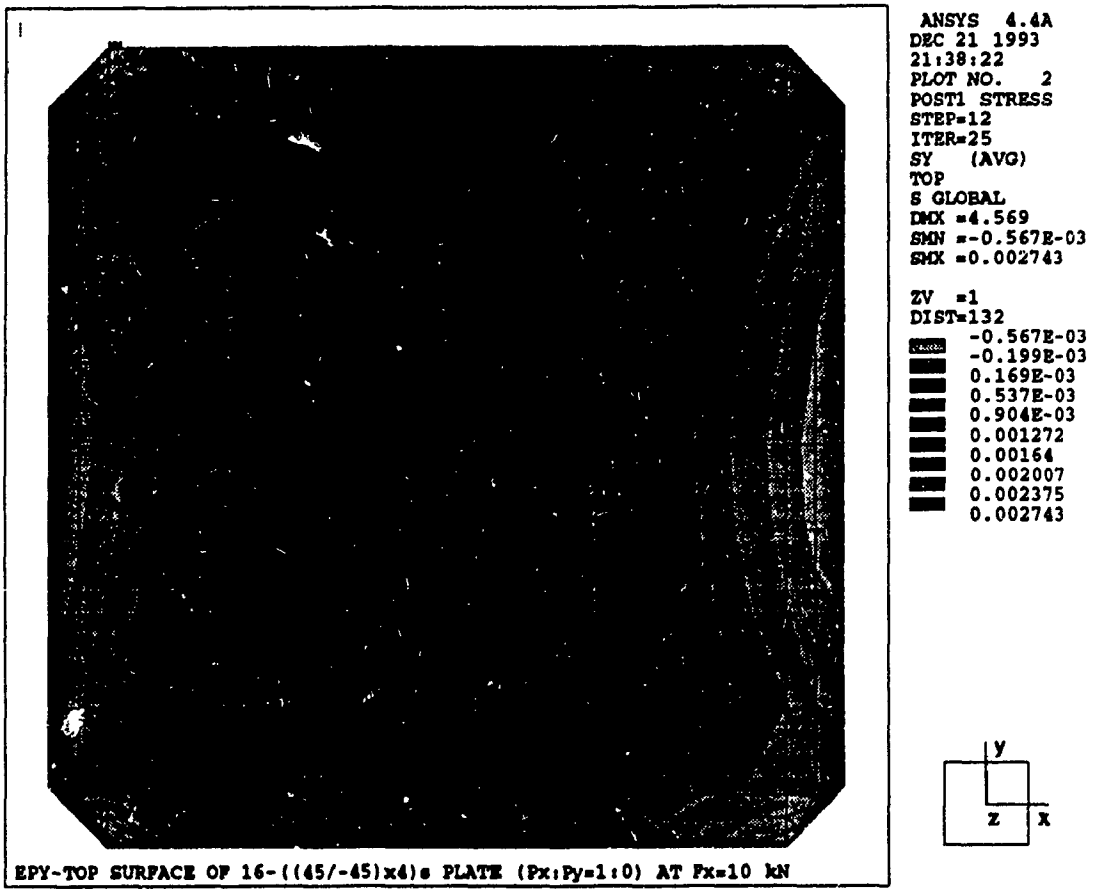

Figure 5.49: Y-strain(ϵ_y) distribution of the 16-layer generally orthotropic plate, OP-16-45 with ((45/-45)x4), by x-uniaxial loading of $P_x = 10$kN ($P_x : P_y = 1 : 0$).

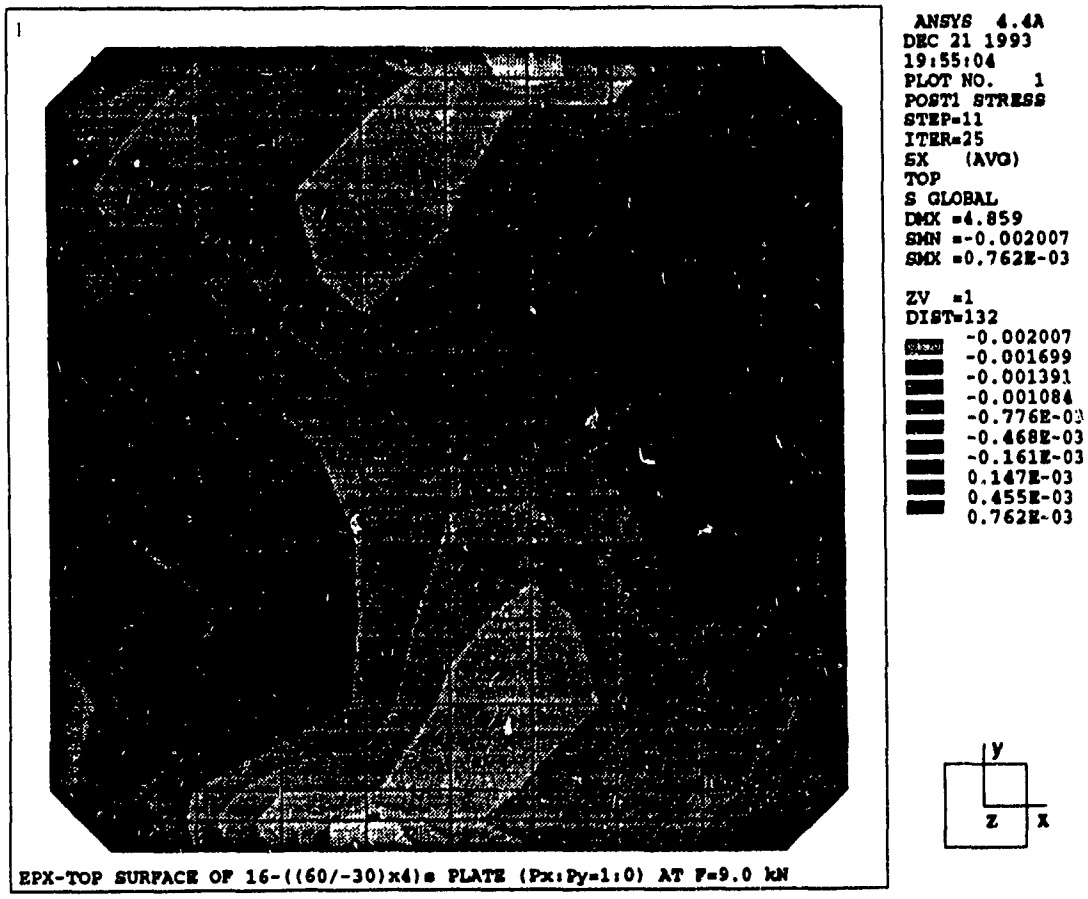

Figure 5.50: X-strain(ϵ_x) distribution of the 16-layer generally orthotropic plate, OP-16-63 with ((60/-30)x4), by x-uniaxial loading of $P_x = 10\text{kN}$ ($P_x : P_y = 1 : 0$).

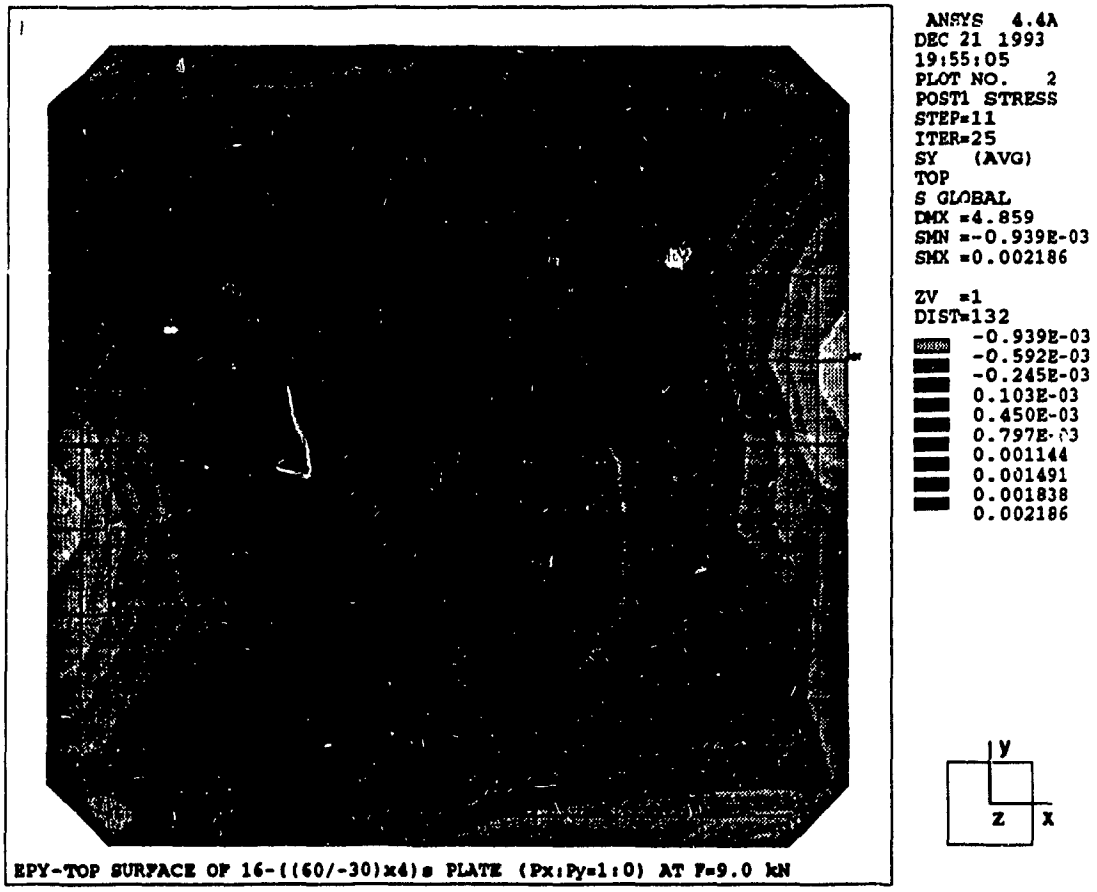

Figure 5.51: Y-strain(ϵ_y) distribution of the 16-layer generally orthotropic plate, OP-16-63 with ((60/-30)x4), by x-uniaxial loading of $P_x = 10\text{kN}$ ($P_x : P_y = 1 : 0$).

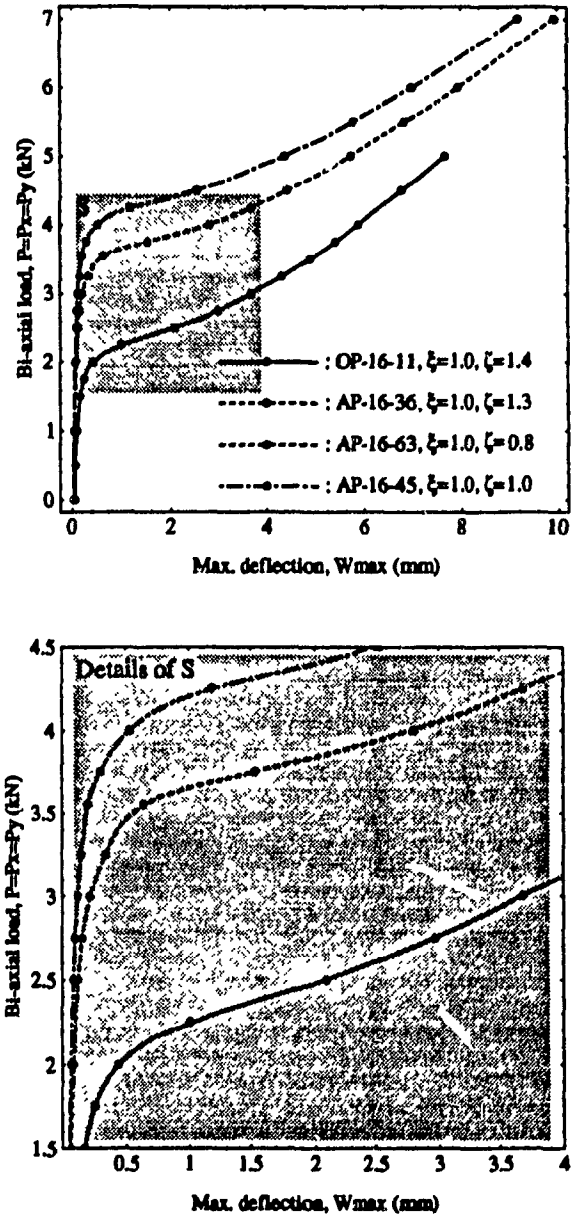

Figure 5.52: Effects of layup angle on the biaxial loading ($P_x : P_y = 1 : 1$) of the 16-layup orthotropic laminate with changing layup angle from (0/-90) to (60/-30) by N-FEA.

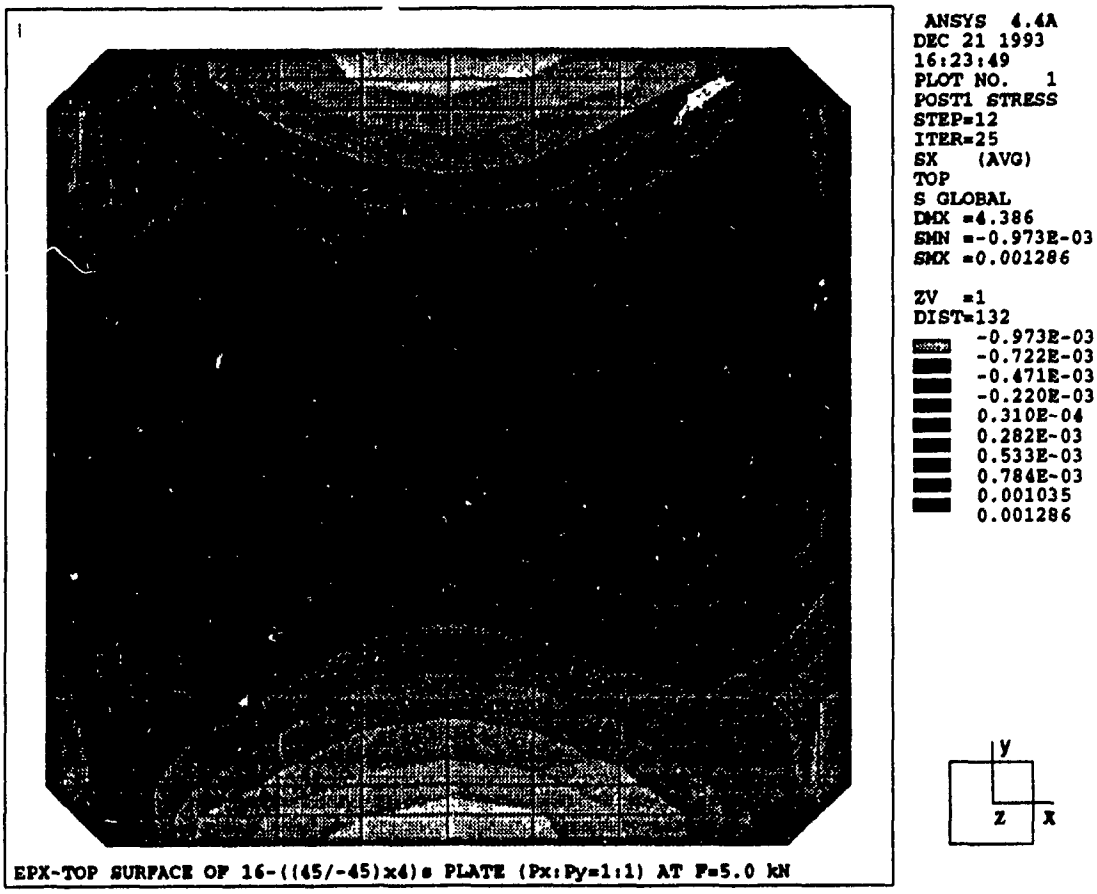

Figure 5.53: X-strain(ϵ_x) distribution of the 16-layer generally orthotropic plate, OP-16-45 with ((45/-45)x4), by biaxial loading of $P_x = P_y = 5$kN ($P_x : P_y = 1 : 1$).

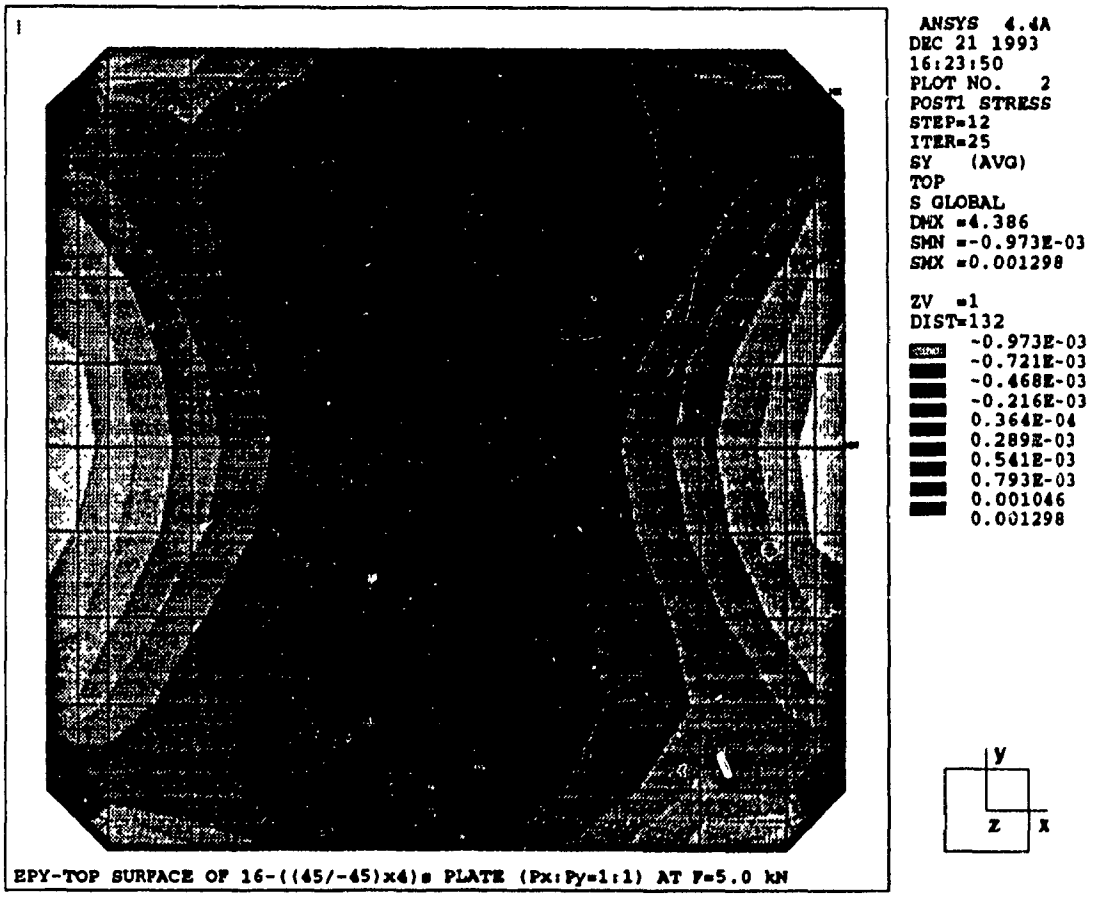

Figure 5.54: Y-strain(ϵ_y) distribution of the 16-layer generally orthotropic plate, OP-16-45 with ((45/-45)x4), by biaxial loading of $P_x = P_y = 5$kN ($P_x : P_y = 1 : 1$).

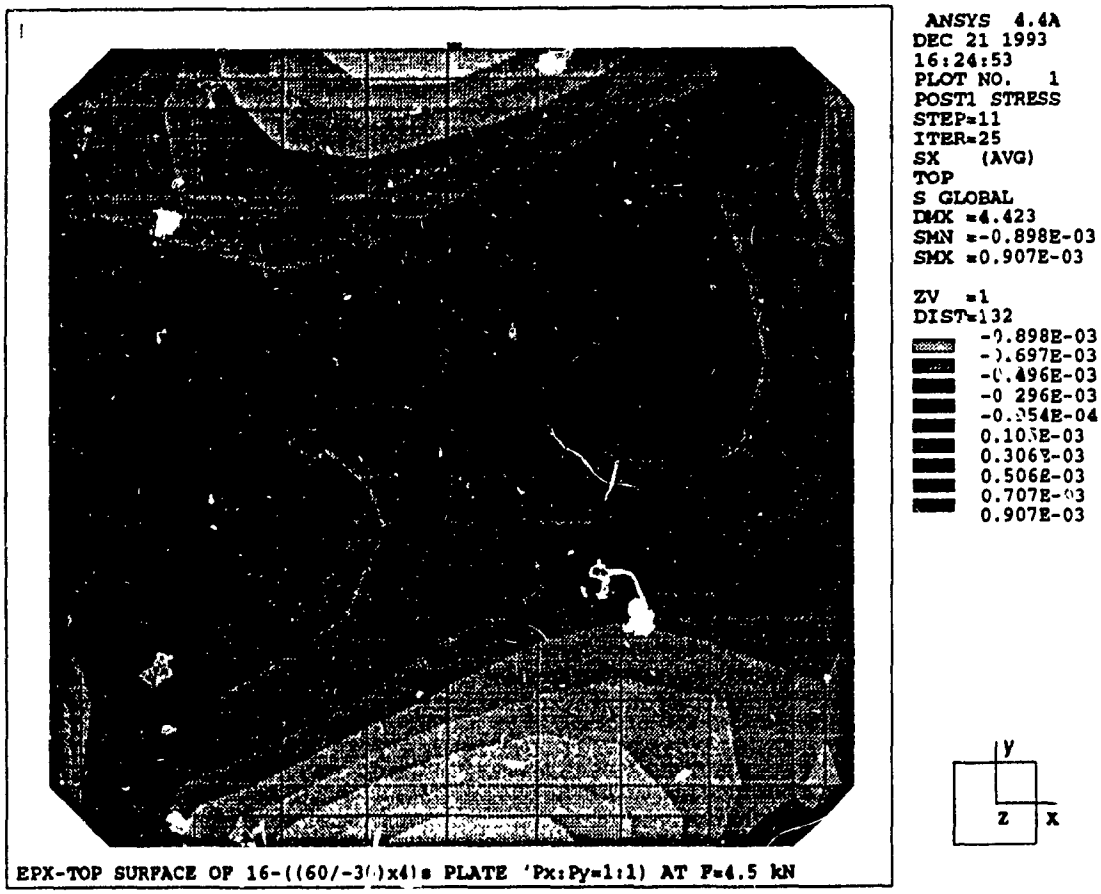

Figure 5.55: X-strain(ϵ_x) distribution of the 16-layer generally orthotropic plate, OP-16-63 with ((60/-30)x4), by biaxial loading of $P_x = P_y = 5$kN ($P_x : P_y = 1 : 1$).

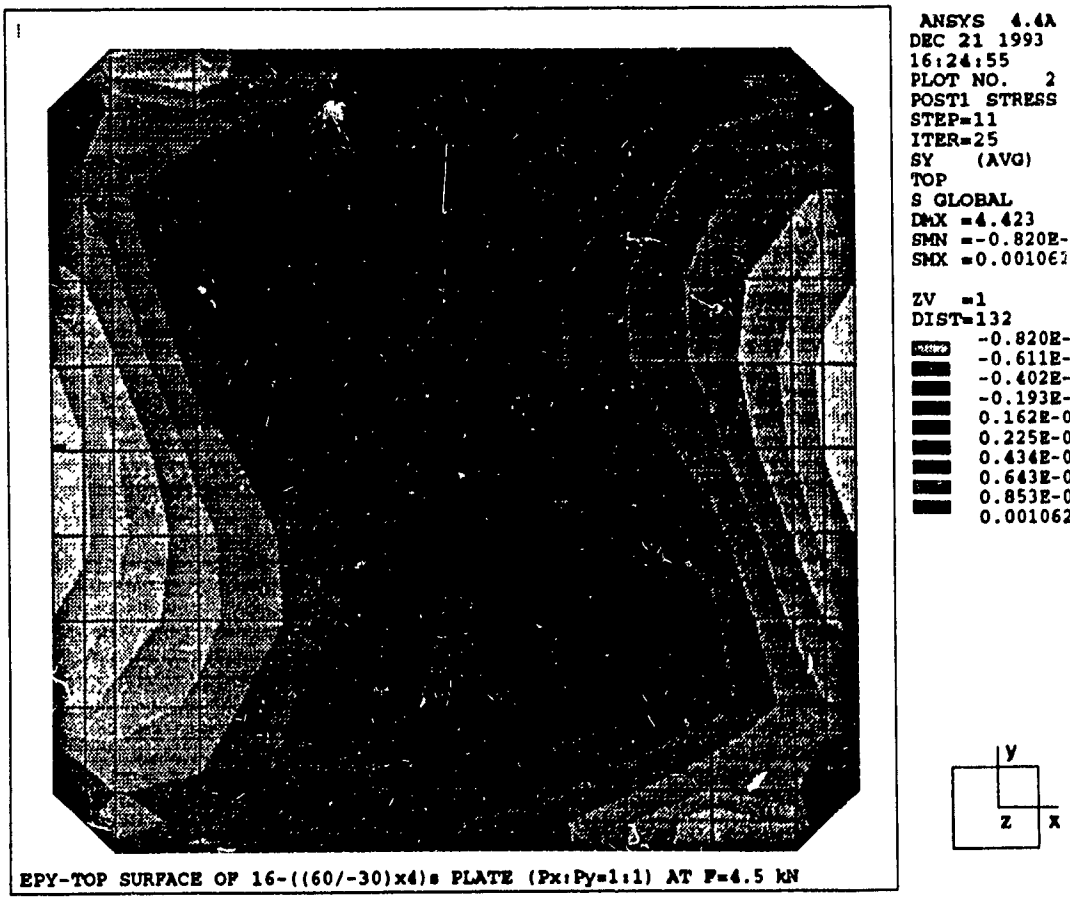

Figure 5.56: Y-strain(ϵ_y) distribution of the 16-layer generally orthotropic plate, OP-16-63 with ((60/-30)x4), by biaxial loading of $P_x = P_y = 5$kN ($P_x : P_y = 1 : 1$).

5.3.2 20-layer Plate Specimen

For the 20-layer plates, all the results of N-FEA are analogous to the case of 16-layer plates. The uniaxial and biaxial loading behaviour of the four plates with different layup angles are integrated in Figures 5-57 and 5-58, where the postbuckling behaviour of specially orthotropic laminates like OP-20-11 plate is more stable than the behaviour of angle-ply laminates like AP-20-36, AP-20-45 and AP-20-63 plate. Here, by the change of lay-up angle, we can expect some enhancement in the value of critical buckling load, up to twice that of the orthotropic laminate, but this is only an analytical point of view. From experiments, the angle-ply laminates do not increase the critical load as much as expected in numerical analysis. The main reason of this phenomenon can be the microscopic relative motion between two plies due to the inter-laminar shear deformation.

Focusing on the global load-deflection curves of Figures 5-57 and 5-58, it is true that the critical buckling load is enhanced according to the increment of layup angle θ, the angle between on-axis and off-axis. However, in the postbuckling behaviour, the plate reaches a higher lateral deflection more quickly with increasing of layup angle, θ.

For the verification of postbuckling deflection, here also the surface strains were obtained and validated in the same manner as 16-layer laminates from N-FEA (not shown here).

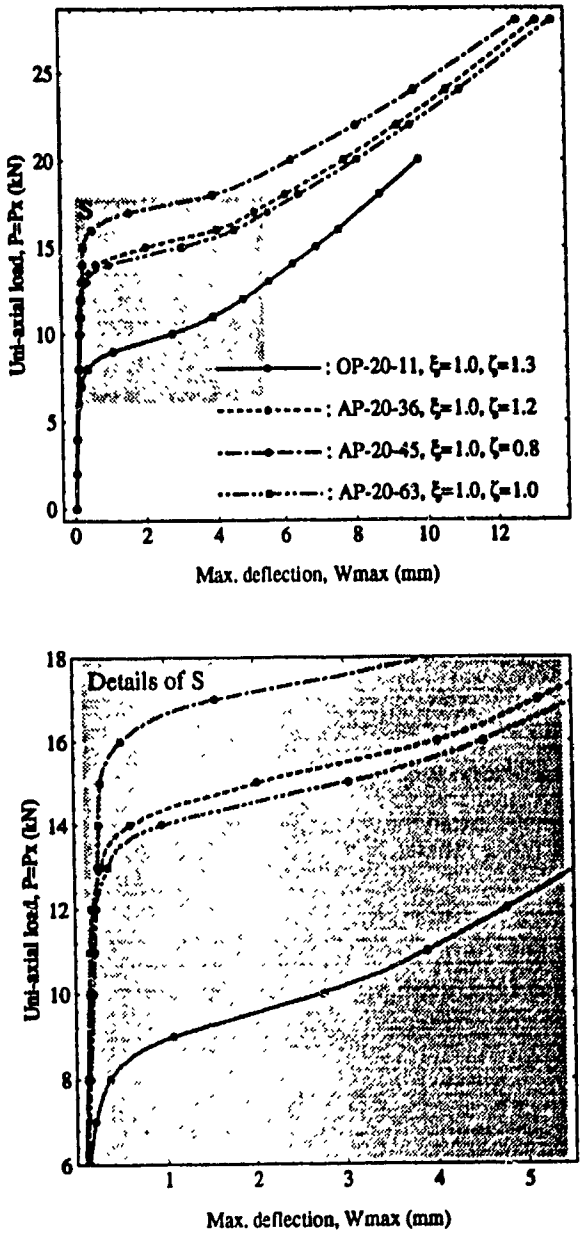

Figure 5.57: Effects of layup angle on the x-loaded buckling ($P_x : P_y = 1 : 0$) of the 20-layup orthotropic laminate with changing layup angle from (0/-90) to (60/-30) by N-FEA.

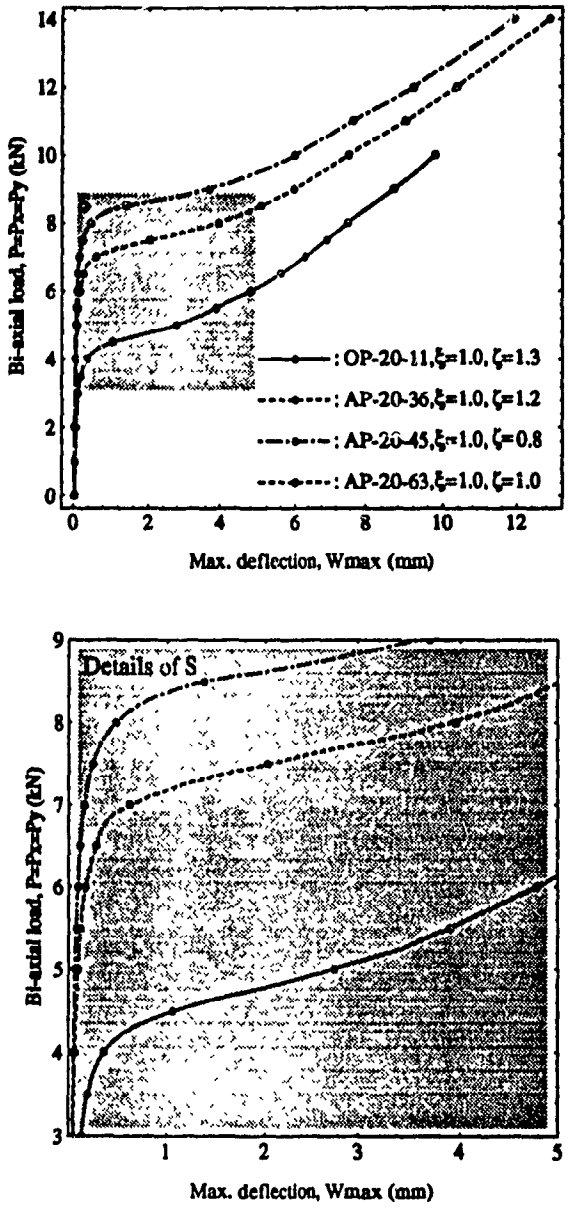

Figure 5.58: **Effects of layup angle to the biaxial loading ($P_x : P_y = 1 : 1$) of the 20-layup orthotropic laminate, with changing layup angle from (0/-90) to (60/-30) by N-FEA.**

Chapter 6

Biaxial Buckling Experiments

6.1 Biaxial Testing Machine

The biaxial testing machine was designed and fabricated in house as shown in Figure 6-1. The machine is comprised of four units, i.e., power unit, control unit, testing unit and recording unit. The power unit, the hydraulic pump having the maximum power of 7.5 GPM(Gallon Per Minute) with 3000 psi, was installed at a remote place from the testing unit to prevent vibration and noise. The control unit was designed employing the proportional position controlling system in order to control the displacements of the four loading grips independently or simultaneously. The input sources of the proportional position controlling system are generated by the DC voltage from four LVDTs (Linear Variable Differential Transducer). This was used to control the displacement of the four cylinders in each direction manually. To acquire uniform compressive displacements of the four loading grips simultaneously, a DC power generator was applied to generate the optimal voltage as the required input source of the controlling system.

The testing unit consists of supporting grips, load cells, guide blocks, hydraulic cylinders which were mounted on the each corner of the main frame. Four load cells

with the maximum capacity of 100 kN were installed between each supporting grip and cylinder to measure the acting load in each direction. The in-plane compressive displacemen's were monitored by the four LVDTs and the transverse deflection on the centre of the plate was measured by a potentiometer. To secure complete contact between the specimen and the four loading grips, a small amount of preloading was prescribed and then the strain values at the four edges were compared. These strain values were used as a guide to ensure uniform contact between the grips and the plate edges .

A recording unit consisting of a digital signal processor, Helios (40-channel data acquisition system from Fluke Inc.), and a PC with on-line data plotting software, Labtech Notebook, was used. All data of the axial loads, in-plane displacements and transverse deflections were plotted on the PC window at a frequency of 12 readings/sec. Also, all strain values were stored into the PC and plotted by MATHEMATICA software in NextStation workstation.

6.2 Visualization by Shadow Moiré

Shadow Moiré technique was employed to visualize the buckling deflections of the plate specimen. This apparatus comprises a collimated light source, a fine-meshed master grating and a white-painted plate to generate topographical shadow fringes on the plate surface as shown in Figure 6-2.

Among various types of Moiré methods, shadow Moiré technique is based on the principle of optical interference between two sets of superimposed parallel lines. This interference produces white and dark bands of Moiré fringes. Master grating was fabricated by the author with the alignment of fine black string. The grating was aligned to have parallel and equal spacing, 0.35 mm spacing and 0.35 mm thickness(14

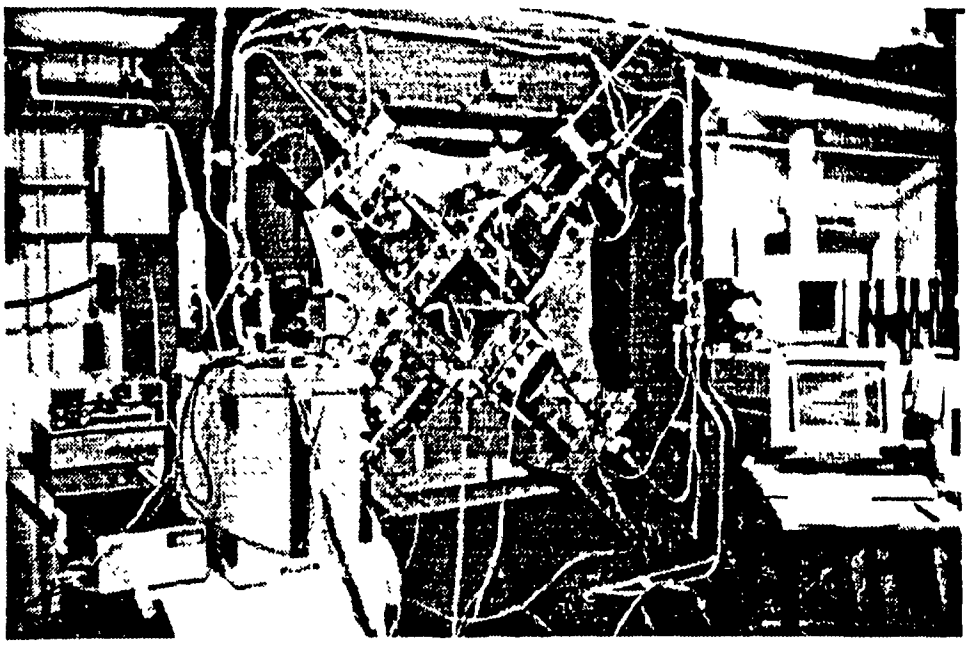

Figure 6.1: The experimental setup for biaxial buckling test.

lines/cm), by using two screw bars fixed on wooden frame. If the grating is illuminated by the collimated light source with an angle ϕ, shadows of grating lines were cast upon the object as shown in Figure 6-2 a). When viewing the undeformed object through the grating, the object does not produce Moiré fringes because of no interference of light. However, for the deformed plate, topographical shadow fringes appear due to the interference between grating and shifted shadows as shown in Figure 6-2 b).

The main purpose of Shadow Moiré visualization work was to obtain the real deflection map of the plate in postbuckling state. Even though the buckling initiation point was detected by measuring the centre deflection of plate specimen with potentiometer, the real shape of buckling deformation can not be figured out by the naked eye. So far, in most analytical approach, the buckling shape has been assumed as a biharmonic function no matter what type of anisotropicity was prescribed by the stacking sequence as discussed in Chapter 2.

Of course, bi-harmonic functions do not exactly comply with the real buckling shape of orthotropic or anisotropic plate because of the twisting and rotation coupling and the effects of varied stiffness ratios ζ and ξ. Those approximations contribute to the error produced between theory and experiment in the values of the critical buckling load and postbuckling behaviour . However, through comparison between the Shadow Moiré topography of the real plate and the theoretical deflection function, the difference my be found and a better theoretical deflection function can be found.

Observation normal to the grating is preferred to avoid experimental error and to have simplified calculations. The observed fringe pattern has a relationship with the topological map of the object's surface because each fringe represents a pitch of displacement from the grating. When the illumination angle is normal to the grating, the relation between each Moiré fringe and the transverse displacement, w, can be presented as follow.

$$w = \frac{s}{\tan \phi} \tag{6.1}$$

where, s represents the pitch of the grating and ϕ is the illumination angle.

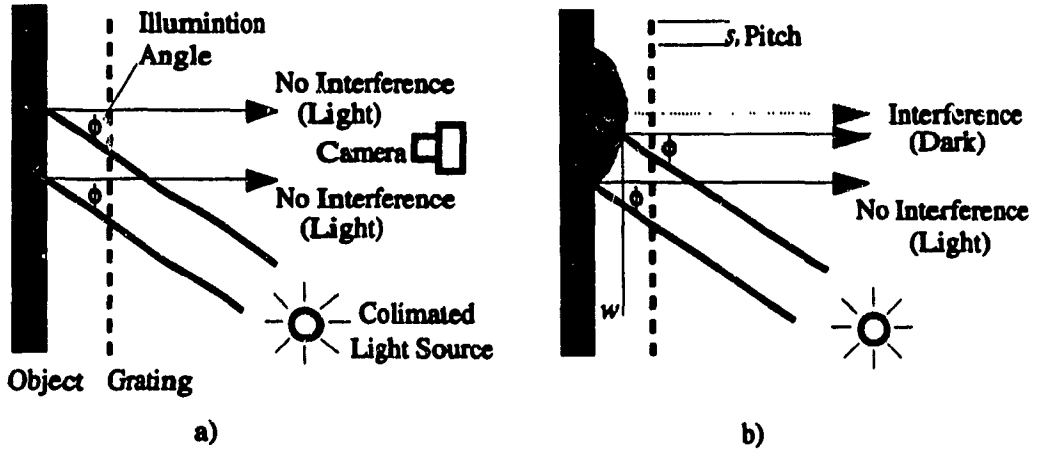

Figure 6.2: A sketch on the mechanism of Shadow Moiré visualization method.

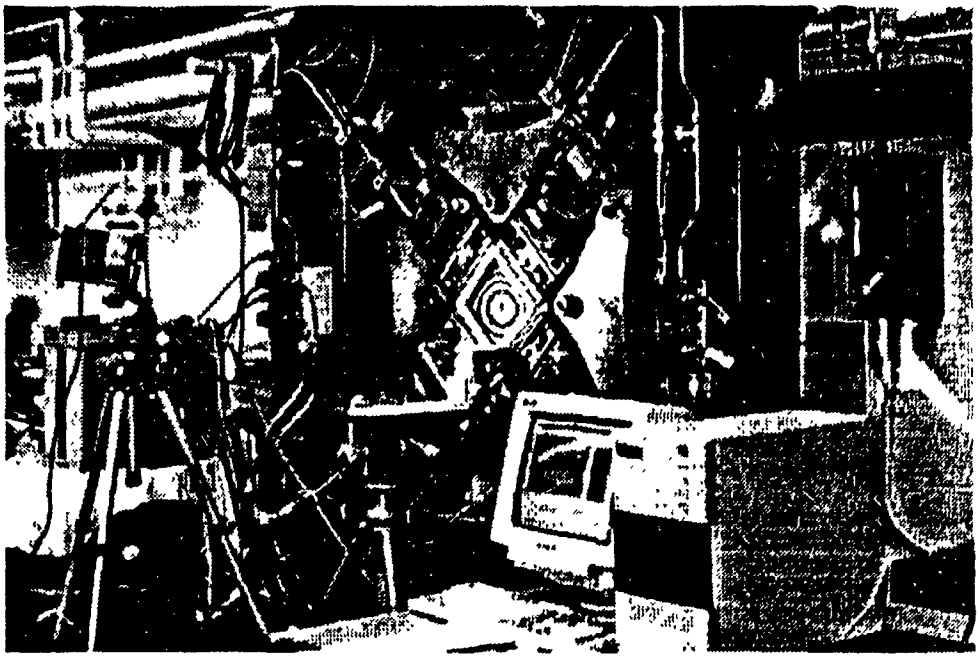

Figure 6.3: The arrangement of Shadow Moiré apparatus used in experiments.

6.3 Buckling Experiments

Generally plate structures are complicated to experiment with, especially in buckling experiments, because it is diffcult for the plate structure to fulfill the given supporting conditions and loading conditions during the experiments. Through the author's experiments for the $240mm$x$240mm$ square plates, normally the specimen experiences its buckling deformation - from starting the inplane compression up to the induced lateral deflection - within 0.05~0.1 mm of end-shortening. Another sensitive problem is stabilizing the fluctuating biaxial loads caused by the correlated deformation along the x and y axes, especially in the case of the plate having high stiffness ratios. Because of these limitations, talent and high signal processing speed are required to controlling the displacement of the loading grips and in monitoring the axial loading, lateral deflection and strain distribution.

All plate specimens were fabricated in house using the same process as mentioned in Chapter 3. Each plate's edge was machined to make a sharpened supporting edge as shown in Figure 4-2 b) i)* of Chapter 4. On the other hand, to check the plate alignment before loading, strains were monitored from several strain gauges attached on the centre and edge areas as shown in Figure 3-14 of Chapter 3. For each specimen, the postbuckled shape was exposed by Shadow Moiré picture and the Moiré fringe was compared with successive views of postbuckling deflection as shown in Figures 5-23~5-25 and also with the strain distributions from N-FEA of Chapter 5.

6.3.1 Uniaxial Loading Experiments

Orthotropic Laminates

Figure 6-4 and Figure 6-5 represent typical view of experimental load-deflection behaviour in the buckling of OP-16-11 plate series for x-axis and y-axis uniaxial loading. From the two figures, the two critical buckling loads are almost the same regardless

of the loading axis and also the two postbuckling behaviours are of the same pattern with a weakened stiffness response compared to the expected values by N-FEA. In this regularly laid-up laminate having a lower stiffness ratio, $\zeta = 1.4$, it is hard to find the buckling point clearly. For this problem, more considerations will be made in the following section.

The uniaxial loading behaviour of OP-16-44 specimens is shown in Figure 6-6 and Figure 6-7, where it is clear that the buckling behaviour under x-axis loading shows higher load response than the buckling with y-axis loading. By Comparing the load-deflection behaviours of OP-16-11 specimens with $\zeta = 1.4$ and OP-16-44 specimens $\zeta = 4.7$, the two load-deflection behaviours along x- and y-axis exhibit different behaviours, i.e., there is almost the same load-deflection curves in x- and y-axis uniaxial loading case for OP-16-11 specimens but there is a clear difference in load-deflection curves for x-axis and y-axis uniaxial loadings. This tendency was not expected from N-FEA but, in experiments, the stiffness ratio effect does exist, i.e., major flexural stiffness(D_{11}) and minor flexural stiffness(D_{22}) have an effect on the buckling response for the direction of loading.

On the other hand, as one of the most irregular layup sequences with $\zeta = 13.9$, OP-16-71 plate series were tested and their buckling behaviours were presented in Figure 6-8 and 6-9. From the two figures, it is clear that the required energy to cause buckling along the strong axis is much higher than along the weaker axis. The critical buckling load with y-axis uniaxial loading(P_{cy}) is less than a half of the critical load with x-axis uniaxial loading(P_{cx}). Also, the experimental P_{cy} value is much less than the critical buckling load resulted from N-FEA and theory. Moreover, buckling mode jumping was found from these experiments and it was also predicted by N-FEA as shown in previous Chapter.

Anisotropic Laminates

In Figures 6-10 and 6-11, the uniaxial buckling responses of angle-ply laminate with AP-16-45 specimens are presented, where the two critical buckling loads, P_{cx} and P_{cy}, are both much lower than that of N-FEA results. In author's point of view, this can be explained from the coupling shear stiffness terms,D_{16} and D_{26}, which attribute to the shear deformation through plate thickness. Normally these terms are small compared to the other stiffness terms and more over they disappear in orthotropic laminates. Also, physically these terms resist the shear rotation in thickness direction. However, these terms are overestimated in N-FEA(because the FEM element model does not allow the inter-laminar slip).

Postbuckling behaviours of other angle-ply laminate AP-16-63 specimens are depicted in Figures 6-12 and 6-13, where the values of critical buckling load from experiments are more than half of the values obtained by N-FEA. These experimental values are much higher than in the case of AP-16-45 plates. From numerical analysis, OP-16-63 plates should provide lower critical buckling load but experiments give a reversed result. This may also be explained by the shear stiffness terms of D_{16} and D_{26}.

Investigating Figures 6-4$\sim$6-13, we can find that the load-deflection data obtained from N-FEA and experiments reveal some differences. These discrepancies can be explained as followings:

In the finite element method formulation, the loading condition is always assumed to be of uniform pressure. However, in the experiments, the loading condition may not be exactly uniform pressure. This loading condition is also a function of the magnitude of the loads

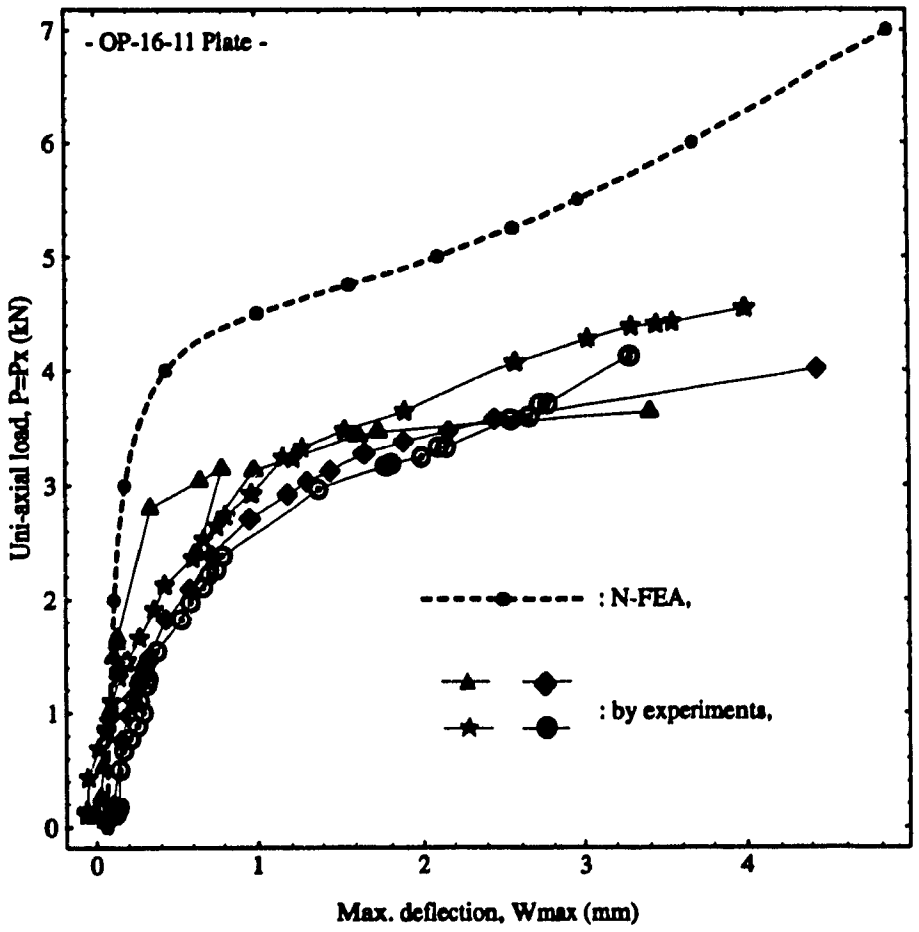

Figure 6.4: Comparison of load-deflection response between experimental and N-FEA results of OP-16-11 plate with uniaxial loading along x-axis ($P_x : P_y = 1 : 0$).

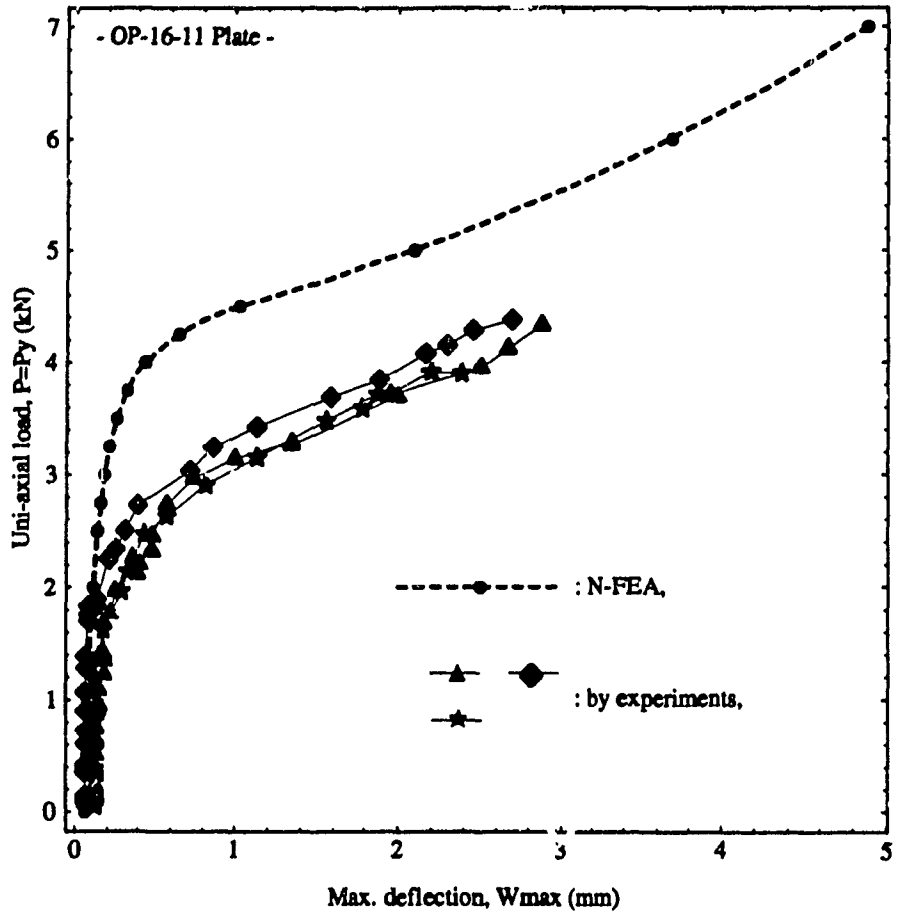

Figure 6.5: Comparison of load-deflection response between experimental and N-FEA results of OP-16-11 plate with uniaxial loading along y-axis ($P_x : P_y = 0 : 1$).

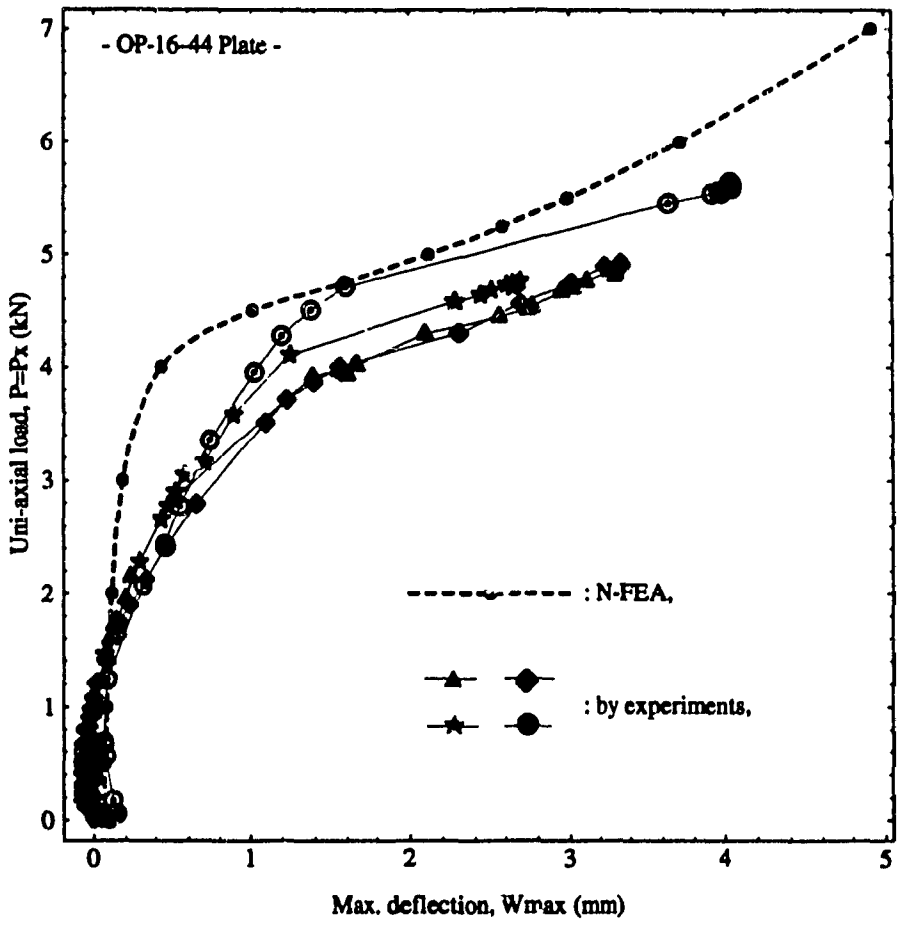

Figure 6.6: Comparison of load-deflection response between experimental and N-FEA results of OP-16-44 plate with uniaxial loading along x-axis ($P_x : P_y = 1 : 0$).

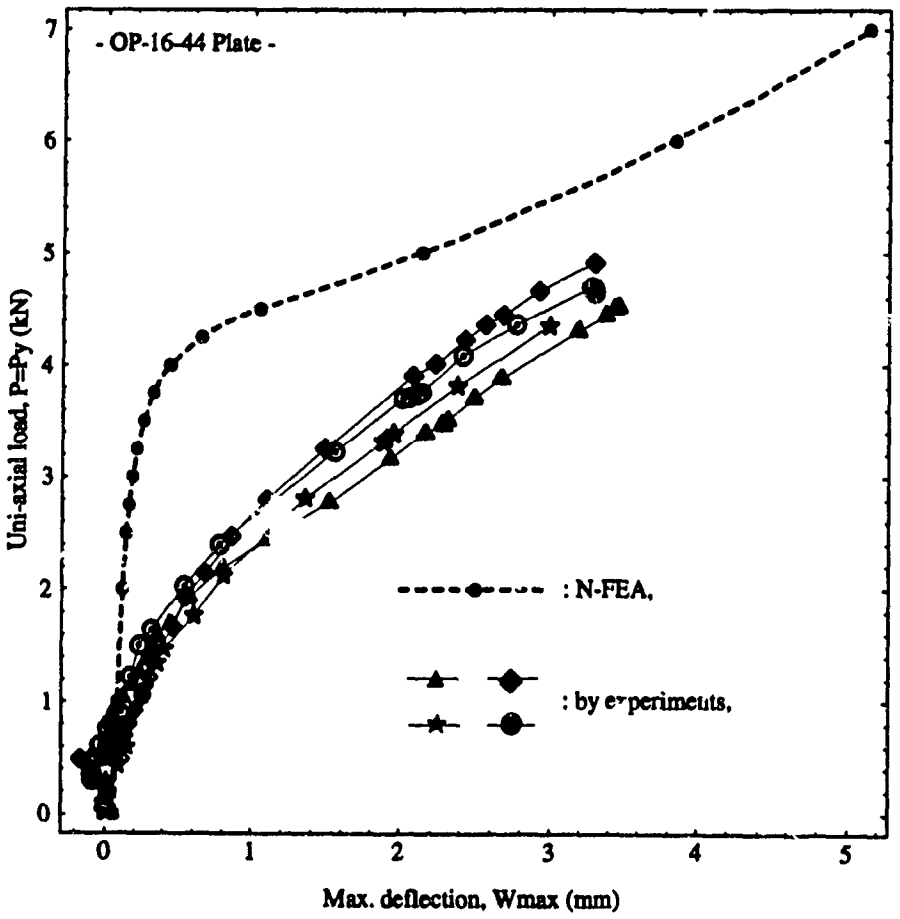

Figure 6.7: Comparison of load-deflection response between experimental and N-FEA results of OP-16-44 plate with uniaxial loading along y-axis ($P_x : P_y = 0 : 1$).

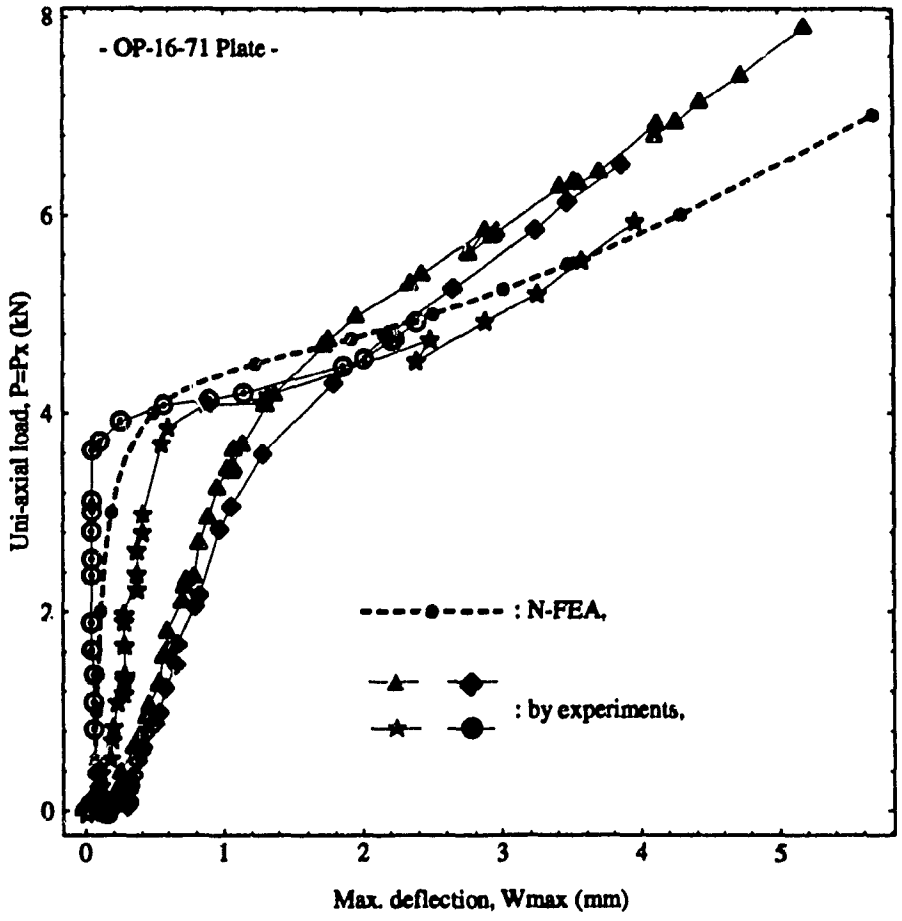

Figure 6.8: Comparison of load-deflection response between experimental and N-FEA results of OP-16-71 plate with uniaxial loading along x-axis ($P_x : P_y = 1 : 0$).

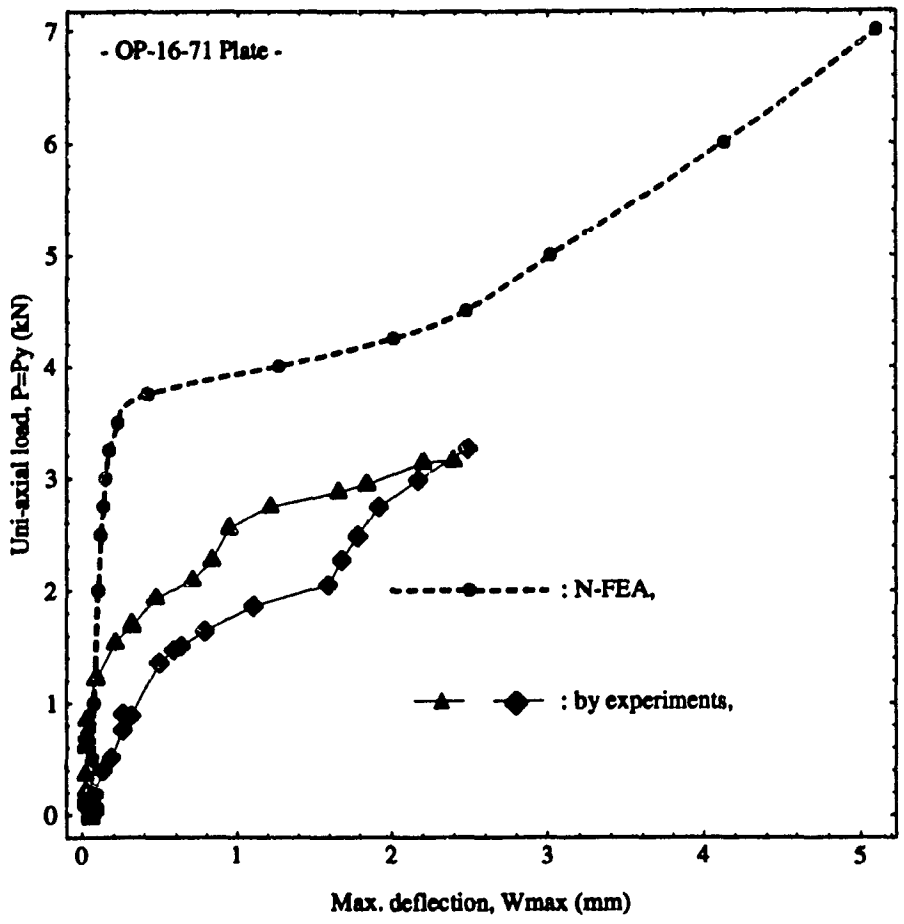

Figure 6.9: Comparison of load-deflection response between experimental and N-FEA results of OP-16-71 plate with uniaxial loading along y-axis ($P_x : P_y = 0 : 1$).

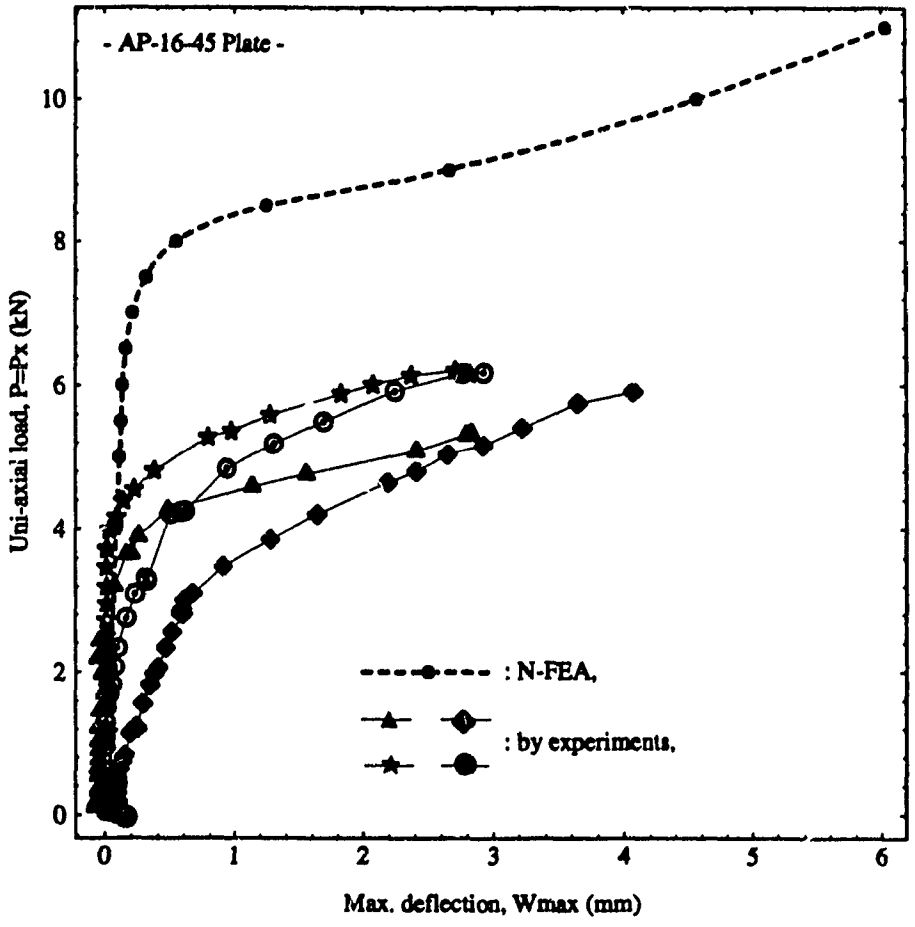

Figure 6.10: Comparison of load-deflection response between experimental and N-FEA results of AP-16-45 plate with uniaxial loading along x-axis ($P_x : P_y = 1 : 0$).

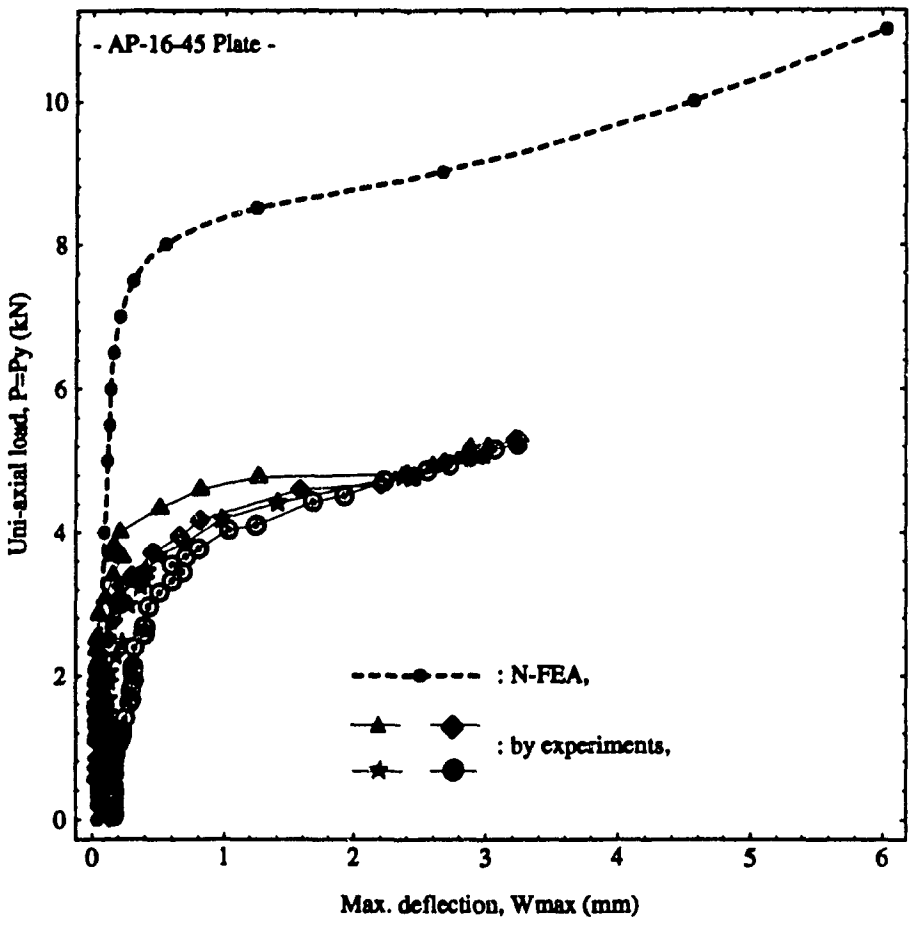

Figure 6.11: Comparison of load-deflection response between experimental and N-FEA results of AP-16-45 plate with uniaxial loading along y-axis ($P_x : P_y = 0 : 1$).

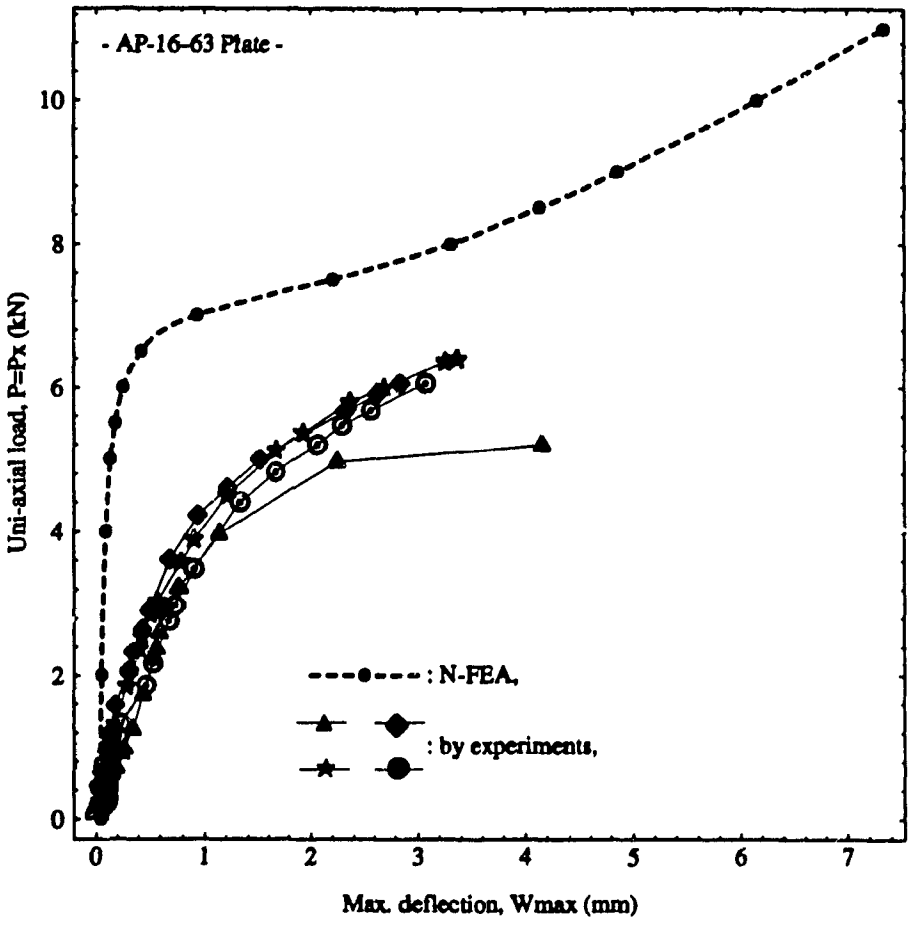

Figure 6.12: Comparison of load-deflection response between experimental and N-FEA results of AP-16-63 plate with uniaxial loading along x-axis ($P_x : P_y = 1 : 0$).

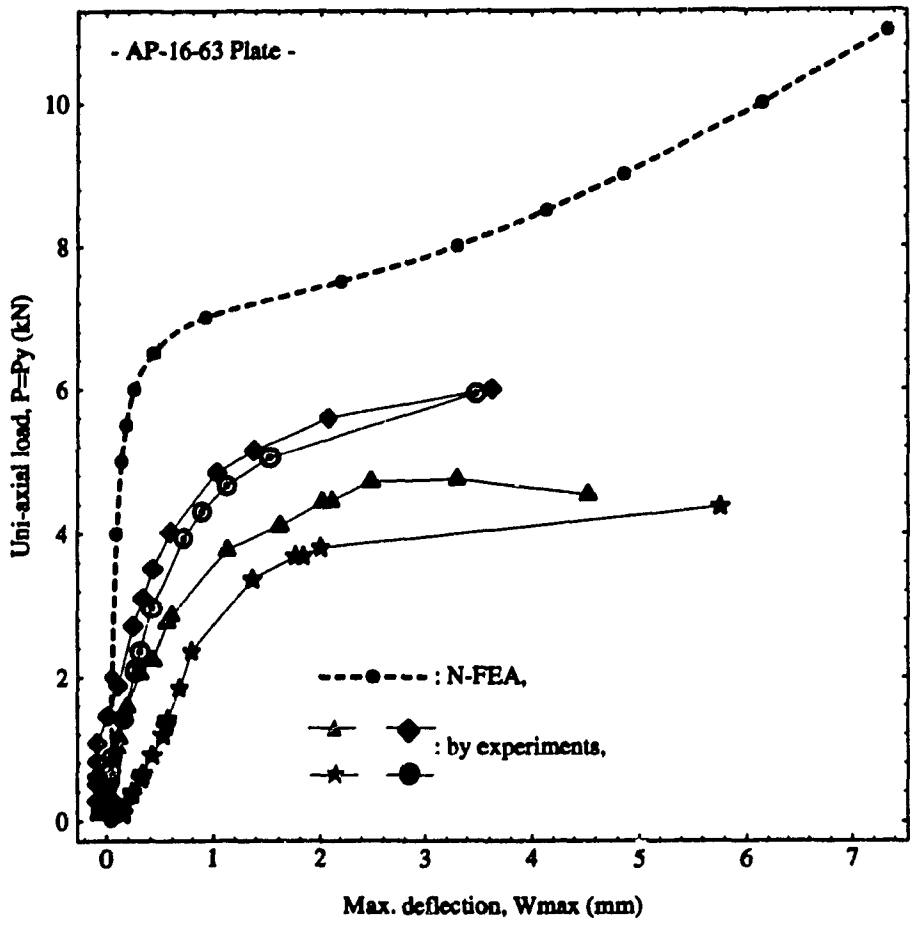

Figure 6.13: Comparison of load-deflection response between experimental and N-FEA results of AP-16-63 plate with uniaxial loading along y-axis ($P_x : P_y = 0 : 1$).

6.3.2 Biaxial Loading Experiments

Orthotropic Laminates

Figures 6-14~6-16 plotted the experimental biaxial loading behaviours of orthotropic laminates. The experimental specimens were chosen to be OP-16-11, OP-16-44 and OP-16-71 plates. In Figure 6-14 and 6-15, all experimental load-deflection curves of OP-16-11 and OP-16-44 plates are well matched with N-FEA solutions. Three different series of specimens demonstrate their responses from weakened to stiffened according to the stiffness ratio from $\zeta = 1.4$ to $\zeta = 13.9$.

However, OP-16-71 plates shown in Figure 6-16 demonstrate quite a different buckling behaviour than predicted by N-FEA. This discrepancy comes from the difficulties of increasing biaxial loads simultaneously and also difficulty of keeping the given loading because of the dynamic reaction of the specimen, especially in the case of the plate having a high stiffness ratio like OP-16-71 plates.

Apparently, from these experimental results, slopes of load-deflection curves do not differ much from numerical results. Therfore, except for severely anisotropic specimens like OP-16-71 plate, these experimental biaxial buckling results are acceptable.

Anisotropic Laminates

In Figures 6-17 and 6-18, buckling responses for biaxial loading of two series of angle-ply laminates, AP-16-45 and AP-16-63, are presented, The experimental critical load of AP-16-45 plates are higher than that of AP-16-63 plates. This result is somewhat different from the uniaxial loading experiments in previous section. In uniaxial loading, OP-16-63 and OP-16-45 plates revealed almost same value but, in biaxial loading case for OP-16-45 plates, the experimental values always exceed the N-FEA results. For biaxial loading on OP-16-63 plates, experimental values sometime exceed N-FEA results.

This phenomenon can also be explained using the coupling shear stiffness terms, D_{16}, D_{26}. In this biaxial loading case, the plate motion is highly restrained due to the fully supported grips. For this reason, the coupling shear stiffness fully contributes to the global buckling stiffness. Therefore the plate requires more energy to be buckled. However, OP-16-63 plates may undergo some shear deformation due to the anisotropic effect from (30/-60) or (60/-30) layups. Thus, they may lose their global stiffness some extent as compared to OP-16-45 plates.

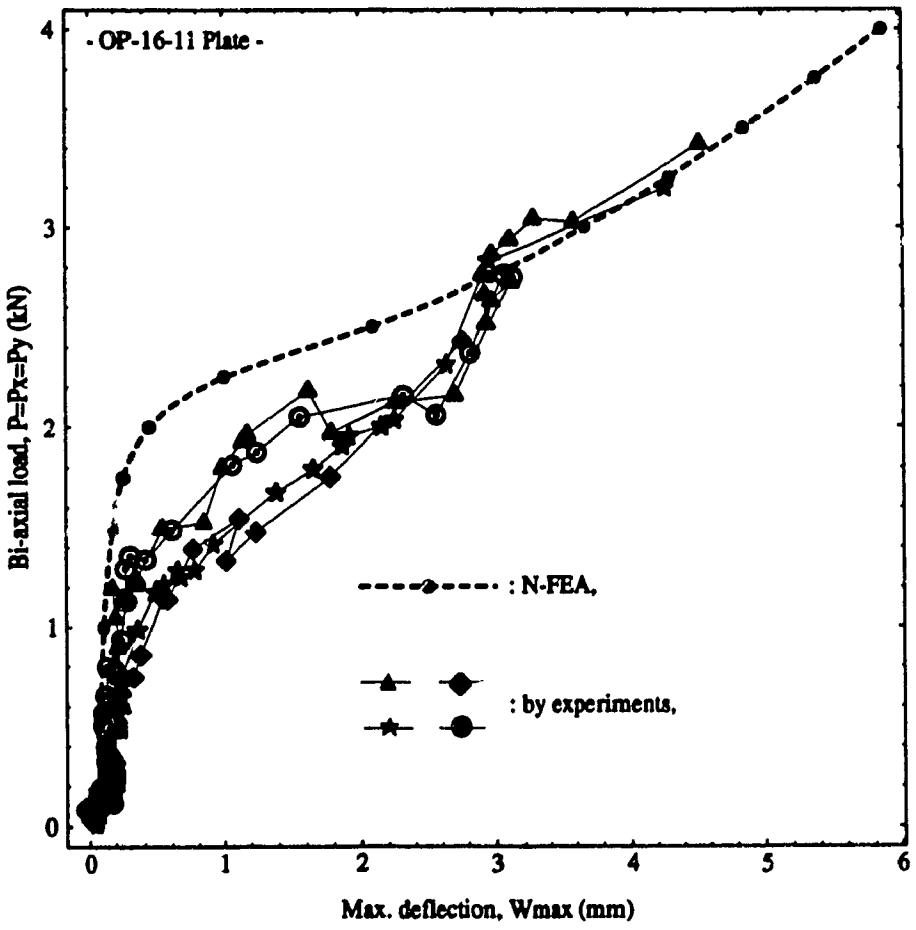

Figure 6.14: Comparison of load-deflection response between experimental and N-FEA results of OP-16-11 plate with biaxial loadings ($P_x : P_y = 1 : 1$).

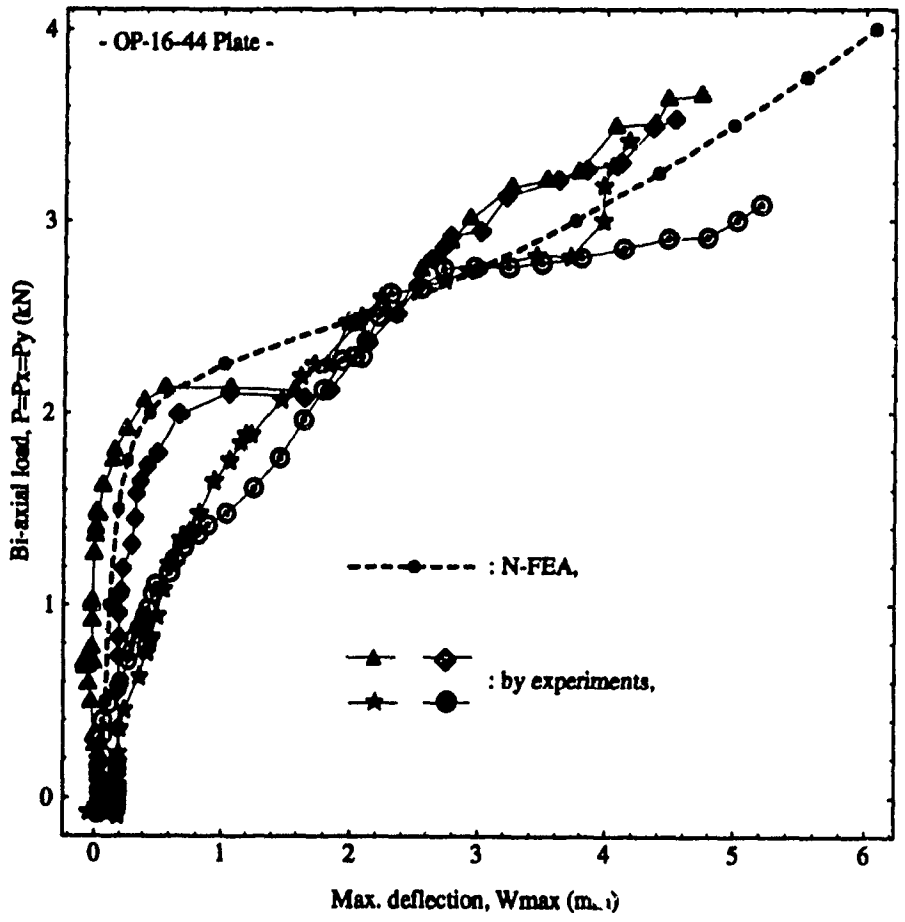

Figure 6.15: Comparison of load-deflection response between experimental and N-FEA results of OP-16-44 plate with biaxial loadings ($P_x : P_y = 1 : 1$).

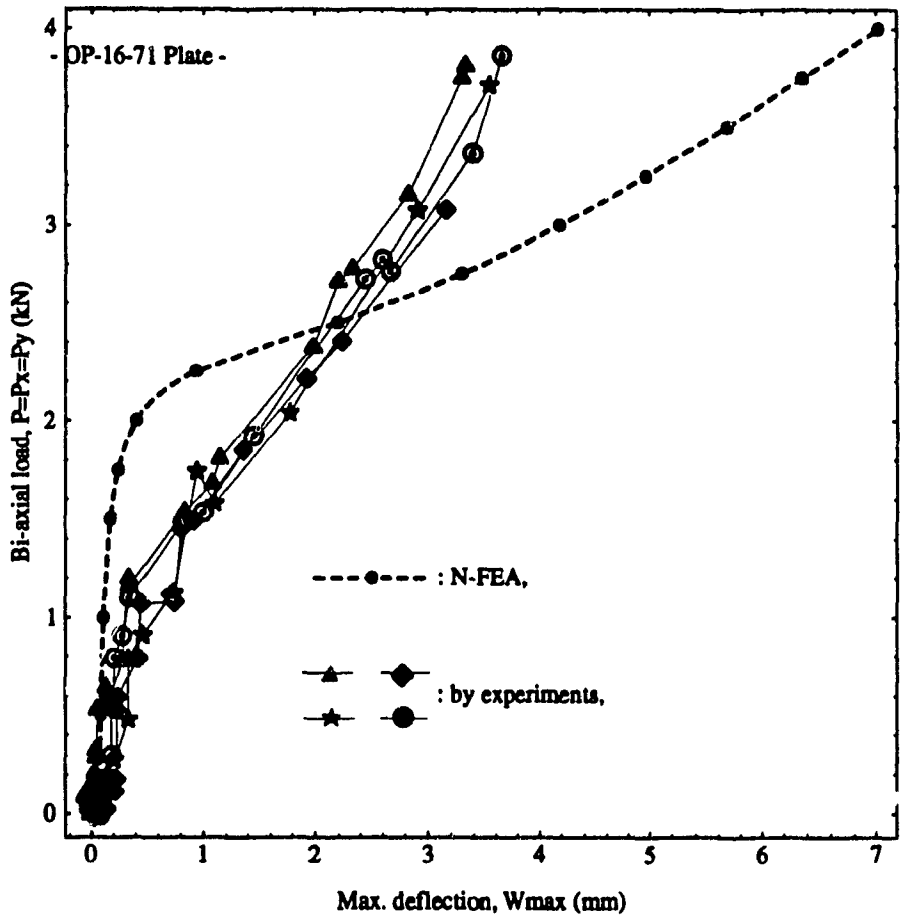

Figure 6.16: Comparison of load-deflection response between experimental and N-FEA results of OP-16-71 plate with biaxial loadings ($P_x : P_y = 1 : 1$).

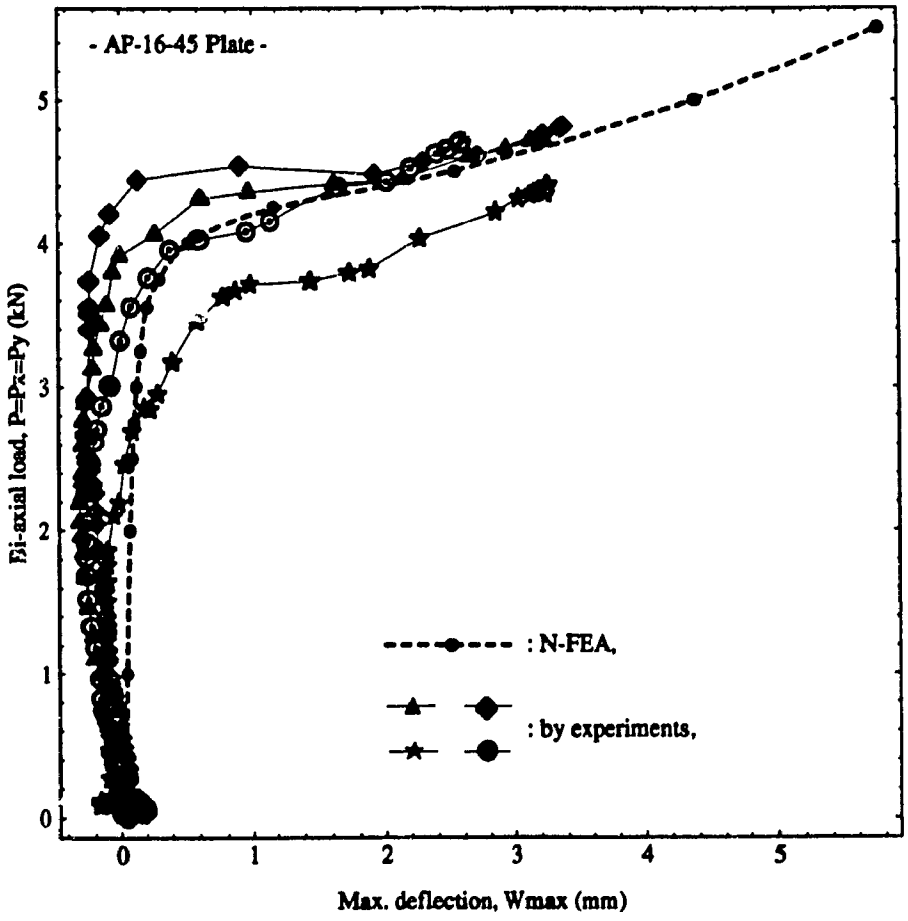

Figure 6.17: Comparison of load-deflection response between experimental and N-FEA results of AP-16-45 plate with biaxial loadings ($P_x : P_y = 1 : 1$).

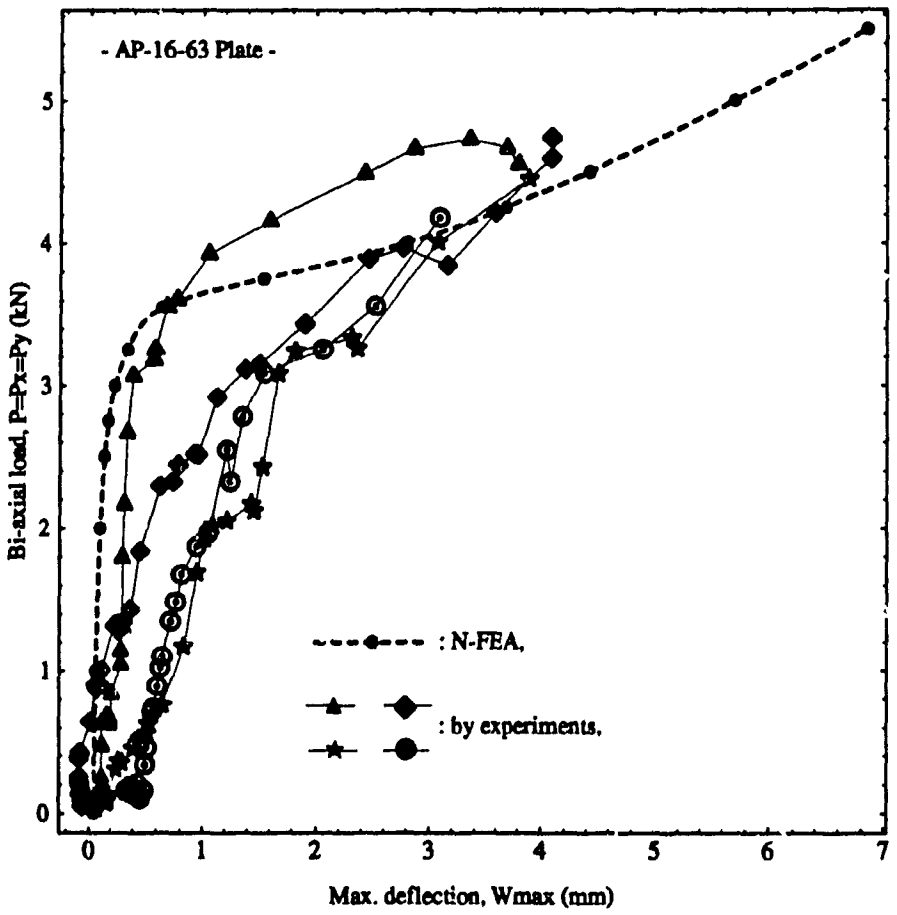

Figure 6.18: Comparison of load-deflection response between experimental and N-FEA results of AP-16-63 plate with biaxial loadings ($P_x : P_y = 1 : 1$).

6.3.3 Shadow Moiré Experiments

Shadow Moiré fringes, for the uniaxially loaded OP-16-11 plates, are shown in Figure 6-19. From this figure, we can find concentric circular fringes in the two cases of uniaxial loading. It means these uniaxial buckling deformations are biharmonic deformations. Also, these pictures confirm the similarity of the uniaxial loading behaviours in Figures 6-4~6-7 of the previous section.

Figure 6-20 shows the Shadow Moiré figures for OP-16-71 plate series. Deformation of the x-axis uniaxial buckling case appears as a rectangular contour in Figure 6-20 a) and it notes that the axis of loading and the stiffening axis are the same. However, Figure 6-20 b) shows a kind of 3rd mode of deflection due to loading along the weaker y-axis. This figure confirms the mode jumping phenomenon from numerical analysis in Chapter 5.

For biaxial buckling cases, Figures 6-21 and 6-22 are presented for the cases of OP-16-11 and OP-16-71. Comparing the two pictures, the shape of postbuckling deflection of regularly layuped plate(OP-16-11) is revealed as a concentric circular contours as shown in Figure 6-21 but, for the case of irregularly layuped plate(OP-16-71), an elliptic contour is found in Figure 6-22. However, regardless of the stiffness ratio, postbuckling deflection appears as an uniform biharmonic function in the case of biaxial loading.

On the other hand, general shapes of biaxial and uniaxial buckling of orthotropic laminate OP-12-11 are shown in Figure 6-23. These pictures back up the previous conclusion. That is, as long as the buckling of balanced laminates like OP-16-11 or OP-20-11 is concerned, the bucking deformation is biharmonic regardless of the loading direction, i.e., x-uniaxial, y-uniaxial or biaxial loading.

Finally the buckling shapes of anisotropic laminates are given in Figures 6-24 and 6-25. For the buckling shape of AP-16-36 plate series, Figure 6-24 shows a skewed elliptic shape due to the direction of major stiffness axis. However, in the buckling shape of AP-16-45 plate series shown in Figure 6-25, the buckling shape can be seen as a circular contours (note that the loading direction is between the two major stiffness axes).

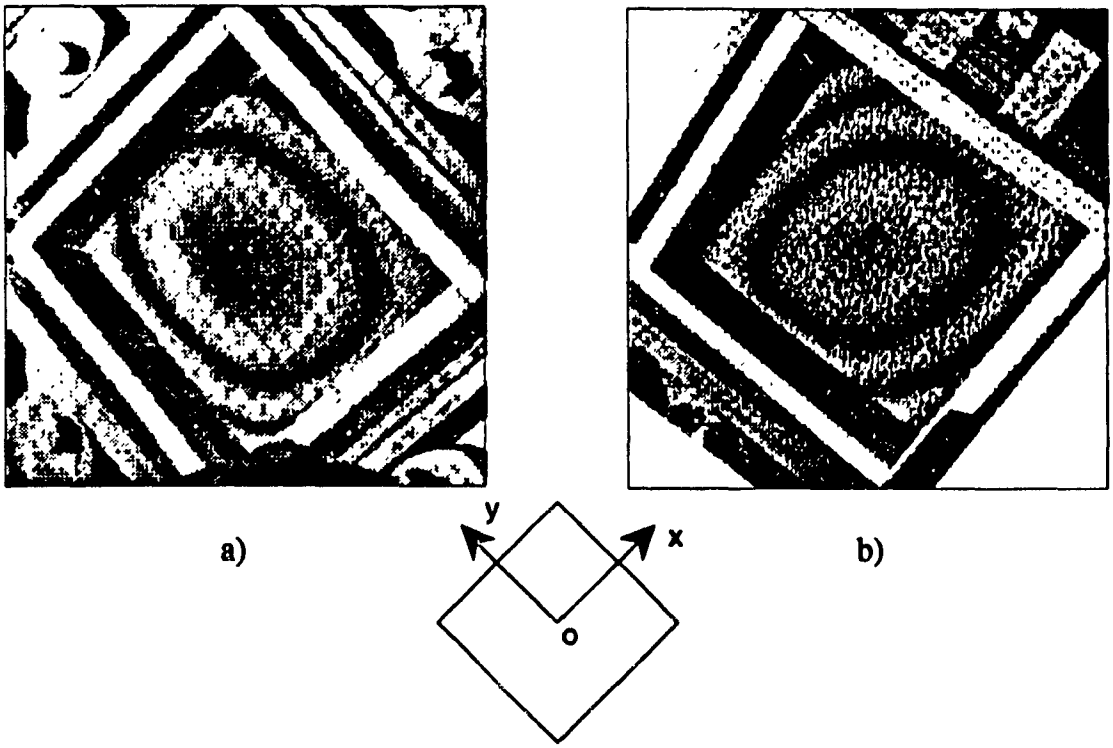

Figure 6.19: Shadow Moiré picture for the 16-layer plates of OP-16-11, a) x-axis uniaxial loading, $P_x : P_y = 1 : 0$, b) y-axis uniaxial loading, $P_x : P_y = 0 : 1$.

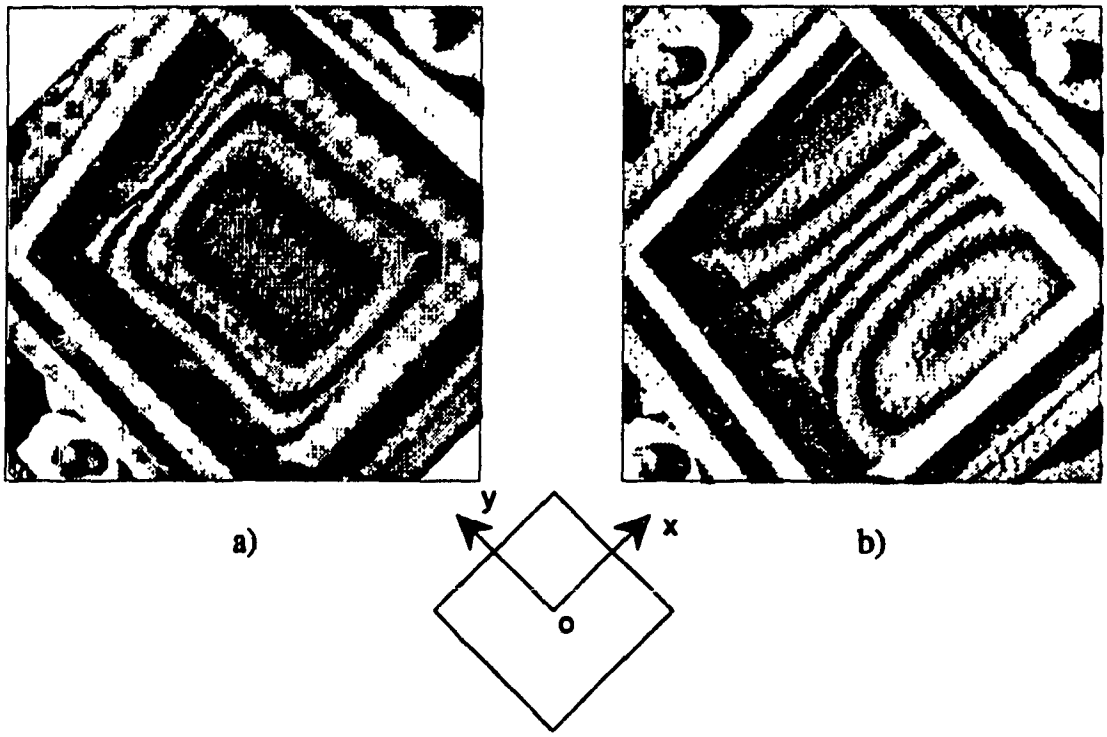

Figure 6.20: Shadow Moiré picture for the 16-layer plates of OP-16-71, a) x-axis uniaxial loading, $P_x : P_y = 1 : 0$, b) y-axis uniaxial loading, $P_x : P_y = 0 : 1$.

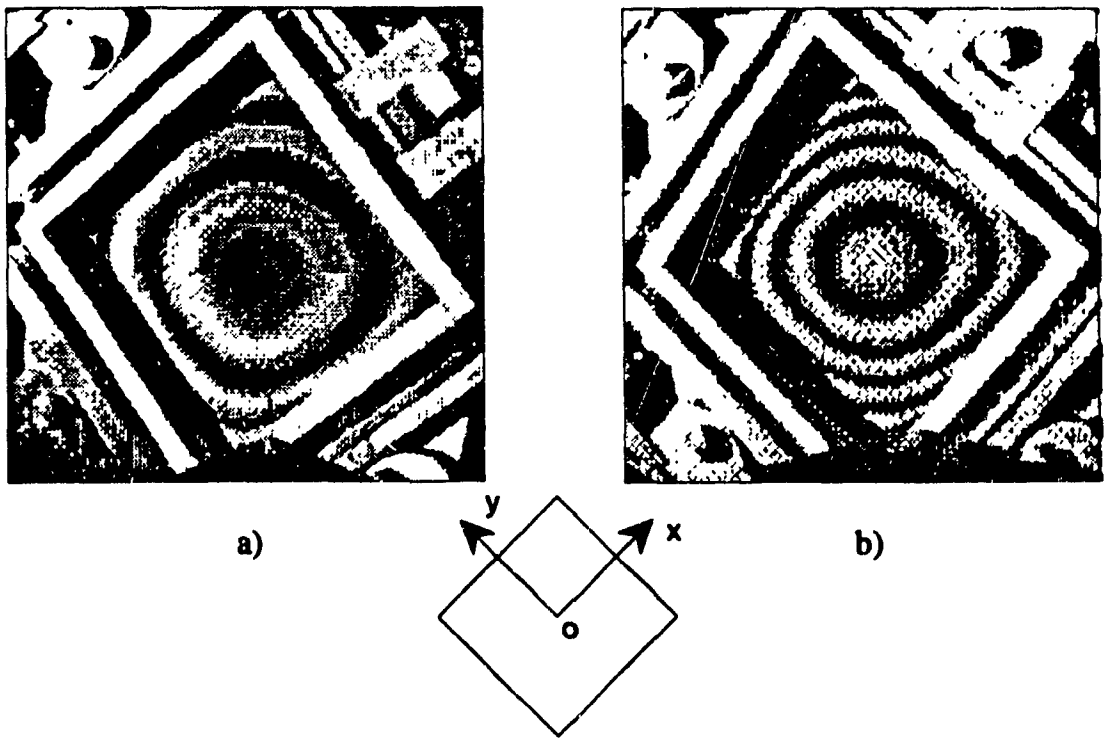

Figure 6.21: Shadow Moiré picture for the 16-layer plates of OP-16-11, a) early state of biaxial buckling, $P_x = P_y$=2 kN, b) full-developed biaxial buckling, $P_x = P_y = 3$kN.

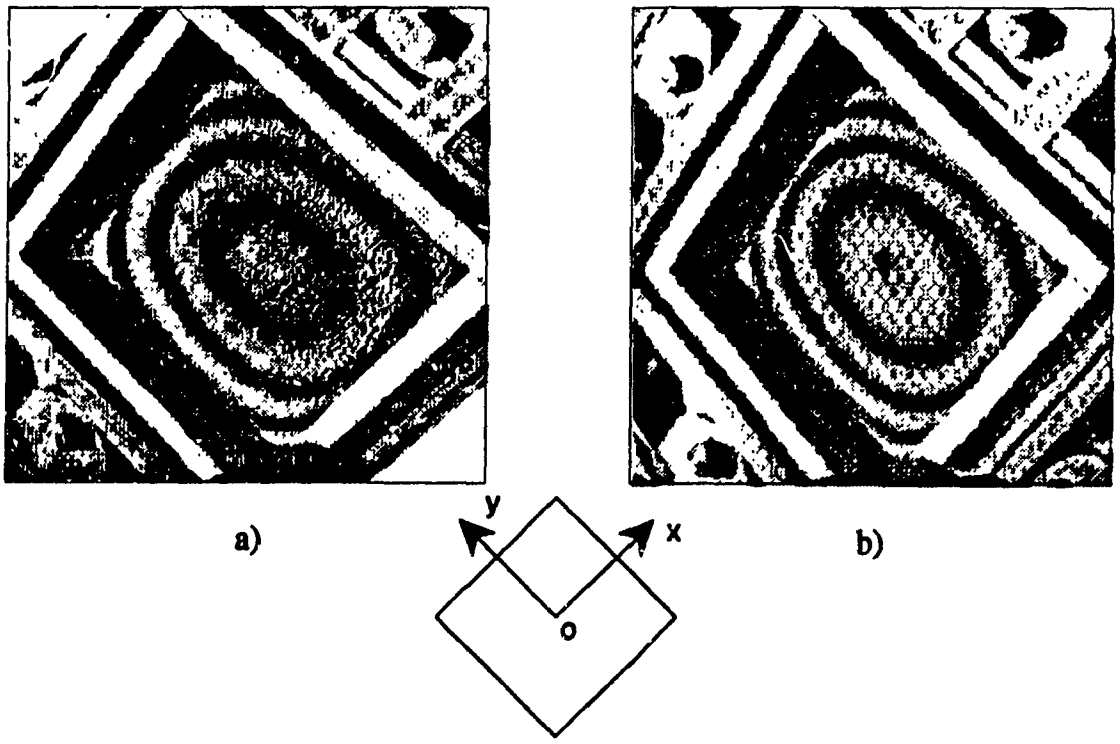

Figure 6.22: Shadow Moiré picture for the 16-layer plates of OP-16-71, a) early state of biaxial buckling, $P_x = P_y$=2 kN, b) full-developed biaxial buckling, $P_x = P_y = 3$kN.

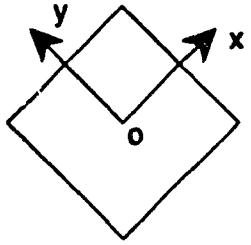

a)

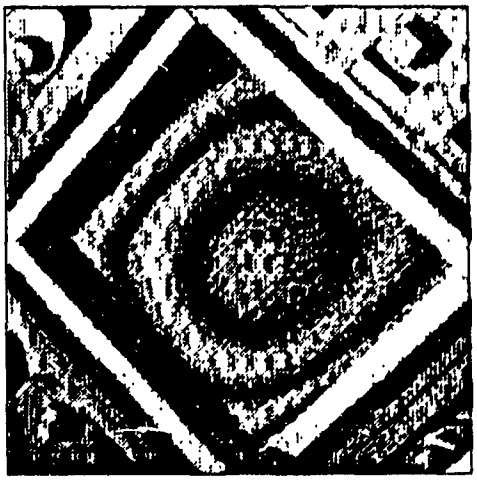

b) c)

Figure 6.23: Shadow Moiré picture for the 12-layer plate, OP-12-11, a) biaxial buckling,$P_x = P_y$, b) x-axis uniaxial buckling, $P_x : P_y = 1 : 0$, c) y-axis uniaxial buckling, $P_x : P_y = 0 : 1$.

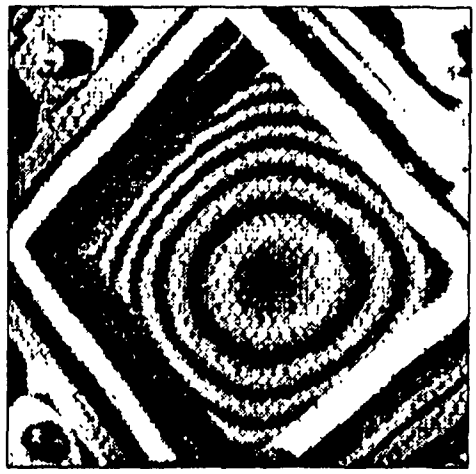

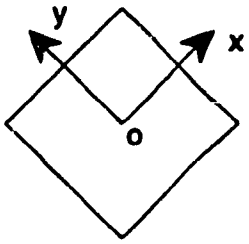

a)

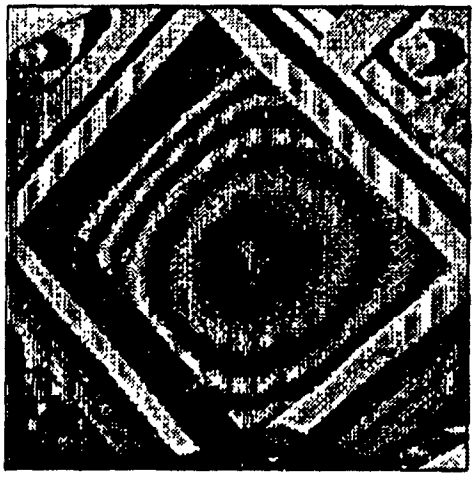

b) c)

Figure 6.24: Shadow Moiré picture for the 16-layer plate, AP-16-36, a) biaxial buckling,$P_x : P_y = 1 : 1$, b) x-axis uniaxial buckling, $P_x : P_y = 1 : 0$, c) y-axis uniaxial buckling, $P_x : P_y = 0 : 1$.

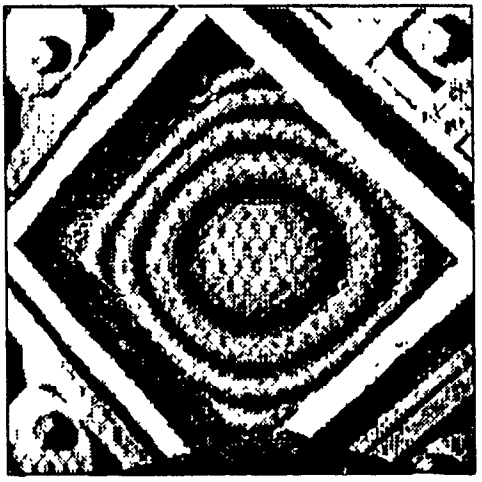

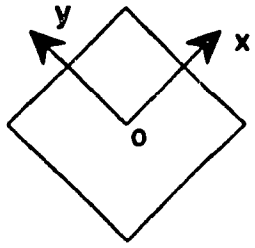

a)

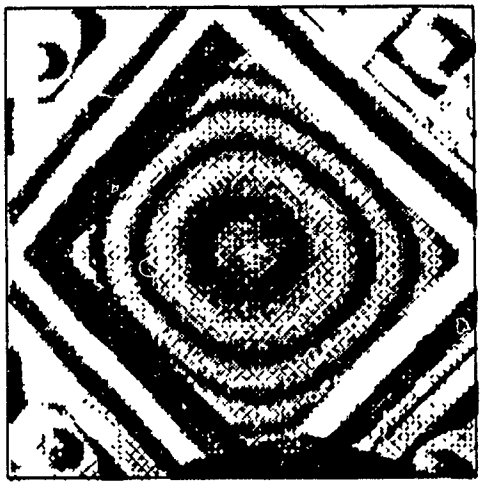

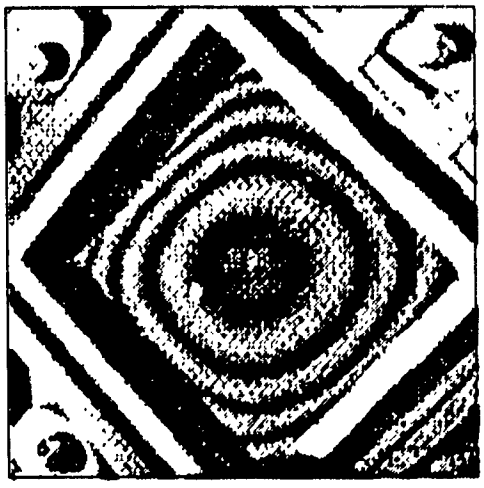

b) c)

Figure 6.25: Shadow Moiré picture for the 16-layer plate, AP-16-45, a) biaxial buckling, $P_x : P_y = 1 : 1$, b) x-axis uniaxial buckling, $P_x : P_y = 1 : 0$, c) y-axis uniaxial buckling, $P_x : P_y = 0 : 1$.

6.4 Experimental Buckling Criteria

6.4.1 Southwell Plot Buckling Criterion (SPBC)

In general, classical laminated plate theory assumes that a plate remains flat as it loaded until the critical load is reached. However all plates have some initial curvature or eccentric loading that may induce deflection as they are loaded. The experimental verification of most buckling theories will require some criteria for determining when the plate would have reached its critical load. Southwell reported, in 1932, a method for determining the critical load for a column with an initial imperfection [60].

At first look, Southwell remarked that the actual load-deflection curve for such a column would be a rectangular hyperbola with asymptotes at zero deflection. Then he proved that the hyperbola could be transformed into a straight line with a slope of $1/P_c$ by changing the coordinates from P vs. δ to δ/P vs. δ. The buckling of plates, particularly those with only the loaded edge supported as S_r-S_f-S_r-S_f, is very similar to the buckling of columns. Southwell, in his original paper, suggested that his method could be applied to plates just as it has been applied to columns. In this section the applicability of the Southwell Plot to plates will be verified by a formulation which closely parallels Southwell's original formulation

A plate with simple-simple boundary conditions, S_r-S_r-S_r-S_r, can be considered as a column with an initial imperfection of the form

$$w_o = a_1 \sin\frac{\pi x}{a}\sin\frac{\pi y}{b} \tag{6.2}$$

By substituting equation (6.2) into the differential equation and applying the boundary conditions to the general solution, the deflection resulting from the load will be [51]

$$w_1 = a_1[\frac{1}{1-\alpha} - 1]\sin\frac{\pi x}{a}\sin\frac{\pi y}{b} \tag{6.3}$$

where

$$\alpha = \frac{N_x}{(N_x)_c} \tag{6.4}$$

and the total deflection will be

$$\begin{aligned} w &= w_o + w_1 \\ &= \frac{a_1}{1-\alpha} \sin\frac{\pi x}{a} \sin\frac{\pi y}{b} \end{aligned} \tag{6.5}$$

when $x = a/2$ and $y = b/2$,

$$\sin\frac{\pi x}{a} \sin\frac{\pi y}{b} = 1 \tag{6.6}$$

If we put the current deflection, δ, as

$$\delta = \frac{\alpha a_1}{1-\alpha} \tag{6.7}$$

by rearranging,

$$\delta - \delta\alpha - \alpha a_1 = 0 \tag{6.8}$$

which is the equation of a hyperbola between δ and α. Dividing by α, we find that

$$\frac{\delta}{N_x} = \frac{1}{(N_x)_c}(\delta + a_1) \tag{6.9}$$

Therefore Southwell's equation for the column can be extended to a plate with all four edges simply supported, subjected to compressive edge loads in the x and y axes. This equation obviously can be generalized to any point on the plate and to any mode. As long as the deflection due to the load overshadows the initial imperfection, and the deflection still remains small, the Southwell Plot can be applied to any portion of the load-deflection curve. This feature of the Southwell Plot is particularly important for the following reasons:

- The critical load can be found experimentally without exceeding the buckling load of the plate. Thus, as long as the deflections can be made large enough to overshadow the initial imperfection without damaging the plate, i.e., the test will be nondestructive.

- The experimental data can be taken at relatively low load levels, and there is less danger of the predicted experimental behaviour being influenced by a deviation of the material from Hooke's Law.

- A test fixture need not be capable of imposing high loads on a very stiff or flat plate. Instead, the plate can be perturbed by a lateral load, and, by buckling behaviour possible, the neutral and the stable-symmetric.

Typical Southwell Plots using the experimental data are shown in Figures 6-26 and 6-27. Figure 6-26 and 6-27 demonstrate the Southwell Plot for the biaxial and uniaxial buckling behaviour for OP-16-11 and OP-16-44 plates. The term $Wmax$ in the figure is as same as δ of the equations. From these figures, it can be seen that the Southwell Plot is very sensitive to the data distribution of load-deflection curves.

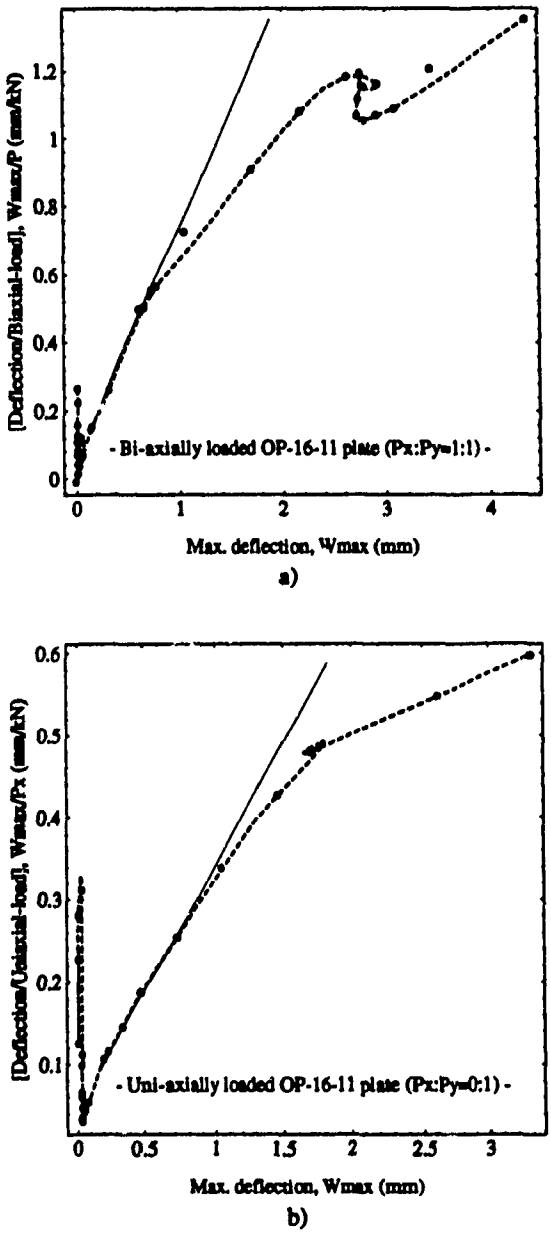

Figure 6.26: Determination of the buckling initiation load from Southwell Plots for the biaxial and uniaxial loading of OP-16-11 plates from the experiments.

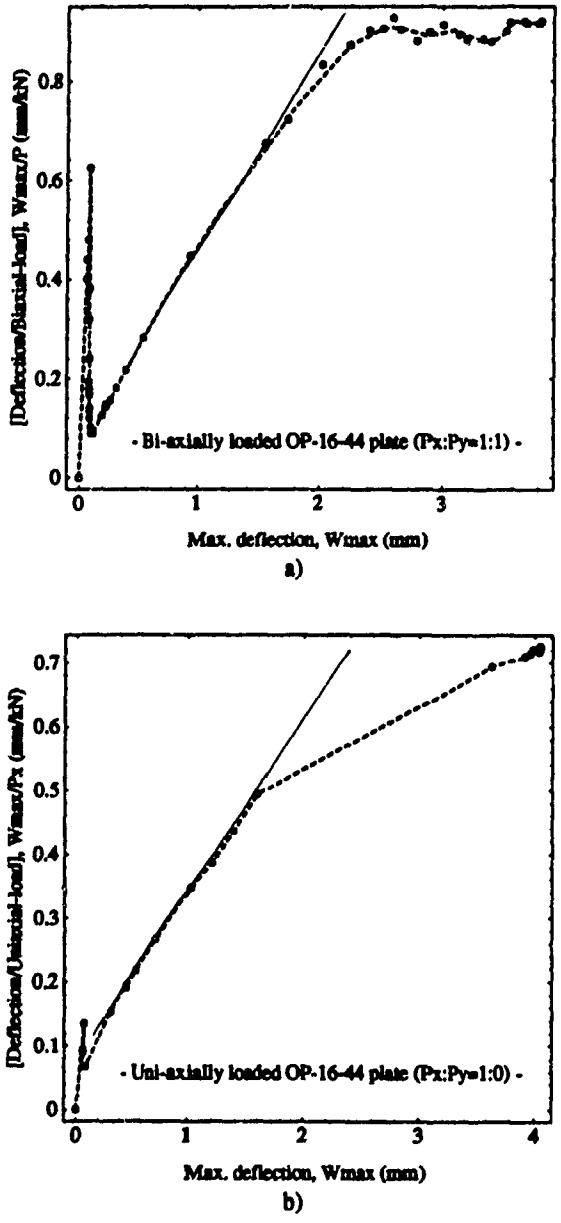

Figure 6.27: Determination of the buckling initiation load from Southwell Plots for the biaxial and uniaxial loading of OP-16-44 plates from the experiments.

6.4.2 Minimum Slope Buckling Criterion (MSBC)

An exact meaning of buckling criterion is finding the correct bifurcation point based on the load-deflection behaviour. This bifurcation point can be found only in case that at least two curves are contacted or intersected. In most buckling theories, the bifurcating point is sought by overlapping two asymptotic lines associated with two curves. For this reason, the bifurcation point establishes only the upper bound of the actual critical buckling point.

For simply supported rectangular plates, the experimental postbuckling behaviour follows the stable load-deflection curve as shown in Figure 6-28. At the early stage of deflection, from Figure 6-28, the global flexural stiffness - slope of the curve - is infinitely high and then the curve may contain one bifurcation point, C_1, which is known as critical buckling load point. In fact the Southwell Plot assigns a lower bound of this critical buckling point, which is very important value from the design point of view.

However, in the designing of large scaled plate structures, some extent of postbuckling might be allowed to secure flexibility. For this purpose, we need to find another criterion for the structure that undergoes a large deflection postbuckling behaviour, i.e., Minimum Slope Buckling Criterion (MSBC). The determination of this minimum slope is shown in Figure 6-28.

The importance and practical meaning of the MSBC can be found from the following discussion. As shown in Figure 6-28, in the buckling of plate structures, there are two possible postbuckling behaviours, i.e., one is a stable mode which is the typical behaviour of fully supported plates and another is an unstable mode which is rarely found for partly supported plates, like beam-plate with the boundary conditions of S_r-S_f-S_r-S_f. From these, we can find a stagnation point, C_2, which is the point of

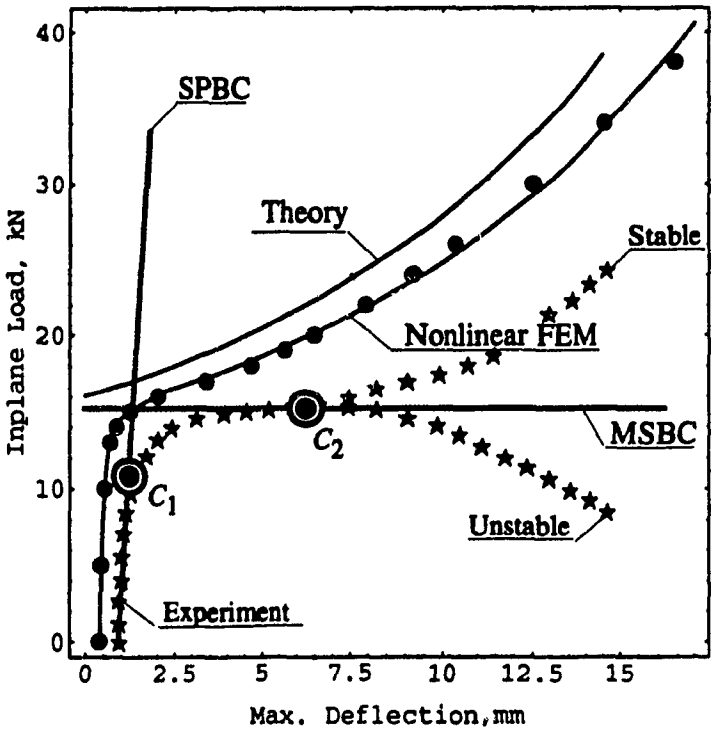

Figure 6.28: Determination of the buckling initiation load by Minimum Slope of Buckling Criterion (MSBC) for the biaxial and uniaxial buckling experiments.

minimum slope for MSBC. Consequently MSBC provides a higher ultimate critical buckling load than SPBC.

Chapter 7

Discussion

7.1 Reliability of Modified Plate Specimen

To propose a suitable plate specimen for biaxial buckling experiment, various numerical and experimental investigations were executed using orthotropic laminate OP-16-11 plate. Two kinds of modified specimen, corner-free and corner cut-model, were initially proposed to overcome the experimental obstacles. Based on the numerical and experimental analysis for the two suggested model, corner-cut model was selected as the modified specimen. The reason was the premature failure at each corner for the corner-free plate as was discussed previously and also presented in [61][62].

In simulating the critical buckling load for the ideal plate from the modified plate, Figure 3-6 can be used as reference curve to determine the reduction rate of the critical buckling load as a function of modification ratio. Thus, the critical buckling load of the ideal plate can be obtained from the experimental data of the modified specimen easily. For example, the unknown critical buckling load P_{c-i} of the ideal plate can be found from the known critical buckling load P_{c-m} of the modified specimen with

$a_c/a = 7.5\%$ as simply as

$$P_{c-i} = P_{c-m} \times (100/90) \tag{7.1}$$

Also, the surface strain distribution was investigated by N-FEA and it was compared favorably with experiment specially on the centre and edge area along S-line.

Consequently, based on the numerical and experimental investigations on the admissibility of the modified plate specimen as a substitute for the ideal plate, it can be concluded that the modified specimen is a reliable model in the determination of critical buckling load and also in the analysis of postbuckling behaviour also if modification ratio, a_c/a, does not exceed 7.5%.

7.2 Effect of Laminate Thickness

As mentioned with equations (2.36)~(2.39) in Chapter 2, the critical buckling load is governed by the values of the flexural stiffness, D_{ij}, or by the value of the global stiffness, D_T, in orthotropic plates. These flexural stiffness values are functions of the plate thickness.

From the N-FEA results plotted in Figure 7-1, thicker plates demonstrate not only higher critical loads but also much clearer bifurcation points and more stable postbuckling behaviour than that of thinner one.

For the 12-, 16- and 20-layer orthotropic composite plates, the values of the experimental critical buckling loads, obtained from SPBC, along with the results from L-FEA and N-FEA, are shown in Figure 7-2.

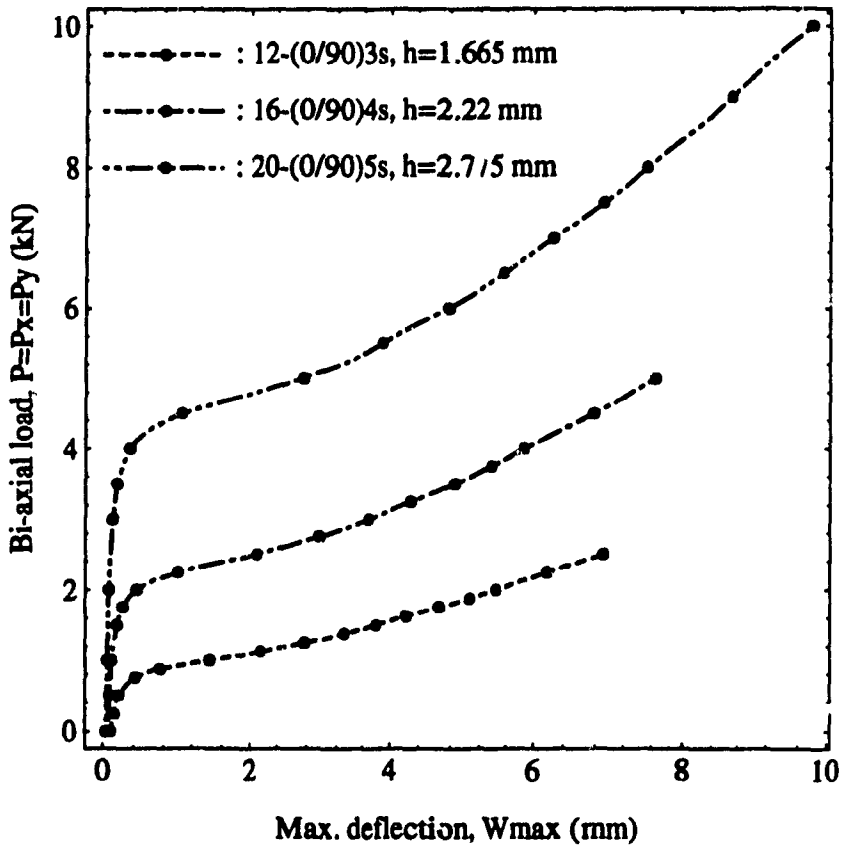

Figure 7.1: Thickness effects on the biaxial buckling response of 12-, 16- and 20-layer symmetric laminate with equal (0/-90)s layup sequence from N-FEA.

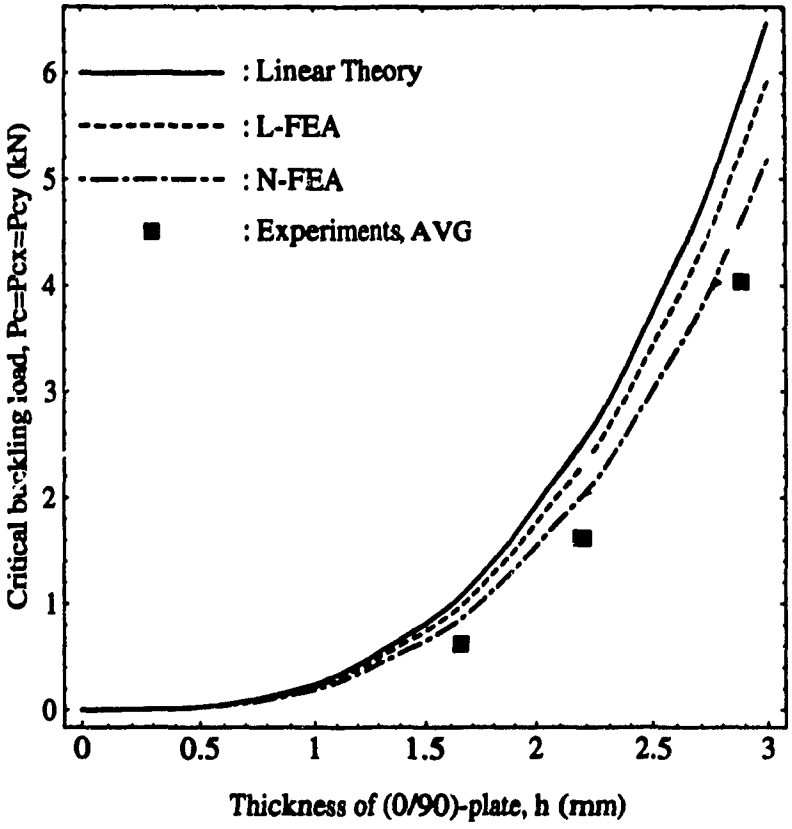

Figure 7.2: Thickness effects on the biaxial buckling response of 12-, 16- and 20-layer symmetric laminate with equal (0/-90)s layup sequence from analytical and experimental results.

7.3 Effect of Layup Angle

Based on the result of L-FEA, N-FEA and experiments, the effect of layup angle is shown in Figure 7-3 and 7-4. Figure 7-3 was constructed by comparing the uniaxial critical buckling loads, P_{cx}, obtained using SPBC, for the case of three different layup angles, $(0/-90)$, $(30/-60)$ and $(45/-45)$. The critical buckling load values from uniaxial buckling are not as high in the experiments as predicted by the numerical analyses. In contrast with the N-FEA result, which gives twice the value for $(45/-45)$, the experimental result shows an increase of only 1.5 times.

Figure 7-4 compares the biaxial P_{cu} values, obtained using SPBC, for the cases of three different layup angles, $(0/-90)$, $(30/-60)$ and $(45/-45)$, showing that the predicted critical load values are realized in the experiments. In $(45/-45)$ plates, The N-FEA results give twice of the critcal values of $(0/-90)$ plates, which agree with the experimental results.

From these results, it may be concluded that the layup angle has effects on critical buckling load in both unaxial and biaxial bucklings. However the effect is stronger in the biaxial buckling case.

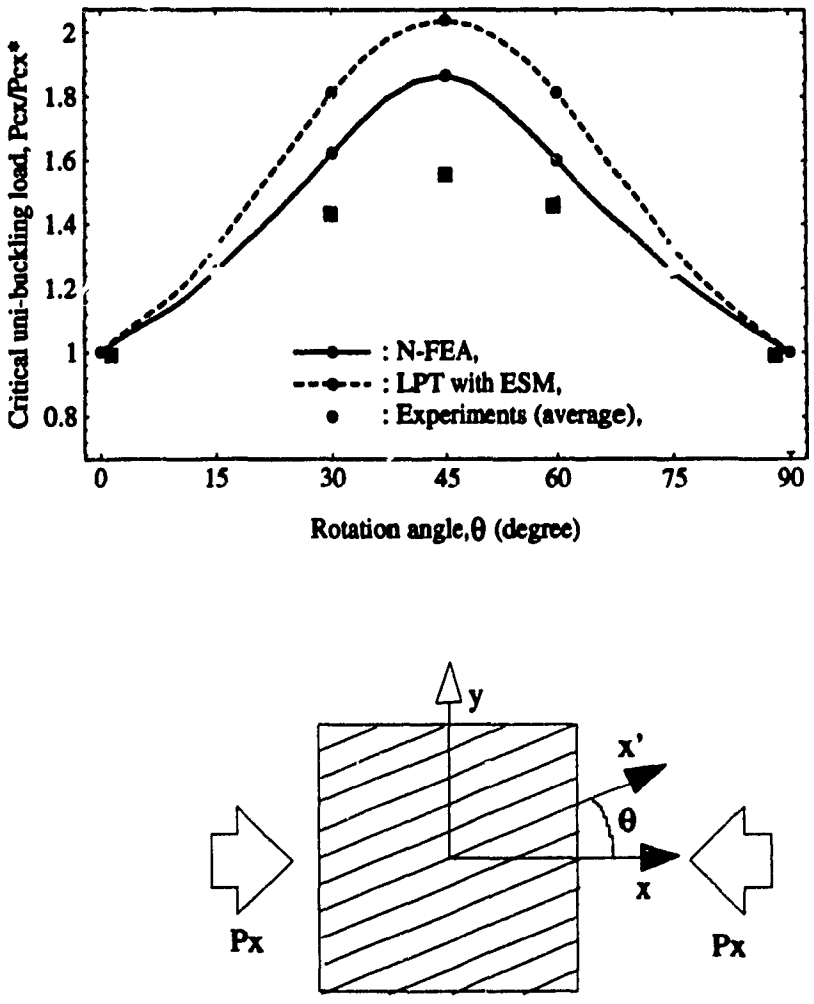

Figure 7.3: Effects of layup angle on the x-uniaxial loading ($P_x : P_y = 1 : 0$) for symmetric cross-ply laminate by CLPT, N-FEA and experiments, where P_{cx}^* is the value of P_{cx} when $\theta = 0$ (P_{cx} is critical load).

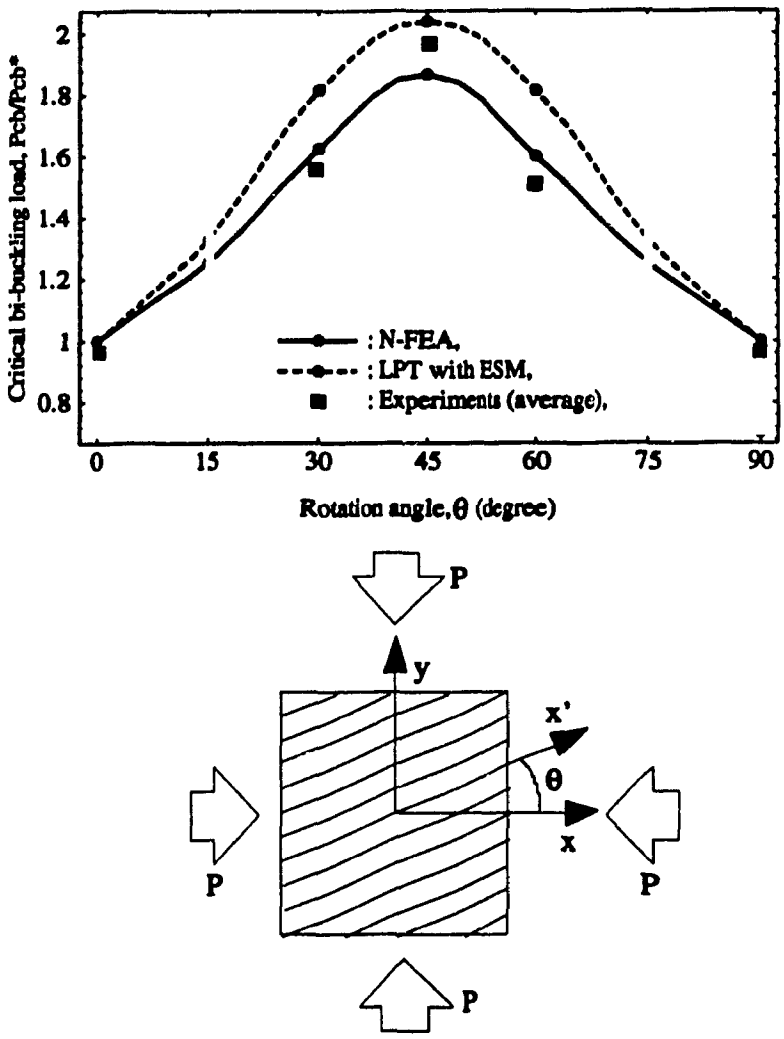

Figure 7.4: Effects of layup angle on the biaxial loading ($P_x : P_y = 1 : 1$) for symmetric cross-ply laminate by CLPT, N-FEA and experiments, where P_{cb}^* is the value of P_{cb} when $\theta = 0$ (P_{cb} is critical load).

7.4 Effect of Stiffness Ratio

7.4.1 Orthotropic Specimen

As the experimental criteria of buckling initiation and catastrophic failure, the two critical buckling loads were obtained by implementing SPBC (Southwell Plot Buckling Criterion) and MSBC (Minimum Slope of Buckling Criterion), and those data were plotted in the same domain of critical values from N-FEA and CLPT. From the figures of regularly layup, such as Figures 7-5 and 7-6 for the 16-ply specimen and Figure 7-9 for the 20-ply specimen, critical loadings of the two uniaxial loading, P_{cx} and P_{cy}, are not much different. It can be understood by considerin the effects of flexural stiffness ratio, ζ, on the critical buckling load which was mentioned in N-FEA of Chapter 4. Also, from these results, the difference of critical buckling load values between SPBC and MSBC is small in uniaxial buckling case but large in biaxial buckling case. This difference also can be understood from considerations of the boundary conditions for biaxial and uniaxial loading.

Let us compare Figures 7-7 and 7-8 and Figures 7-10 and 7-11 for the irregular layup laminates with a high value of the stiffness ratios, $\zeta \geq 12.8$. Here the critical buckling loads for the two uniaxial buckling case, P_{cx} and P_{cy} show a big difference from each other. It also can be understood by the considerations of the stiffness ratio. Because for the case of loading along the weaker axis, there is a change in the buckling mode.

In these figures, the difference of critical buckling load value between SPBC and MSBC is much larger than the buckling of regular layup laminates. However, for the case of irregular layup plates, the two critical buckling loads obtained of SPBC and MSBC show scattered distribution with a small amount of difference in unaxial loading as shown in Figures 7-8 and 7-11. Some of this has been published in [63][64][65].

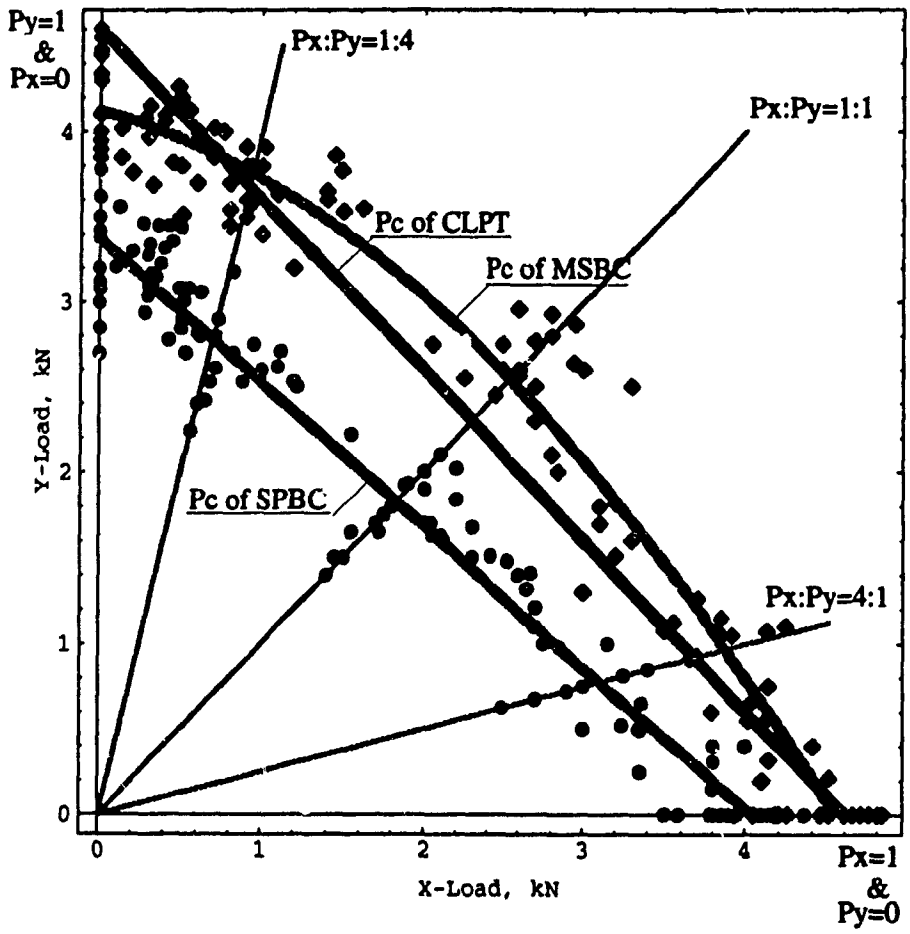

Figure 7.5: Experimental determination of the buckling initiation load from SPBC (Southwell Plot Buckling Criterion) and ultimate load from MSBC (Minimum Slope of Buckling Criterion) for OP-16-11 plate with various loadings (1st data).

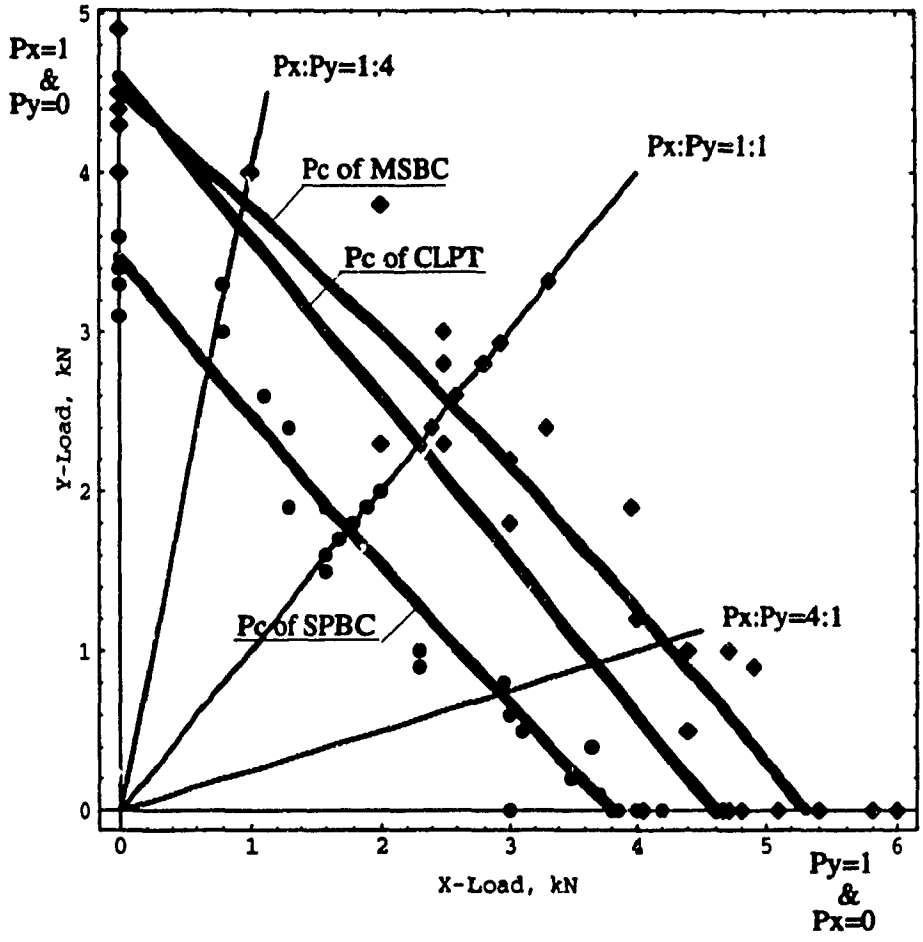

Figure 7.6: Experimental determination of the buckling initiation load from SPBC (Southwell Plot Buckling Criterion) and ultimate load from MSBC (Minimum Slope of Buckling Criterion) for OP-16-11 plate with various loadings (2nd data).

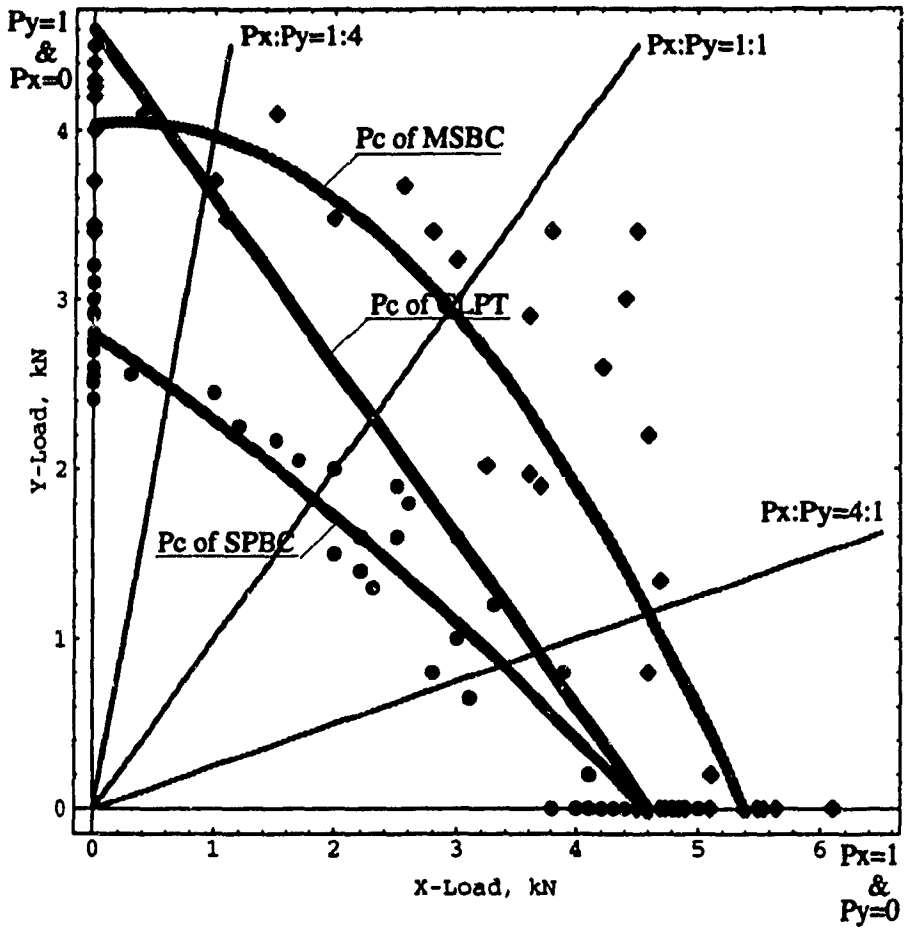

Figure 7.7: Experimental determination of the buckling initiation load from SPBC (Southwell Plot Buckling Criterion) and ultimate load from MSBC (Minimum Slope of Buckling Criterion) for OP-16-44 plate with various loadings.

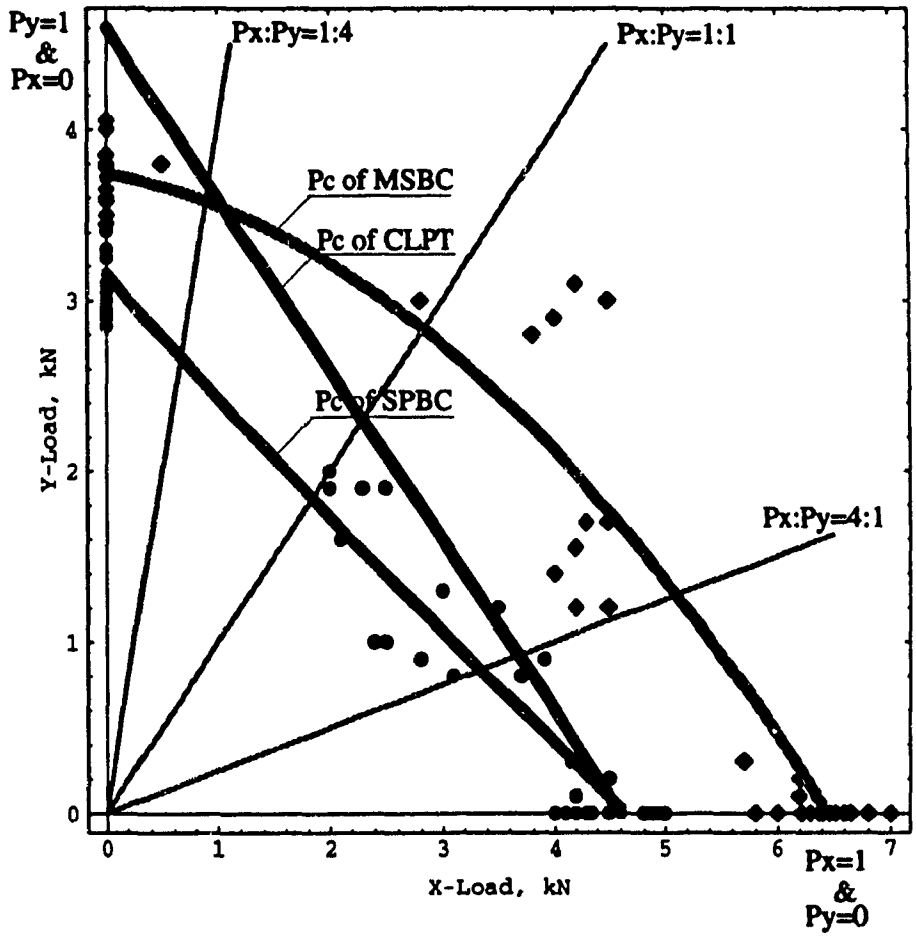

Figure 7.8: Experimental determination of the buckling initiation load from SPBC (Southwell Plot Buckling Criterion) and ultimate load from MSBC (Minimum Slope of Buckling Criterion) for OP-16-71 plate with various loadings.

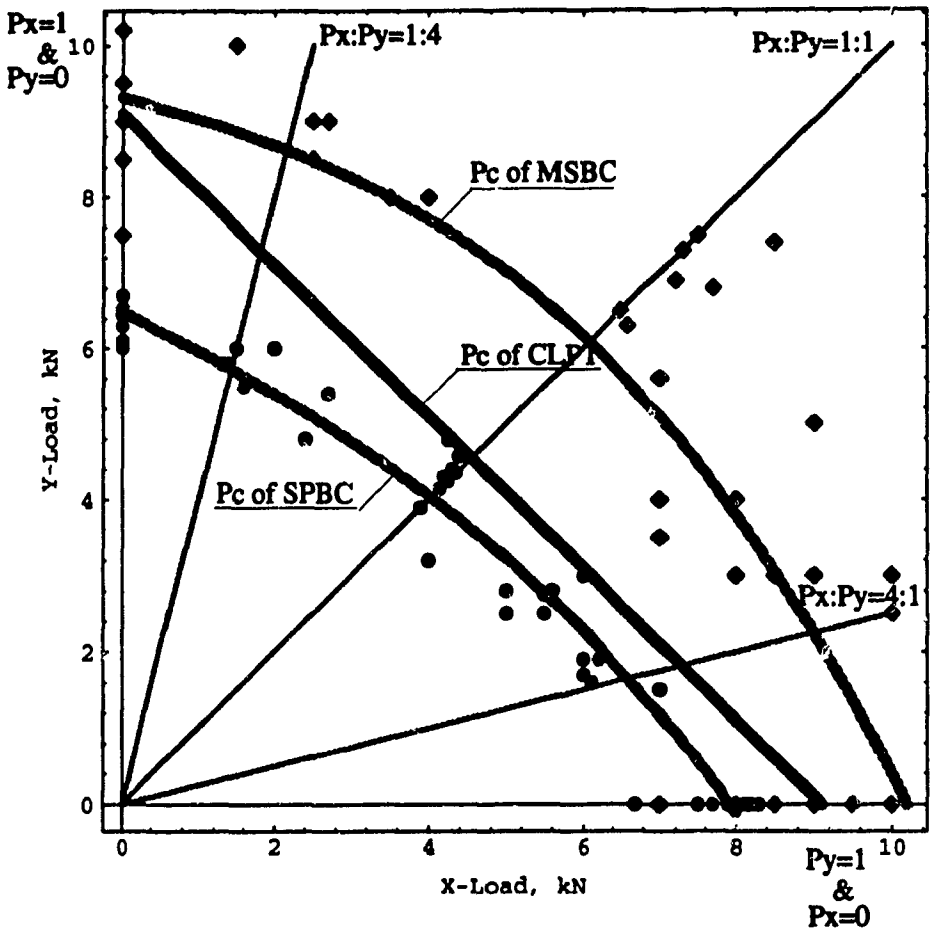

Figure 7.9: Experimental determination of the buckling initiation load from SPBC (Southwell Plot Buckling Criterion) and ultimate load from MSBC (Minimum Slope of Buckling Criterion) for OP-20-11 plate with various loadings.

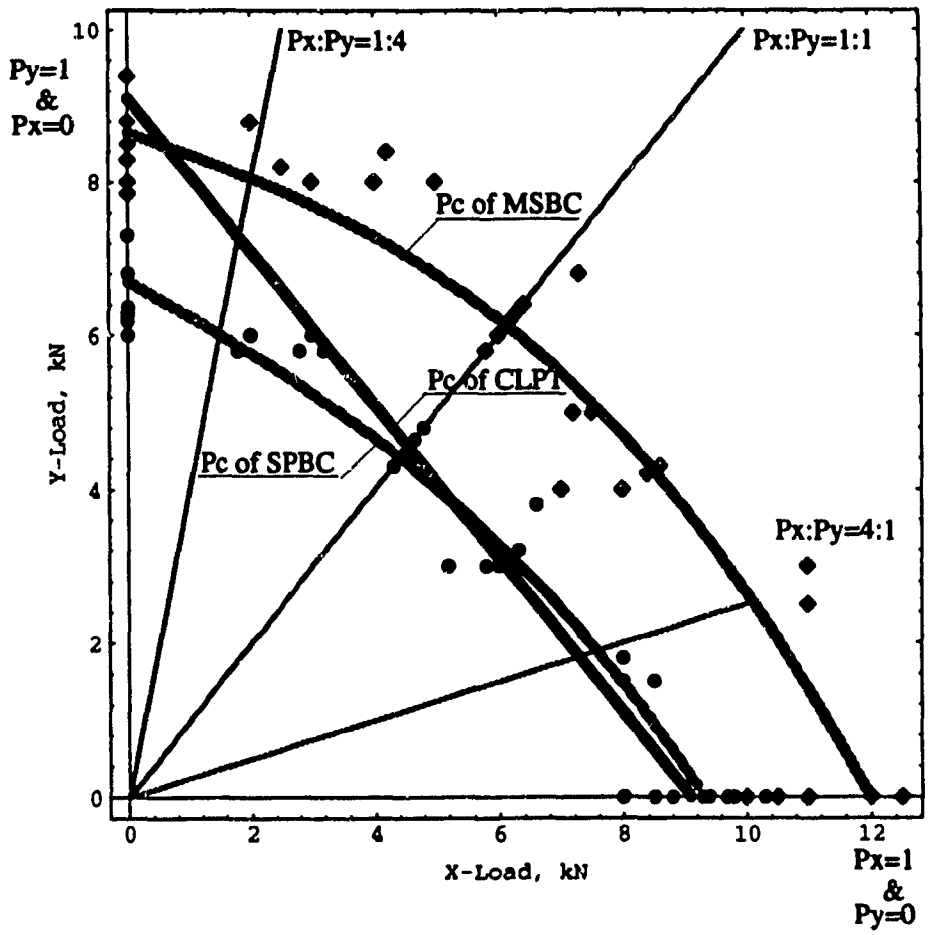

Figure 7.10: Experimental determination of the buckling initiation load from SPBC (Southwell Plot Buckling Criterion) and ultimate load from MSBC (Minimum Slope of Buckling Criterion) for OP-20-55 plate with various loadings.

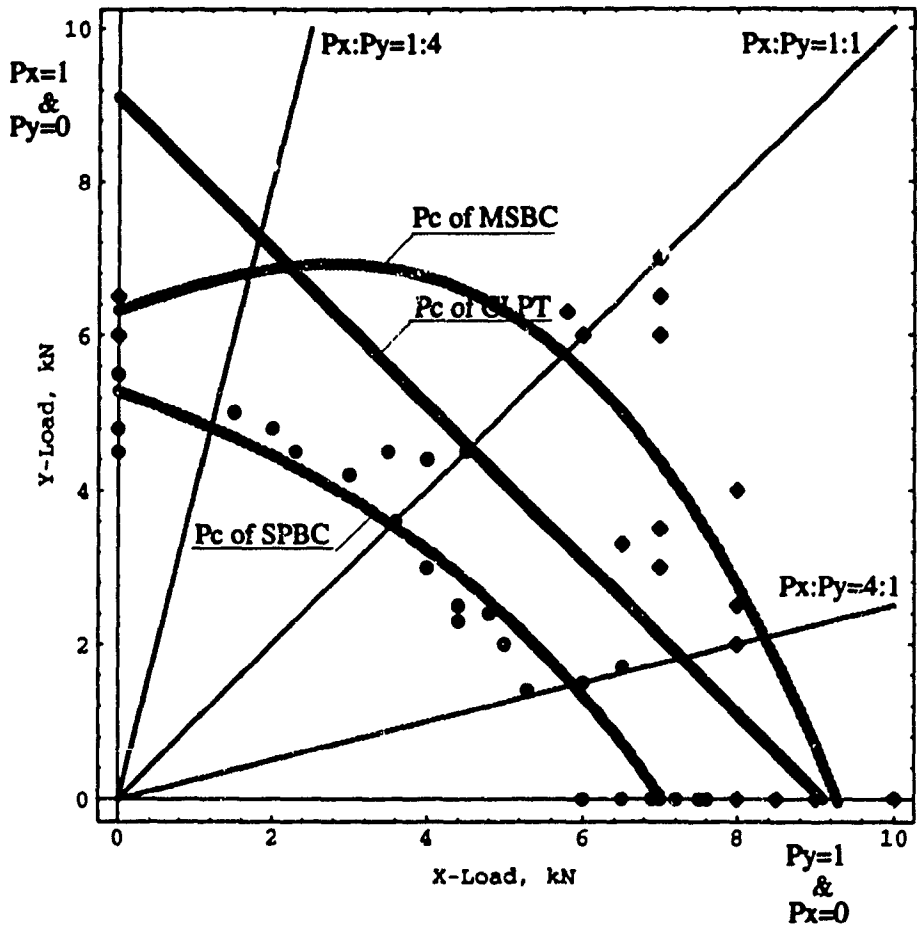

Figure 7.11: Experimental determination of the buckling initiation load from SPBC (Southwell Plot Buckling Criterion) and ultimate load from MSBC (Minimum Slope of Buckling Criterion) for OP-20-82 plate with various loadings.

7.4.2 Anisotropic Specimen

The critical buckling loads and the ultimate critical loads, obtained from SPBC and MSBC, are plotted in the same domain of critical values from N-FEA and CLPT, in Figures 7-12~7-13 for 16 ply specimens and Figures 7-14 and 7-15 for 20-ply angle-ply laminates from $(45/-45)$ to $(60/-30)$ anisotropic plates.

Comparing these four figures with the figures of orthotropic $(0/-90)$ laminates (in Figures 7-5 and 7-6), angle-ply laminates show a stronger resistance in biaxial buckling. Some results of this work were presented in [62][63].

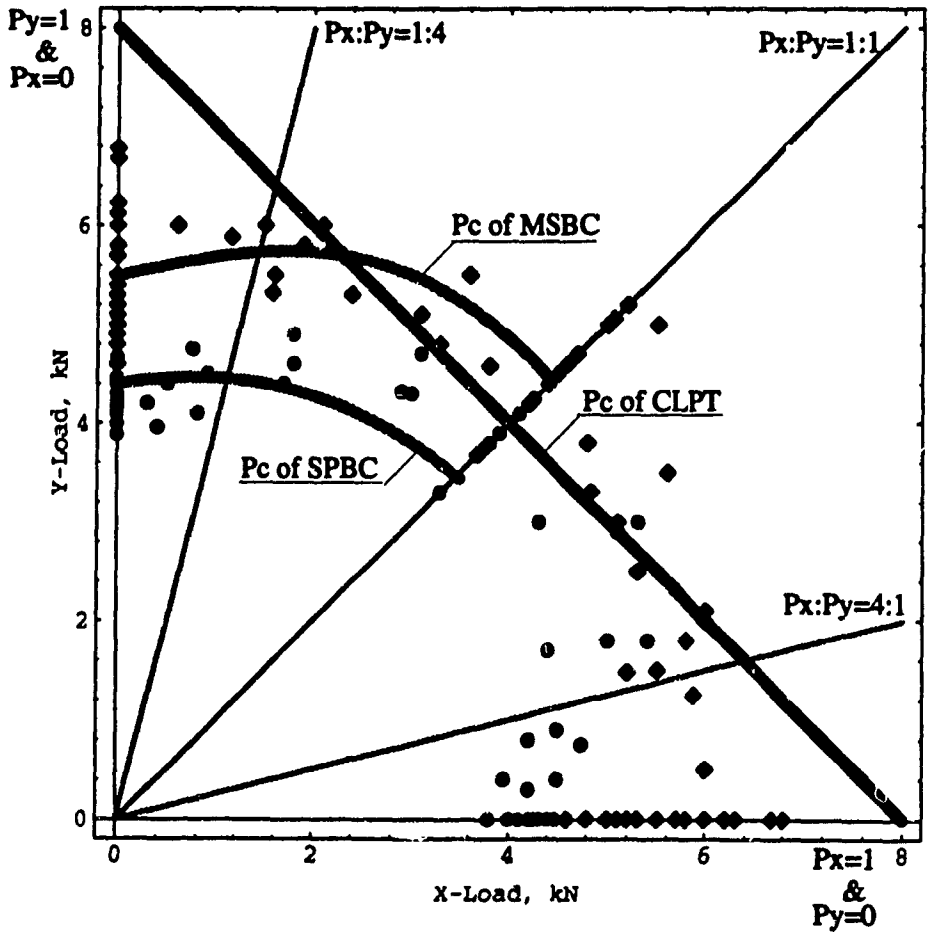

Figure 7.12: Experimental determination of the buckling initiation load from SPBC (Southwell Plot Buckling Criterion) and ultimate load from MSBC (Minimum Slope of Buckling Criterion) for OP-16-45 plate with (45/-45)x4, under various loadings.

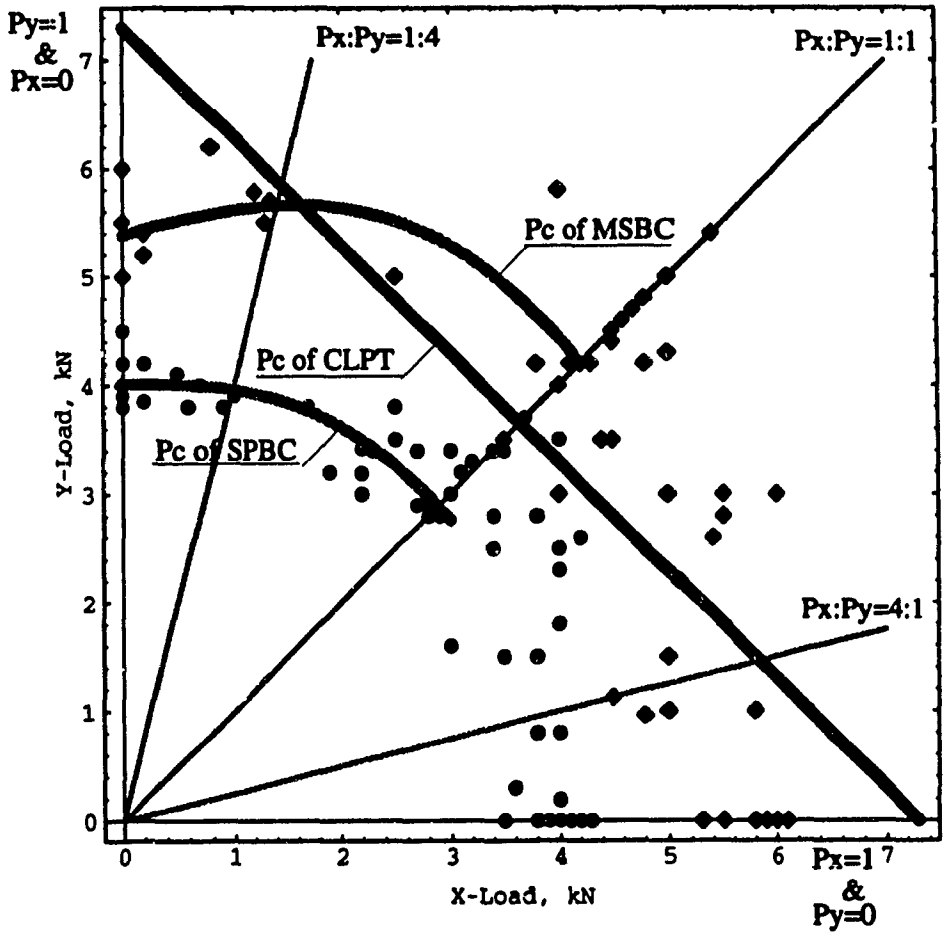

Figure 7.13: Experimental determination of the buckling initiation load from SPBC (Southwell Plot Buckling Criterion) and ultimate load from MSBC (Minimum Slope of Buckling Criterion) for OP-16-63 plate with (60/-30)x4, under various loadings.

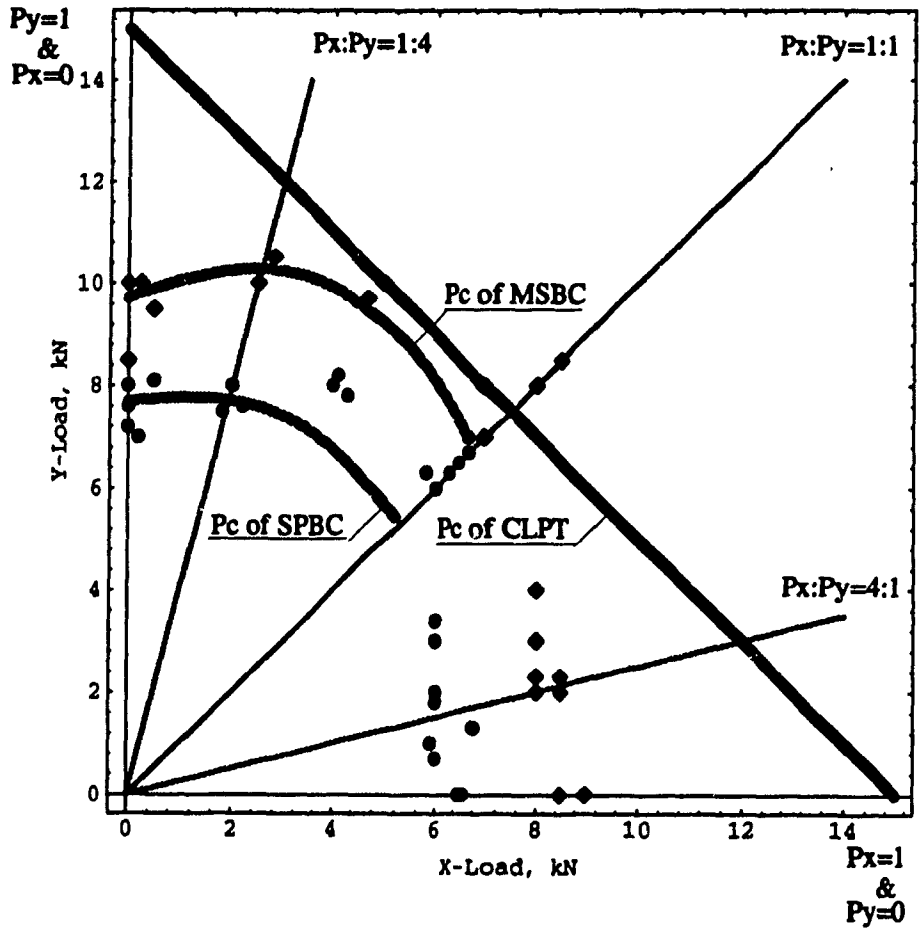

Figure 7.14: Experimental determination of the buckling initiation load from SPBC (Southwell Plot Buckling Criterion) and ultimate load from MSBC (Minimum Slope of Buckling Criterion) for OP-20-45 plate with (45/-45)x5, under various loadings.

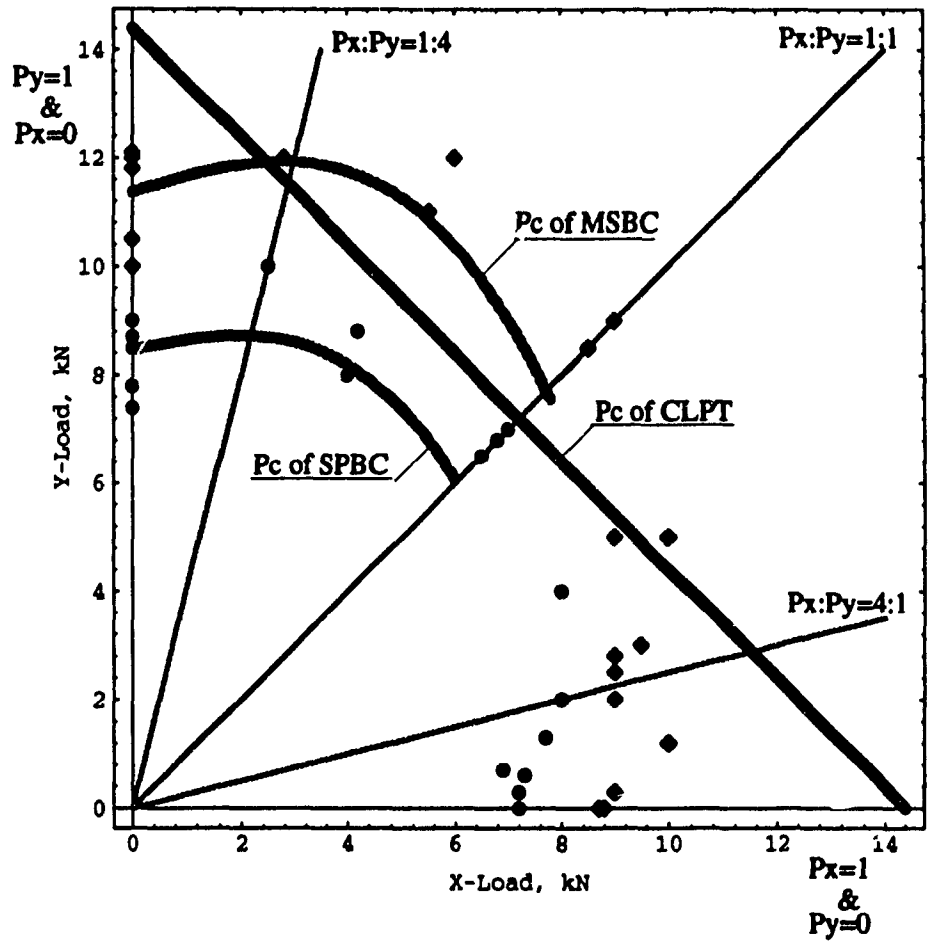

Figure 7.15: Experimental determination of the buckling initiation load from SPBC (Southwell Plot Buckling Criterion) and ultimate load from MSBC (Minimum Slope of Buckling Criterion) for OP-20-63 plate with (60/-30)x5, under various loadings.

7.4.3 Mode Jumping Analysis

As shown in the Figures 5-12, 5-15, 5-20~5-21, 5-37, 5-40~5-41, buckling mode jumping phenomenon was obtained with N-FEA for the orthotropic plates having a higher stiffness ratio, ζ. On the other hand, this mode jumping was obtained in experimental works through the Shadow Moiré method as presented in Figure 6-20 again. Based on these numerical and experimental results, here we can analyze the mode jumping phenomenon theoretically from the stiffness ratio data in Table 3.4 and Table 3.5 directly.

For the buckling analysis of orthotropic square plate, mainly the critical buckling load value of the major axis (N_{xcr}) was considered as an important design parameter. However, the critical load on the minor axis (N_{ycr}) is also important because it also attribute to the mode jumping phenomenon.

Now, we can obtain the critical buckling load equation along minor axis as the same manner of equation (2.35) as follow,

$$\begin{aligned} N_{ycr} &= \frac{\pi^2[D_{11}n^4 + 2(D_{12} + 2D_{66})n^2m^2R^2 + D_{22}m^4R^4]}{R^2b^2(n^2 + km^2R^2)} \\ P_{ycr} &= \int_0^a N_{ycr}dx \\ R &= \frac{a}{b} \\ k &= \frac{N_x}{N_y} \end{aligned} \tag{7.2}$$

where $R = 1$ and $k = 0$ in case of y-axis uniaxial loading. Therefore, above equation can simplified as following equations with allowing the variation of m and m :

$$N_{ycr} = \frac{\pi^2[D_{11}n^4 + 2(D_{12} + 2D_{66})n^2m^2 + D_{22}m^4]}{b^2(n^2)}$$
$$P_{ycr} = \int_0^a N_{ycr}dx \tag{7.3}$$

In this critical buckling load formulation, our concerning point is to find the the minimum value of N_{ycr} for the various laminated composite plates. Generally, in the balanced composite laminate, the minimum value of N_{ycr} can be obtained from the first buckling mode condition, i.e., $m = 1$ and $n = 1$. However, in case that the orthotropic plate has a higher stiffness ratio as appeared in Table 3.5, m and n are not the same value.

Some useful analyses for the mode jumping were presented for OP-16-71 and OP-16-80 in Figure 7-16, where we can find a higher mode shape corresponding to the minimum value of critical buckling load, N_{ycr}.

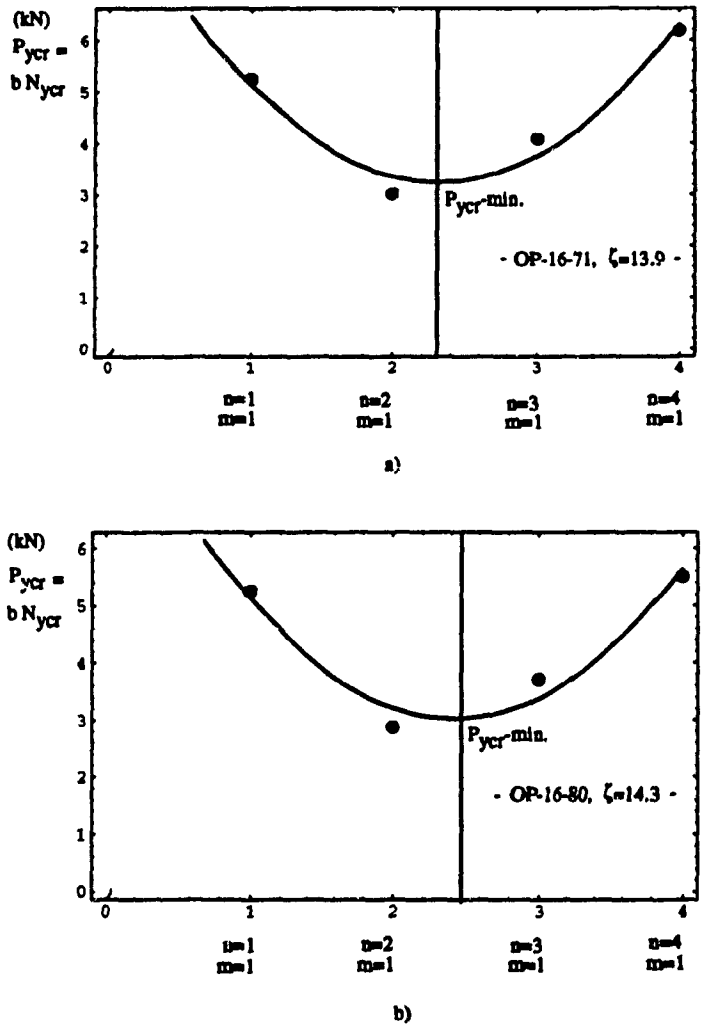

Figure 7.16: Mode jumping analysis for the orthotropic laminates having higher stiffness ratios, a)for OP-16-71 plate, b)for OP-16-80 plate.

Chapter 8

Contributions and Conclusions

Through the whole research on the buckling of biaxially loaded laminated composite plates, some important remarks can be made in the following. It was shown that the biaxial buckling analysis produces more relevant design data for the applications of laminated composite plates in dynamic structures constructions. Unified design parameters can be obtained for various loading conditions with one time experiment of biaxial buckling. A useful biaxial buckling testing methodology was introduced and its admissibility was verified from numerical analyses and experiments. Several contributions are summarized as followings.

- A modified plate specimen has been developed to determine the biaxial buckling behaviour of composite plates by experiment. With small modifications, a_c/a less than 7.5%, the critical buckling load reductions due to the modification of plate model are not severe. This means the modified plate specimen is an admissible model for the determination of biaxial buckling behaviour and the critical buckling load in the experiments.

- Through the analyses for the boundary conditions, it was found that analyses with the uniform pressure loading condition rendered solutions that agrees better with the experimental results than with uniform end-shortening condition.

- The effects of load ratio k on the biaxial buckling behaviour of laminated composite rectangular plates were found. From the results, it is observed that the buckling behaviour is affected by the combinations of axial loads. The critical buckling load decreased exponentially when the axial load ratio was changed from zero to one, i.e., from uniaxial loading state to full biaxial loading state.

- The flexural stiffness ratio, ζ, and inplane stiffness ratio, ξ, govern the postbuckling mode. In case of a high value of flexural stiffness ratios, $\zeta \geq 12.8$, a mode jumping was obtained.

- A new buckling criterion, MSBC (Minimum Slope Buckling Criterion) was proposed by the author to determine the ultimate loads for plates in the postbuckling state.

Bibliography

[1] Lekhnitskii, S. G. *Anisotropic Plates.* translated from Russian by Tsai, S. W. and Cheron, T., Gordon and Breach Science Publishers, Inc., New York, second edition, 1968.

[2] Leissa, A. W. "Buckling of Laminated Composite Plates and Shell Panels". AFWAL-TR-85-3069, Final Report for Flight Dynamics Lab., Wright-Patterson Air Force Base, Ohio, pp.439, 1985.

[3] Ashton, J. E. and Whitney, J. M. *Theory of Laminated Plates.* Technomic Publishing Co., Stamford, Conn., U.S.A., 1970.

[4] Whitney, J. M. *Structural Analysis of Laminated Anisotropic Plates.* Technomic Publishing Co., Lancaster, Penn., U.S.A., 1987.

[5] Ashton, J. E. and Waddoups, M. E. "Analysis of Anisotropic Plates". *Journal of Composite Materials*, 3:pp.148–165, 1969.

[6] Ashton, J. E. "Analysis of Anisotropic Plates II". *Journal of Composite Materials*, 3:pp.470–479, 1969.

[7] Whitney, J. M. "Fourier Analysis of Clamped Anisotropic Plates". *Trans. ASME, J. of Applied Mechanics*, 38:pp.530–532, 1971.

[8] Whitney, J. M. and Leissa, A. W. "Analysis of a Simply Supported Laminated Anisotropic Rectangular Plates". *AIAA Journal*, 8(1):pp.28–33, 1970.

[9] Leissa, A. W. "A Review of Laminated Composite Plates Buckling". *Applied Mechanics Reviews, ASME Book No. AMR019*, 40(5):pp.261–270, May 1987.

[10] Von Karman, Th. "Festigkeitsprobleme im Maschinenbau". *Encyk. der Math. Wiss.*, Vol. IV(4):pp.348–352, 1910.

[11] Von Karman, Th., Sechler, E. E. and Donnell, L. H. "The Strength of Thin Plates in Compression". *Trans. ASME*, 54:pp.53–57, 1932.

[12] Cox, H. L. "The Buckling of Thin Plates in Compression". *R. & M. No.1554, British A.R.C.*, 1933.

[13] Timoshenko, S. P. and Gere, J. M. *Theory of Elatic Stability.* McGraw-Hill Book Co., second edition, 1962.

[14] K. Marguerre. "The Apparent Width of the Plate in Compression". Technical report, English Translation, NACA, TM 833, 1937.

[15] Minguet, P. J., Dugundji, J. and Lagace, P. "Postbuckling Behavior of Laminated Plates Using a Direct Energy-Minimization Technique". *AIAA Journal*, 27(12):pp.1785–1792, 1989.

[16] Levy, S. "Buckling of Rectangular Plates With Built-In Edges". *Trans. ASME, J. of Applied Mechanics*, 9:pp.A171–A174, 1942.

[17] Coan, J. M. "Large Deflection Theory for Plates with Small Initial Curvature Loaded in Edge Compression". *Trans. ASME, J. of Applied Mechanics*, 18:pp.143–151, 1951.

[18] Yamaki, N. "Post-Buckling Behavior of Rectangular Plates with Small Initial Curvatures Loaded in Edge Compression" *Trans. ASME, J. of Applied Mechanics*, 26:pp.407–414, 1959.

[19] Yusuff, S. "Large Deflection Theory for Orthotropic Rectangular Plates Subjected to Edge Compression". *Trans. ASME, J. of Applied Mechanics*, 19:pp.446–450, 1952.

[20] Harris, G. Z. "Buckling and Postbuckling of Orthotropic Plates". *AIAA Journal*, 14(11):pp.1505–1506, 1976.

[21] Prabhakara, M. K. and Chia, C. Y. "Postbuckling of Angle-Ply and Anisotropic Plates". *Ingenieur-Archiv*, 45:pp.131–140, 1976.

[22] Prabhakara, M. K. "Post-Buckling Behaviour of Simply-Supported Cross-Ply Rectangular Plates". *Aeronautical Quarterly*, 27(4):pp.309–316, November 1976.

[23] Stein, M. "Loads and Deformations of Buckled Rectangular Plates". Technical Report R-40, NASA, Langley Research Center, Hampton, Virginia, 1959.

[24] Chandra, R. and Raju, B. B. "Postbuckling Analysis of Rectangular Orthotropic Plates". *Int. J. Mech. Sci.*, 15:pp.81–97, 1973.

[25] Walker, A. C. "The Post-Buckling Behaviour of Simply Supported Squareplates". *Aeronautical Quarterly*, 20:pp.203–222, 1969.

[26] Rhodes, J. and Harvey, J. M. "Plates in Uniaxial Compression with Various Support Conditions at the Unloaded Edges". *Int. J. Mech. Sci.*, 13:pp.787–802, 1971.

[27] Stein, M. "Postbuckling of Orthotropic Composite Plates Loaded in Compression". *AIAA Journal*, 11(12):pp.1729–1735, 1983.

[28] Turvey, G. J. and Wittrick, W. H. "The Large Deflection and Post-Buckling Behavior of Some Laminated Plates". *Aeronautical Quarterly*, 24:pp.77–86, May 1973.

[29] Chia, C. Y. *Nonlinear Analysis of Plates.* McGraw-Hill Inc., New York, 1980.

[30] Harris, G. Z. "The Buckling and Postbuckling Behaviour of Composite Plates Under Biaxial Loading". *Int. J. Mech. Sci.*, 17:pp.187–202, 1975.

[31] Turvey, G. J. "Biaxial Buckling of Moderately Thick Laminated Plates". *J. Strain Analysis*, 12(2):pp.89–95, 1977.

[32] Tung, T. K. and Surdenas, J. "Buckling of Rectangular Orthotropic Plates under Biaxial Loading". *Journal of Composite Materials*, 21:pp.124–128, 1987.

[33] Lo, K. H., Christensen, R. M. and Wu, E. M. "A High-Order Theory of Plate Deformation, Part 1: Homogeneous Plates". *Trans. ASME, J. of Applied Mechanics*, 44:pp.663–668, December 1977.

[34] Lo, K. H., Christensen, R. M. and Wu, E. M. "A High-Order Theory of Plate Deformation, Part 2: Laminated Plates". *Trans. ASME, J. of Applied Mechanics*, 44:pp.669–676, December 1977.

[35] Reddy, J. N. "A Refined Nonlinear Theory of Plates with Transverse Shear Deformation". *Int. J. Solids Structures*, 20:pp.881–896, 1984.

[36] Reddy, J. N. "A Refined Shear Deformation Theory for the Analysis of Laminated Plates". Contractor Report 3955, NASA, Viginia Polytechnic Institute and State University, Blacksburg, Virginia, 1986.

[37] Cho, K. N., Striz, A. G. and Bert, C. W. "Bending Analysis of Thick Bimodular Laminates by Higher-Order Individual-Layer Theory". *Composite Structures*, 15:pp.1–24, 1990.

[38] Chang, J. S. and Huang, Y. P. "Geometrically Nonlinear Static and Transiently Dynamic Behavior of Laminated Composite Plates Based on a Higher Order Displacement Field". *Composite Structures*, 18:pp.327–364, 1991.

[39] Moazzami, M. and Sandhu, R. S. "A Higher Order Discrete Theory for Laminated Plates". *Composite Structures*, 23:pp.205–220, 1993.

[40] Kant, T., Pavichandran, R. V., Pandya, B. N. and Mallikarrjuna. "Finite Element Transient Dynamic Analysis of Isotropic and Fiber Reinforced Composite Plates Using a Higher-Order Theory". *Composite Structures*, 9:pp.319–342, 1988.

[41] Yuan, F. G. and Miller, R. E. "A Higher Order Finite Element for Laminated Beam". *Composite Structures*, 14:pp.125–150, 1990.

[42] Berger, H. M. "A New Approach to the Analysis of Large Deflection of Plates". *Trans. ASME, J. of Applied Mechanics*, 22:pp.465–472, 1955.

[43] Zaghloul, S. A. and Kennedy, J. B. "Nonlinear Behavior of Symmetrically Laminates Plates". *Trans. ASME, J. of Applied Mechanics*, 42:pp.234–236, 1975.

[44] Sathyamoorthy, M. "Vibration of Plates Considering Shear and Rotatory Inertia". *AIAA Journal*, 16:pp.285–286, 1978.

[45] Timoshenko, S. P. and Woinowsky-Krieger, S. *Theory of Plate and Shells.* McGraw-Hill Book Co., second edition, 1959.

[46] Szilard, R. *Theory and Analysis of Plates.* Prentice-Hall, New Jersey, 1974.

[47] Elzein, A. *Plate Stability by Boundary Element Method.* Lecture Note in Engineering, Vol.64, Springer-Verlag, 1991.

[48] Laschet, G. and Jeusette, J. P. "Postbuckling Finite Element Analysis of Composite Panels". *Composite Structures*, 14:pp.35–48, 1990.

[49] Chen, W.-H. and Yang, S.-H. "Buckling Analysis of General Composite Laminates by Hybrid-Stress Finite Element Method". *AIAA Journal*, 29(1):pp.140–147, 1991.

[50] Swanson Anaysis Systems, Inc. *ANSYS User's Manuals for Rev. 4.4A & Rev. 5.0.* Swanson Anaysis Systems, Inc., Houston, U.S.A., 1993.

[51] J. F Mandell. "An Experimental Investigation of the Buckling of Anisotropic Fiber Reinforced Plastic Plates". AFML-TR-68-281 pp.315, Technical Report for Air Force Materials Lab., Wright-Patterson Air Force Base, Ohio, 1968.

[52] Ashton, J. E. and T. S. Love. "Experimental Study of the Stability of Composite Plates". *Journal of Composite Materials*, 3:pp.230–243, 1969.

[53] Spier, E. E. "Stability of Graphite/Epoxy Structures with Arbitrary Symmetrical Laminates". *Experimental Mechanics*, xx:pp.401–408, November 1978.

[54] Englestad, S. P., Reddy, J. N. and Knight Jr., N. F. "Postbuckling Response and Failure Prediction of Graphite-Epoxy Plates Loaded in Compression". *AIAA Journal*, 30(8):pp.2106–2113, 1992.

[55] Chai, G. B., Banks, W. M. and Rhodes, J. "An Experimental Study on Laminated Panels in Compression". *Composite Structures*, 19:pp.67–87, 1991.

[56] Libove, C. "Buckling Pattern of Biaxially Compressed Simply Supported Orthotropic Rectangular Plates". *Journal of Composite Materials*, 17:pp.45–48, 1983.

[57] Bathe, K. J. *Finite Element Procedures in Engineering Analysis.* Prentice-Hall Inc., Englewood Cliffs, 1982.

[58] Tsai, S. W. and Hahn H. T. *Introduction to Composite Materials.* Technomic Publishing Co., Lancaster, Pennsylvania, 1980.

[59] Tsai, S. W. *Theory of Composite Design.* Think Composites, Dayton, Ohio, 1992.

[60] Southwell, R. V. "On the Analysis of Experimental Observations in Problems of Elastic Stability". In *Proc. of the Royal Society of London*, number Vol. 135 in A, pages pp.601–616. Harrison and Sons, LTD, 1932.

[61] Kim, Y. S. and Hoa, S. V. "Biaxial Buckling Behavior of Composite Rectangular Plates". *The 2nd International Symposium on Composite Materials and Structures (ISCMS), Beijing, China, Edited by Sun, C. T. and Loo, T. T.*, pp.495-500, 1992.

[62] Kim, Y. S. and Hoa, S. V. "Effects of Load Combination on Biaxial Buckling of Laminted Composite Rectangular Plates. *Proceedings of the 9th International Conference on Composite Materials(ICCM/9), Madrid, Spain, Edited by A. Miravete*, Vol. IV, pp.495-502, 1993.

[63] Kim, Y. S. and Hoa, S. V. "Postbuckling Behavior of Simply Supported Composite Rectangular Plates Under Biaxial Loading. *The Second Canadian International Conference on Composites(CANCOM'93) Ottawa, Canada*, pp.787-797, Sept., 1993.

[64] Kim, Y. S. and Hoa, S. V. "Biaxial Buckling Behaviour of Composite Rectangular Plates". *Composite Structures*, Accepted in Nov., 1993.

[65] Kim, Y. S. and Hoa, S. V. "Effects of Stacking Sequence on the Biaxial Buckling of Laminated Composite Plates. *International Conference on Design and Manufacturing Using Composites(ATMAM'94), Montreal, Canada*, pp.365-374, Aug., 1994.